

Assessing the impact of motion on treatment planning during stereotactic body radiotherapy of lung cancer

LEON DUNN

BSc (Hons) Applied Physics

A thesis submitted in fulfilment of the requirements for the
degree of Doctor of Philosophy

School of Applied Science
College of Science, Engineering and Health
RMIT University
May 2013

DECLARATION

I certify that except where due acknowledgement has been made, the work is that of the author alone; the work has not been submitted previously, in whole or in part, to qualify for any other academic award; the content of the thesis is the result of work which has been carried out since the official commencement date of the approved research program; any editorial work, paid or unpaid, carried out by a third party is acknowledged; and, ethics procedures and guidelines have been followed.

Leon Dunn

31st of May 2013

DEDICATION

This dissertation is dedicated to my parents, Helen and Carl

Thank you for everything...

“What one fool can do, another can.”

- Ancient Simian proverb

PUBLICATIONS AND PRESENTATIONS ARISING FROM THIS WORK

Results of this work have been published and presented. The design and validation of two phantoms have been described in:

- **L. Dunn**, T. Kron, P. Johnston, L. McDermott, M. Taylor, J. Callahan, R. Franich, "A programmable motion phantom for quality assurance of motion management in radiotherapy". Australasian Physical & Engineering Sciences in Medicine, **v35**, pp93-100, 2012.
- **L. Dunn**, T. Kron, M. Taylor, J. Callahan and R. Franich, "A phantom for testing of 4D-CT for radiotherapy of small lesions," Medical physics, **v39**, pp5372-5384, 2012.

The affects of motion on imaging and treatment planning appear in:

- **L. Dunn**, T. Kron, M. Taylor, J. Callahan and R. Franich, "A phantom for testing of 4D-CT for radiotherapy of small lesions," Medical physics, **v39**, pp5372-5384, 2012.

The upgraded QUASAR respiratory motion phantom platform described in this work has been utilised in the following:

- T. Kron, N. Clements, Y. Aarons, **L. Dunn**, B. Chesson, J. Miller, K. Roozen and D. Ball, "Radiochromic film for individual patient QA in extracranial stereotactic lung radiotherapy," Radiation Measurements, **v46**, pp1920-1923, 2011.
- J. Callahan, D. Binns, **L. Dunn** and T. Kron, "Motion effects on SUV and lesion volume in 3D and 4D PET scanning," Australasian Physical & Engineering Science in Medicine, **v34**, pp489-495, 2011.
- Clements, N., T. Kron, R. Franich, **L. Dunn**, P. Roxby, Y. Aarons, B. Chesson, S. Siva, D. Duplan, and D. Ball. "The effect of irregular breathing patterns on internal target volumes in four-dimensional CT and cone-beam CT images in the context of stereotactic lung radiotherapy." Medical Physics, **v40**, 021904, 2013.

Monte Carlo modelling aspects of this work have been described in:

- M. Taylor, **L. Dunn**, T. Kron, F. Height and R. Franich, "Determination of peripheral underdosage at the lung-tumor interface using Monte Carlo radiation transport calculations," *Medical Dosimetry*, **v37**, pp61-66, 2011.

The following publications are in preparation and arise directly from this work:

- **L Dunn**, J Callahan, T Kron and RD Franich, The effect of motion on images acquired with PET: A Monte Carlo study with GATE and the XCAT phantom, *Medical Physics*, (in prep)
- **L Dunn**, T Kron, ML Taylor and RD Franich, Is dose calculation on an average intensity projection sufficient for radiation therapy of a moving target? A Monte Carlo investigation, in prep.

The following work pertaining to this thesis has been presented at conferences:

-2011-

- **L Dunn**, ML Taylor, R Smith, T Kron and RD Franich, *Modelling lung tumour motion in Geant4: A Monte Carl model of the QUASAR respiratory motion phantom*, Engineering and Physical Sciences in Medicine (EPSM) 14-18 2011, Darwin, Australia
- **L Dunn**, T Kron, ML Taylor and RD Franich, *A lung equivalent insert for a moving phantom to study dose in extracranial stereotactic radiotherapy for lung cancer*, Engineering and Physical Sciences in Medicine (EPSM) 14-18 2011, Darwin, Australia
- ML Taylor, **L Dunn**, F Height, T Kron and RD Franich, *Characterisation of lung tumour underdosage for interpretation of clinical trial data*, Engineering and Physical Sciences in Medicine (EPSM) 5-9 2010, Melbourne, Australia
- **L Dunn**, T Kron, RD Franich and ML Taylor, *Dosimetric consequences of planning on the average*, Engineering and Physical Sciences in Medicine (EPSM) 5-9 2010, Melbourne, Australia
- T Kron, N Clements, Y Aarons, **L Dunn**, B Chesson, J Miller, K Roozen and D Ball ,

Radiochromic Film for Quality Assurance for Individual Patients in Extracranial Stereotactic Lung Radiotherapy, 16th Solid State Dosimetry (SSD) Conference, 15 – 18 Sep 2010, Sydney, Australia

- ML Taylor, **L Dunn**, T Kron and RD Franich, *Dose inhomogeneity in radiotherapy of lung tumours: Calculation of peripheral underdosage*, European Society for Therapeutic Radiology and Oncology (ESTRO), 12 -16 Sep 2010, Barcelona, Spain
- **L Dunn**, T Kron and RD Franich, *See-saw motion phantom for 4D-CT QA*, American Association of Physicists in Medicine (AAPM), 18 – 22 July 2010, Philadelphia, USA

The following work arising from this thesis has been presented at seminars and workshops:

-2010-

- The delivery of radiation to moving targets: A physical model for the detection and treatment of tumours affected by respiratory motion, seminar for Prof. R. Mackie: RMIT University, Melbourne, Australia
- High resolution dosimetry at interfaces of dissimilar media using Geant4: A Geant4 Monte Carlo study. GEANT4 users' workshop, Wollongong, Australia.

-2011-

The NCAT phantom, Peter MacCallum Cancer Centre, Melbourne, Australia

Table of Contents

CHAPTER 1. INTRODUCTION	7
1.1. Propositum.....	9
1.2. Cancer.....	9
1.2.1. Lung cancer	9
1.3. External beam radiotherapy.....	10
1.4. The radiotherapy process.....	11
1.5. Imaging and diagnosis.....	11
1.5.1. Computed Tomography (CT)	11
1.5.2. Positron Emission Tomography (PET).....	15
1.6. Treatment planning in external beam radiotherapy	16
1.6.1. Organs at Risk (OAR)	18
1.6.2. Dose specification.....	19
1.6.3. Treatment plan evaluation	19
1.7. Treatment delivery in external beam radiotherapy	20
1.7.1. Image-Guided Radiation Therapy.....	21
1.8. Treatment Verification.....	21
1.9. Quality assurance in external beam radiotherapy	22
1.10. Stereotactic Body Radiation Therapy (SBRT).....	22
1.10.1. Introduction	22
1.10.2. SBRT	22
1.11. Radiation delivery to a moving target.....	25
1.11.1. Complications due to motion of lung tumours in conventional radiotherapy.....	25
1.11.2. Lung cancer SBRT and tumour motion: The current problem	26
1.12. Aim & objectives.....	28
Objective 1: Assess the effect of motion on the identification and delineation of small, moving tumours.	28
Objective 2: Quantify the influence of lesion size and motion amplitude on data acquired from 4D-CT	28
Objective 3: Determine the degree to which the same relationships affect PET data if and when this imaging modality is incorporated into the treatment planning process.....	28
Objective 4: To assess the mitigation of motion effects in PET that can be achieved by implementing 4D phase-binned PET	28
Objective 5: To evaluate dose calculation on lung tumours, in particular quantifying the differences between 4D calculations, which explicitly account for dynamic geometry and conventional 3D calculation, based on average intensity projection data from 4D-CT.....	28
1.13. Approach	28
CHAPTER 2. LITERATURE REVIEW: MOTION MANAGEMENT IN RADIOTHERAPY	31
2.1. Introduction	33
2.2. Intrafractional tumour motion.....	33
2.2.1. Biomechanics of breathing	33
2.2.2. Magnitude of lung tumour motion caused by respiratory function.....	34
2.3. The effect of intrafractional tumour motion during imaging	39
2.3.1. Introduction	39
2.3.2. The effect of tumour motion on images acquired with Computed Tomography	39
2.3.2.1 Artifacts in conventional CT.....	40
2.3.2.1.1. Physics based artifacts	40
2.3.2.1.2. Scanner based artifacts.....	40

2.3.2.1.3. Reconstruction based artifacts	41
2.3.2.1.4. Patient based artifacts	41
2.3.2.2 Artifacts and the effect of motion in 4D-CT.....	42
2.3.3. The effect of tumour motion on images acquired with Positron Emission Tomography (PET)...	44
2.3.3.1 PET used in conjunction with CT (PET/CT).....	44
2.4. The effect of tumour motion on radiation delivery.....	45
2.5. Concepts of motion management in radiotherapy	46
2.5.1. Surrogate markers.....	46
2.5.2. Respiratory gating	48
2.5.2.1 Gating based on external surrogates.....	48
2.5.2.2 Gating based on internal fiducial markers	49
2.5.3. Breath hold techniques	49
2.5.3.1 Voluntary breath-hold methods	49
2.5.4. Mechanically assisted motion reduction methods	51
2.5.5. Biofeedback for improving respiratory regularity	52
2.6. Motion management during imaging for treatment planning	53
2.6.1. Motion management for CT	53
2.6.1.1 Slow CT scanning.....	53
2.6.1.2 Time-resolved CT (4D-CT).....	54
2.6.1.2.1. Prospective gated CT imaging.....	56
2.6.1.2.2. Retrospective (image space) sorting.....	56
2.6.2. Motion management for PET	58
2.6.2.1 Gated PET	58
2.7. Motion management during treatment delivery.....	59
2.7.1. Real-time tumour tracking.....	59
2.7.1.1 Target tracking using imaging (identifying the target).....	60
2.7.1.2 Tracking using internal fiducial markers.....	60
2.7.1.3 Predicting the target location using external surrogate markers	60
2.7.1.4 Forward prediction and latency reduction	61
2.7.1.5 Dynamic delivery of the treatment beam.....	61
2.8. Motion management quality assurance devices: Phantoms.....	62
2.9. difficulties in dose calculation for sbrt	63
2.9.1. Radiation equilibrium.....	63
2.9.1.1 Charged particle equilibrium.....	65
2.9.1.2 Transient charged particle equilibrium	65
2.9.2. Current problems associated with dose calculation in SBRT of lung lesions: Dosimetry considerations.....	66
2.9.2.1 Current problems associated with dose calculation in SBRT of lung lesions: Heterogeneity calculations in small-fields	66
2.10. Monte Carlo simulation and respiratory induced tumour motion.....	67
2.10.1. Dose calculation using Monte Carlo methods	67
2.10.2. Currently available Monte Carlo codes	68
2.10.3. Monte Carlo radiation transport codes employed in this work.....	69
2.10.3.1 Geant4.....	69
2.10.3.1.1. The accuracy of Geant4.....	73
2.10.3.2 GATE	74
2.10.3.2.1. Software architecture	75
2.10.3.2.2. Systems available for simulation	76
2.10.3.2.3. Geometry	77
2.10.3.2.4. Physics.....	78
2.10.3.2.5. Production cuts	79
2.10.3.2.6. Positron emission.....	79
2.10.3.2.7. Radioactive sources	80

2.10.3.3 The NURBS based CARDiac and Torso (NCAT) and eXtended CARDiac and Torso (XCAT) phantoms.....	80
2.10.3.4 Using the NCAT or XCAT phantom in conjunction with GATE.....	83
2.10.3.5 EGSnrc.....	83
2.10.3.5.1. Radiation interactions in EGSnrc.....	83
2.10.3.5.2. The accuracy of EGSnrc.....	85
2.10.4. Monte Carlo simulation and tumour motion.....	85
2.10.5. Stereotactic radiotherapy and tumour motion.....	86
2.10.6. Key points.....	86
CHAPTER 3. THE DEVELOPMENT OF MOTION PHANTOMS.....	88
3.1. Introduction.....	90
3.1.1. Surrogate markers.....	90
3.1.1.1 The Varian RPM system.....	90
3.1.1.2 Phillips Bellows system.....	93
3.1.2. MATLAB.....	93
3.2. Development of motion phantoms - The see-saw motion phantom.....	93
3.2.1. Materials.....	94
3.2.2. Methods.....	97
3.2.2.1 Validation of a mathematical model defining the AP and SI motion profiles.....	97
3.2.2.2 Inter-vendor compatibility tests: GE Discovery STE PET/CT acquisition methodology.....	97
3.2.3. Results – The see-saw motion phantom.....	97
3.2.3.1 Accuracy of the motion model.....	99
3.2.3.2 Compatibility of the see-saw phantom with different acquisition protocols.....	101
3.2.4. Discussion – The see-saw motion phantom.....	102
3.3. Development of motion phantoms: The QUASAR respiratory motion phantom upgrade.....	103
3.3.1. Materials.....	103
3.3.1.1 The QUASAR Respiratory motion phantom from Modus Medical.....	103
3.3.1.2 Upgrade components: Mot-102 stepper motor.....	104
3.3.1.3 Upgrade components: M325 micro-stepping driver.....	105
3.3.1.4 Upgrade components: Stepper Motor Controller Model kta-190.....	105
3.3.1.5 Upgrade components: Separate chest-wall motion platform.....	106
3.3.2. Methods.....	107
3.3.2.1 Control system and hardware upgrade.....	107
3.3.2.2 Software development for motion control.....	108
3.3.2.3 Respiratory pattern analysis software.....	113
3.3.3. Results – The QUASAR respiratory motion phantom upgrade.....	119
3.3.3.1 Patient replication.....	119
3.3.3.2 Test patterns.....	121
3.3.4. Discussion – The QUASAR respiratory motion phantom.....	123
CHAPTER 4. THE IMPACT OF MOTION: CT IMAGING.....	124
4.1. Introduction.....	126
4.2. Materials.....	127
4.3. Methods.....	128
4.3.1. Phillips Big Bore Brilliance CT setup.....	128
4.3.2. HU consistency of moving and stationary objects.....	129
4.3.3. MIP and AIP artifacts as a function of the number of phase-bins.....	130
4.3.4. Geometric consistency between MIP images and reality.....	130
4.4. Results.....	130
4.4.1. HU consistency between moving and stationary objects.....	130
4.4.2. The quality of MIP and AIP with respect to the number of phase-bins.....	133
4.4.3. XCAT simulations of the undersampling effect as a function of lesion size.....	138
4.4.4. The geometrical consistency of MIP images.....	140
4.5. Discussion.....	142

4.5.1. Inter-phase variation in HU	142
4.5.2. The accuracy of projections from 4D-CT	142
4.6. Concluding remarks on the effect of motion on images obtained from 4D-CT	144
CHAPTER 5. THE IMPACT OF MOTION: PET IMAGING	146
5.1. Introduction	148
5.2. Background	149
5.3. MATERIALS	151
5.3.1. Experimental materials	151
5.3.2. Monte Carlo materials	152
5.4. Methods	152
5.4.1. Experimental methods	152
5.4.1.1 Phantom	152
5.4.1.2 Data acquisition	153
5.4.1.3 Data analysis	153
5.4.2. Monte Carlo simulations	153
5.4.2.1 XCAT phantoms	153
5.4.2.2 Construction of the Phillips Allegro PET scanner	154
5.4.2.3 Incorporating the XCAT phantom into GATE	158
5.4.2.4 PET Acquisition settings	160
5.4.2.5 4D- PET simulations	160
5.4.2.6 Data output	163
5.5. Results	164
5.5.1. Experimental results	164
5.5.2. Monte Carlo and XCAT simulations	167
5.5.2.1 3D-PET GATE activity distributions for a 10:1 (tumour:background) activity ratio	168
5.5.2.2 4D simulations for a 10:1 activity ratio and 10 mm lesion size	173
5.6. Discussion	177
5.6.1. Experimental phantom study	177
5.6.2. Computational simulations to determine the effect of motion on images acquired with PET	177
5.6.3. Simulation results: GATE 3D PET Simulations	178
5.6.4. Simulation Results: GATE 4D-PET simulations	179
5.6.5. Limitations and future direction for the use of Monte Carlo and computational phantoms	180
5.6.6. Comparisons between results obtained via experimental and Monte Carlo methodologies	180
5.6.7. Comparisons to published data	181
5.6.8. Clinical consequences	182
CHAPTER 6. THE IMPACT OF MOTION: TREATMENT PLANNING	
AND DOSE CALCULATION	183
6.1. Introduction	185
6.2. Background: incorporation of 4D information into dose calculation	186
6.3. Materials	187
6.4. Methods	188
6.4.1. METHOD I: Determination of peripheral underdosage at the lung-tumor interface using Monte Carlo radiation transport calculations	188
6.4.2. METHOD II: The incorporation of 4D information into dose calculation	191
6.4.3. Computing hardware	196
6.5. Results	196
6.5.1. RESULTS I: Determination of peripheral underdosage at the lung-tumor interface using Monte Carlo radiation transport calculations	196
6.5.1.1 The dose reduction factor (DRF)	198
6.5.2. RESULTS II: The incorporation of 4D information into dose calculation	200
6.5.2.1 Comparisons between U10V and AVG: Characteristic points	200
6.5.2.2 Comparisons between U10V and AVG: DVH analysis	206

6.5.2.2.1. DVH analysis: Parallel opposed arrangement.....	207
6.5.2.2.2. DVH analysis: Single field arrangement.....	207
6.5.2.2.3. DVH analysis: Target motion perpendicular to the beam.....	208
6.5.2.2.4. DVH analysis: Dependence on motion profile	209
6.6. Discussion.....	210
6.6.1. Determination of peripheral underdosage at the lung-tumor interface using Monte Carlo radiation transport calculations – Discussion of results.....	211
6.6.2. Determination of peripheral underdosage at the lung-tumor interface using Monte Carlo radiation transport calculations – Clinical relevance	212
6.6.3. The incorporation of 4D information into dose calculation.....	213
6.6.4. Clinical application.....	216
6.6.5. Chapter summary.....	216
6.6.5.1 The Dose Reduction Factor (DRF).....	216
6.6.5.2 Dose calculation on U10V versus AVG.....	216
CHAPTER 7. CONCLUSIONS & OUTLOOK.....	218
7.1. Introduction	220
Objective 1: Assess the effect of motion on the identification and delineation of small, moving tumours.	220
Objective 2: Quantify the influence of lesion size and motion amplitude on data acquired from 4D-CT	220
Objective 3: Determine the degree to which the same relationships affect PET data if and when this imaging modality is incorporated into the treatment planning process.....	220
Objective 4: To assess the mitigation of motion effects in PET that can be achieved by implementing 4D phase-binned PET.....	220
Objective 5: To evaluate dose calculation on lung tumours, in particular quantifying the differences between 4D calculations, which explicitly account for dynamic geometry and conventional 3D calculation, based on average intensity projection data from 4D-CT.....	220
7.2. Development of motion phantoms.....	220
7.3. The impact of motion on images acquired with CT and 4D-CT.....	222
7.4. The impact of motion on images acquired with PET.....	223
7.5. The impact of motion on treatment planning and dose calculation	224
7.6. Outlook.....	225

TABLE OF FIGURES

Figure 1.1. An outline of the radiotherapy process, from imaging to treatment verification and delivery.....	11
Figure 1.2. The evolution of fan-beam to cone-beam CT in the early 2000s. Where M is the number of slices, t_{rot} is the scanner's rotational period and S is the slice width.....	14
Figure 1.3. Schematic of a 3 rd generation CT scanner showing the X-ray source and detection system moving continuously around the patient.....	15
Figure 1.4. Schematic of the ICRU Report 50 and 62 definition of treatment volumes (Podgoršak and Agency, 2005). The 'Gross Tumour Volume' (GTV) is described as the gross demonstrable extent and location of the malignant growth. The 'Clinical Target Volume' (CTV) is a tissue volume that contains a demonstrable GTV and/or subclinical malignant disease undetectable by imaging that must be eliminated. The Internal Target Volume (ITV) is a margin which is added to the CTV to account for all movements of the CTV during treatment and the 'Planning Target Volume' (PTV) is an added margin to the ITV to account for variations in patient position and beam position both intrafractionally and interfractionally.	17
Figure 1.5. Cumulative dose volume histogram, showing ideal target volume DVH, with 100% of the target receiving 100% of the prescribed dose, typical DVH shown by the solid black line and a typical organ at risk DVH (red line).	19
Figure 1.6. Schematic of an MLC showing tungsten leaves and the field projection at isocentre.	20
Figure 1.7. The potential for normal tissue sparing with MLCs. The MLC can be used to protect organs at risk whilst still maintaining adequate target coverage.....	21
Figure 1.8. Comparison of dose distributions between a 4-field conventional lung radiotherapy plan (A) and a 7-field stereotactic lung radiotherapy plan (B). (Courtesy of Brent Chesson, Radiation Therapist, Peter MacCallum Cancer Centre, Melbourne, Australia).	24
Figure 1.9. A literature search based on publications relating to stereotactic radiotherapy, both intracranial and SBRT. Note the logarithmic scale.	25
Figure 1.10. Overview of several key studies reviewed in the paper by Taylor <i>et al</i> (2011). The number of patients, N , dose, local control rate and number of fractions are shown.	26
Figure 1.11. Graph showing the consequences of prescription to a lower covering isodose. The steepness of the dose gradient when prescribing to a lower covering isodose results in greater dose heterogeneity within the tumour volume.	27
Figure 2.1. (a) A typical diaphragm motion profile and (b) the corresponding AP chest-wall motion profile..	34
Figure 2.2. A computer generated example of a tumour's SI motion as a function of the respiratory phase. These images were generated with the XCAT phantom which is discussed in Section 2.10.3.3. In these images, 0% corresponds to the peak-exhale phase and 40% corresponds to peak-inhale phase. The red dashed line represents the starting position of the mass's excursion. The lesion can be seen to move in and out of this region over a complete respiratory cycle.....	36
Figure 2.3. Six separate patients' AP chest-wall motion as a function of time showing the variability between patients, and within the breathing profiles of individual patients. Data is taken from six patients involved in the CHISEL clinical trial.	37

Figure 2.4. Six patients' phase versus chest wall amplitude variability (from Figure 2.3). This data shows each respiratory cycle overlaid on top of one another. The grouping of these traces represents the degree of respiratory regularity.	38
Figure 2.5. (a) Simulated CT using the XCAT phantom for a static anatomy, (b) Simulated CT of a moving anatomy showing the distortion due to motion.....	42
Figure 2.6. A schematic diagram of the construction of the MIP and AIP data-sets. To form the MIP, the maximum voxel value across all ten phase-bins is derived; the voxel with the maximum then becomes the corresponding voxel on the MIP. Conversely, for the AIP, the mean value is taken.	55
Figure 2.7. To achieve retrospective 4D-CT, CT data is tagged with the time stamp which is then compared to the respiratory cycle data. For example, if one wanted to reconstruct a slice corresponding to peak-inhale, then that point is tagged in the raw data and the data from $\pm 90^\circ$ + the fan angle is then binned into the peak-inhale data-set. This data corresponds to 180° gantry rotation, which is the minimum rotation needed to collect enough data for reconstruction. Adapted from (Wolthaus, 2009).	57
Figure 2.8. Time-resolved CT in a retrospective cine acquisition. The couch stays still during acquisition (multiple steps) and there is a continuous acquisition of slices for the time interval equal to the cine length plus the slice acquisition time. The beam is then switched off and the couch moves to the next position. After the complete volume is imaged, reconstructed slices are then sorted based on either the respiratory phase or amplitude. Adapted from (Riegel, Chang <i>et al.</i> , 2009).....	58
Figure 2.9. The standard QUASAR respiratory motion phantom. 1D sinusoidal motion with coupled chest-wall motion is possible with this phantom. Since patient lesion motion is often complex, it would be beneficial if complex programmable motion could be simulated, thus providing a more clinically relevant simulation platform. The dashed lines represent the directions of movement for the moving parts.....	63
Figure 2.10. The top level class diagram of the Geant4 toolkit adapted from (Agostinelli, Allison <i>et al.</i> , 2003)	70
Figure 2.11. The structure of GATE, adapted from (Jan, Santin <i>et al.</i> , 2004).....	76
Figure 2.12. (a) Male and (b) female renderings of the XCAT phantom with different levels of detail shown building up to the complete model. The skeletal muscles, circulatory system, organs and glands are shown. Adapted from (Segars, Sturgeon <i>et al.</i> , 2010).	81
Figure 2.13. (a) Posterior, (b) anterior and (c) saggittal renderings of the XCAT phantom showing the anatomical realism of the organs and their placements. Adapted from (Segars, Mahesh <i>et al.</i> , 2008).....	82
Figure 2.14. Modeling of respiratory motion in the XCAT phantom. Adapted from (Segars, Sturgeon <i>et al.</i> , 2010).....	82
Figure 2.15. Series of XCAT CT images showing a tumour in the left lung. Five different phases of respiratory motion are shown. The red dashed lines indicate the deviation of the position of the tumour from the 0% phase of the respiratory cycle.	82
Figure 3.1. The Varian RPM's infrared camera system capturing the motion of a reflective marker placed on the patient's abdomen and the resulting waveform showing the position of the marker as a function of time. 91	
Figure 3.2. Respiratory motion data output from the RPM system. (a) The amplitude of the reflective marker as a function of time (arbitrary units). (b) The phase of the patient's respiratory cycle as a function of time (arbitrary units) and (c) the amplitude as a function of phase.....	92
Figure 3.3. An illustration of the Phillips Bellows system. The expansion and contraction of the chest-wall	

cause the pressure inside the belt to change, which, in turn is converted to a respiratory signal.	93
Figure 3.4. (a) An experimental QA setup designed to compare moving and static HUs within the FOV. (b) An overlay of the see-saw phantom’s motion profile. In this image, the AP motion platform can be seen. This adjustable platform, along with the adjustable anterior-posterior platform, provides coupled motions in two dimensions.....	96
Figure 3.5. Schematics of the see-saw motion phantom (dimensions (l x w x h): 30 x 15 x 15 cm). Variables which determine the motion of the phantom are shown in blue with dash-dot lines representing adjustments that can be made to change the amplitude of motion in both AP and SI directions.	96
Figure 3.6. The phantom’s AP motion profile. The solid blue line indicates the profile as recorded by the Varian RPM system and the red line indicates the motion described by Equation 3.1. (a) Large amplitude motion with the drive wheel close to the central pivot point, (b-f) the five other drive wheel locations in order of increasing distance from the central pivot (decreasing amplitude).	100
Figure 3.7. A phantom SI platform motion profile. The blue line shows the motion profile as measured with the RPM and the red line shows the profile as modelled by Equation 3.2.	101
Figure 3.8. Sagittal reconstructions of (a) stationary see-saw phantom. (b) 3D Helical acquisition with moving phantom, amplitude 2.0 cm period 4 s, (c) AIP from a 4D-CT (cine mode) reconstructed into ten distinct phase-bins and (d) MIP from a 4D-CT (cine mode) acquisition. In the AIP and the MIP, the motion amplitude was 2 cm in the AP direction with a period of 4 s. The amplitude of the platform in the SI direction was 2.5 cm.....	101
Figure 3.9. (a) The standard QUASAR respiratory motion phantom shell without any inserts or motion control systems (b) The QUASAR™ respiratory motion phantom from Modus Medical shown with moving insert and standard motion control system.	104
Figure 3.10. Custom built separate chest-wall motion platform. Showing the stepper motor, Teflon guide bushes and custom made 3 mm pitch raising / lowering screw.....	107
Figure 3.11. The control architecture for the upgraded QUASAR phantom. A PC with custom software is used to communicate with a serial stepper motor controller. The serial stepper motor controller then sends pulse signals to the M325 stepper motor driver which in turn sends step signals to the motor.....	107
Figure 3.12. Wiring diagram for the components that make up the control system.	108
Figure 3.13. Version 1.1 of the Graphical User Interface of the motor control software. Key features are highlighted with details of the various functions outlined in Section 3.3.2.2.....	110
Figure 3.14. Demonstration of the need for a moving average filter to smooth RPM prior to peak detection for respiratory cycle analysis to be effective.....	111
Figure 3.15. Peak detection: The location of the maxima and minima detected by the code is shown overlaid on a patient’s respiratory trace. The green line shows a line connecting all locations of the maxima and the red line shows a line connecting all locations of the minima.	111
Figure 3.16. (a) A single breath recorded with the RPM system. (b) The trace in (a) broken down into 10 points (blue crosses) between successive minima. The x-axis show the arbitrary time base and the y-axis shows arbitrary amplitude.	112
Figure 3.17. Examples of motion patterns that can be designed by the user. (a) A continuous prostate target drift as described by (Kupelian, Willoughby <i>et al.</i> , 2007). (b) A commonly seen respiratory pattern where the	

duration of inhale is less than the duration of exhale. (c) The inverse of (b), where the inhale period is longer than the exhale period. (d) A breath-hold scenario where a single breath is replicated before a 10-second breath-hold..... 113

Figure 3.18. GUI of respiratory analysis software, showing the imported trace from the Varian RPM system, the baseline drift of the trace, as selected by the drop-down menu, amplitude and phase histograms showing the distribution of chest-wall positions and phase distributions. Statistics for the trace are shown on the right hand panel..... 115

Figure 3.19. GUI of respiratory analysis software, showing the imported trace from the Varian RPM system, a stem plot of the time spent in exhale and the time spent in inhale phases per full respiratory cycle and phase and amplitude distributions Statistics for the trace are shown on the right hand panel. 116

Figure 3.20. GUI of respiratory analysis software, showing the imported trace from the Varian RPM system and a stem plot of the ratio of time spent in inhale per cycle compared to time spent in exhale along with the usual statistics and amplitude and phase distributions..... 117

Figure 3.21. The complete QUASAR motion phantom with additional accessories. (1) Laptop showing control software. (2) Custom built lift platform on separate stepper motor. (3) Upgraded QUASAR motion phantom with upgraded motor attached. (4) Bladder insert. (5) Film insert. (6) Ion chamber insert. (7) Ion Chamber. (8) Exposed film showing moving insert dose distributions. 118

Figure 3.22. Patient AP motion recorded with the RPM system (solid blue line) compared to AP motion replicated with the upgraded phantom system (dashed red line). 119

Figure 3.23. Replication of an irregular patient trace with base-line drift and irregularities in amplitude. 120

Figure 3.24. Test patterns designed to commission and test the RPM system. In these diagrams, the red line indicates that the RPM considers the motion unpredictable. The figures also indicate where the RPM has initiated a ‘beam OFF’ signal, this can be seen where the square wave gate signal pulse representing the ‘beam ON’ time drops to zero. (a) Respiratory pattern that tests the termination of gating where patient respiratory motion differs from prediction. This can be seen by the red line in (a). (b) Sinusoidal trace with small amplitude to test predictability / gateability and resolution of the RPM system in dealing with small amplitude motions. (c) Example of a large amplitude / period (~15s) to test the RPM’s ability to accurately predict large motions. (d) Example of a ten second breath-hold simulation..... 122

Figure 4.1. MIP images (Cropped to 365 x 365 mm): Amplitude analysis, (a) axial and (b) sagittal mid plane, upper-surface to upper-surface point at minimum and maximum arm elevation used to measure amplitude. (Note: sagittal image has had window and leveling modified for better visualisation.) The red rectangle in (a) shows an example of the ROI used for HU determination. The dashed white line in (b) shows the extent of motion excursion from a sagittal perspective. 129

Figure 4.2. (a) Inter-phase variation in the HU of water. Random variations about the ‘true’ HU for water show no systematic dependence on phase-bin over all amplitudes of motion. A standard ROI shown in Figure 3.4 (area = 377 pixels) was used for all measurements. (b) The effect of motion frequency on HU variation. For a large motion amplitude of 6.0 cm a comparison was made between the HU of water for a moving and stationary object in the 50% phase-bin. Error bars represent the standard uncertainty in the measured HU values..... 131

Figure 4.3. (a) MIP using ten phases 0 – 90% with an amplitude of 6.0 cm. (b) Average reconstruction for an amplitude of 6.0 cm. (c) MIP of 2.5 cm amplitude motion using ten phases. (d) Average reconstruction (2.5 cm amplitude)..... 134

Figure 4.4. Sagittal MIPs for reconstructions based on (a) 5 (0,20,40,...,80%), (b) 10 (0,10,20,...,90%) and

(c) 20 (0,5,10,...,45%) phase-bins. 20 phase-bins were constructed by exploiting the symmetrical nature of the motion and using ten phase-bins over half the motion cycle..... 135

Figure 4.5. The interplay between motion amplitude and object size. Ten phase-bins used over three different amplitudes 4.0, 2.0 and 1.0 cm demonstrating the object amplitude / size interplay and the concept of a discontinuous data set for a MIP. The data-points represented by solid grey circles represent a small object moving with an amplitude of 1.0 cm, for this motion, the MIP constructed from the ten phase-bins would appear as a solid object. For the same size object with an amplitude of 2.0 (red circle) or 4.0 cm (green circle), gaps would appear in the MIP since only ten phase-bins are used..... 136

Figure 4.6. The maximum bin-to-bin displacement as a function of the number of phase-bins for a tumor moving with a sinusoidal profile. If the diameter of the tumor is smaller than its bin-to-bin displacement, an insufficient number of phase-bins will result in gaps appearing in the MIP. Data for sinusoidal peak-to-peak amplitudes of 0.5, 1.0, 2.0, 3.0, 4.0, 5.0 and 6.0 cm are shown..... 138

Figure 4.7. Simulations with the XCAT phantom and a maximum diaphragm extension of 4.0 cm. Gaps can be seen to appear in these MIP images for small lesions (10, 15 mm) if an insufficient number of phase-bins are implemented. 139

Figure 4.8. Simulations with the XCAT phantom and a maximum diaphragm extension of 2.0 cm. The reduced diaphragmatic motion and therefore reduced lesion migration results in a reduction in the gaps appearing in MIP images as a result of insufficient phase-bin assignment. 140

Figure 4.9. MIP's for five different amplitudes. (a) 1.5 cm, (b) 2.0 cm, (c) 2.5 cm, (d) 3.0 cm and (e) 6.0 cm. Each of these amplitudes was measured using the method shown in Figure 4.1 and data was binned using a ten phase-bin protocol. The MIP delineated amplitude was compared with the known amplitude..... 141

Figure 5.1. Upgraded QUASAR motion phantom left with moving insert right. The insert contains 5, 10,15 and 20 mm diameter reservoirs each 15 mm in height. An 'L' shaped reservoir can also be seen. 151

Figure 5.2. Location of the lesion within the right lung for GATE simulations..... 154

Figure 5.3. (a) Schematic of the Phillips Allegro scanner detection geometry in GATE. (b) The same scanner with the voxelised XCAT phantom shown..... 158

Figure 5.4. A diagram illustrating the way XCAT phantoms are incorporated into the GATE Monte Carlo framework. 160

Figure 5.5. XCAT phantoms generated for use in the GATE Monte Carlo simulations, showing a (a) **10 mm**, (b) **20 mm** and (c) **30 mm** diameter lesion residing in the lower right lung with a **10:1 activity ratio**. The phantom's diaphragmatic amplitude was varied from 0 to 3.0 cm. Note: the motion in GATE occurs in real-time, and depictions of the motion shown in these images are used to indicate the magnitudes of lesion motion that were set using the XCAT phantom and therefore, the motion that occurred during the Monte Carlo PET simulations. 162

Figure 5.6. XCAT generated phantoms used in Monte Carlo GATE simulations. Activity ratios of 5:1 and 2:1 (lesion:background) respectively are shown. Here phantoms with the diaphragm amplitude set to 3.0 cm are shown, as stated previously, the motion is in real-time during the Monte Carlo simulation and these average intensity phantoms are shown for display purposes only to highlight the degree of motion that was assigned to the phantoms. The complete list of XCAT phantoms created for use with GATE is shown in Table 5.3. 163

Figure 5.7. 3D (top row) and 4D (bottom row) PET images of (a) a 15 RPM 1cm motion, (b) a 15 RPM 2 cm motion and (c) a 15 RPM 4.0 cm motion. Data from the 1st phase bin was taken for the 4D data. 165

Figure 5.8. 4 cm of displacement split into ten phase-bins.....	165
Figure 5.9. (a) Apparent lesion maximum activity normalised to the injected activity concentration as a function of motion displacement and lesion size for a 3D scan. (b) The activity recorded through a 4D acquisition. (c) Volume overestimation as a function of lesion size and amplitude for a 3D scan. (d) Volume recovery with a 4D scan.	166
Figure 5.10. The impact of the motion frequency rate on activity, A_{max} , normalised to the injected activity concentration, for three motion frequencies (2 cm motion amplitude).....	167
Figure 5.11. Sagittal activity distributions for a 30 mm diameter tumour moving in the SI direction with a sinusoidal motion profile. The tumour's activity was set to 10 kBq, with the background of the lungs set to 1 kBq. (a) Static 30 mm diameter tumour, (b) 0.5 cm amplitude, (c) 1.0 cm amplitude, (d) 2.0 cm amplitude and (e) a 3.0 cm amplitude. (f) Line profiles through the centre of the lesion as indicated by the vertical dashed line in (a) – (e). The colourbars show the normalised activity with respect to the stationary case. The coarseness of the resolution in these images arises from the 5 mm ³ voxel size of the XCAT phantom.....	169
Figure 5.12. 3D isosurfaces of constant activity levels of 0.1 (green), 20 (red) and 60 % (blue) of the maximum activity demonstrating the increase in apparent lesion size. (a) Static 30 mm lesion and (b) the same lesion with a 3.0 cm amplitude.	170
Figure 5.13. Sagittal activity distributions for a slice through the centre of a 10 mm diameter tumour moving in the SI direction with a sinusoidal motion profile. The tumour's activity was set to 10 kBq, with the background of the lungs set to 1 kBq. (a) Static 10 mm diameter tumour, (b) 3.0 cm amplitude, (c) line profiles showing overestimation of lesion size and reduction in apparent activity. Note the colour bar scale in image (b) is normalised to the maximum activity found in the static case. The background activity of the lung can also be seen. Compared to the 30 mm lesion, the reduction in apparent activity is greater for a moving lesion of smaller dimensions.	170
Figure 5.14. PET scans simulated with the GATE system using the XCAT phantom as the source. A consistent reduction in the apparent activity can be seen for all activity ratios as the amplitude increased beyond 1 cm. (a) Reduction in maximum activity across a line-profile through the centre of the lesion for a 10:1 activity ratio, (b) 5:1 activity ratio and (c) 2:1 activity ratio.....	172
Figure 5.15. Illustration of 'spill-in', 'spill-out' effects taken from (Soret, Bacharach <i>et al.</i> , 2007). The measured image (D) of the true activity distribution (A) is the result of the sum of the spill-out (B) and spill-in (C).....	172
Figure 5.16. Line profiles through the centre of a 10 mm diameter lesion over 5 phase-bins from a 4D PET simulation. The 3D line profile is shown with a blue dashed line and circle markers. The displacement of the diaphragm was set to 3.0 cm with a 4 s respiratory period and the lesion's activity set to 10 kBq with the lung background at 1 kBq. (a) All phase-bin and 3D simulation line profiles superimposed, (b) the 0% phase-bin from 4D-PET compared with the 3D simulation.....	174
Figure 5.17. Line profiles through the centre of a 10 mm diameter lesion over 10 phase-bins from a 4D PET simulation. The 3D line profile is shown with a blue dashed line and circle markers. The displacement of the diaphragm was set to 3.0 cm with a 4 s respiratory period and 10:1 activity ratio. (a) All phase-bin line profiles superimposed, (b) the 0% phase-bin from 4D-PET compared with the 3D simulation.....	175
Figure 5.18. Line profiles through the centre of a 10 mm diameter lesion over 20 phase-bins from a 4D PET simulation. The 3D line profile is shown with a blue dashed line and circle markers. The displacement of the diaphragm was set to 3.0 cm with a 4 s respiratory period and 10:1 activity ratio. (a) All phase-bin line profiles superimposed, (b) the 0% phase-bin from 4D-PET compared with the 3D simulation. With 20 phase bins, there is a considerable increase in noise due to the reduction in counts per phase-bin.	176

Figure 5.19. Comparison of the reduction in maximum activity measured as a function of lesion amplitude for the two methods. Lesions with diameters of 10 and 20 mm are shown with the lesion activity set to 10 kBq in the Monte Carlo simulations. Experimental, in phantom results showed the highest decrease in activity compared to Monte Carlo. Note that a 4 cm motion amplitude was not possible in the Monte Carlo simulation due to limitations in the XCAT phantom's motion simulation..... 181

Figure 6.1. Monte Carlo geometry. A photon beam of energy E and field size FS is incident upon a region of tissue equivalent density representative of the chest-wall ($20 \times 80 \times 80 \text{ mm}^3$). The chest-wall is then followed by a region of lung equivalent density with dimensions ($110 \times 80 \times 80 \text{ mm}^3$). Inside the lung tissue region, a spherical lesion of diameter \varnothing is placed at a distance d from the chest-wall. The distances (d) and tumour size (\varnothing) are variable. The tumour's size determines the field size. 189

Figure 6.2. (a) The scoring geometry simulated with Geant4. The 1 mm diameter voxels; entrance (Ent), exit (Ext), Reference (Ref) and lateral dose points both vertical and horizontal (Lat) are shown. (b) A schematic of the key dose points indicating the regions of interest for scoring dose. The points are marked with a black X and the field in both views is indicated by a shaded region..... 190

Figure 6.3. (a) 6 MV and (b) 15 MV photon spectrum from (Mohan, Chui *et al.*, 1985). This data was used as the photon spectra incident on the chest-wall as seen in Figure 6.1. 190

Figure 6.4. Beam, geometry and motion direction arrangements for the present study. (a) Geometry and beam arrangements showing a 40 mm diameter tumour in a region of lung equivalent density ($160 \times 160 \times 120 \text{ mm}^3$), a $10 \times 10 \text{ cm}^2$ field of 6MV photons is incident on a tissue equivalent region ($160 \times 160 \times 20 \text{ mm}^3$) with a parallel opposed beam arrangement, in this scenario, the tumour's motion is parallel to the beam direction. (b) A single field scenario with the tumour's motion again occurring parallel to the beam direction. (c) A parallel opposed arrangement with the tumour's motion occurring perpendicular to the beam direction and (d) a single field arrangement with the tumour motion occurring perpendicular to the beam direction... 192

Figure 6.5. The motion profiles that were chosen as the basis for determining the location of the tumour within each of the ten phase-bins. (a) Motion 1 - symmetrical (b) Motion 2 - asymmetrical: Inspiration < expiration, (c) Motion 3 - asymmetrical: inspiration > expiration and (d) Motion 4 - Asymmetrical with a pause in-between breaths..... 193

Figure 6.6. A schematic of the comparison between the two dose calculation methodologies. At each of the ten phases the entrance (A), central (B) and exit (C) doses are recorded as well as the dose to GTV. The entrance, central and exit doses, as well as the dose to the ITV (AVG) volume are also recorded for comparison. The dose to the lesion volume in each phase-bin is added to form the U10V. Note the assignment of phases in this scenario is arbitrary. The AVG is derived from the 10 phases from 4D-CT. Its boundary is defined by the MIP and the distribution of densities within the ITV derived directly from the AIP. In this work, simulations are conducted with the lesion moving in both the SI and AP directions relative to the beam. The parallel opposed fields are in the AP direction..... 195

Figure 6.7. Analysis of characteristic points over all motion profiles and amplitudes simulated for a parallel opposed beam arrangement. Data presented here is the ratio of the accumulation of the point over the ten phases, to the single point on the AIP. Here, $R(A)$ represents the ratio of the entrance voxels, $R(B)$ the ratio of central dose voxels and $R(C)$, the ratio of exit dose voxels. The method of comparison is outlined in Figure 6.6. The four motion types outlined in Figure 6.5 are shown. (a) Sinusoidal motion (motion Type 1) (b) inspiration period less than expiration (motion Type 2) (c) inspiration period greater than expiration (motion Type 3) and (d) inspiration and expiration period followed by a pause (motion Type 4). 202

Figure 6.8. Analysis of characteristic points over all motion profiles and amplitudes simulated for a single field. Data presented here is the ratio of the accumulation of the point over the ten phases, to the single point on the AIP. Here, $R(A)$ represents the ratio of the entrance voxels, $R(B)$ the ratio of central dose voxels and $R(C)$, the ratio of exit dose voxels. The method of comparison is outlined in Figure 6.6. The four motion types

outlined in Figure 6.5 are shown. (a) Sinusoidal motion (motion Type 1) (b) inspiration period less than expiration (motion Type 2) (c) inspiration period greater than expiration (motion Type 3) and (d) inspiration and expiration period followed by a pause (motion Type 4). The schematic above illustrates the points of interest.203

Figure 6.9. (a) Dose differences between the two methodologies per phase. Here, the points represent the dose to the entrance, central and exit voxels on the tumour in each of the ten phases. The straight lines represent the dose measured on the average intensity projection dataset formed by the ten phases for the same points (A, B, C). This method is outlined Figure 6.6. (a) 5.0 cm amplitude with motion of Type 1 (sinusoidal), in a parallel opposed field arrangement. (b) 0.5 cm amplitude motion for a parallel opposed field and motion of Type 1. (c) A 5.0 cm amplitude motion of Type 1 in a single field arrangement and (d) 0.5 cm motion of Type 1 in a single field arrangement. Note the y-axis scale differences between multiple and single field scenarios, respectively.205

Figure 6.10. The two methods (U10V and AVG) produce different volumes for treatment. The U10V method involves contouring the target volume in each of the respiratory phases and then registering and summing the individual dose distributions. The AVG method, on the other hand performs a single dose calculation on the ITV (if the PTV is set to ITV). Data presented here is for a parallel opposed arrangement and sinusoidal motion profile.206

Figure 6.11. (a) DVHs for a 5.0 cm amplitude sinusoidal motion with **parallel opposed** fields, showing U10V (red line) and AVG (blue line). (b) 3.5 cm amplitude (c) 2.0 cm amplitude and (d) 0.5 cm amplitude.207

Figure 6.12. (a) DVHs for a 5.0 cm amplitude sinusoidal motion with a **single field**, showing U10V (red line) and AVG (blue line). (b) 3.5 cm amplitude (c) 2.0 cm amplitude and (d) 0.5 cm amplitude.208

Figure 6.13. Motion of the lesion perpendicular to the beam. Comparison of the two methods for a 3.5 and 0.5 cm amplitude of motion respectively. The target's motion relative to the beam results in greater agreement in single fields for motion perpendicular to the beam direction compared to the parallel motion scenario.209

Figure 6.14. (a) The effect of motion profile on the cumulative dose-volume histograms (U10V) and (b) the effect of differing motion profiles on dose-volume histograms calculated from AVG.210

TABLE OF TABLES

Table 1.1. Approximate attenuation coefficients (μ_{abs}) of various human tissues for 100 kVp X-rays.	12
Table 1.2. Modern CT scanners with multi-row detector systems showing the number of detector rows and the number of slices, along with the year. Adapted from (Kalender, 2006). The GE LightSpeed 16 and Phillips Brilliance 64 scanners (†) were used in the present study.	13
Table 1.3. Comparison of conventional radiotherapy (3D / IMRT) and SBRT adapted form (Benedict, Yenice <i>et al.</i> , 2010).	23
Table 2.1. The magnitude of respiratory motion as observed in several studies. The disease site, mean range of motion in mm in three dimensions (Superior Inferior [SI], Anterior Posterior [AP], Left Right [LR]) is reported (if available) as well as the maximum and minimum tumour motion in brackets. Where maximum and minimum are not reported the plus/minus standard deviation is shown.	36
Table 2.2. Summary of the effects of motion on SUV underestimation and volume overestimation. Maximum values found over the entire study are presented except where noted.	45
Table 2.3. Reported variations in the correlation between internal target motion and external surrogates.	47
Table 2.4. Chronological development of 4D imaging techniques.	55
Table 2.5. List of motion phantoms, both commercial and custom made and their motion capabilities.	62
Table 2.6. Geant4 photon interaction physics processes and the models governing the interactions. For a detailed description of the physics models, the reader is pointed to the Geant4 Physics Manual (Collaboration, 1999).	72
Table 2.7. Electron / positron interaction physics and the models governing the interactions.	73
Table 2.8. Systems available for simulation via the GATE platform. The first column shows the type of system. The second column describes the keywords used to define the system, the third column outlines the shape of the entire ‘mother’ volume and the fourth column shows the available outputs. This table was adapted from (Jan, Santin <i>et al.</i> , 2004).	77
Table 2.9. Photon interactions and their modeling in EGSnrc (descriptions of the interactions are provided in Table 2.6).	84
Table 2.10. Electron interactions and their modeling with EGSnrc (descriptions of the interactions are provided in Table 2.7).	85
Table 3.1. Specifications of the see-saw motion phantom.	98
Table 3.2. Motion capabilities of the see-saw phantom. Both the AP amplitudes and SI amplitudes are continuously variable between these minimum and maximum amplitudes.	98
Table 3.3. The physical specifications of the Mot-102 stepper motor.	105
Table 3.4. kta-190 motor commands to be sent from the PC to the kta-190 controller. Taken form the manufacturer’s operators manual.	106
Table 3.5. Six patient respiratory traces recorded with the RPM system and their correlation to data replicated	

with the upgraded QUASAR phantom.	120
Table 4.1. Overview of relevant materials and their approximate tissue equivalence. The static HU were measured with a consistent region of interest for all materials from scans using the Phillips Big Bore Brilliance CT.	127
Table 4.2. Comparison of the mean HU for water measured on all ten phase-bins to the HU of water as measured on the AIP. Comparisons were performed for both the stationary and moving objects within the same FOV. The global mean and standard deviation for all stationary measurements is 0.07 ± 1.5 (-31 – 34).132	
Table 4.3. Comparison between MIP derived amplitudes and physical amplitudes. The amplitude of the objects was calculated for five AP amplitude settings using Equation 3.1. For the MIP derived amplitudes, the ruler function from ImageJ was used.....	141
Table 5.1. Technical features of the Phillips Allegro PET scanner (Tarantola, Zito <i>et al.</i> , 2003).	157
Table 5.2. Physical performance and other features of the Philips Allegro PET scanner (adapted from (Tarantola, Zito <i>et al.</i> , 2003).	157
Table 5.3. Complete list of simulations with the XCAT phantom and GATE Monte Carlo platform.	161
Table 5.4. Summary of the 3D PET MC results as a function of lesion size, amplitude, and activity ratio with respect to the background.	178
Table 6.1. Systematic simulation parameters.	188
Table 6.2. The density and elemental composition of the relevant tissues modeled in the study. Values are presented as percentage by weight. Lung carcinoma data was determined by combustion studies of excised squamous cell lung carcinoma reported by (Maughan, Chuba <i>et al.</i> , 1997). Soft tissue and lung tissue definitions were taken from ICRU Report 44 (Units, Measurements <i>et al.</i> , 1989).	191
Table 6.3. Dose ratios (Equation 6.1) for a 6MV photon spectrum from Figure 6.3 (a). The entrance-to-central dose, exit-to-central dose and average of the lateral-to-central dose is shown. The standard uncertainty is shown in brackets.	197
Table 6.4 Dose ratios (Equation 4.2) for a 15MV photon spectrum from Figure 6.3 (b). The entrance-to-central dose, exit-to-central dose and average of the lateral-to-central dose is shown. The standard uncertainty is shown in brackets. The standard uncertainty is shown in brackets.	198
Table 6.5. DRFs calculated using Equation 6.2 for a 6MV photon spectrum as a function of the tumour's size ($\varnothing r$) and distance from the chest-wall (d). Standard uncertainty is 0.5%.	199
Table 6.6. DRFs calculated using Equation 6.2 for a 15MV photon spectrum as a function of the tumour's size ($\varnothing r$) and distance from the chest-wall (d). Standard uncertainty is 0.5%.	199

SCIENTIFIC ABSTRACT

Cancer is a leading cause of death in Australia and approximately 52% of cancer patients will require radiotherapy at some stage in their treatment. In recent years, stereotactic radiotherapy has emerged as an increasingly common treatment modality for small lesions in various sites of the human body.

Stereotactic Body Radiation Therapy (SBRT) and Stereotactic Ablative Body Radiotherapy (SABR) techniques deliver a larger dose per fraction than conventional radiotherapy. Therefore, the efficacy of the treatment depends on the accurate delivery of radiation to the target whilst minimising radiation to healthy tissues. Because of the large doses involved, smaller treatment margins are needed and in the context of lung cancer, SBRT faces the challenge of respiratory induced target motion. The aim of this work was to assess the impact of motion on both planning (imaging) and dose calculation in SBRT for lung cancer.

Motion affects all aspects of the SBRT treatment planning process. It is well known that image quality is affected by motion for both PET and CT. In SBRT treatment planning however, the target to be imaged may often be smaller than that imaged in conventional radiation therapy treatment planning. To facilitate the investigation into the effects of imaging small mobile lesions, a see-saw 4D-CT phantom was developed. This phantom was used to investigate phase-binning artifacts that can be present when assigning an insufficient number of phases to 4D-CT data. The interplay between a lesion's size and its amplitude, and the effects this relationship has on 4D-CT data is also investigated. An upgrade to a commercially available respiratory motion phantom was also pursued in order to replicate patient motion recorded with the Varian RPM system. Monte Carlo methods were used to determine the impact of motion on PET data by incorporating a computational moving phantom (XCAT) with a full Monte Carlo model of a commercially available PET scanner.

To assess the impact of motion on treatment planning and dose calculation, two treatment planning scenarios were simulated using Monte Carlo. The traditional method of calculating dose on an average intensity projection from 4D-CT was compared to 4D dose calculation, in which tumour motion data from 4D-CT is explicitly incorporated into the treatment plan. Monte Carlo methods are also employed to evaluate the degree of underdosage at the periphery of lesions arising from electronic disequilibrium associated with density changes.

Results presented in this work suggest that small lesions typically seen in SBRT of lung cancer require extra care when considering treatment planning, motion mitigation, and treatment delivery. The upgraded QUASAR phantom allows for patient specific verification of SBRT/SABR treatment plans to be conducted and was found to replicate patient motion accurately. Respiratory analysis software presented in this work enables detailed statistics of a patient's respiratory characteristics to be evaluated. These statistics can then be compared with post-biofeedback statistics to determine if there is an improvement in reproducibility in the patient's breathing. This software can also inform clinicians if there would be any benefit in using gated radiotherapy, and if so, where best to enable the beam ON.

When assessing the impact of motion and small lesion sizes on 4D-CT, the see-saw phantom, designed for cheap, fast and accurate 4D-CT QA was found to be useful. Data collected in this work indicates that lesion size and amplitude are important factors when assessing the quality of projections from 4D-CT. The number of phase-bins required to mitigate banding artifacts is quantified in a simple equation for sinusoidal motion. Furthermore, large amplitude motions, greater than the diameter of the lesion, result in banding artifacts in maximum and average intensity projections and care needs to be taken when using such images for treatment planning. It was also found that for lesion with diameters greater than 2.0 cm and amplitudes less than 4.0 cm, ten phase-bins are adequate to negate all banding artifacts in projection images.

Experimental and Monte Carlo investigations into the impact of motion on images acquired with PET and 4D-PET revealed that the motion of small lesions, subject to both the partial-volume effect and motion related effects should be assessed and mitigated carefully. Motion greater than 1.0 cm resulted in a demonstrable reduction in activity that increased with motion amplitude for lesion sizes of 5 – 30 mm in both experimental and Monte Carlo studies. The decrease in apparent activity was proportional to an increase in apparent lesion size. 4D-PET was found to partially mitigate these effects.

In assessing the impact of motion on treatment planning and dose calculation, Monte Carlo simulations using both EGSnrc and Geant4 were used to assess the degree of peripheral underdosage that occurs as a result of electronic disequilibrium in lung lesions and determine differences between 4D and 3D dose calculation methods. A Dose Reduction Factor (DRF) metric was developed which is defined as the ratio of the average of the dose to the periphery of the

lesion to the dose in the central portion. The mean of the DRF was found to be 0.97 and 0.92 for 6 MV and 15 MV photon beams respectively, for lesion sizes ranging from 10 – 50 mm. The DRF was found to be dependant on the location of the lesion relative to the chest-wall, lesion size and the photon beam energy. The dynamic scenario was simulated with 4D dose calculation methods of registering and adding the dose distributions in each phase-bin from 4D-CT. The dose-volume distributions compared well with 3D (AIP) methods if multiple beams were used and the amplitude of motion was less than 3.0 cm. Motion profiles of varying degrees of symmetry were seen to have little effect on the agreement provided multiple beams were used.

In this work, tools have developed and tested phantoms that have been implemented clinically for patient specific QA of SABR/SBRT treatment plans. QA devices for 4D imaging modalities have also been presented, tested and used for QA purposes. The effects of motion on images acquired with 4D-CT and PET have been investigated as well as treatment planning and dose calculation strategies determining and incorporating the effects of motion into dose calculation. It is hoped that this work will increase the understanding of the impact of motion on all aspects of SBRT and enhance the efficacy of motion management strategies and clinical use of SBRT.

ACKNOWLEDGEMENTS

Throughout my candidature of just over four years, I have been incredibly fortunate to have met and collaborated with amazing individuals. At the beginning of this journey, my primary supervisors were Professor Peter Johnston and Associate Professor Rick Franich. Upon Peter's appointment as the Head of the Medical Radiation Services Branch at ARPANSA, my supervisory situation changed and Professor Tomas Kron became a primary supervisor. Each of these people do deserve my sincere gratitude.

Firstly, I would like to begin by thanking Associate Professor Rick Franich and Professor Tomas Kron, who I have spent most of my candidature with. I have gained so much from knowing Rick and having him as my supervisor that it's hard to put into words. Rick has a tireless work ethic and vast knowledge in both nuclear and medical physics. He can generally pick up one of his 17 or so students' work and know exactly what the work entailed, what needs doing and provide invaluable feedback. This is quite a feat that I really don't think many people could accomplish, even with the standard three or four students under their supervision. His ability to juggle and organise so many varying commitments is not only an inspiration, it's incredible to see. No matter how busy I think I am, juggling work, life, and my PhD, I can always walk past Rick's office and think...it's not that bad! Rick's guidance as a supervisor has not only shaped the quality of work I produce, he has also taught me to value and have pride in my work. Specifically, he taught me that you shouldn't try and publish something just for the sake of a publication. He has an expectation of quality which is hard to meet, but nonetheless makes your work better from having gone through the process with him as a supervisor. This is an invaluable lesson that is only learnt through trial after trial. One of the great experiences throughout this PhD was travelling to AAPM in Philadelphia with Rick and for this I am extremely grateful.

Tomas is a master of all things Medical Physics and an inspiration. His almost encyclopedic knowledge was demonstrated innumerable times while working with him. A remarkable thing that happened time and time again when Tomas would suggest a particular investigation or experiment was that he would know the answer to within a percent before I even began. I would go away for months slaving away at a particular problem, only to find that the answer was pretty much what Tomas predicted it would be several months earlier over coffee. I would often get asked how the results of a particular experiment turned out by colleagues, to which I would reply "like Tomas said they would". His ability to grasp the crux of a particular problem and predict what the end

result should look like constantly amazes me. Tomas has also facilitated a number of collaborations with others in the medical physics community and for this I am thankful. I have the utmost respect for Tomas and his enthusiasm and guidance have shaped me into a better person and I look forward to continuing to work with him in the future.

Professor Peter Johnston was my primary supervisor during honours and the reason I even got into nuclear / medical physics. I have a great amount of respect and admiration for Peter and am thankful to him for giving me the opportunity to work in Darwin for a month with a great group of people during my honours year. This was a great experience and one I surely won't forget. Peter has an amazing breadth of knowledge of Nuclear and Medical Physics. I was very fortunate to have him as my supervisor early on in my PhD and am very happy to still be working with him today in a professional capacity at ARPANSA.

I am grateful to Dr Michael Taylor, Dr Ivan Williams, Natalie Clements and Jason Callahan. Michael has been great to work with on a number of projects. Michael has a great deal of knowledge in both Medical and Nuclear Physics which seems beyond his years. This stems from a great intellect and a lot of hard work. Michael is always the last to leave the office and there is nothing like getting an email from him on a Sunday to make you feel like you should be working harder. I am forever grateful to Michael for also helping me to become a better writer (I hope...). Anyone that has read anything from the pen of Michael will attest that he has a way with words and a great command of scientific writing. I look forward to continuing to work with him in the future.

Dr Ivan Williams is the director of the Australian Clinical Dosimetry Service operating out of ARPANSA. I have had the great pleasure of working with Ivan over the two years and recently he has been providing invaluable feedback on each part of this thesis. His comments, in particular, his help in providing a clinical context to this work as well as general tips, have helped shape the structure and relevance of the work presented here. Ivan has proved an invaluable resource in carefully reading through this work and the benefit of his 'fresh eyes' cannot be overstated. I would also like to take this opportunity to thank Natalie Clements and the staff at all Peter MacCallum centres. Natalie is a wonderful person to work with and she has helped me through many late nights at Peter MacCallum Cancer Centres. I'm indebted to her for her time spent helping me as she was extremely busy with her own Masters and TEAP training. Thanks Nat. I

was also very fortunate to work closely with Jason Callahan through a number of experiments in which I learned a great deal about PET imaging. Thanks Jason.

I would also like to thank the physics faculty at RMIT University. Each member of staff has helped me at some stage, whether it be through teaching, supervision or general help. Special thanks to Bruce Robinson who built many of the phantoms and their add-ons and whose ingenuity helped make many of my designs many times better!

My family has been a constant source of support throughout the years. My mother, Helen, father, Carl, grandma, Peg, and my brothers, Marcus, Chris, Nick, Peter and Michael (I think that's all of them). My mother and father have always been an inspiration. They have both worked incredibly hard to provide for all of us and been nothing but supportive in any endeavor that my brothers and I have wanted to pursue. I hope dedicating this thesis to them will provide some minor form of thanks.

Last but not least, I would like to thank my wonderful partner Kelly Flanigan. Over the past 5 years she has provided support in innumerable ways, listened to me moan and complain and been as patient and tolerant as a saint. Kelly, thank you, hopefully I won't put you through anything like this ever again!

Chapter 1. Introduction

*“I was born not knowing
and have only had a little time to change that
here and there.”*

- Richard Phillips Feynman

1.1. PROPOSITUM

The main aim of this thesis is to address and evaluate the effects of motion on treatment planning of small lesions affected by motion as commonly seen in stereotactic radiotherapy of lung cancers. The issue of tumour motion affects all three stages of stereotactic radiotherapy; imaging, treatment planning and treatment delivery. Much is already known about the impact of motion in conventional radiation therapy treatment planning and delivery, however, its impact in the burgeoning field of stereotactic body radiation therapy (SBRT) is less well documented. The fact that SBRT employs *fewer* fractions with *higher* doses per fraction than conventional radiotherapy means that accurate targeting of the lesion itself is critical to the treatment efficacy and patient outcome. In the case of SBRT, motion management and understanding of the effects of motion throughout the treatment chain is critical. This thesis considers motion effects, such as target size determination in anatomical imaging (Computed Tomography), functional imaging (Positron Emission Tomography) and SBRT planning on average intensity projections and estimation of dosimetric discrepancies in treatment delivery.

1.2. CANCER

Cancer is a major cause of death in Australia (AIHW, 2008). In 2010 there were 114,000 new cases of cancer diagnosed and 43,000 died from the disease. With the Cancer Council Australia stating that one in two Australians will be diagnosed with cancer by the age of 85, it is important that research into improving the effectiveness of treatments employing radiotherapy be undertaken.

1.2.1. Lung cancer

Lung cancer is the fifth most common cancer in Australia. The majority of lung cancers (four out of five) are non-small cell lung carcinomas (NSCLC) and the bulk of discussion here will be dedicated to NSCLC. NSCLC's can be broadly divided by their main cell type into squamous cell, adenocarcinoma and large cell. In Australia, there are approximately 9,700 cases of lung cancer diagnosed each year. This amounts to 9% of all cancer diagnoses (AIHW, 2008).

For early stage NSCLC diagnoses, the most common form of treatment is surgery with an aim to cure. Prior to surgical intervention, all cases have to undergo careful pre-operative assessment to assess:

- Histological proof of disease
- Staging of disease
- Fitness for surgery

The alternative therapy for those individuals not suitable for surgery is radical radiation therapy usually combined with chemotherapy. Radical radiation therapy is the use of ionising radiation to kill malignant cells and is usually employed for patients with stage II or above NSCLC. According to Tyldesley *et al* (2001), approximately 64% of NSCLC cases require radiation therapy, with 45.9% requiring radiation therapy in the initial treatment stage and 18.3% later in the course of the illness due to the inability to provide surgical intervention. The standard international dose and fractionation is 60 Gy in 30 fractions delivered daily over six weeks (Tyldesley, Boyd *et al.*, 2001). Higher doses than this generally cannot be given due to the increased risk of pulmonary toxicity. Local control of NSCLC using the standard international dose and fractionation protocol is very poor and much work is being done to investigate the possibility of dose escalation to improve this.

1.3. EXTERNAL BEAM RADIOTHERAPY

Radiation therapy, or radiotherapy, is the treatment of disease by exposure to ionising radiation. Modern radiation therapy is usually carried out with high energy (megavoltage range) photons and electrons produced via a Linear Accelerator or LINAC. At the megavoltage (MV) energies typically used in external beam radiotherapy, the primary process by which a 'dose' is delivered to biological cells is via high-energy electrons liberated from the atomic orbitals of cell atoms by the primary photon flux. Cell damage occurs when electrons interacting within the cells lose their kinetic energy in discrete ionisation events within the cell. DNA is recognised as the primary target for cell inactivation by ionising radiation. As a result of exposure to ionising radiation, cell death is usually attributed to lack of repair or disrepair of single and double strand breaks resulting in mitotic cell daughters. External beam radiotherapy is usually carried out with multiple radiation beams, optimised to achieve a uniform dose distribution inside the target volume whilst minimising dose to healthy tissues surrounding the target. Modern radiotherapy treatment can be carried out with a variety of beam energies and field sizes to achieve this goal.

1.4. THE RADIOTHERAPY PROCESS

The steps in a typical radiotherapy process are outlined in Figure 1.1

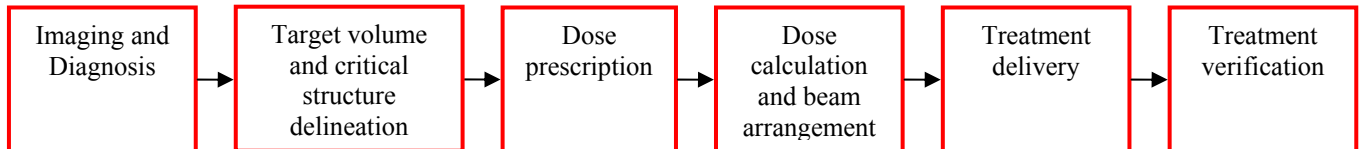


Figure 1.1. An outline of the radiotherapy process, from imaging to treatment verification and delivery.

1.5. IMAGING AND DIAGNOSIS

Medical imaging is a tool used to examine and diagnose disease or injury. In recent decades, medical imaging techniques have evolved rapidly with numerous techniques now available. In the context of cancer diagnoses, examination and radiotherapy treatment planning an accurate three-dimensional (3D) representation of the patient's anatomy is required. The standard approach to gathering information about the patient for the purposes of treatment planning usually involves Computed Tomography (CT), Positron Emission Tomography (PET) and or Magnetic Resonance Imaging (MRI). Depending on the disease site, combinations of these three main imaging modalities may be used. Recent developments have steered hybrid merging of existing technologies so that functional, as well as anatomical data can be acquired in a single scan. For lung cancer, PET and CT are the most important modalities and therefore all work presented in this thesis is dedicated to these modalities.

1.5.1. *Computed Tomography (CT)*

Tomography literally means, 'slice imaging'. Computed tomography uses the attenuation of X-rays to produce cross-sectional images of the human body. It differs from conventional projection radiography whereby images of full three dimensional structure of the body are collapsed into a two dimensional representation. CT images are formed by scanning a single plane from multiple directions and reconstructing an image from a number of projections. Computed tomography has evolved in a number of technological generations since the first conception by Hounsfield in 1973 (Hounsfield, 1973). Although the evolution of CT has progressed rapidly with each technological

generation, the same physics lies behind the modern CT as previous generations. Essentially, the linear attenuation of X-rays depicts an object's ability to attenuate X-rays of a characteristic energy. Attenuation coefficients are used for medical imaging since different anatomical structures have different attenuation coefficients. Bone, for example, has a much higher absorption coefficient than soft tissue, and, generally, soft tissues themselves will have variable absorption coefficients. Since CT's inception, the clinical use of CT has increased with technological advances in detector and X-ray technology, as well as computational processing power. As modern detector array technology improved in the 1990s, so too did the generation of CT scanners. Today, CT allows imaging of whole organs or the whole body in 5 – 20 s with sub-millimeter isotropic resolution (Kalender, 2006). Table 1.1 gives the absorption coefficients of various human tissues in Hounsfield units. This is a dimensionless quantity defined by Equation 1.1 and is the comparison of the absorption coefficient of a particular tissue / bone to the absorption coefficient of water. Table 1.2 shows a list of modern CT scanners post 1998, when multi-detector array technology became prevalent. Wider detector arrays allow for faster scanning and a more effective use of the available X-ray tube flux due to an increased solid angle.

In diagnostic imaging, the success of CT critically depends on the fact that normal and cancerous tissues have slightly different attenuation coefficients due to differing effective atomic numbers.

$$\mathbf{H}_{tissue} = \frac{\mu_{tissue} - \mu_{water}}{\mu_{water}} \times 1000 \quad (1.1)$$

Table 1.1. Approximate attenuation coefficients (μ_{abs}) of various human tissues for 100 kVp X-rays.

Material	μ_{abs} in Hounsfield units
Water	0
Air	-1000
Bone	1086
Blood	53
Fat	-61
Brain white/gray	-4
Breast tissue	9
Muscle	41
Soft tissue	51

Numerous methods exist to determine the pixelised linear attenuation coefficient matrix. These methods are broadly grouped into convolution and back projection methods. The interested reader is directed to the classic textbook by Webb for further information on these methods (Webb, 1988).

The modern evolution of CT and detector array technology is shown in Figure 1.2 and a schematic of a modern 3rd generation CT scanner is shown in Figure 1.3. In this schematic, the CT source rotates around the patient in coincidence with the detector bank. In contrast, a 4th generation CT scanner has a stationary detection ring surrounding the patient with a rotating X-ray source. Although 4th generation scanners became available, the introduction of multi-row detection systems marked the end of the 4th generation scanner and a return to the 3rd generation. The latest and most powerful CT scanners offered commercially are all 3rd generation scanners. The routine use of CT is commonplace in clinics today and is the basis for most radiotherapy treatment plans. Modern CT scanners allow detailed, reproducible and accurate examinations of anatomy. With 64-slice CT and scan time of less than 10 s, (Kalender, 2006) modern CT scans can be completed quickly and non-invasively. Table 1.2 lists a number of modern CT scanners with multi-row detector systems.

Table 1.2. Modern CT scanners with multi-row detector systems showing the number of detector rows and the number of slices, along with the year. Adapted from (Kalender, 2006). The GE LightSpeed 16 and Phillips Brilliance 64 scanners (†) were used in the present study.

Manufacturer	Scanner type	Number of detector rows	Number of Slices	Year
GE	LightSpeed 16 †	16	16	2001
Phillips	IDT 16	24	16	2001
Siemens	SOMATOM Sensation 16	24	16	2001
Toshiba	Aquilion	40	16	2001
GE	VCT 64	64	64	2004
Phillips	Brilliance 64 †	64	64	2004
Siemens	SOMATOM Sensation 64	40	64	2004
Toshiba	Aquilion 64	64	64	2004
Toshiba	Prototype	256	256	2004
Siemens	SOMATOM Definition	2 x 40	2 x 64	2005

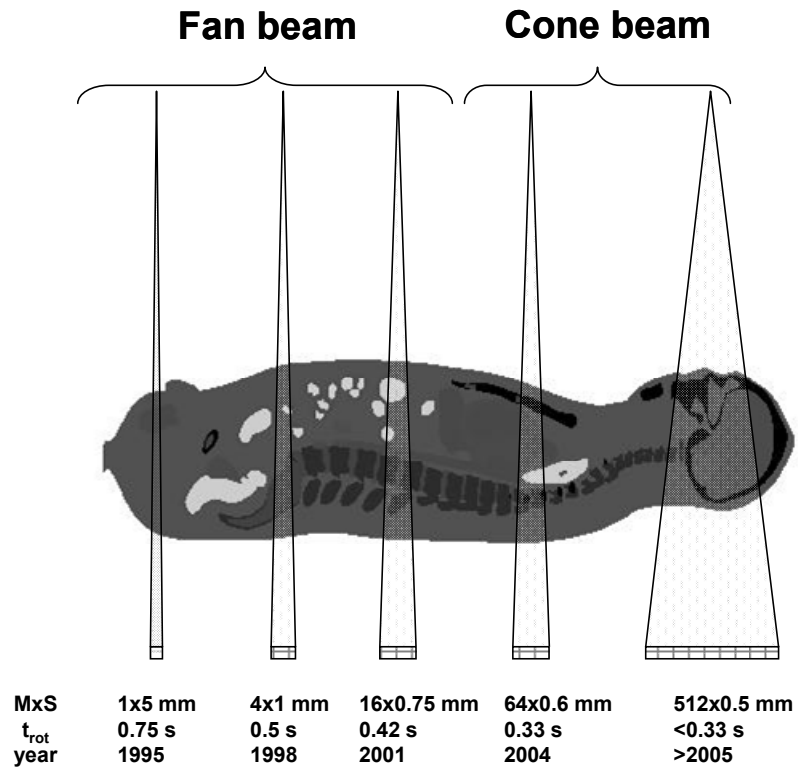


Figure 1.2. The evolution of fan-beam to cone-beam CT in the early 2000s. Where M is the number of slices, t_{rot} is the scanner's rotational period and S is the slice width.

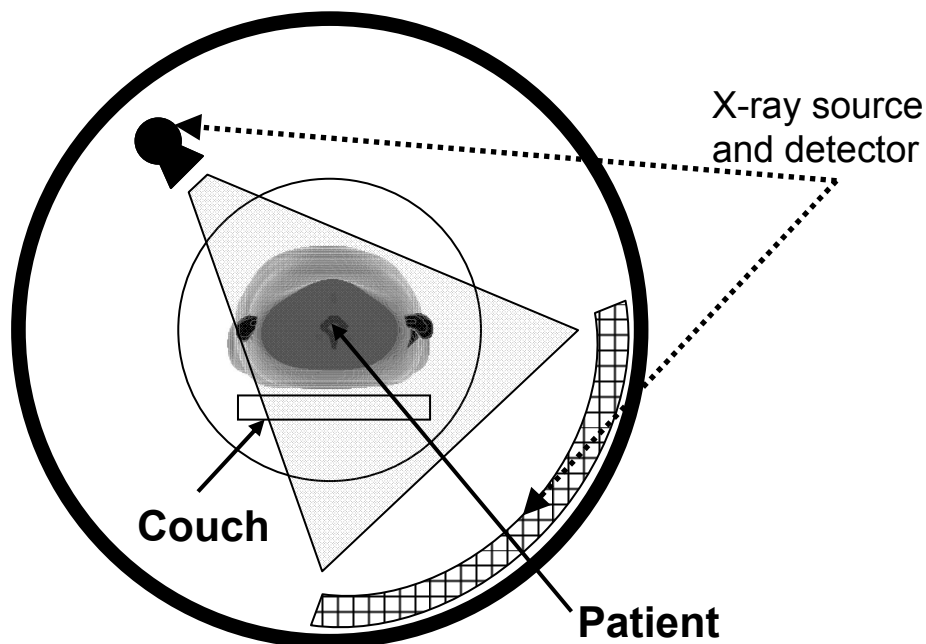


Figure 1.3. Schematic of a 3rd generation CT scanner showing the X-ray source and detection system moving continuously around the patient.

CT images have become the standard treatment planning tool as CT images provide excellent soft tissue contrast allowing for greater tumour localisation and definition. Furthermore, electron density information from CT is useful in the calculation of dose inhomogeneities due to differing tissue densities.

1.5.2. Positron Emission Tomography (PET)

Positron Emission Tomography (PET) is a nuclear imaging technique that allows clinicians to detect and quantify various physiological processes and depict metabolic activity. To begin, an amount of radioactive tracer, commonly FDG (flouro-deoxy-glucose ¹⁸F-FDG) is added to the body usually via injection into the blood stream. As the isotope undergoes β^+ decay, it emits a positron. The positron encounters many electrons undergoing coulomb scattering until the positron's energy is low enough at which point annihilation occurs between the matter-antimatter pair. Upon annihilation, two 511 keV gamma-rays are emitted in opposite directions to preserve conservation of momentum. These annihilation quanta can be detected via a ring of scintillation detectors. From those coincidence events and data from tens of thousands of paths through the object a localisation of the source can be achieved. Since uptake of FDG is concentrated within

cancerous tissue (FDG signal \propto Cancer cells in the volume), this effectively means that a tumour can be located and imaged within the body.

PET is also clinically used to diagnose and monitor treatment efficacy. The amount of uptake of FDG by the tumour is characterised by a semi-quantitative index, which reflects glucose metabolism. Clinicians often use this value, known as the *Standard Uptake Value* (SUV) (Hubner, Buonocore *et al.*, 1996), to differentiate between benign and malignant lesions. A standard uptake value of > 2.5 measured using a filtered back projection algorithm is generally used as an identifying feature for a greater probability of malignancy. The PET defined volume based on SUV is dependent on a number of variables including image threshold, size of the lesion, the presence of tumour motion and the scanning protocol (Yaremko, Riauka *et al.*, 2005).

Together, PET and CT provide important diagnostic information for treatment planning. CT provides anatomical information whilst PET provides information on the metabolic function of organs and allows for cancerous cells to be detected. PET images can also be mapped onto CT data-sets enabling a radiologist to contrast two imaging modalities which exploit fundamentally different physical processes. While both CT and PET can be used to isolate tumour masses, each technique has weaknesses that can lead to false negative and positive diagnoses. This usually occurs when $\Delta\mu$ or ΔSUV is too small for the respective modality to resolve. PET-CT combined on the other hand largely negates these issues as it is very rare for a tumour to have the same SUV *and* attenuation characteristics as surrounding tissues.

1.6. TREATMENT PLANNING IN EXTERNAL BEAM RADIOTHERAPY

Treatment planning in conventional external beam radiotherapy refers to the assignment of beam directions and dose weightings. Treatment planning is a complex process and requires the definition of treatment volumes for meaningful 3D treatment planning and accurate dose specification. Modern radiotherapy is carried out with a variety of beam energies and increasingly complex treatment fields and beam shaping devices such as multi-leaf collimators (MLCs). A discussion about treatment planning would not be complete without a definition of the principle volumes which make up the treatment volume, as outlined by ICRU reports 50 and 62 (ICRU, 1993, ICRU, 1999). The following volumes have been defined in the reports: Gross Tumour Volume (GTV), Clinical Target Volume (CTV), Internal Target Volume (ITV), Planning Target Volume (PTV) and Organ At Risk (OAR).

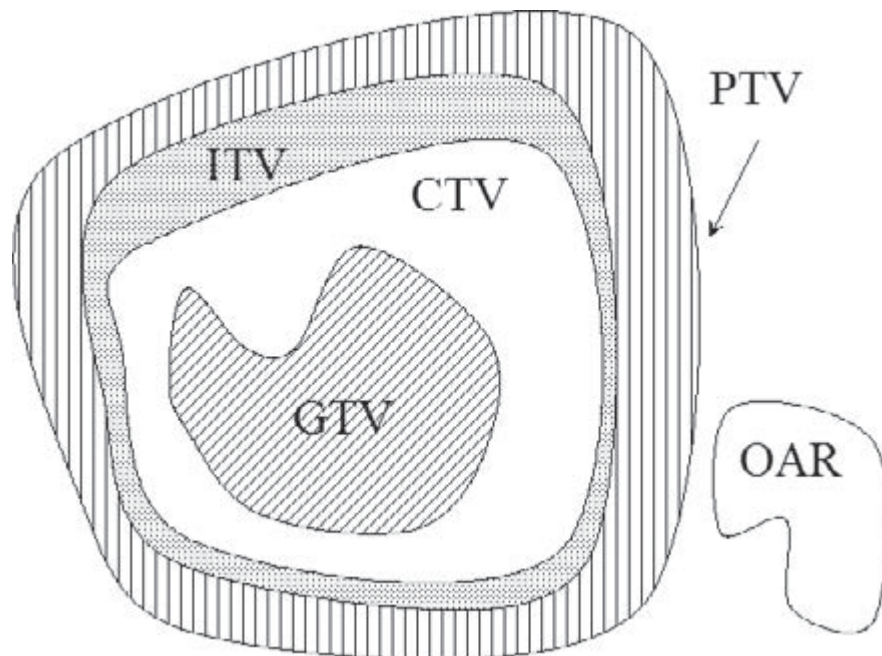


Figure 1.4. Schematic of the ICRU Report 50 and 62 definition of treatment volumes (Podgoršak and Agency, 2005). The 'Gross Tumour Volume' (GTV) is described as the gross demonstrable extent and location of the malignant growth. The 'Clinical Target Volume' (CTV) is a tissue volume that contains a demonstrable GTV and/or subclinical malignant disease undetectable by imaging that must be eliminated. The Internal Target Volume (ITV) is a margin which is added to the CTV to account for all movements of the CTV during treatment and the 'Planning Target Volume' (PTV) is an added margin to the ITV to account for variations in patient position and beam position both intrafractionally and interfractionally.

The following definitions are outlined by ICRU Report 50 and 62:

- Gross Tumour Volume (GTV)
- “The Gross Tumour Volume is the gross palpable or visible/demonstrable extent and location of malignant growth” (ICRU, 1993)
- Clinical Target Volume (CTV)
- “The clinical target volume is the tissue volume that contains the demonstrable GTV and/or sub-clinical microscopic malignant disease, which has to be eliminated. This volume thus has to be treated adequately in order to achieve the aim of therapy, cure or palliation” (ICRU, 1993)
- Internal Target Volume (ITV)
- Of particular relevance to this work is the internal target volume. This internal margin is designed to take into account the variations in the size, shape and position of the CTV relative to the patient’s reference frame. The ITV takes into account movement of the target volume due to respiration, and deformation due to other bodily functions.
- Planning Target Volume (PTV)
- “The planning target volume is a geometrical concept, and it is defined to select appropriate beam arrangements, taking into consideration the net effect of all possible geometric variations, in order to ensure that the prescribed dose is actually absorbed in the CTV”

1.6.1. *Organs at Risk (OAR)*

An organ at risk is an organ whose sensitivity and location relative to the treatment volume means that it may receive a significant dose. Beam arrangements are generally arranged to minimise dose to these organs. An OAR does not only have to be an organ that is relatively close to the CTV, but can be an organ whose radiation sensitivity is such that it has a very low tolerance dose. During respiration, some OARs may move into the ITV and this must be taken into account.

1.6.2. Dose specification

In the context of external beam radiotherapy, the specification of the dose reporting point, along with detailed information regarding the total dose is important. ICRU report number 23 and report number 50 provide several dosimetric endpoints for specifying the dose. The key values are; the minimum dose, obtained from either, a distribution or dose-volume histogram, the maximum target dose, again, from a distribution or dose-volume histogram and the mean target dose.

1.6.3. Treatment plan evaluation

After dose has been prescribed, the plan is evaluated by a radiation oncologist. Dose distributions are often evaluated by analysing key points, contour plots and 3D dose distributions. Dose volume histograms also provide a useful way to summarise the information contained in a 3D dose distribution. Examples of cumulative Dose Volume Histograms (DVH) are shown in Figure 1.5. An ideal plan would be one in which 100% of the target volume receives 100% of the prescribed dose and an organ at risk receives 0% of the prescribed dose. However, in reality, this is not the case due to the expanding of treatment margins to compensate for uncertainties in patient positioning, target motion, patient motion, and delineation errors / uncertainties.

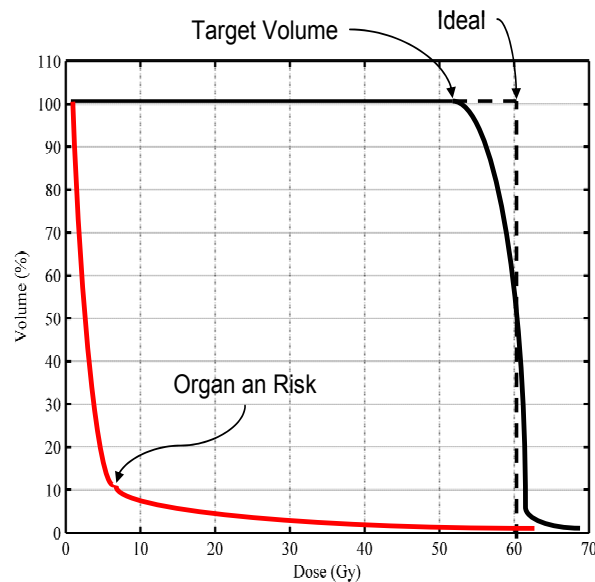


Figure 1.5. Cumulative dose volume histogram, showing ideal target volume DVH, with 100% of the target receiving 100% of the prescribed dose, typical DVH shown by the solid black line and a typical organ at risk DVH (red line).

Plan optimisation based on the analysis of contours, specific dose points and DVHs is then carried out by determining the best arrangement of beams and their energies, which enables the treatment to maximise the dose to the PTV whilst minimising dose to OARs.

1.7. TREATMENT DELIVERY IN EXTERNAL BEAM RADIOTHERAPY

Treatment delivery for external beam radiotherapy is usually carried out with multiple beams from differing angles. Modern radiotherapy is characterised by highly conformal radiation such as Intensity Modulated Radiation Therapy (IMRT) (Van Houtte, 2003). IMRT uses a multi leaf collimator (MLC) to modulate the intensity and spatial characteristics of the treatment beam. An MLC is a set of pairs of 20 to 80 narrow tungsten leaves in a closely abutting arrangement. Each leaf provides a projection width of approximately 3 - 10 mm at isocentre and the dynamic nature of the leaves means irregular field shapes can be achieved. Modern linacs may come with the MLC as an integral part of the machine head or as an attachment. Figure 1.6 shows the layout of multi-leaf collimation and Figure 1.7 shows how an MLC can be used to shield organs at risk whilst still providing good PTV coverage.

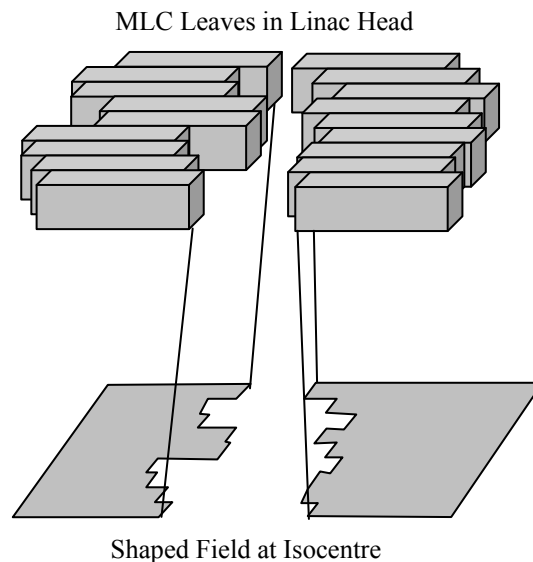


Figure 1.6. Schematic of an MLC showing tungsten leaves and the field projection at isocentre.

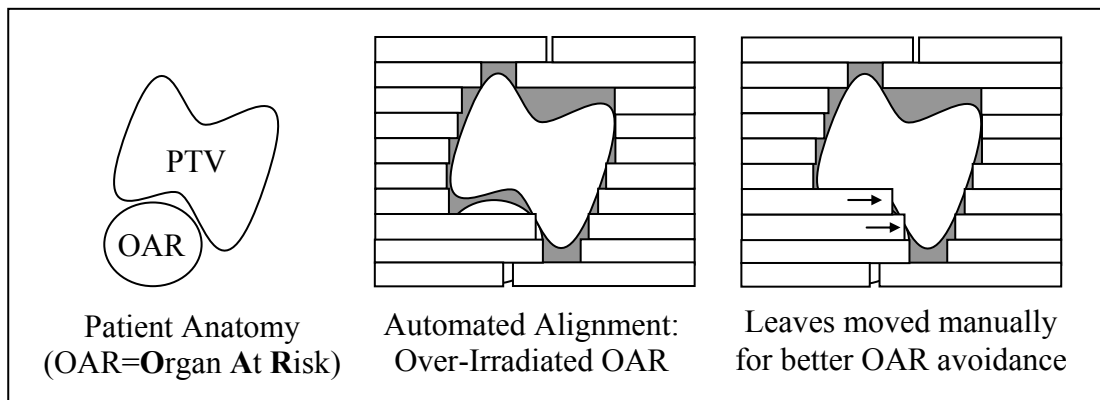


Figure 1.7. The potential for normal tissue sparing with MLCs. The MLC can be used to protect organs at risk whilst still maintaining adequate target coverage.

1.7.1. Image-Guided Radiation Therapy

Image-guided radiation therapy (IGRT) involves imaging the patient anatomy shortly before the delivery of a fraction of radiation therapy. The benefit of this technique is that intermittent verification of the target's position is afforded. Therefore, the target volume location can be actively compared with the reference location obtained from planning. Coupled with the increased delivery efficacy from IMRT, IGRT has the potential to be a vital aid in the development of reduced treatment margins, dose escalation, normal tissue sparing and avoidance of geographical misses.

1.8. TREATMENT VERIFICATION

The final step in the radiotherapy process is treatment verification. Treatment verification can be divided into simulation and *in-vivo*. *In-vivo* treatment verification is usually achieved through online portal imaging and *in vivo* dosimetry. *In vivo* dose measurements may be used to check the dose delivery by making measurements on the patient's skin surface or intracavity dose measurements. Due to the difficulty of *in vivo* measurements, phantom measurements can also be performed to verify a particular treatment procedure as part of quality assurance.

1.9. QUALITY ASSURANCE IN EXTERNAL BEAM RADIOTHERAPY

Quality assurance (QA) in external beam radiotherapy is an integral part of the radiotherapy process. It can be broadly defined in the context of radiotherapy, as all procedures that ensure the consistency and accuracy of the medical dose prescription, within the target volume, with minimal dose to normal tissue, minimal exposure to personnel and adequate patient monitoring. Comprehensive QA of radiotherapy is involved across all stages, from planning to delivery. QA is important since it reduces uncertainties in equipment, treatment planning, and treatment delivery and therefore improves the geometric accuracy and precision of the dose delivery and reduces the risk of catastrophic errors.

1.10. STEREOTACTIC BODY RADIATION THERAPY (SBRT)

1.10.1. Introduction

Stereotactic radiotherapy (SRT) emerged as a radiation therapy strategy in 1951 and was first implemented by Lars Leksell. Leksell, a Swedish neurosurgeon, developed a machine to deliver large doses of radiation to intracranial tumours (Leksell, 1983). Leksell's machine allowed neurosurgeons to administer non-invasive ionising radiation to successfully treat inoperable intracranial tumours. Stereotactic radiotherapy requires accurate localisation of the target in three dimensions and as such requires the use of stereotactic frames to reduce movement of the patient's head completely.

1.10.2. SBRT

Recently, Stereotactic Radiation Therapy/surgery has been extended to treat small tumours in other areas of the human body. This development has been termed Stereotactic Body Radiation Therapy (SBRT). The most common treatment sites employing SBRT are the lung, liver and spine (Taylor, Kron *et al.*, 2011). The rationale for SBRT is that delivering a few fractions of large dose in a short overall treatment time results in a more potent biological effect (Timmerman, 2008, Benedict, Yenice *et al.*, 2010). SBRT is highly effective in controlling early stage primary and oligometastatic cancers throughout the thoracic cavity and abdomen (Benedict, Yenice *et al.*, 2010). The key differences between SBRT and conventional radiotherapy are the dose delivered and the total number of fractions the prescribed dose is delivered in. Typical SBRT doses of up to > 54 Gy can be given in less than five fractions, whereas in conventional radiotherapy, lower doses per fraction (2 - 3 Gy / fraction) up to the prescribed dose are generally given. Table 1.3

summarises the main differences between conventional radiotherapy and SBRT and Figure 1.8 demonstrates the differences between a conventional radiation therapy plan and an SBRT plan. Figure 1.9 gives an indication of present research interest into SBRT giving the sum of PubMed based search results as a function of disease site for both intracranial and SBRT treatment.

Table 1.3. Comparison of conventional radiotherapy (3D / IMRT) and SBRT adapted form (Benedict, Yenice *et al.*, 2010).

Feature	3D/IMRT	SBRT
Dose / Fraction	1.5 – 3 Gy	6-30 Gy
No. of fractions	10- 30	1-5
Target def.	GTV / CTV / ITV / PTV	GTV / CTV / ITV / PTV
Treatment planning imaging	CT / MR / PET-CT	CT / MR / PET-CT
Margins	Centimeters	Millimeters
Need for respiratory motion management	Moderate	High
Radiobiology	mitotic cell death	ablative
Technology implementation	High	High

SBRT has been shown to increase tumor control probability (Wulf, Haedinger *et al.*, 2004, Wulf, Hadinger *et al.*, 2004, Uematsu, Shioda *et al.*, 2001, Timmerman, Papiez *et al.*, 2003, Onishi, Kuriyama *et al.*, 2004, Onishi, Araki *et al.*, 2004, Nyman, Johansson *et al.*, 2006, Nagata, Takayama *et al.*, 2005, McGarry, Papiez *et al.*, 2005, Lee, Choi *et al.*, 2003, Hof, Herfarth *et al.*, 2003, Fukumoto, Shirato *et al.*, 2002). Although the large doses have been shown to improve treatment outcome, there is also a strong relationship between increasing the dose per fraction and the complication rate should normal tissue be irradiated. In the case of stereotactic radiotherapy of lung cancer, the increase in mean lung dose has been shown to increase the incidence of radiation pneumonitis, pulmonary complications, and other toxicity related concerns (Kwa, Theuws *et al.*, 1998, Kwa, Lebesque *et al.*, 1998, Nagata, Matsuo *et al.*, 2007). Therefore, the practice of SBRT requires conformation of high doses to the target as well as a high degree of confidence throughout the entire treatment delivery procedure. These conditions, coupled with the added complexities of dose calculation in the lung, as well as potential target motion, mean that if higher doses per fraction are to be used, smaller margins, accurate localisation, and understanding / management of target motion are required.

Owing to the high degree of accuracy required to ensure treatment efficacy and reduce normal tissue exposure, a number of immobilisation devices can be used in SBRT. These immobilisation apparatus can range from vacuum bags (Lax, Blomgren *et al.*, 1994) to body frames such as the Elekta Body Frame (Elekta Oncology, Stockholm, Sweden). Typical uncertainties using these devices range from 1.8 – 5 mm (Taylor, Kron *et al.*, 2011).

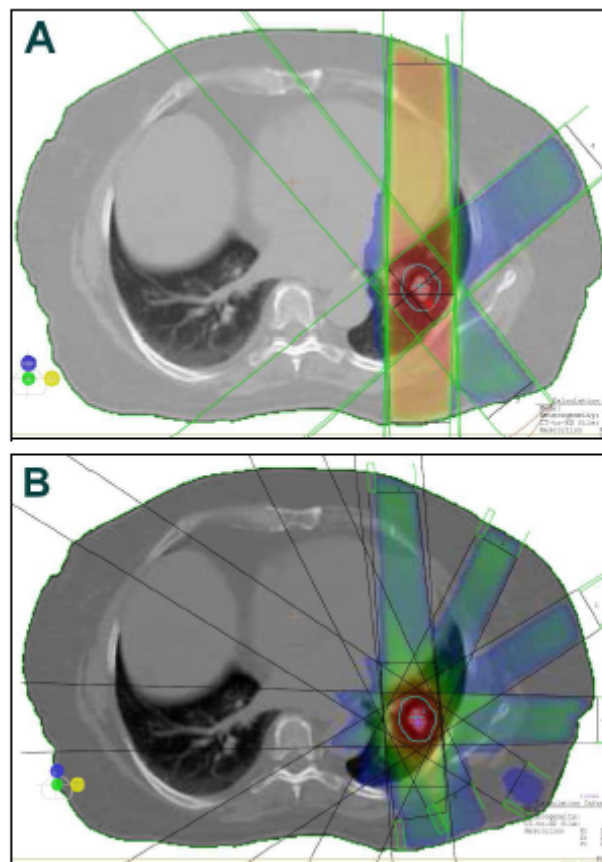


Figure 1.8. Comparison of dose distributions between a 4-field conventional lung radiotherapy plan (A) and a 7-field stereotactic lung radiotherapy plan (B). (Courtesy of Brent Chesson, Radiation Therapist, Peter MacCallum Cancer Centre, Melbourne, Australia).

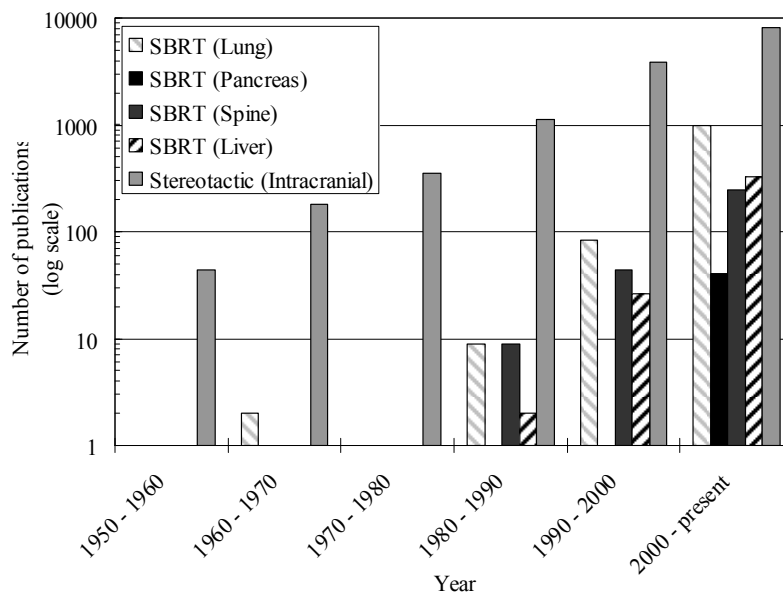


Figure 1.9. A literature search based on publications relating to stereotactic radiotherapy, both intracranial and SBRT. Note the logarithmic scale.

1.11. RADIATION DELIVERY TO A MOVING TARGET

The potential for dose escalation in SBRT in the lung is complicated by tumour motion. Tumours in the abdominal region often undergo motion due to the patient's respiratory function and the potential for dose escalation is reduced due to the inherent uncertainties involved in the target's position, along with the possibility of excess exposure to healthy tissues surrounding the target.

1.11.1. *Complications due to motion of lung tumours in conventional radiotherapy*

In effect, all tumours move to some extent during treatment. In the past, tumour motion has been managed by expanding the field size of conventional radiotherapy beams to ensure that the tumour receives exposure at all times along its trajectory. This method is sub-optimal as the volume of healthy tissue increases as R^3 , (where R is the radius of a sphere) it is clear that a small increase in the margin around the CTV will result in a large amount of healthy tissue being exposed. Numerous motion management methods have been proposed in the literature and will be covered in the literature review in Chapter 2. Each motion management method has its associated advantages and disadvantages and the choice of a particular method depends on the magnitude of displacement and the patient's ability to tolerate the chosen procedure.

1.11.2. Lung cancer SBRT and tumour motion: The current problem

The problem of radiation delivery to a moving target is compounded in SBRT due to the higher doses per fraction as well as the increased need for highly localised delivery. Recent research suggests a direct correlation between dose escalation and local control. For example, Machtay *et al* (2012) recently determined that there is an associated 18% decrease in the risk of death from primary disease with every 10 Gy increase in biologically equivalent dose. Figure 1.10, taken from an excellent review paper by Taylor *et al* (2011) shows the key findings of several studies on SBRT for the treatment of primary lung cancer.

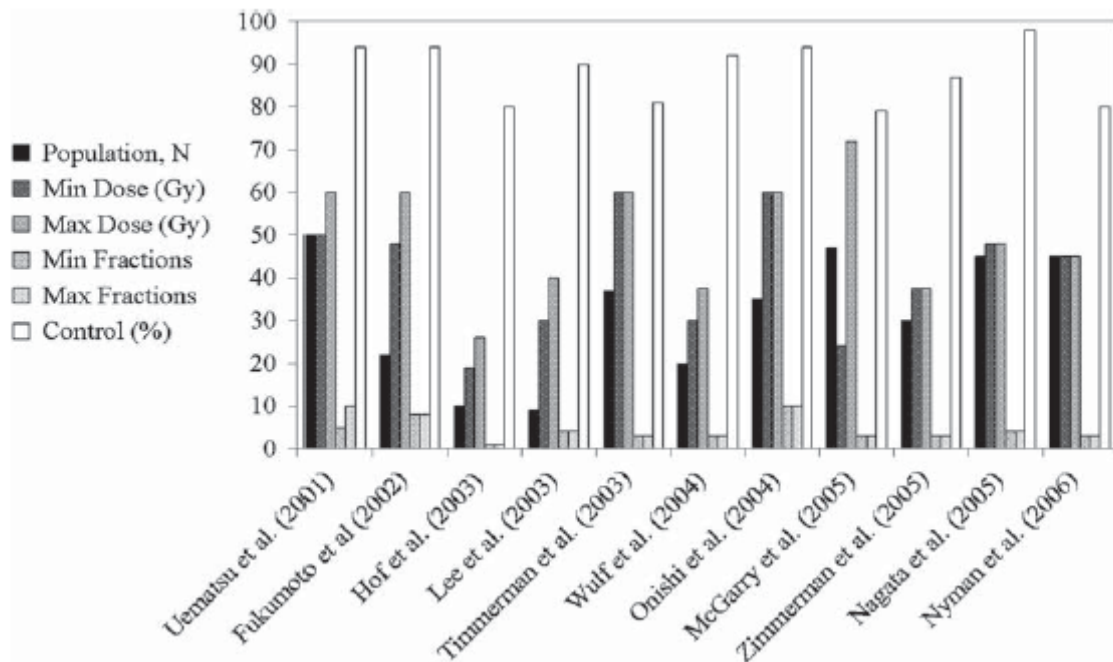


Figure 1.10. Overview of several key studies reviewed in the paper by Taylor *et al* (2011). The number of patients, N, dose, local control rate and number of fractions are shown.

However, research has also shown that the probabilities of complications from the treatment itself, such as radiation pneumonitis, are also directly correlated to the mean lung dose (Seppenwoolde, Lebesque *et al.*, 2003, Kwa, Lebesque *et al.*, 1998).

One of the primary concerns in SBRT is the difficulty in choosing a prescription point or volume. The standard protocol for prescribing and reporting dose is outlined by the International Commission on Radiation Measurements and Units (ICRU) reports 52 and 62 (ICRU, 1999, ICRU, 1993). This protocol specifies that the variation in dose within the target should be kept between -5% and +7% of the prescribed dose. It is for this reason that the 95% isodose line is chosen for target coverage in conventional radiotherapy. In SBRT, a lower isodose line, such as the 80% isodose line, is used for prescription. The rationale for this is to improve the dose fall-off outside the target volume (Figure 1.11) which therefore helps spare organs at risk (Benedict, Yenice *et al.*, 2010) however, the choice of a lower isodose prescription also reduces dose homogeneity within the target itself. This is well known and accepted in intracranial stereotactic radiotherapy. Heterogeneity within the dose distribution can result in hotspots within the target. Hotspots are often deemed acceptable, as the objective in SBRT is ablative, as long as there is no overlap into normal tissue regions (Cardinale, Wu *et al.*, 1999, Fowler, Tome *et al.*, 2004).

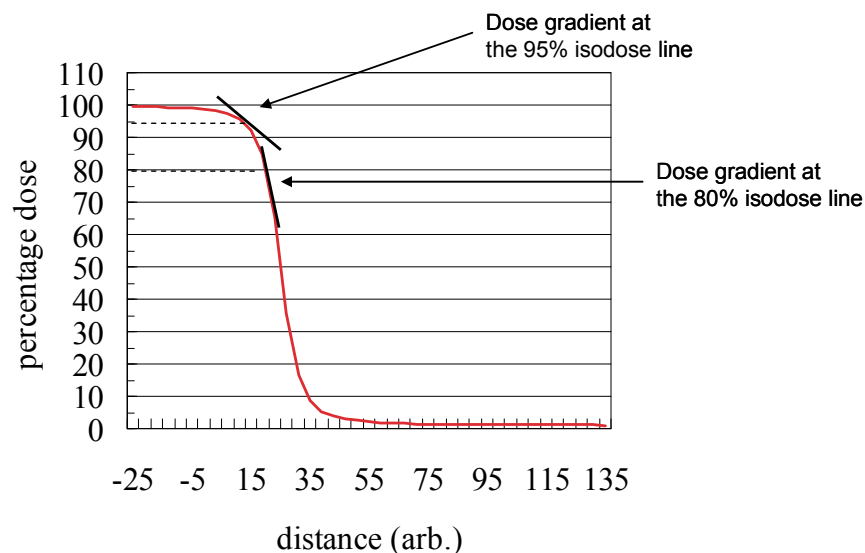


Figure 1.11. Graph showing the consequences of prescription to a lower covering isodose. The steepness of the dose gradient when prescribing to a lower covering isodose results in greater dose heterogeneity within the tumour volume.

If dose escalation is to be utilised in a safe, accurate and effective manner, then increasingly conformal fields and strict quality assurance protocols must be developed across all stages of the radiotherapy cycle. Motion management must take into account the size of the lesion and the treatment methodology. Tumour motion presents a challenge for SBRT due to the high doses involved and the relatively small margin for error. This fact, coupled with the reduced number of fractions SBRT is usually delivered in, means that errors in delivery and planning could result in far greater detriment to the patient. If methodologies and technologies can be developed to understand and account for small lesion motion, then increased localisation and accuracy in radiation delivery can be expected. This in turn will allow an increased potential for dose escalation and may help to improve the balance between complications and cure.

1.12. AIM & OBJECTIVES

The main aim of this thesis is to make an assessment of the impact of motion on the treatment of small lesions affected by motion as commonly seen in stereotactic radiotherapy of lung cancers. This includes the elements of imaging, treatment planning methods and dose calculation which are all affected by motion.

To address this aim the following objectives were set:

Objective 1: Assess the effect of motion on the identification and delineation of small, moving tumours.

Objective 2: Quantify the influence of lesion size and motion amplitude on data acquired from 4D-CT

Objective 3: Determine the degree to which the same relationships affect PET data if and when this imaging modality is incorporated into the treatment planning process.

Objective 4: To assess the mitigation of motion effects in PET that can be achieved by implementing 4D phase-binned PET.

Objective 5: To evaluate dose calculation on lung tumours, in particular quantifying the differences between 4D calculations, which explicitly account for dynamic geometry and conventional 3D calculation, based on average intensity projection data from 4D-CT.

1.13. APPROACH

This thesis is organised as follows: Chapter 2 presents a literature review on the effect of tumour

motion during imaging and treatment delivery. This section firstly focuses on the biomechanics of respiratory motion and tumour motion, with attention paid to the magnitudes of these motions as reported in the literature. The effect of motion on images acquired with conventional CT and PET is then discussed with a review of the substantial literature on this topic. Motion effects that compromise radiation delivery and dose calculation are then presented.

The latter half of Chapter 2 presents currently available motion management strategies that have been both presented in the literature and are available clinically. Firstly, surrogate markers and respiratory gating are reviewed with both gating based on external and internal surrogates being discussed. Breath-hold techniques are then described with the literature on both voluntary and mechanically assisted methods reviewed. Motion management in the context of treatment planning is outlined for CT and PET imaging modalities and the literature is reviewed. Literature on the methods to combat motion effects, such as slow CT scanning and time-resolved 4D-CT is presented and reviewed. For PET, gated (4D) acquisitions are described and the literature reviewed. The literature and methods of complex motion management techniques, such as real-time tumour tracking are then presented. A section on motion phantoms is included in this chapter since their design and construction is important in the context of this thesis. Finally, Monte Carlo methods are presented, starting with a summary of currently available Monte Carlo codes. The limited literature on the use of Monte Carlo and simulation of dose delivery to moving lesions is then outlined. Finally, SBRT and the need for a better understanding of the effects of tumour motion in both treatment planning and delivery of SBRT is discussed leading into Chapter 3.

Chapter 3 describes the development of two motion phantoms. The development of a see-saw phantom used in this work is presented followed by an assessment of its motion capabilities and the accuracy of a mathematical model describing its motion. This phantom was specifically designed to be compatible with CT imaging and is used to determine the magnitude of errors that can occur in 4D-CT imaging of moving lesions. These errors are evaluated as a function of lesion size and amplitude and are presented in Chapter 4. The upgrade of a commercially available motion phantom, so that realistic patient-like motion can be achieved is then presented. The methods and materials involved in the upgrade are outlined and the results are presented highlighting the accuracy of the upgrade in reproducing patient-like motion.

Chapter 4 examines the impact of motion on images acquired with 4D-CT. The results presented in this chapter were obtained experimentally with a small computational component utilising the XCAT phantom described in Section 2.10.3.3. The experimental data was acquired using the seesaw phantom described in Section 3.2. Results pertaining to the effect of motion on images acquired with 4D-CT are then presented (Objectives 1 & 2). These results focus on the HU consistency of phase-bin data, the quality and accuracy of maximum and average intensity projections (MIP & AIP) with respect to the minimum number of phase-bins needed to produce an accurate description of the tumour motion. The XCAT phantom is then used to simulate scenarios to corroborate the experimental results and verify the finding that the quality of MIP and AIP is a function of the lesion size and amplitude.

Chapter 5 presents experimental and computational results for the investigation into the impact of motion on images acquired using PET. Specifically, this work pertains to Objective 3, with the effect of motion on 3D-PET images assessed for a variety of lesion sizes and motion amplitudes. Results of 4D-PET simulations in a Monte Carlo framework are then presented (Objective 4).

Chapter 6, the impact of motion on treatment planning and dose calculation (Objective 5) is then presented. In this section, Monte Carlo simulations using static lesions of various sizes and distances from the chest wall boundary are performed to establish the peripheral underdosage of the lesion that occurs as a result of these conditions. Following this, results comparing 4D dose calculation, that is, the explicit incorporation of temporal information into dose calculation, to performing dose calculation on an AIP are presented (Objective 5). Chapter 7, the conclusion, presents a summary of the results presented in thesis and focuses on clinical outcomes and outlook.

Chapter 2. Literature review: Motion management in radiotherapy

“If I have seen further it is by standing on the shoulders of giants.”

-Sir Isaac Newton

The previous chapter provided the relevant introductory material relating to radiotherapy and stereotactic radiotherapy. This chapter serves as a literature review of the current status of motion management in radiotherapy.

2.1. INTRODUCTION

Meeting the specific goal of radiotherapy is a challenging endeavor, which is further complicated by motion of the patient's anatomy. Traditionally, in dealing with motion, a volume larger than the tumour boundary was irradiated to ensure adequate dose coverage of the target over its excursion. This method is outlined in ICRU Reports 50 and 62 (ICRU, 1999, ICRU, 1993) and an overview of the methodology is shown in Figure 1.4. From Figure 1.4, it can be seen that margins to account for clinical spread of disease and patient setup uncertainty increase the amount of healthy tissue irradiated. The volume is further increased when another additional margin, the Internal Margin (IM) must be added to the standard margins to account for expected physiological movements and variations in size, shape and position of the CTV during therapy. Motion management is one of the primary research areas in radiotherapy today and progress has been made across all stages of the radiotherapy cycle. The rest of this chapter will be devoted to describing the issues and current motion management methods available clinically.

2.2. INTRAFRACTIONAL TUMOUR MOTION

Intrafractional motion (motion *during* treatment) can be caused by physiological, cardiac, gastrointestinal and muscular motion. However, the main cause of concern, regarding motion management in radiotherapy is concerned with target motion caused by patient respiratory function. Respiratory induced tumour motion is of greater concern than other physiological movements due to the large spatial displacements that can occur.

2.2.1. Biomechanics of breathing

The basic function of the human respiratory system is to allow gas exchange between blood and air to maintain normal levels of pressure in the arterial blood. Respiratory motion is involuntary, however, humans have some control over the frequency and amplitude of respiration. The diaphragm controls the inspiration cycle of respiration by contracting inferiorly and anteriorly into the abdomen (see Figure 2.1 showing a typical diaphragm profile and the resulting anterior-posterior (AP) chest-wall profile.). In doing so, the intercostal muscles that connect adjacent ribs

contract, the ribs are then pulled superiorly and anteriorly expanding the dimensions of the thoracic cavity which draws air in to fill the cavity created. Exhalation is an elastic function whereby the chest-wall and lungs return passively to their pre-inhalation state. Respiratory function and the subsequent breathing profile varies from subject to subject and can be different depending on, but not limited to, posture, breathing type (chest or abdominal) and location and extent of disease based respiratory function degradation. In addition to the lungs, the liver, pancreas, breast, prostate and kidneys can all move with breathing. Furthermore, during the radiotherapy process the patient's breathing can change in period, amplitude and regularity further complicating the procedure (Vedam, Kini *et al.*, 2003, George, Vedam *et al.*, 2005, Seppenwoolde, Shirato *et al.*, 2002a). In the coming sections, the effects of respiratory motion in the radiotherapy process will be summarised for lung tumours. Current methods to manage motion in radiotherapy will also be discussed.

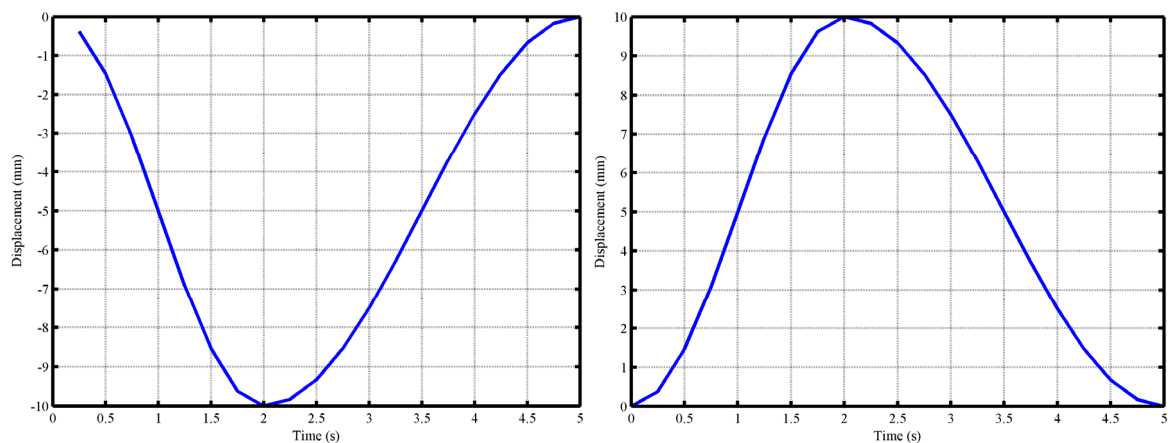


Figure 2.1. (a) A typical diaphragm motion profile and (b) the corresponding AP chest-wall motion profile.

2.2.2. Magnitude of lung tumour motion caused by respiratory function

Table 2.1 is a summary of the reported magnitudes of respiratory induced lung tumour motion amplitudes (Keall, Mageras *et al.*, 2006a). The magnitude of tumour motion varies depending on a number of factors. The type of breathing (shallow or deep), the patient's disease site (lung / abdomen etc.) and, especially for lung, the disease site with respect to the diaphragm can modify the magnitude of the effects of respiratory motion on tumour motion. From the literature, it is clear that in most cases tumour motion occurs in all three dimensions, Superior-Inferior (SI), Left-Right (LR) and Anterior-Posterior (AP), however, the magnitude of tumour motion seems to be greater

in the SI direction with the LR and AP motion components being of a smaller magnitude. The average motion of tumours in the lower regions of the lung has also been shown to be of greater magnitude than of tumours located in the middle or upper lung (Barnes, Murray *et al.*, 2001, Kubo and Hill, 1996). Tumour trajectories also experience hysteresis as was shown by (Seppenwoolde, Shirato *et al.*, 2002a). Hysteresis occurs when the tumour's trajectory during inhale is different from that during exhale. Using fluoroscopic imaging of implanted fiducial markers, Seppenwoolde *et al* (2002a), observed hysteresis in tumour motion trajectories in half the patients. Their results showed a 1-5 mm separation between inhalation and exhalation. It is also clear from the literature that there are no simple models that can be applied to respiration. From patient to patient, it is clear that no assumptions can be made about respiratory behavior. If respiratory motion is affecting the treatment volume significantly, then it *must* be monitored and accounted for during planning and treatment using radiotherapy. Figure 2.2 shows typical respiration induced tumour motion as simulated with the XCAT phantom. The tumour's motion is divided into 10 distinct phases. Figure 2.3 and Figure 2.4 demonstrate the variability in respiratory function seen between different patients. The significance of this is that motion can be large; and quite variable; therefore strategies for assessing the impact on imaging, planning and dose delivery should incorporate studies of a variety of motion patterns / amplitudes. As a result, the motion phantoms presented in this thesis and the investigations performed include motion patterns which vary in regularity as well as amplitude.

Table 2.1. The magnitude of respiratory motion as observed in several studies. The disease site, mean range of motion in mm in three dimensions (Superior Inferior [SI], Anterior Posterior [AP], Left Right [LR]) is reported (if available) as well as the maximum and minimum tumour motion in brackets. Where maximum and minimum are not reported the plus/minus standard deviation is shown.

Observer	Disease Site	Direction		
		SI (mm)	AP (mm)	LR (mm)
(Weiss, Wijesooriya <i>et al.</i> , 2007)	Lower Lobe		15.4 (3D-Vector) (11.4 - 24.0)	
	Upper Lobe		4.54 (3D-Vector) (1.3 - 11.6)	
(Seppenwoolde, Shirato <i>et al.</i> , 2002a)	-	5.8 (0 - 25)	2.5 (0.8)	1.5 (0-3)
(Shirato, Suzuki <i>et al.</i> , 2006)	-	10.7 (2.1 - 28.0)	8.9 (2.4 - 28.4)	8.1 (2.2 - 24.6)
(Gierga, Chen <i>et al.</i> , 2004)	-	7.4 (0 - 18)	3.8 (0 - 8.7)	--
(Plathow, Ley <i>et al.</i> , 2004)	Lower Lobe	9.5 (4.5-16.4)	6.1 (2.5-9.8)	6.0 (2.9-9.8)
	Middle Lobe	7.2 (4.3-10.2)	4.3 (1.9 -7.5)	4.3 (1.5-7.1)
	Upper Lobe	4.3 (2.6 -7.1)	2.8 (1.2-5.1)	3.4 (1.3 -5.3)
(Ekberg, Holmberg <i>et al.</i> , 1998)	-	3.9 (0-12)	2.4 (0-5)	2.4 (0-5)
(Erridge, Seppenwoolde <i>et al.</i> , 2003)	-	12.5 (6-34)	9.4 (5-22)	7.3 (3-12)
(Britton, Starkschall <i>et al.</i> , 2007)	-	8.6 ± 1.9	3.9 ± 0.8	1.9 ± 0.5
(Chen, Weinhaus <i>et al.</i> , 2001)	-	(0-50)		
(Hanley, Debois <i>et al.</i> , 1999)	-	12 (1-20)	5 (0-13)	1 (0-1)

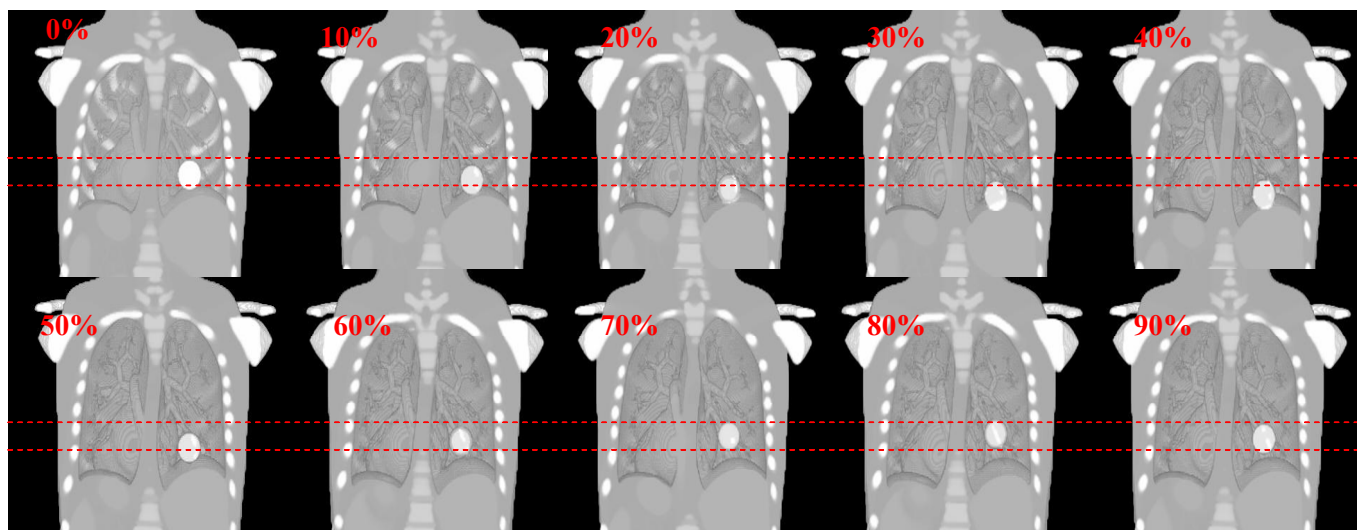


Figure 2.2. A computer generated example of a tumour's SI motion as a function of the respiratory phase. These images were generated with the XCAT phantom which is discussed in Section 2.10.3.3. In these images, 0% corresponds to the peak-exhale phase and 40% corresponds to peak-inhale phase. The red dashed line represents the starting position of the mass's excursion. The lesion can be seen to move in and out of this region over a complete respiratory cycle.

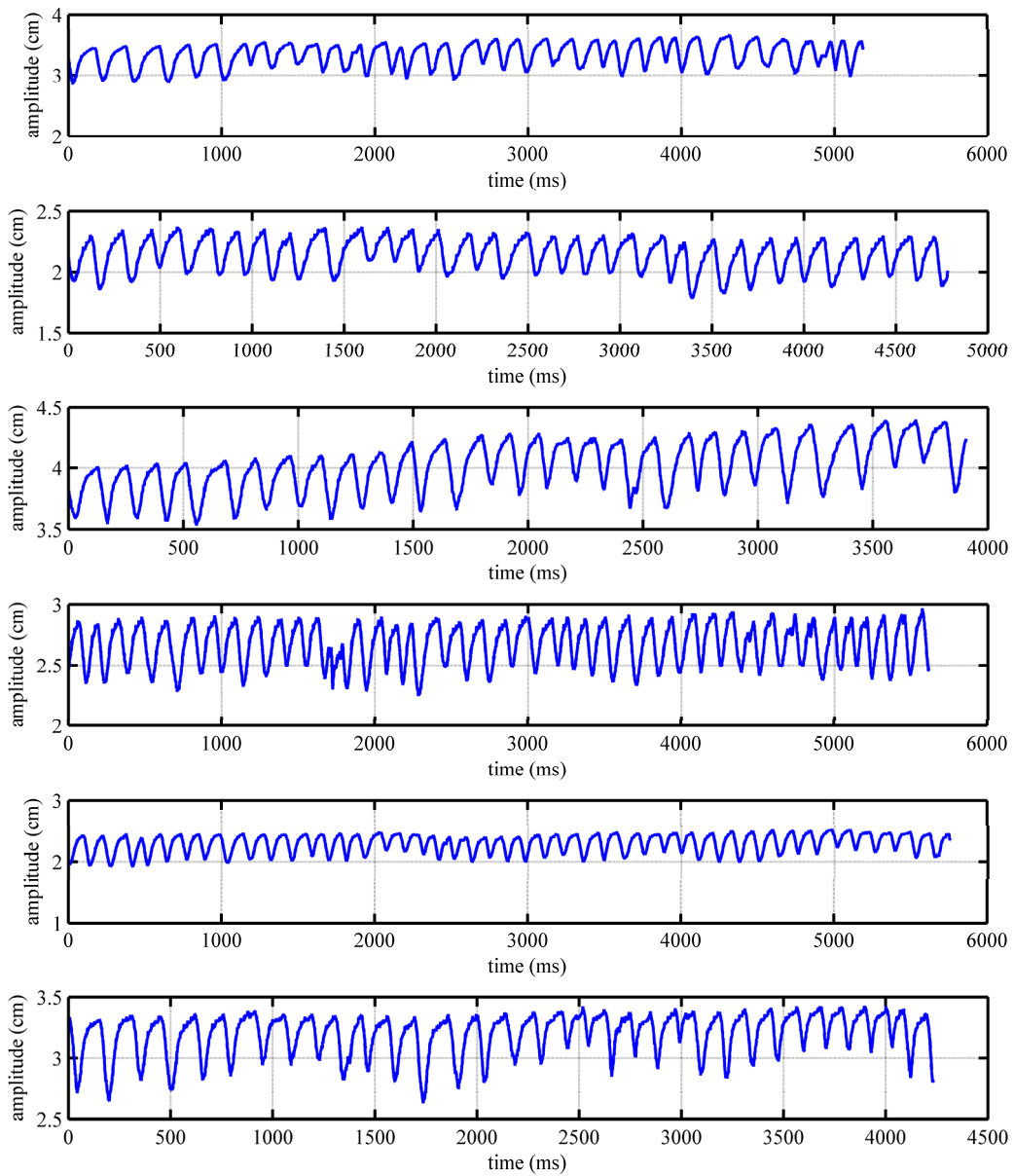


Figure 2.3. Six separate patients' AP chest-wall motion as a function of time showing the variability between patients, and within the breathing profiles of individual patients. Data is taken from six patients involved in the CHISEL clinical trial¹.

¹ A randomised phase III trial of highly Conformal Hypofractionated Image guided ("Stereotactic") radiotherapy (HypoRT) versus conventionally fractionated radiotherapy (ConRT) for inoperable early stage I Non-small cell Lung cancer.

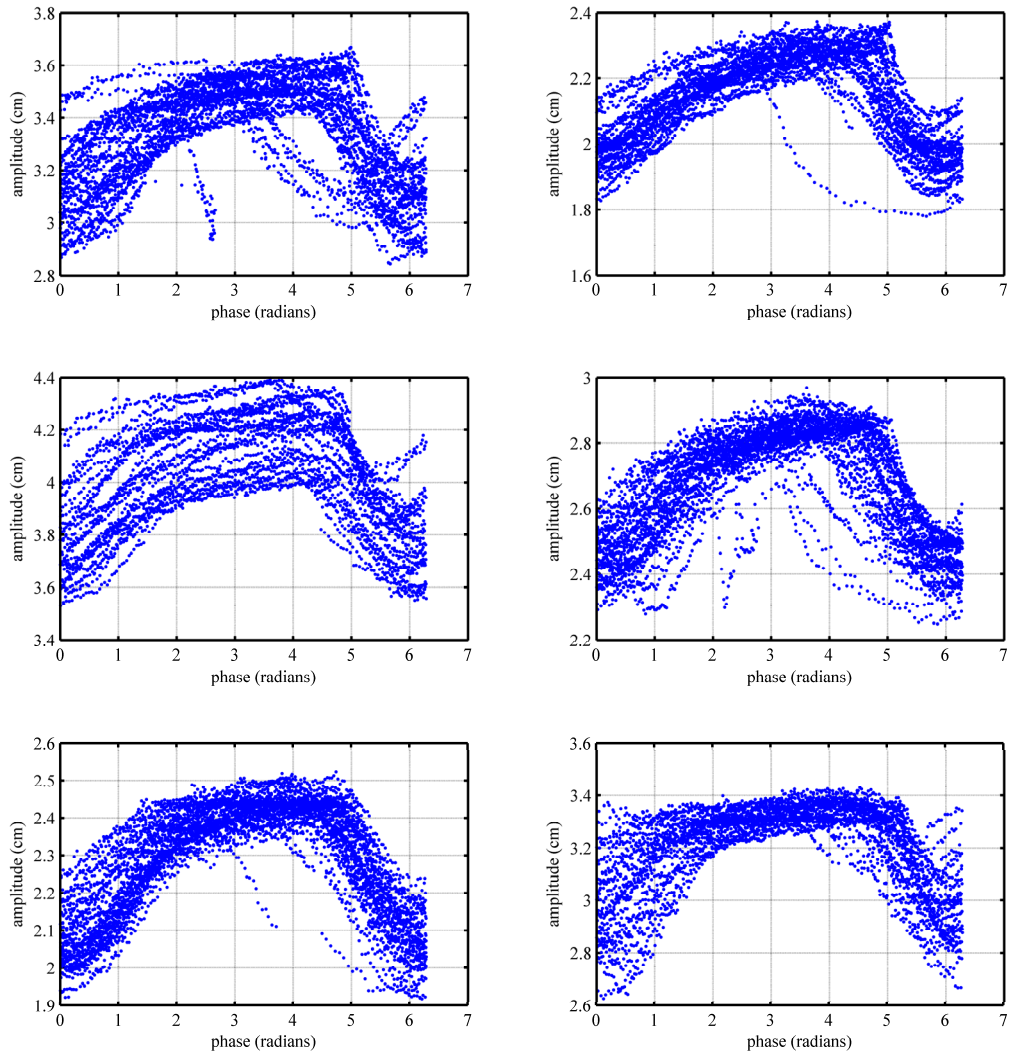


Figure 2.4. Six patients' phase versus chest wall amplitude variability (from Figure 2.3). This data shows each respiratory cycle overlaid on top of one another. The grouping of these traces represents the degree of respiratory regularity.

2.3. THE EFFECT OF INTRAFRACTIONAL TUMOUR MOTION DURING IMAGING

2.3.1. Introduction

Imaging is critical to the diagnosis of cancer and subsequent radiotherapy treatment planning. Common tumours, such as those occurring in the lung, breast and colon are typically diagnosed via imaging using X-ray CT, ultrasound, mammography or Magnetic Resonance Imaging. Further imaging of the disease depends on the tumour type and its methods of spread. Imaging is also used to monitor treatment, whereby, the primary tumour's size and metastatic spread in response to radiotherapy treatment can be determined. These examinations allow the oncologist to determine if further intervention, i.e. chemotherapy, is needed in addition to radiotherapy. Furthermore, imaging is also used in screening for cancer. Mammography screening of breast cancer, for example, is widely accepted for improving detection rates for women aged between 40 and 70 and thus provides an improvement for breast cancer mortality (Ohuchi, Yoshida *et al.*, 1993, Elwood, Cox *et al.*, 1992, Fletcher, Black *et al.*, 1993).

Radiotherapy planning requires imaging to define the tumour / target volume. This is often achieved with the use of Computed Tomography (CT), Magnetic Resonance Imaging (MRI) and Positron Emission Tomography (PET). The importance of 3D / volumetric imaging during treatment planning of cancer cannot be overstated. With regard to motion, standard techniques generally assume a static geometry, therefore, motion of anatomy due to respiration can cause artifacts in the images and needs to be explicitly accounted for.

2.3.2. The effect of tumour motion on images acquired with Computed Tomography

Computed tomography is the primary method of imaging for stereotactic lung cancer patients undergoing radiotherapy. Since CT images are used to determine the treatment plan and calculate dose distributions, the accuracy of the images and information about anatomical / target motion is critical. Primarily, respiratory motion causes artifacts in image acquisition since the method of image reconstruction assumes a static anatomy. Artifacts in computed tomography can cause distortions in the tumour's apparent location and measured size. The cause of the artifacts in CT is generally due to different parts of the anatomy being imaged moving in and out of the CT slice window. The CT image reconstruction algorithms assume invariance of anatomy, and thus, when the slices are combined to form the image, distortions can be present. The degree and type of

artifact is dependent on a number of factors, such as the position of the tumour relative to the diaphragm, depth of respiration, patient movement during acquisition and interplay between scanner acquisition methodology and motion, for example, helical or cine acquisition.

2.3.2.1 Artifacts in conventional CT

An accurate CT relies on a static anatomy at the time of acquisition. This is often impossible to achieve as the human body is continually in motion internally. The result of patient motion during the acquisition of CT data is artifacts in the resulting images. In CT, the term artifact is defined as any systematic discrepancy between the CT numbers in the reconstructed image and the true CT number of the object being imaged (Barrett and Keat, 2004). The types of artifacts that may occur can generally be classified as physics based, scanner based, reconstruction based and patient based. They can generally be grouped as (a) Streaking (Sheridan, Keller *et al.*, 1980), due to an inconsistency in a single measurement, (b) shading, due to the gradual deviation of a group of channels or views. (c) rings (Tsai, Chen *et al.*, 2011, Sadi, Lee *et al.*, 2010, Abu Anas, Lee *et al.*, 2010), due to errors in individual detector calibration and (d) distortion (Nishimaru, Utsunomiya *et al.*, 2005). Most of the artifacts described here are applicable to filtered back projection methods.

2.3.2.1.1. Physics based artifacts

Physics based artifacts result from the physical processes involved in the acquisition of CT data. Beam hardening occurs as photons pass through an object. Beam hardening results in an increase in the mean energy of the spectrum of photons passing through an object due to the greater absorption of lower energy photons in the object. There are two types of artifacts that can result from beam hardening: cupping and streaks, or dark bands. Cupping artifacts occur since the rate at which the beam is attenuated decreases as the beam passes through the object. At the detectors, the beam is more intense than would be expected if hardening had not occurred. Dark bands occur between two dense objects on an image. Dark bands occur because the portion of the beam that passes through one of the objects at a certain tube position is hardened less than when it passes through both objects in other tube positions.

2.3.2.1.2. Scanner based artifacts

Scanner based artifacts are those related to the detection system itself. For example, Ring artifacts on a third generation CT scanner (both tube and detection system rotating) can arise due to one of the detectors being out of calibration. This detector will give a consistently incorrect reading at each angular position resulting in a circular ‘ring’ artifact.

2.3.2.1.3. Reconstruction based artifacts

The quality of images from CT is highly dependent on the number of projections used for reconstruction. Too large an interval between projections can lead to undersampling, where the computer misregisters data relating to sharp edges and small objects. Undersampling generally leads to aliasing artifacts where fine stripes are present radiating outwards from the edges of dense structures. Aliasing artifacts may not greatly affect the diagnostic quality of an image, however, where resolution is important aliasing artifacts need to be avoided since these artifacts may cause errors in dose calculation.

2.3.2.1.4. Patient based artifacts

Patient based artifacts can generally be grouped into metal implant artifacts and patient motion (voluntary, involuntary or anatomical) related artifacts. Patient motion can result in a variety of artifacts, with the degree of impact on the diagnostic or planning quality of an image being dependent on the magnitude of the motion during image acquisition. Patient motion management and the effect of patient motion on images acquired with CT are of the greatest importance for SBRT (Zamora, Riegel *et al.*, 2010b, Timmerman, Park *et al.*, 2007, Timmerman, Abdulrahman *et al.*, 2007).

Figure 2.5 shows a CT data-set simulated with the XCAT phantom. In Figure 2.5 (a), there is no motion present during the acquisition of the scan and the image appears artifact free. Figure 2.5 (b) on the other hand has motion enabled and the distortion of the image is clearly evident. Several authors have investigated the artifacts formed by moving objects. Chen *et al* (2004) investigated the interplay between helical acquisition and moving objects of a known geometry. A phantom was used to simulate motion with amplitude of 1 cm and motion period of 4 seconds. High speed scans were acquired at incremental phases of respiration and the image quality was assessed. The resulting scans showed that moving spherical objects can be shortened by up to 2 cm (twice the motion amplitude). Furthermore, the spherical object's shape was significantly distorted with the geometric centre being displaced by up to 0.8 cm in either direction. An interesting result of their study was that even if the amplitude was decreased to 0.5 cm, the effects were still observable. Balter *et al* (1996b) studied patients with abdominal and thoracic tumours and compared free-breathing CTs to breath-hold CTs. Their results showed that free-breathing CT studies may incorrectly estimate volumes and positions of critical structures and therefore may lead to incorrect plan evaluation when using DVHs and Normal Tissue Complication Probability (NTCP) criteria.

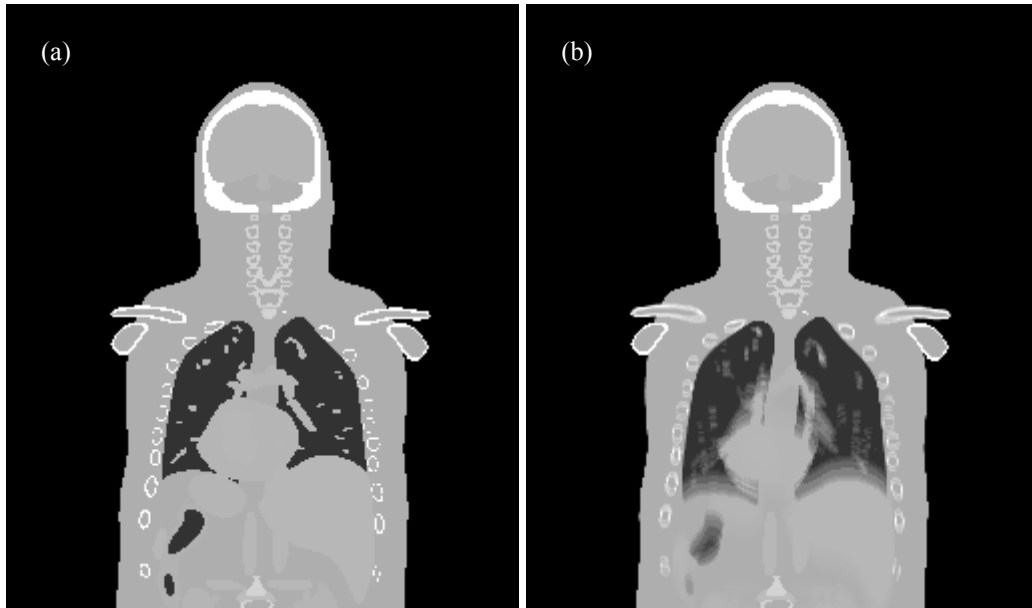


Figure 2.5. (a) Simulated CT using the XCAT phantom for a static anatomy, (b) Simulated CT of a moving anatomy showing the distortion due to motion.

2.3.2.2 Artifacts and the effect of motion in 4D-CT

Respiratory induced tumour motion results in a blurring or distorted image set in conventional CT where the tumour's position can move through multiple slices as well as within individual slices. This blurring of anatomy and the target itself can result in misdiagnoses and incorrect planning information about target size, structures in connection with the target and the average position of the target. Breathing triggered 4D-CT was developed by Vedam (spiral) (Vedam, Keall *et al.*, 2003b) and Keall (multi-slice helical) (Keall, Starkschall *et al.*, 2004). The goal of 4D-CT is to gather information on anatomic variation as well as highly detailed visualisations of patient anatomy. The spatiotemporal information provided by 4D-CT mitigates many of the respiratory motion artifacts associated with conventional CT by binning the CT data as a function of an external surrogate based respiratory signal. However, irregular motion (Rietzel and Chen, 2006a) and binning artifacts as a result of irregular motion are still an area of concern (Mutaf, Antolak *et al.*, 2007). Furthermore, the finite slice acquisition times in 4D-CT mean that residual motion over a typical scanner rotation time will exist within each phase-bin. These issues indicate that 4D-CT should be used with some caution and the accuracy and limitations of 4D-CT scanner technology

evaluated accordingly.

In SBRT of thoracic targets, 4D-CT is critical to inform the clinician of the position of the tumour over a complete respiratory cycle, the average position of the target, the size of the target and the regularity with which the patient breathes. Moreover, due to the high doses per fraction, errors are no longer blurred over a larger number of fractions, and therefore the accuracy, and verification of the accuracy of 4D-CT is vital.

While there are other methods to assess a tumour's range of motion such as fluoroscopy (Chen, Weinhaus *et al.*, 2001), 4D-CT is the most widely used method clinically (Hugo, Vargas *et al.*, 2006, Pan, Sun *et al.*, 2008, Wink, Panknin *et al.*, 2006). 4D-CT provides useful projections from the phase-bin data which can be used for SBRT treatment planning purposes. Individual projections will give a more realistic estimate of the real lesion size and its boundaries over its range of motion. Furthermore, the Average Intensity Projection (AIP) (Figure 2.6) is commonly used for dose calculation since it is a representation of the average density over the course of a respiratory cycle (Huang, Park *et al.*, 2010a, Vinogradskiy, Balter *et al.*, 2009b). The Maximum Intensity Projection (MIP) (Figure 2.6) is used to delineate the ITV showing a 'motion envelope' encompassing the maximum minimum and inter-maxima phases of the tumour's trajectory (Bradley, Nofal *et al.*, 2006, Admiraal, Schuring *et al.*, 2008b, Rietzel, Chen *et al.*, 2005a, Huang, Park *et al.*, 2010a, Underberg, Lagerwaard *et al.*, 2005, Muirhead, McNee *et al.*, 2008). In this work, artifacts relating to an object's size and motion on images and projections obtained from 4D-CT were investigated.

SBRT requires precise localisation of targets and accurate delineation of patient anatomy to aid in treatment planning. Three dimensional data is often obtained from CT or 4D-CT for visualisation and dose calculation, with PET images being used to assist in visualisation and target definition (Chen, Kung *et al.*, 2004). Motion causes problem in traditional imaging. Free breathing spiral CT may not represent the true target position since the target can be imaged at different respiratory phases at each slice (Chen, Kung *et al.*, 2004).

Previous studies have shown that motion can lead to an over/under estimation of lesion size in CT imaging. However to date this has only been shown for relatively large lesions undergoing quite small displacements. It has not been analysed for small mobile lesions typical of SBRT targets.

This is addressed in this thesis in Chapter 4.

2.3.3. The effect of tumour motion on images acquired with Positron Emission Tomography (PET)

In radiotherapy treatment planning, PET is most commonly used in conjunction with CT to provide additional metabolic information and help inform treatment planning decisions. During PET imaging, data is usually acquired over 3 - 7 minutes per bed position (Nehmeh and Erdi, 2008). Since many respiratory cycles occur during the acquisition and the rate remains the same, the activity profile of the moving tumour is 'smeared' across the tumour's range of motion. Small lesions undergoing motion are particularly troublesome for PET since the resolution is of the order of 4 - 6 mm, and as a result moving small lesions may be lost against the background activity.

2.3.3.1 PET used in conjunction with CT (PET/CT)

Since PET scanning only supplies functional metabolic information, clinically it requires anatomical information to add a localisation along with attenuation correction. For this, computed tomography (CT) is used. The fusion of these two technologies has allowed for increased accuracy of diagnostic information and therefore the potential for increased treatment accuracy (Rajagopalan and Heron, 2010). Lung tumour motion presents a number of challenges for conventional PET. Previous authors have generally characterised the effects as the underestimation of SUV and the overestimation of the tumour's size and volume (Senan and De Ruyscher, 2005, Allen-Auerbach, Yeom *et al.*, 2006, Mac Manus, Hicks *et al.*, 2006).

In a large patient study conducted by Liu *et al* (2009), 1295 respiratory traces were acquired during whole body static PET/CT imaging. By investigating this large population, a characterisation of the dependence on motion profile variables for SUV_{max} underestimation and volume overestimation was achieved. Overall, their population study revealed respiratory motion can have a significant impact on PET/CT imaging, depending on; motion amplitude, lesion location, size of lesion, choice of attenuation map and respiratory irregularity. On average, the study found that motion induced an underestimation in SUV_{max} of 28% and an average overestimation of lesion volume of 130%. The study also found that mismatched attenuation correction can be partly compensated by using a respiratory-averaged CT, however, the tumour quantification and delineation is further complicated by using this method. To summarise, tumour motion causes the following issues for PET and PET-CT imaging:

1. Metabolic PET activity images taken of moving tumours represent the average of the different positions successively occupied by the tumour. This means that a 'hot' lung lesion's activity profile is smeared over its range of motion.
2. Since activity concentration is smeared, the volume of the lesion is overestimated.
3. SUVs are underestimated since the artifactually large lesion's activity profile is smeared (Liu, Pierce *et al.*, 2009).
4. In static PET/CT of the thorax, tumour motion can lead to a distortion of the combined PET/CT (Liu, Pierce *et al.*, 2009)
5. Misalignment of PET/CT images can reduce diagnostic accuracy and increase treatment margins resulting in excessive dose to normal-tissue, and or, organs at risk or underdosage of the lesion's periphery.
6. PET and CT have largely different scan times; meaning, accurate co-registration between the two image sets with meaningful results can be difficult.
7. Accurate quantification of tracer activity concentration requires CT provided attenuation correction. This is difficult to achieve when registering images that are not breathing-phase correlated. (Nehmeh, Erdi *et al.*, 2004a, Ponisch, Richter *et al.*, 2008). An outcome of this is that accurate attenuation correction can only be achieved when the position of the lesion is the same on 4D-CT and 4D-PET images (Osman, Cohade *et al.*, 2003).

Table 2.2 shows the results of several studies assessing the impact of motion on both the tumour's apparent volume and the underestimation of SUV.

Table 2.2. Summary of the effects of motion on SUV underestimation and volume overestimation. Maximum values found over the entire study are presented except where noted.

Observer	Motion range (mm)	SUV _{MAX} underestimation (%)	Volume overestimation (%)
(Liu, Pierce <i>et al.</i> , 2009)	6 – 16	28	130
(Pevsner, Nehmeh <i>et al.</i> , 2005)	0 – 20	75	--
(Callahan, Binns <i>et al.</i> , 2011)	0 – 40	450 (5 mm lesion) , 150 (20 mm lesion)	72
(Nagel, Bosmans <i>et al.</i> , 2006)	2.5 – 4.8	75	370

2.4. THE EFFECT OF TUMOUR MOTION ON RADIATION DELIVERY

As outlined in Chapter 1, motion not only affects the imaging portion of the SBRT cycle, but also the delivery of radiation to the target during treatment. This section looks at the effects of tumour motion on radiation delivery.

Radiation delivery to moving targets results in a blurring of the static dose distribution possibly leading to mistreatment. If the motion of the target is not explicitly accounted for, a discrepancy between the planned and delivered dose distributions can result. Generally, as discussed earlier, a static field must be made large enough so that the tumour's motion does not place the PTV near the beam edges. This approach is sub-optimal and where tumour motion is significant, say, greater than 5 mm, an unnecessary irradiation of healthy tissue often occurs. The effect of blurring during radiation delivery to a moving target may be exacerbated during IMRT delivery due to the interplay between target motion and that of the MLC leaves and steep dose gradients. For stereotactic treatments, motion of tumours during delivery presents a unique challenge. Targets moving in small fields, coupled with the high doses and very steep dose gradients involved mean that motion needs to be explicitly managed if the dose escalation afforded in SBRT is to be pursued. Although tumour motion is predominately perpendicular to the beam direction, for multiple field techniques (SBRT), the motion direction may also be parallel to the beam direction. In this scenario, although there is a shallower dose gradient, the dose received by the target is subject to influence from variations in electron equilibrium associated with the overlying inhomogeneities at varying distances.

2.5. CONCEPTS OF MOTION MANAGEMENT IN RADIOTHERAPY

Before an in-depth discussion about motion management methodologies specific to imaging and subsequently treatment delivery, methods that are common to both: surrogate markers, gating and breath-hold methods, will be discussed in the coming sections.

2.5.1. *Surrogate markers*

The near Z independence of attenuation in the MV range means that it is difficult to directly measure the target's position during therapy. Surrogates are therefore often used on the basis that their position has a strong correlation to relevant internal anatomy. There are both internal and external surrogate markers. The diaphragm, for example, can be imaged with fluoroscopy during treatment to get an indication of the target's location if the target cannot be directly seen. This is an example of an internal surrogate. Conversely, external surrogates are structures like the chest-wall which rises and lowers depending on the respiration state, or the volume of air entering and exiting the mouth. When using a surrogate, without observing the target directly, there is an inherent uncertainty based on the correlation between the surrogate and the target itself. Numerous authors

have observed phase-shifts and complex changing relationships between the coupling of the external surrogate and target itself (Ahn, Yi *et al.*, 2004, Jiang, Cerviño *et al.*, 2009, Ionascu, Jiang *et al.*, 2007, Hunjan, Starkschall *et al.*, 2010, Hoisak, Sixel *et al.*, 2004, Gierga, Brewer *et al.*, 2005, Beddar, Kainz *et al.*, 2007, Tsunashima, Sakae *et al.*, 2004, Mageras, Pevsner *et al.*, 2004a). The results of these studies are summarised in Table 2.3. Several other studies noted that the motion of the diaphragm may not be a good surrogate for lung cancer patients due to decreased pulmonary function (Stevens, Munden *et al.*, 2001, Giraud, De Rycke *et al.*, 2001).

The Varian Real-time Position Management system (Section 3.1.1.1) and the Phillips bellows system (Section 3.1.1.2) are two commercially available surrogate based respiratory monitoring systems used in this thesis and are described in 3.1.1. Other commercially available surrogate marker monitoring systems are the Anzai belt (Siemens Medical Systems, Concord, CA, USA) and the ExacTrac Gating/Novalis Gating system (BrainLAB, Heimstetten, Germany). These however will not be discussed here even though the issues are similar.

Table 2.3. Reported variations in the correlation between internal target motion and external surrogates.

Observer	Surrogate	<i>N</i> (patients)	Correlation Range
(Ahn, Yi <i>et al.</i> , 2004)	Abdominal Displacement	43	0.41 – 0.94
(Hoisak, Sixel <i>et al.</i> , 2004)	Spirometry	11	0.39 – 0.99
(Tsunashima, Sakae <i>et al.</i> , 2004)	Abdominal Displacement	26	1
(Gierga, Brewer <i>et al.</i> , 2005)	Fluoroscopy (ext. / int. clips)	4	0.85 – 7.1
(Beddar, Kainz <i>et al.</i> , 2007)	Abdominal Displacement	8	Linear ($R^2 = 0.9298$)
(Cervino, Chao <i>et al.</i> , 2009)	Fluoroscopy (Diaphragm)	10	0.94 - 0.98
(Mageras, Pevsner <i>et al.</i> , 2004a)	Abdominal Displacement	9	0.74 – 0.98

2.5.2. Respiratory gating

Respiratory gating is the synchronisation of imaging or radiation delivery with respiration, such that the radiation delivery / image acquisition occurs during a specific part of the patient's respiratory cycle (Keall, Mageras *et al.*, 2006b). Monitoring the patient's respiratory cycle determines the start and duration of the beaming time on, termed "gate". Respiratory gating has been achieved using both external surrogates (Wu, Zhao *et al.*, 2008) and implanted fiducial markers (Gierga, Brewer *et al.*, 2005). Since the beam is only actually on for a smaller duration, gated treatments / image acquisition periods are longer than conventional procedures.

Respiration can generally be characterised by two variables, displacement and phase. Consequently, gating can also be split into displacement or phase based gating. During displacement based gating, the radiation beam is activated whenever the respiration signal is within a pre-set window of relative positions. Conversely, during phase-based gating, the radiation beam is activated whenever the respiration signal *phase* is within some pre-defined phase window of the total cycle ($0 - 2\pi$). Generally, a gate window would be chosen based on observation of the location or phase where tumour motion is considered to be minimal. This method ensures that any residual motion within the pre-defined window is at a minimum. The ratio of the beam on time within the gate to the overall treatment time is referred to as the 'duty-cycle'.

2.5.2.1 Gating based on external surrogates

As discussed previously, gating of the beam can be achieved by monitoring the patient's respiratory motion through an external surrogate. Kubo *et al* (1996) evaluated a number of different methods of acquiring an external respiratory signal and monitoring respiration. Thermistors, thermocouples, strain gauges and pneumotachographs were all investigated and it was found that temperature and strain-gauge based methods provided the most accurate and reproducible results. Newer methods of monitoring patient respiration involve using optical based methods that track the rise and fall of the chest wall via a CCD camera and an IR reflective marker (see Section 3.1.1.1.) Gating is now a commonly available method of motion management with numerous commercial vendors now including the option of gated delivery. The potential benefits / pitfalls of gated delivery have been investigated by a number of authors (Kubo, Len *et al.*, 2000, Vedam, Keall *et al.*, 2001, Verellen, Depuydt *et al.*, 2010, Smith and Becker, 2009, Ramsey, Scaperoth *et al.*, 1999, Saito, Sakamoto *et al.*, 2009, Saito, Sakamoto *et al.*, 2010, Saito, Sakamoto

et al., 2011). Investigations into the optimal parameters have been reported (Kuechler, Hoinkis *et al.*, 2004) as have the desired beam properties (Ramsey, Cordrey *et al.*, 1999). The overall clinical efficacy of gating has also been reported (Ramsey, Scaperoth *et al.*, 1999).

A typical gated radiotherapy treatment would occur as follows. During treatment, the reflective marker or other external surrogate is positioned as it is in simulation. The fundamental principle behind the external surrogate method is that the external surrogate has a motion profile that is strongly correlated to the internal motion of anatomy. The internal / external correlation can be verified by comparing digitally reconstructed radiographs (DRRs), from the gated planning CT, to gated radiographs or portal images. Once satisfactory pre-determined gating / beam conditions have been established, beam delivery is initiated. A beam-on signal will trigger only when the external marker is within the predefined conditions and the radiation beam will be on whilst the condition remains *true*. This allows the synchronisation between imaging and treatment, therefore allowing for CTV-PTV margin reduction by decreasing the PTV margin (since we are only interested in a specific portion of the complete tumour trajectory).

2.5.2.2 Gating based on internal fiducial markers

An alternative method of gating uses internal fiducial markers as the basis for locating the target. In this scenario, markers usually made of gold are inserted directly into, or near the tumour. The marker's position can then be imaged and tracked via fluoroscopy. When each marker is within a desired range the beam is turned on. Although this method is more accurate than the external method, it is also more invasive and therefore may not be available for all patients. Furthermore, a dual kV fluoroscopic and MV imaging system is preferable to locate the fiducials in coincidence (Wiersma, Mao *et al.*, 2008).

2.5.3. Breath hold techniques

2.5.3.1 Voluntary breath-hold methods

A simple way to minimise respiration induced tumour motion is to instruct the patient to hold his or her breath during the acquisition of images or delivery of radiation. Breath-hold methods can either be voluntary or assisted with the aid of devices such as the Active Breathing Control (ABC) system. (Wong, Sharpe *et al.*, 1999, Remouchamps, Letts *et al.*, 2003a). If the ABC system is not used, and patient involvement is necessary, the patient is instructed to hold his or her breath at a particular point in the respiratory cycle. During the breath-hold period the lesion's motion is

assumed minimal, enabling beam delivery with a semi-static target. Generally, it is preferable to involve respiratory monitoring (Wurm, Gum *et al.*, 2006, Wong, Tung *et al.*, 2010, Weckesser, Stegger *et al.*, 2006, Peng, Vedam *et al.*, 2011) in this process since the patient's hold time and reproducibility can be irregular owing to the decreased lung function commonly seen in lung cancer patients.

In treatment planning, modern CT scanners have fast acquisition times and some early stage and therefore reasonably healthy patients are able to perform a breath-hold for the entire scan duration. During a breath-hold CT (BHCT) (Nehmeh, Erdi *et al.*, 2007), the patient's respiration is monitored and the patient is asked to hold their breath at some point in the respiratory cycle, typically peak-inhale or peak-exhale. Due to the deteriorated lung function of lung cancer sufferers this method may only be achievable in patients who are able to produce repeatable breath-holds. A benefit of using BHCT is that a tumour-encompassing volume can be created by acquiring both inhale and exhale BHCTs. A maximum intensity projection (MIP) of the CT data-set would show the tumour's maximum and minimum positions in space and the encompassing volume can then be delineated as the boundary of these extremes. The patient's ability to produce repeatable breath holds can be improved with audio based coaching (Nakamura, Narita *et al.*, 2009a) or biofeedback. Biofeedback, involves giving the patient feedback on their performance and enabling them to learn to increase their breathing reproducibility through visual / auditory stimuli (Kini, Vedam *et al.*, 2003).

Breath-hold treatments generally occur at deep inspiration or expiration depending on the nature of the respiratory cycle, target location and levels of stability at each extreme. Deep Inspiration Breath Hold (DIBH) involves verbally or visually (or both) coaching the patient to a reproducible breath hold at deep inhale. The patient's respiration is monitored via a spirometer or other monitoring system that enables the therapist to observe the patient's breathing whilst coaching. The general technique used is known as the slow vital capacity technique and involves the patient deeply inhaling, deeply exhaling, second deep inhale followed by the hold. DIBH has been shown to be advantageous in reducing internal motion. In conjunction with DIBH, it is common to monitor the respiratory profile of the patient during the radiation delivery (Mageras and Yorke, 2004).

The use of external surrogate monitoring can ensure that the patient's breath-hold is reproducible as well as providing a beam-off safeguard should the patient's respiratory motion deviate from that seen during planning CT. Wong *et al* (2010) evaluated the efficacy of the technique in terms of tumour immobility and treatment setup accuracy. In their study of 14 patients with non-small cell lung carcinoma, the group found that DIBH in conjunction with external respiratory monitoring allowed a substantially reduced PTV margin, as well as good tumour immobility and accurate treatment positioning. Their group also found that there was decreased lung toxicity owing to the expanded cavity and decreased lung density. Hanley *et al* (1999) found that the DIBH method allowed for reduced margins (due to minimised motion), as well as, decreasing lung density which contributed to a reduced lung dose by moving the lung tissue out of the high dose region. Rosenzweig *et al* (2000) also found that out of seven patients (164 treatment sessions), the estimated normal tissue complication probabilities decreased in all patients at their prescribed dose when compared to free breathing. Furthermore, the authors also showed that the dose to which patients could be treated with DIBH increased, on average, from 69.4 Gy to 87.9 Gy, without increasing the risk of toxicity. There are currently two commercially available systems that are compatible with the DIBH method. These are the VMAX Spectra 20C (VIASYS Healthcare Inc, Yorba Linda, CA, USA) and the SpiroDyn'RX (Dyn'R, Muret, France) system.

2.5.4. Mechanically assisted motion reduction methods

Forced Shallow Breathing (FSB) was developed by Lax and Blomgren at the Karolinska Hospital in Stockholm (Lax, Blomgren *et al.*, 1994, Blomgren, Lax *et al.*, 1995). Originally, the method was used for patients undergoing stereotactic radiotherapy of small lesions located in the lung and liver. The technique uses a stereotactic body frame with an attached plate that can be pressed onto the abdomen. The position of the plate is controlled by a screw and is measured on a scale attached to the screw mechanism. This allows reproducibility of the abdominal restriction from simulation to delivery. The tumour's superior inferior motion can be monitored using fluoroscopy and should the target's motion exceed 5 mm, the pressure would be increased. By applying pressure to the abdomen, the patient's diaphragmatic motion is restricted, resulting in shallower breathing amplitude. The restriction of the patient's respiratory motion results in a smaller internal organ displacement associated with respiration. The stereotactic body frame and the FSB method have been used in a number of stereotactic studies (Timmerman, Papiez *et al.*, 2003, Papiez, Timmerman *et al.*, 2003, Wulf, Hadinger *et al.*, 2000). For a detailed report on the accuracy and reproducibility of this method, the reader is pointed to the paper by Negoro *et al* (2001).

The Active Breathing Control system (ABC) (Wong, Sharpe *et al.*, 1999, Remouchamps, Letts *et al.*, 2003a) is another assisted breath-hold device. ABC was developed at William Beaumont Hospital (Royal Oak, MI, USA.) and was subsequently commercialised by Elekta Inc. (Norcross, GA). The device aims to initiate a reproducible breath-hold at any stage of the respiratory cycle. It consists of a digital spirometer connected to a balloon valve. Once the patient reaches the specified lung volume the valve is inflated with air via a compressor for a predetermined period of time, thereby holding the patient's breath. The period of time for which the device can sustain a hold is determined by the patient's ability (typically 15 – 30 seconds). The device has been shown to achieve substantial and reproducible internal organ movement in clinical scenarios (Remouchamps, Letts *et al.*, 2003b).

Abdominal compression has been shown to reduce overall tumour motion and a number of commercially available devices exist. Han *et al* (2010) found that both the Bodyfix and the Abdominal Compression Plate (ACP) significantly reduced the superior-inferior (SI) and overall respiratory tumour motion compared to free breathing (4.6 and 4.0 vs. 5.3mm; 5.3 and 4.7 vs. 6.1mm, respectively, $p < 0.05$). The ACP further reduced the SI and overall respiratory tumour motion compared to the Bodyfix ($p < 0.05$). Heinzerling *et al* (2008) investigated the effectiveness of different abdominal compression levels on tumor and organ motion during stereotactic body radiotherapy of lower lobe lung and liver tumors using 4D-CT. Their study showed a significant difference in the control of both superior-inferior (SI) and overall motion of tumors with the application of medium compression (47.6 +/- 16.0 N) and high compression (90.7 +/- 27.1 N) when compared with no compression ($p < 0.0001$ for both).

2.5.5. Biofeedback for improving respiratory regularity

Should the patient demonstrate irregular respiratory function, biofeedback, or respiratory coaching can be implemented to increase regularity (Cossmann, Stuessi *et al.*, 2007, Locklin, Yanof *et al.*, 2007, Park, Kim *et al.*, 2011, George, Chung *et al.*, 2006, Raghu, Amit *et al.*, 2008, Cui, Gopalan *et al.*, 2010). Raghu *et al* (2008) studied the effectiveness of two audio-visual biofeedback systems for a total of 90 respiratory waveforms. Their results showed a significant improvement in respiratory regularity compared to free breathing. Although most authors cited have found an improvement in respiratory regularity following implementation of biofeedback respiratory coaching, Neuner *et al* (2010) found that over 11 patients (88 4D-CTs), the mean ITV (MIP) is nearly 20% smaller than the mean ITV_{10} (ITV formed from addition of ten phases) with all 4D-CT

techniques tested. Their results suggested that biofeedback using the two methods described did not improve the match between ITV (MIP) and ITV_{10} in any parameter examined in patients with both thoracic and abdominal tumors. Based on this, they recommended using an ITV derived from a MIP with caution for treatment planning regardless of 4D-CT technique if the goal is to fully account for tumor motion.

2.6. MOTION MANAGEMENT DURING IMAGING FOR TREATMENT PLANNING

In the previous sections, motion management methods common to both treatment planning and delivery have been described. In this section, motion management methods specific to treatment planning only, or treatment delivery only are outlined.

Currently, a number of methods are available for managing motion during image acquisition. The AAPM Task Group 76 (Keall, Mageras *et al.*, 2006b) investigated many of the methods available for respiratory motion management and provided guidelines for minimising potential errors. The methods themselves do not provide a complete solution. Instead, they provide a means to improve image quality and reduce motion artifacts.

2.6.1. Motion management for CT

2.6.1.1 Slow CT scanning

A simple solution for motion management during treatment planning using CT is the slow scanning method. In this method, a CT scan is acquired very slowly with the intention of including multiple respiration cycles in the scan data. By oversampling the anatomical data, a time-averaged image of the tumour's motion over a number of respiratory cycles is acquired. The resulting images then show the extent of anatomical motion that occurred during the period of acquisition. Slow CT scanning has the advantage of being able to be used for target delineation (Seki, Kunieda *et al.*, 2007, Nakamura, Narita *et al.*, 2008, de Koste, Lagerwaard *et al.*, 2003, Chinneck, McJury *et al.*, 2010, Smeenk, Gaede *et al.*, 2007), however, respiratory motion can change between planning and treatment and therefore additional margins must be added. Another advantage is that dose calculation performed on a slow CT is more representative of the average density distribution that is present during treatment.

2.6.1.2 Time-resolved CT (4D-CT)

Recently, a solution to the problems caused by motion in the acquisition of CT scans has become available. The development of four-dimensional computed tomography (4D-CT) is shown in Table 2.4 (Vedam, Keall *et al.*, 2003b, Ford, Mageras *et al.*, 2003a, Low, Nystrom *et al.*, 2003, Keall, 2004a, Keall, Starkschall *et al.*, 2004, Rietzel, Chen *et al.*, 2003, Rietzel, Liu *et al.*, 2004, Mageras, Pevsner *et al.*, 2004a, Pan, Lee *et al.*, 2004, Dinkel, Hintze *et al.*, 2009). 4D-CT provides the means to image the tumour over a complete respiratory cycle by simultaneously recording a respiratory signal and binning the CT data into distinct respiratory phase bins. Essentially, 4D-CT provides a snapshot of the tumour in a number of locations. 4D-CT has been used to determine the tumour's mean position and range of motion (Starkschall, Forster *et al.*, 2004) and to provide added data for dose calculation (Riegel, Sun *et al.*, 2008, Glide-Hurst, Hugo *et al.*, 2008, Seco, Sharp *et al.*, 2008, Bradley, Nofal *et al.*, 2006) and target delineation (Rietzel, Chen *et al.*, 2005a, Rietzel, Chen *et al.*, 2003, Rietzel, Liu *et al.*, 2008a, Rietzel, Liu *et al.*, 2008b, Rietzel, Liu *et al.*, 2006b, Rietzel, Pan *et al.*, 2005).

Table 2.4. Chronological development of 4D imaging techniques.

Author	Year	Technology Development
(Vedam, Keall <i>et al.</i> , 2003a, Ford, Mageras <i>et al.</i> , 2003b)	2003	Single slice helical
(Pan, Lee <i>et al.</i> , 2004)	2003	Multi-slice cine (commercial)
(Low, Nystrom <i>et al.</i> , 2003)	2003	Multi-slice cine
(Keall, Starkschall <i>et al.</i> , 2004)	2004	Multi-slice helical
(Nehmeh, Erdi <i>et al.</i> , 2004a)	2004	Multi-slice PET/CT
(Sonke, Zijp <i>et al.</i> , 2005)	2005	Cone beam

A particularly useful feature of 4D-CT is the ability to generate Maximum Intensity Projections (MIP) and Average Intensity Projections (AIP). A MIP is formed from taking the maximum voxel-by-voxel values across all phase-bin data sets and forming a new 3D data-set. MIPs have been used for target volume delineation (Rietzel, Chen *et al.*, 2005a, Underberg, Lagerwaard *et al.*, 2005) since they show a volume which is defined by the tumour’s maximum excursion. Correspondingly, an AIP is formed from taking the voxel-by-voxel arithmetic mean across all phase-bin data sets and forming a new 3D data set. This process is shown Figure 2.6.

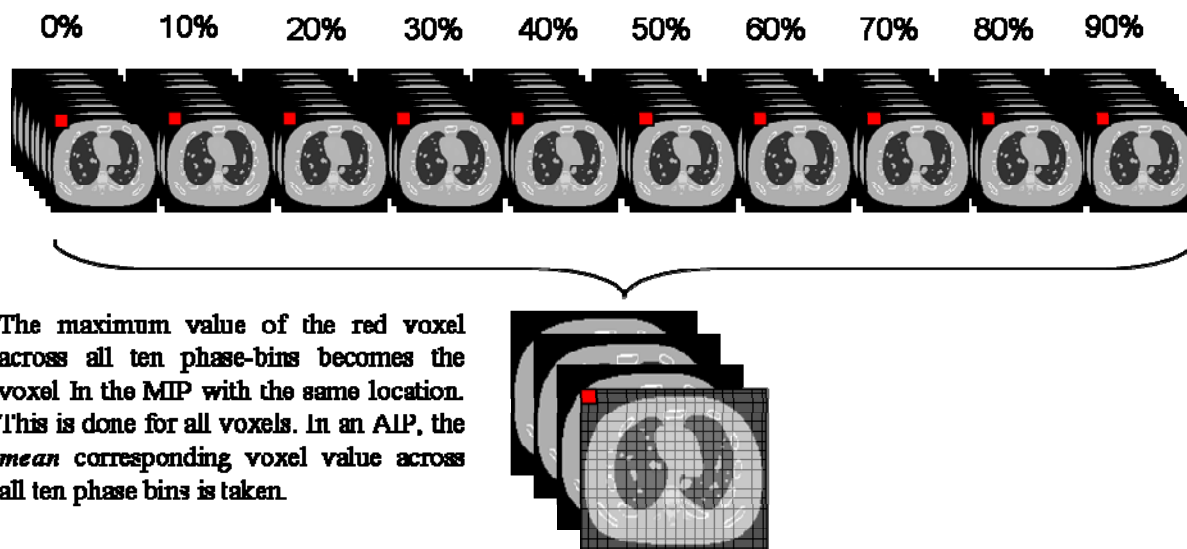


Figure 2.6. A schematic diagram of the construction of the MIP and AIP data-sets. To form the MIP, the maximum voxel value across all ten phase-bins is derived; the voxel with the maximum then becomes the corresponding voxel on the MIP. Conversely, for the AIP, the mean value is taken.

AIPs can be used for dose calculation since the voxel density values in a 3D AIP data-set are more representative of the *true* density values that would be present during treatment. 4D-CT is becoming increasingly popular with multiple vendors now offering surrogate acquisition systems to allow time resolved acquisition.

Images in 4D-CT need to be sorted according to their respective place amongst the respiratory cycle, depending on whether amplitude or phase based gating was used. To accomplish this, 4D-CT can be split into two subtypes; prospective and retrospective.

2.6.1.2.1. Prospective gated CT imaging

Prospective gated CT imaging involves the acquisition of one projection set acquired at a distinct period or phase of the breathing/cardiac cycle. The result is a CT data-set at a specified time-point. The acquisition of gated CT scans between the respiratory induced motion extremes is still an issue (Vedam, Keall *et al.*, 2003b).

2.6.1.2.2. Retrospective (image space) sorting

In retrospective based sorting, the projections are tagged based on the respiratory cycle and the phase or amplitude interval they were acquired in. Following this, the images are reconstructed and sorted corresponding to their tag. The result is several CT data-sets each at a specified time-point (e.g. 0%, 10%, 20%, 30%,...,90%). Figure 2.7 demonstrates this principle and Figure 2.8 shows how a 4D-CT is acquired for a cine acquisition.

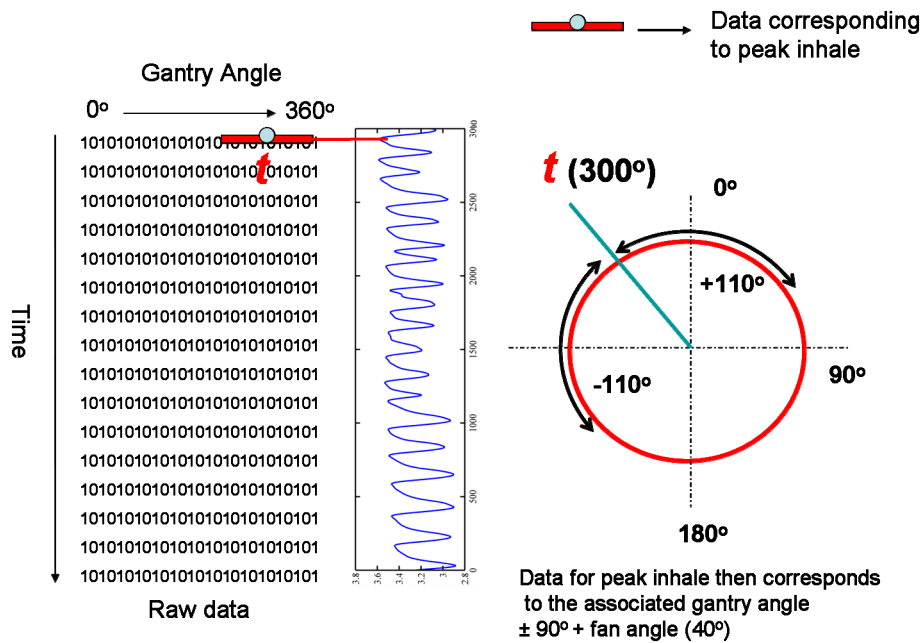


Figure 2.7. To achieve retrospective 4D-CT, CT data is tagged with the time stamp which is then compared to the respiratory cycle data. For example, if one wanted to reconstruct a slice corresponding to peak-inhale, then that point is tagged in the raw data and the data from $\pm 90^\circ +$ the fan angle is then binned into the peak-inhale data-set. This data corresponds to 180° gantry rotation, which is the minimum rotation needed to collect enough data for reconstruction. Adapted from (Wolthaus, 2009).

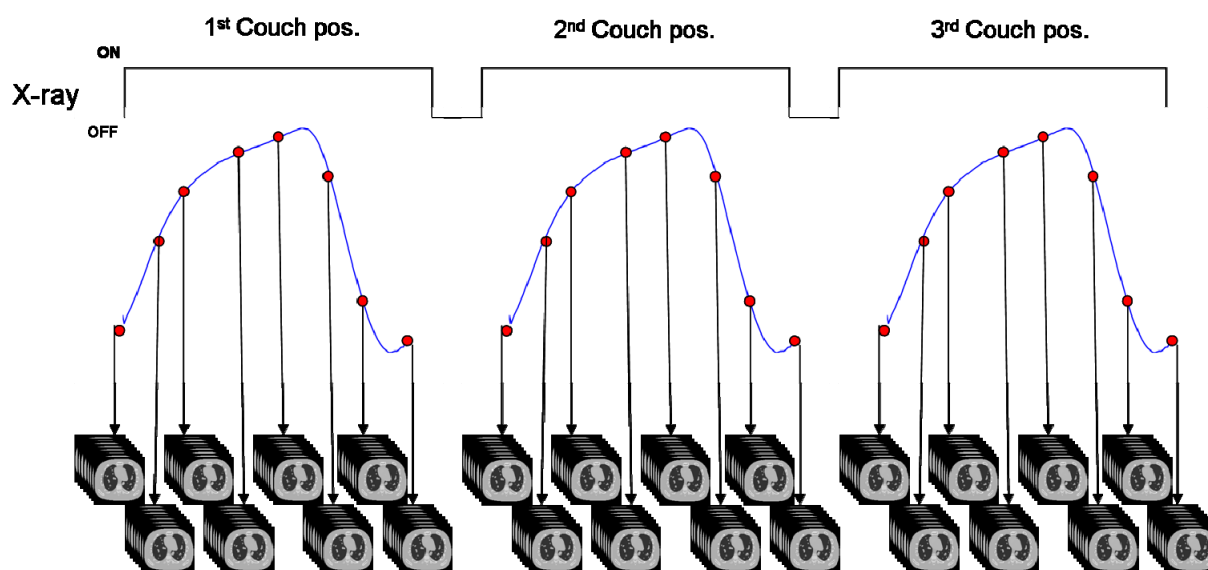


Figure 2.8. Time-resolved CT in a retrospective cine acquisition. The couch stays still during acquisition (multiple steps) and there is a continuous acquisition of slices for the time interval equal to the cine length plus the slice acquisition time. The beam is then switched off and the couch moves to the next position. After the complete volume is imaged, reconstructed slices are then sorted based on either the respiratory phase or amplitude. Adapted from (Riegel, Chang *et al.*, 2009).

2.6.2. Motion management for PET

As discussed in Section 2.3.3, PET images are acquired over several minutes per bed position. As a result the images are affected by blurring caused by respiratory motion (Visvikis, Lamare *et al.*, 2006, Nestle, Kremp *et al.*, 2006, García Vicente, Soriano Castrejón *et al.*, Edet-Sanson, Dubray *et al.*, Chuang, Chen *et al.*, 2006, Aristophanous, Berbeco *et al.*, 2012b).

2.6.2.1 Gated PET

As with other gating methods discussed in 2.5.2, gated PET involves acquiring a PET scan along with the respiratory cycle recorded with surrogate markers. The acquired PET data is then binned according to the respiratory cycle in what is termed 4D-PET. Generally, a gated PET scan is acquired for a longer length of time than a standard acquisition to increase the number of counts per respiratory bin and reduce the noise associated with the reduction in counts. Several authors have investigated the benefits of a gated acquisition in terms of both SUV recovery as well as increased accuracy in target volume delineation.

Garcia *et al* (2009) compared 4D-PET to 3D-PET in 12 patients with 18 pulmonary lesions with sizes ranging from 0.8 - 4 cm. Their results showed that for 17 out of the 18 lesions, an increased SUV_{max} was found when compared to 3D scanning. Interestingly, 4D-PET scans resulted in the

reclassification of three of the lesions from benign to malignant. Their study concluded that 4D-PET provided a more accurate means to correctly classify malignant lesions. Aristophanous *et al* (2012b) also investigated the ability of 4D-PET to reduce the errors associated with 3D-PET. Their group investigated 10 patients with NSCLC (22 distinct lesions) and found that 4D-PET may better define the full physiological extent of moving tumours and improve radiation treatment planning. In particular, the reduction in distortion compared to 3D acquisition allows for increased accuracy when analysing regional disease spread. In a recent study by Callahan *et al* (Callahan, Binns *et al.*, 2011), the upgraded QUASAR phantom developed as part of this thesis (Dunn, Kron *et al.*, 2011a) was used to determine the potential for 4D-PET to recover SUV loss and reduce errors in volume delineation. The study found that when using 4D-PET, larger lesions showed better count recovery, compared with un-gated scans. The study also showed that un-gated imaging of small mobile lesions decreases the apparent SUV significantly.

2.7. MOTION MANAGEMENT DURING TREATMENT DELIVERY

Aside from gating and breath-hold methods described in 2.5.2 - 2.5.3, a number of advanced delivery techniques have been, and are currently being, investigated. These methods generally fall under the category of motion adaptive techniques such as real-time tumour tracking. These advanced techniques show promise in increasing the accuracy of radiation delivery to moving targets. Presently, these techniques offer the potential for the most specific knowledge of tumour motion profiles during delivery, therefore tracking methods benefit most from studies of profile-dependant effects such as those presented in this thesis.

2.7.1. *Real-time tumour tracking*

As the name suggests, Real time tumour tracking (RTTT) involves tracking the tumour's position relative to the beam in real time. The technique is relatively new and usually incorporates Multi Leaf Collimators (MLCs) or linacs mounted on a robotic arm. Tumour tracking involves repositioning the beam in real-time in response to the tumour's motion, therefore negating the tumour's motion relative to the beam. If real-time tumour tracking is fully realised, then margins in place to account for target motion can be significantly reduced or, eliminated entirely. The commercially available SynchronyTM Respiratory Tracking System coupled with the CyberKnife® robotic linear accelerator (Accuray Incorporates, Sunnyvale, CA), allows for real-time tumour tracking. In general, there are three things real-time tumour tracking must achieve in order to be effective:

- Identify the target using imaging.
- Predict the target's future position to overcome mechanical latency.
- Adjust the beam to the location of the target.

2.7.1.1 Target tracking using imaging (identifying the target)

In order to effectively track the tumour, the location of the tumour must be explicitly known. For the delivery to be effective, a number of methods are available for locating the target in real time. Fluoroscopy, tracking using internal fiducials implanted within the target, external surrogate methods and determining the location of an electromagnetic radio frequency device implanted within the patient have all been reported and are under development for implementation clinically (Zhang, Hugo *et al.*, 2008, Wiersma, Mao *et al.*, 2008, Smith, Sawant *et al.*, 2009, Seppenwoolde, Shirato *et al.*, 2002b, Santanam, Malinowski *et al.*, 2008). The challenge for imaging the target is achieving the temporal resolution needed to provide accurate feedback into the prediction algorithms, whilst minimising the additional dose to the patient. Given the irregular nature of respiratory function, this is a somewhat difficult task.

2.7.1.2 Tracking using internal fiducial markers

The most accurate way to locate the target within an image is to implant high-Z metal markers within the target itself. The high densities of the markers enable increased contrast to the surrounding anatomy and can readily be seen in X-ray images. Using multiple markers allows the rotation and translation of the target to be determined in real time, and is favored instead of using a single marker (Chen, Weinhaus *et al.*, 2001). The implanted markers that have been used in studies are either 2 mm diameter spherical gold balls or 0.8 mm by 4 mm cylindrical gold seeds (Shirato, Shimizu *et al.*, 2000). The high frequency imaging needed for real time tumour tracking means that the patient will receive extra dose, this can be mitigated using a hybrid imaging technique (Schweikard, Shiomi *et al.*, 2004, Sharp, Jiang *et al.*, 2004, Murphy, 2004, Ozhasoglu and Murphy, 2002). This imaging technique combines occasional radiographic imaging with monitoring of an external respiratory signal. It is based on the assumption that the external respiratory signal can “fill in the gaps” for prediction during the time between images being acquired.

2.7.1.3 Predicting the target location using external surrogate markers

Tracking based on internal fiducials is not always available for a variety of reasons. If this method is unavailable, the location of the tumour can be ascertained from an external respiratory signal. In order for prediction to be accurate, and therefore real time tracking to be effective, a strong correlation between the external respiratory signal and the internal anatomic motion needs to be present. Generally however, this method is considered unsafe due to the unpredictable nature of

irregular respiratory function, coupled with the fact that drifts in correlation may occur during treatment (Tsunashima, Sakae *et al.*, 2004, Hoisak, Sixel *et al.*, 2004, Ahn, Yi *et al.*, 2004). The unstable correlation between an external surrogate and the internal 3D position of the target can be corrected by updating the model with periodic imaging. The added data can then be used to update the adaptive filter algorithm and the external/internal correlation can be reassessed (Schweikard, Shiomi *et al.*, 2004).

2.7.1.4 Forward prediction and latency reduction

The mechanical response of a linac cannot occur instantaneously. Therefore, forward prediction models are required to account for the latency between the input of motion data and the mechanical adjustment of the beam delivery system. The delay between the location of the tumour and beam delivery is due to a number of factors. Images need to be computationally processed, and the location of the fiducial marker needs to be ascertained. This is usually ascertained through a computational algorithm and the repositioning of the beam takes additional time. Latencies down to 90 ms have been reported (Seppenwoolde, Shirato *et al.*, 2002b) between the recognition of a fiducial marker and the subsequent delivery of radiation in a gated beam delivery system. Increasingly complex mechanical systems, such as the CyberKnife system have a longer latency (200 ms) between the acquisition of the target's location and the mechanical repositioning of the beam.

To overcome this latency, predictive algorithms are used to synchronise the beam delivery with the actual target's position. The prediction of time dependent behavior, such as respiratory induced target motion is difficult. The errors in prediction can be compounded due to cycle-to-cycle fluctuations in the respiratory regularity, with the general rule being that the greater the system latency, the greater the error in prediction (Vedam, Keall *et al.*, 2004, Sharp, Jiang *et al.*, 2004).

2.7.1.5 Dynamic delivery of the treatment beam

Dynamic adjustment of the beam is achieved by MLCs or robotic arms. Dynamic MLCs are commercially available from a number of vendors and present a viable solution to altering the beam properties in real time. Several groups have investigated dynamically moving the MLC to track targets (Neicu, Shirato *et al.*, 2003, Papiez, McMahon *et al.*, 2007, Papiez and Abolfath, 2008).

2.8. MOTION MANAGEMENT QUALITY ASSURANCE DEVICES: PHANTOMS

In the context of medical physics, phantoms are surrogates for human patients. Generally, they are made from materials which have the same radiological properties as tissues and structures found in the human body. Phantoms are used extensively to provide quality assurance and validation of treatment methodologies and are often used in conjunction with radiation detectors. In research, phantoms can be used to study the effects of a new technology or treatment methodology before it is put into use clinically. Recently, moving phantoms have become commercially available. Moving phantoms contain structures which represent parts of the human anatomy that move during treatment (usually the tumour itself) and a component of the phantom representing the chest-wall.

Moving phantoms have now become essential for commissioning of motion management equipment, credentialing of clinical trials involving new protocols involving patient motion, and quality assurance (Keall, Mageras *et al.*, 2006a). A number of commercially available motion phantoms, and upgrades enabling motion have become available, a list of which is shown in Table 2.5. An example of a commercially available motion phantom is shown in Figure 2.9. With the increasing ability of delivery and imaging technology, phantoms that are capable of programmable, complex motion are becoming increasingly necessary to provide QA for the implementation. In this thesis, software that can import actual patient and lesion motion profiles extracted from devices like the Varian RPM system is presented. These upgrades allow for more clinically relevant testing of motion management protocols and patient specific treatment plan quality assurance.

Table 2.5. List of motion phantoms, both commercial and custom made and their motion capabilities.

Manufacturer	Model	Motion capabilities	Programmable	Surrogate motion coupling	Use
CIRS	Dynamic thorax phantom Model 008a	Complex 3D tumour motion within the lung	True	Independent	PET / CT and dosimetry
Modus Medical Devices	QUASAR™ Programmable Respiratory Motion Phantom	1D linear sinusoidal (standard phantom) / upgradeable to programmable 3D motion	True	Coupled	PET/CT and dosimetry
(Nakayama, Mizowaki <i>et al.</i> , 2008)	3D movable phantom system	Complex 3D whole phantom motion (range = 100 mm)	True	N/A	Mount existing phantoms.
(Nioutsikou, Seppenwoolde <i>et al.</i> , 2008)	PULMONE	Sinusoidal accordion -like deformation	False	N/A	Film dosimetry
Washington University	4D QA system	3D motion of translation stage + surrogate motion	True	Independent	Mount existing phantoms
(Kashani, Lam <i>et al.</i> , 2007)	N/A	Deformable sponge insert for existing human torso phantom	True	N/A	kV + MV imaging and dosimetry

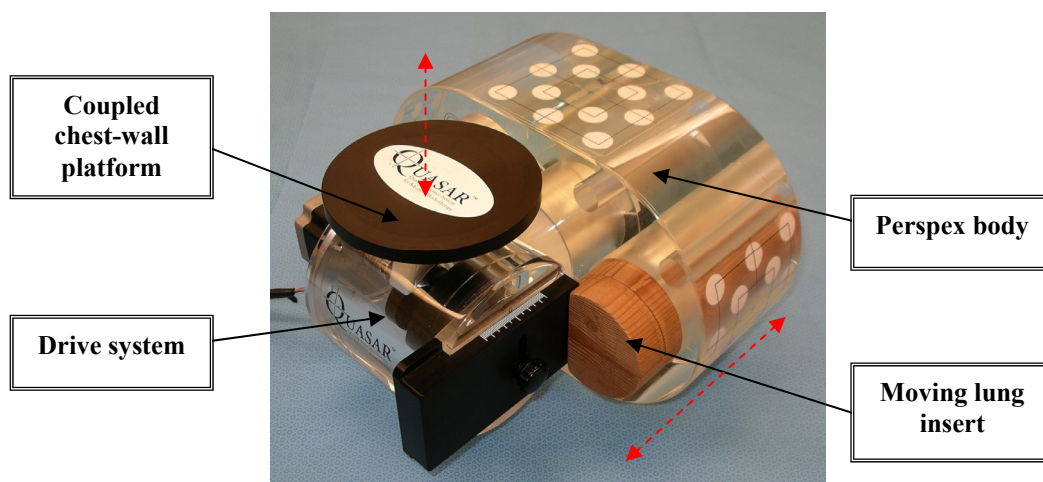


Figure 2.9. The standard QUASAR respiratory motion phantom. 1D sinusoidal motion with coupled chest-wall motion is possible with this phantom. Since patient lesion motion is often complex, it would be beneficial if complex programmable motion could be simulated, thus providing a more clinically relevant simulation platform. The dashed lines represent the directions of movement for the moving parts.

2.9. DIFFICULTIES IN DOSE CALCULATION FOR SBRT

Even without considering tumour motion, dose calculation in SBRT of lung cancer is a complicated. It is known that inhomogeneous density distributions within regions like the lung and lesion interface can cause an errors in dose calculation due to electronic disequilibrium (Ding, Duggan *et al.*, 2007, Disher, Hajdok *et al.*, 2012, Engelsman, Damen *et al.*, 2001, Kavanagh, Ding *et al.*, 2006). The concepts of radiation equilibrium will thus be outlined as the first part of Chapter 6 deals with the issue of dose calculation in regions of heterogeneous density distributions such as those encountered in SBRT of lung cancer.

2.9.1. Radiation equilibrium

The deposition of energy in tissue from a photon beam is fundamentally a two step process. (1) Photons interact in the medium to impart kinetic energy to charged particles, (2) charged particles the deposit their given energy through ionisation and excitation along a track. Radiation equilibrium arises when there is a 'steady state' between the radiant energy entering a volume, and the radiant energy exiting a volume. Conceptually, one can consider an extended volume containing a distribution of a radioactive source with a smaller internal volume. Radioactivity of this source is emitted isotropically and for there to be radiation equilibrium, the maximum

penetration distance of any emitted ray and its progeny (scattered, secondary rays) must be less than the minimum separation distance of the boundaries of the outer and inner volumes. Radiation equilibrium exists for the inner volume if the following conditions exist throughout the outer volume:

- The atomic composition of the medium is homogeneous
- The density is homogeneous
- The radioactive source is uniformly distributed
- There are no external electric or magnetic fields present

For a more rigorous definition of radiation equilibrium, one may consider a plane that is tangent to the inner volume at a certain point. In the nonstochastic limit, there will be a perfect reciprocity of rays of a certain type and energy crossing both ways across the plane due to the uniform distribution of the source. If this is true for all possible orientations of the tangent planes around the inner volume, then for each ray of a certain type and energy entering the inner volume, an identical ray leaves the volume and radiation equilibrium is achieved. As a direct consequence of this, the energy carried in and out of the inner volume are in balance for both directly and indirectly ionising radiations. This may be written as the following:

$$(\bar{R}_{in})_u = (\bar{R}_{out})_u \quad \text{and} \quad (\bar{R}_{in})_c = (\bar{R}_{out})_c \quad 2.1$$

Where u and c represent the energy carried by uncharged and charged particles respectively. If these conditions are met, then the mean energy $\langle \bar{\varepsilon} \rangle$ imparted to the matter in the inner volume is equal to that emitted by the radioactive material contained in the inner volume or:

$$\langle \varepsilon \rangle = \langle \sum Q \rangle \quad 2.2$$

Where $\sum Q$ represents the release of rest mass energy (Krane and Halliday, 1987). Since $D = d\varepsilon / dm$ under the conditions of radiation equilibrium, then the absorbed dose is simple equal to the expectation value of the energy released by the radioactive material per unit mass at that point. i.e.:

$$\frac{d}{dm} \langle \sum Q \rangle \quad 2.3$$

For almost all practical cases, the condition of radiation equilibrium is not satisfied, however, it

may be approximately satisfied if charged particle equilibrium exists.

2.9.1.1 Charged particle equilibrium

Like radiation equilibrium, charged particle equilibrium (CPE) refers to a steady state occurring between all the charged particles entering and leaving a small region of interest. If pure CPE is attained, then the primary dose becomes exactly equal to the collisional kinetic energy released to charged particles only per unit mass (KERMA). i.e.:

$$D = K_c \quad 2.4$$

The conditions for CPE are as follows:

- The atomic composition of the medium is homogeneous
- The density of the medium is homogeneous
- There exists a uniform field of indirectly ionising radiation. I.e. the attenuation of the indirectly ionising radiation is negligible.
- No inhomogeneous electric or magnetic fields present

Satisfying the condition of uniform charged particle fluence is impossible for photon beams due to beam divergence and photon attenuation (Podgoršak, 2010, Podgoršak and Agency, 2005). Fortunately a state of *transient* charged particle equilibrium (TCPE) is easier to achieve than full CPE (Johns and Cunningham, 1983).

2.9.1.2 Transient charged particle equilibrium

Transient charged particle equilibrium is achievable along a central ray in a uniform absorber at depths which are greater than the maximum forward range of the particles created. This state is achievable on the condition that the width of the beam is of magnitude greater than the maximum lateral motion of particles launched (lateral equilibrium). In this specific case, the absorbed dose becomes proportional, but not equal to the collisional KERMA.

2.9.2. Current problems associated with dose calculation in SBRT of lung lesions: Dosimetry considerations

SBRT and IMRT can employ small fields and beamlets down to 10 mm in diameter to achieve the highly focused and modulated dose distributions conforming to the target. Dosimetry of such small fields is complicated by the loss of lateral electronic equilibrium (Bjarngard, Tsai *et al.*, 1989, Bjarngard, Tsai *et al.*, 1990). Furthermore, volume averaging effects, collimator effects, detector position, and detector interface effects make measurement in small photon beams difficult.

2.9.2.1 Current problems associated with dose calculation in SBRT of lung lesions: Heterogeneity calculations in small-fields

Lesions residing in the lungs represent a challenging environment for accurate dose calculation due to the lack of equilibrium conditions discussed previously. When a target is surrounded by a low-density tissue like the lungs, some dose calculation algorithms employed by current treatment planning systems fail to account for lateral electron scattering, and therefore, can yield incorrect results. In the context of SBRT, most treatment planning systems make use of more advanced photon dose calculation methodologies which may be based on pre-calculated data from Monte Carlo dose-spread kernels. Unlike conventional treatment planning methods that only consider photon transport, and are primarily approximation based, newer algorithms can incorporate recoil electron transport. However, although treatment planning dose calculation methodologies for SBRT have improved, heterogeneity calculations are still only an approximation. The Radiological Physics Centre conducted a study comparing the validity of inhomogeneity corrections in small field scenarios (Martens, Reynaert *et al.*, 2002, Woo and Cunningham, 1990) as part of a multi-institutional trial (RTOG 0236 – protocol for lung tumours). Their results showed that the use of convolution / superposition and pencil beam algorithms matched well at the centre of the PTV embedded within the phantom. However at the periphery of the ‘lesion’, there were significant differences (Lee, Fox *et al.*, 2006).

The AAPM reviewed current methods of heterogeneity corrections for megavoltage photon beams and concluded that inhomogeneity corrections should be used when considering patient dose calculation (Papanikolaou, Battista *et al.*, 2004). However, the group urged caution when using several commercially available heterogeneity correction algorithms. Specifically, the group discourages the use of pencil beam algorithms in the situation where the target is surrounded by a low density tissue, as these algorithms do not take into account the lateral scattering in the small field sizes commonly used in SBRT. In contrast to this, the report also found that while heterogeneity corrected dose calculations were not accurate in certain situations, it was better than using no correction at all. Timmerman *et al* (2007) demonstrated the consequence of such dose

calculation difficulties where a prescribed fractions 20 Gy per fraction dose (totaling 60 Gy) was found to be only 18 Gy per fraction (totaling 54 Gy). The error arose due to a lack of appropriate tissue heterogeneity corrections.

Currently, Monte Carlo calculation methods provide the most accurate means of determining the dose to lesions surrounded by a low-density tissue. The aim of the work presented in Chapter 6 was to determine clinically relevant factors that would allow clinicians to accurately determine the reduction in dose to the periphery of lesions residing in the lung using Monte Carlo methods. This work could be considered the first-order approximation to the moving lesion case, presented in the latter half of Chapter 6 as a number of lesion sizes and varying chest-wall to lesion distances are investigated.

2.10. MONTE CARLO SIMULATION AND RESPIRATORY INDUCED TUMOUR MOTION

In this work, Monte Carlo methods are used to determine the absorbed dose to lung lesions in an effort to determine degree of underdosage that can occur at the periphery of a lesion embedded in lung equivalent material (See Objective 4).. Monte Carlo methods are also used to evaluate two distinct dose calculation methodologies for SBRT based on 4D-CT (See Objective 5). Monte Carlo methods are often used to address problems that are not amenable to other calculation methods, or are difficult (or impossible) to measure directly. In the context of radiation therapy, Monte Carlo methods currently provide the most accurate means to model the dose distributions in complex heterogeneous density environments. In general, the Monte Carlo method is a numerical solution to any problem where an object interacts with other objects or their environment. It attempts to model large scale dynamic problems by breaking the system down to the essential dynamics which make up the end result. It is, in essence, a solution to a macroscopic system through simulation of its microscopic interactions (Bielajew, 2001). To achieve this, random number generation is the critical element in any Monte Carlo simulation. Since computer generated random numbers are never truly ‘random’ (they are generated via algorithmic methods), the numbers that are generated in Monte Carlo simulation are essentially ‘pseudo’ random numbers. The interactions of radiation with matter are a perfect system for simulation with Monte Carlo methods and since Monte Carlo methods are a step-by-step approach, it is in principle, straight forward to ‘update the geometry’ periodically to represent motion.

2.10.1. Dose calculation using Monte Carlo methods

Monte Carlo methods currently provide the most accurate means of dose calculation by modeling the interactions of primary and secondary radiations. The stochastic nature of Monte Carlo

simulation means that the inherent uncertainty in any simulation is dependent on the number of primary radiations simulated or ‘histories’. It is for this reason that with a single central processing unit (CPU), Monte Carlo simulations take a large amount of time to produce reasonably accurate results. In a clinical setting, this is the primary reason why full Monte Carlo simulations are not implemented to calculate dose for radiation therapy treatment planning purposes. However, the evolution of computing power, Moore’s Law (Moore, 2006) means that the time constraints placed on the clinical use of Monte Carlo methods may someday be a thing of the past and full Monte Carlo dose calculation may be implemented as the primary means of dose distribution calculation. Currently, semi-analytical algorithms are employed as the basis for most treatment planning system (TPS) calculated dose distributions. TPS dose calculation algorithms produce acceptably accurate results for many treatment scenarios. However, their accuracy is limited in the presence of inhomogeneities within the human body (tissues of varying densities / bone / cavities) (Aarup, Nahum *et al.*, 2009, Carrasco, Jornet *et al.*, 2004, Fotina, Kragl *et al.*, 2011, Schuring and Hurkmans, 2008). Furthermore, presently there is no explicit capability for motion. In stereotactic radiotherapy, the trend towards higher doses to smaller volumes in fewer fractionations means the accuracy of dose calculation is critical.

2.10.2. Currently available Monte Carlo codes

There are presently a large number of Monte Carlo simulation packages available for radiotherapy applications including, but not limited to:

- Electron Gamma Shower (EGS) codes including BEAMnrc (Rogers, Faddegon *et al.*, 1995, Rogers, 2006, Kawrakow, 2000b).
- PENetration and Energy LOSS of Positrons and Electrons (PENELOPE) (Baró, Sempau *et al.*, 1995).
- Monte Carlo N-Particle (MCNPX) (Briesmeister, 1986).
- Geometry AN Tracking 4 (GEANT4) (Agostinelli, Allison *et al.*, 2003).
- FLUktuierende KAskade (FLUKA) (Battistoni, Muraro *et al.*, 2007).
- Geant4 Application for Tomographic Emission (GATE) (Jan, Benoit *et al.*, 2011, Jan, Santin *et al.*, 2004).

The most widely used Monte Carlo code in the context of radiotherapy in particular, stereotactic radiotherapy is EGSnrc (Taylor, Kron *et al.*, 2011). However, the extension of the high-energy codes such as Geant4, to medical applications (low energy [keV-MeV] compared to particle physics [GeV-TeV]) has seen a rise in use of this particular code. In this work, both Geant4 and EGSnrc are used.

2.10.3. Monte Carlo radiation transport codes employed in this work

2.10.3.1 Geant4

Geant4 is an object oriented C++ toolkit for the simulation of particle transportation through matter. The toolkit includes full functionality for tracking, geometry, physics and hit detection. The physics processes in Geant4 cover a large energy range (250 eV to TeV) and include electromagnetic, hadronic, optical, long lived particles, materials and elements. It is versatile in that it can accommodate wide variety of physics simulation applications. Originally developed by CERN for high-energy nuclear and particle physics, it has recently been used in a wide variety of applications from astrophysics to food irradiation. The toolkit is showing increasing popularity in the field of medical physics. The key components of a Geant4 simulation as outlined in (Agostinelli, Allison *et al.*, 2003) are:

- Geometry and materials.
- Particle interactions in matter.
- Tracking.
- Digitisation and hit management.
- Event and track management.
- Visualisation.
- User interface.

The top level class diagram of the Geant4 toolkit and basic ‘G4’ nomenclature is shown in Figure 2.10. In this representation, the categories connected by open circles indicate a ‘using’ relationship where the category at the circle end uses the adjoined category (Agostinelli, Allison *et al.*, 2003).

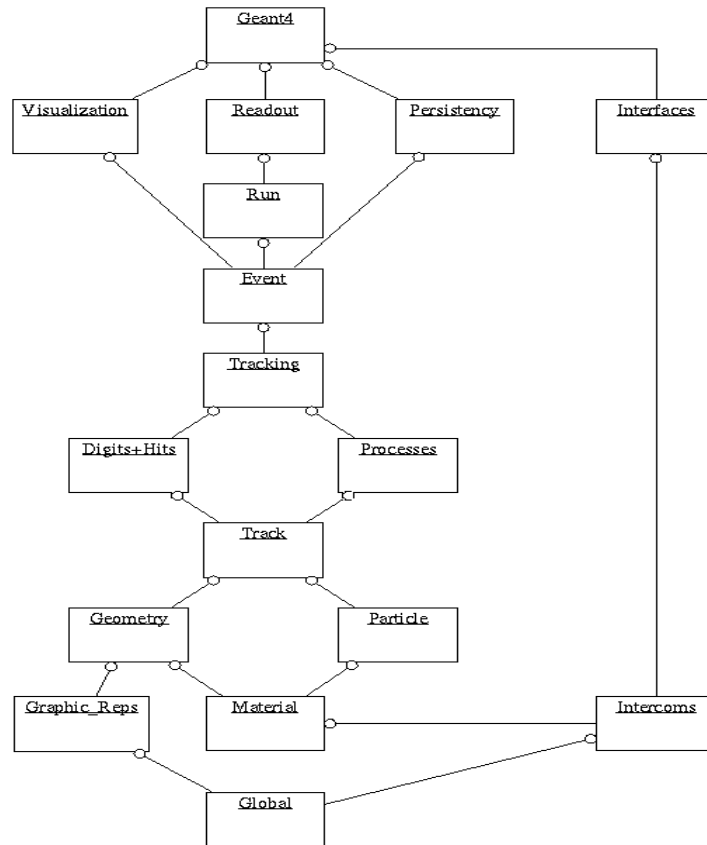


Figure 2.10. The top level class diagram of the Geant4 toolkit adapted from (Agostinelli, Allison *et al.*, 2003)

A particularly advantageous functionality present in Geant4 is the ability to generate innumerable geometric shapes and unions of shapes as the simulation geometry. In Geant4, geometry components are described as *logical* and *physical* volumes. A logical volume represents a detector element of a certain shape and material that can have other shapes (termed *daughters* or *grand daughters*) within its boundary. A physical volume then represents a spatial positioning of a logical volume within the *world* or simulation universe. Using logical and physical volumes, a hierarchical tree of logical volumes, consisting of daughters / grand daughters can be constructed with each larger volume containing smaller volumes. Geometrical functions which can define geometries include: constructive Solid Geometry (CGS) which are simple shapes (boxes, spheres, cones etc.), solids defined by their bounding surfaces (planes, second order surfaces, or B-splines) and geometries imported from Computer Aided Design (CAD) systems. Recently, user specific classes have allowed the importation of voxelised patient geometries from the DICOM format (Kimura, Yamashita *et al.*, 2010, Kimura, Aso *et al.*, 2004, Jiang and Paganetti, 2004).

Materials in Geant4 can be described by assigning the various elements into specific compounds and atomic properties or read in from an extensive database. Once the geometry and materials are defined, the user can then describe the physics applicable to their simulation. Relevant (radiotherapy) radiation interactions for photons and electrons in Geant4 are outlined in Table 2.6 and Table 2.7. Several *pre-built* physics lists exist depending on the particular application and can be activated by the user. The electromagnetic physics list, for example, manages the electromagnetic interactions of leptons, photons, hadrons and ions. Two electromagnetic packages, the standard and low energy electromagnetic packages discussed in (Section 2.10.3.2.4), can be used in simulations pertaining to radiotherapy.

Tracking in Geant4 is achieved by moving each particle step by step. All physics processes associated with the specific particle are associated with the notion of a *step*. Depending on the particle and physics process, the following actions are handled by the tracking classes of Geant4, *at rest* for particles at rest, *along step* for behavior such as continuous energy loss during a step and *post step* which is called at the end of a step, e.g. secondary particle generation by interaction. Another key feature of the Geant4 toolkit is the notion of an *event*. It is the event class structure where the user can keep information that is meaningful to the simulation for processing post simulation. An event may be a particle depositing energy in a particular voxel. This event would be tallied and all other events of no use to the user are disregarded.

Table 2.6. Geant4 photon interaction physics processes and the models governing the interactions. For a detailed description of the physics models, the reader is pointed to the Geant4 Physics Manual (Collaboration, 1999).

Photon Interaction	Description	GEANT4 – Summary of physics for SEP and LEP
Cross-section	data source	Standard: Hubbell, Gimm and Overbo (Hubbell, 1980), Storm and Israel. Low energy: The Evaluated Photon Data Library (EPDL97), Evaluated Atomic Data Library (EADL) (Cullen, October 1991)
Photoelectric effect	Incident photon is absorbed resulting in the ejection of an electron with energy equal to that of the initial photon less the binding energy of the ejected electron.	Standard: Cross-section for photo absorption determined by F. Biggs and R. Lighthill (Biggs, 1990) angular sampling determined from Sauter – Gavrilla (1959) method. In the current method atomic relaxation is not simulated, however it is counted as a local energy deposit. Low energy: The total photo-electric cross-section is calculated using the Stepanek method, the sub-shell from which the electron was emitted is determined from interpolation of cross-section data obtained from EPDL97. De-excitation is simulated from the data obtained in the Livermore Evaluation Atomic Data Library (EADL)
Coherent scatter	A.k.a Rayleigh scattering. Elastic scattering of photons from atoms.	Standard: N/A Low energy: Cross-section data is determined from Stepanek, the coherently scattered photon angle is sampled according to the product of the Rayleigh formula $(1 + \cos^2\theta)$ $\sin \theta$ with the square of Hubbell's (Hubbell, 1979) atomic form factor.
Incoherent scatter	Compton scattering – An atomic electron is ejected by an incident photon. The wavelength of the recoiling photon is changed by an amount depending on the energy transferred to the electron.	Standard: Klein-Nishina method, cross-section data is empirically determined from a fit to the Hubbell data (down to 10 keV), as well as the Storm and Israel data. Standard Compton includes cross section suppression, but samples final state according to Klein-Nishina formula. Low energy: Cross section determined from Stepanek, simulation of scattering is handled via standard method with the addition of Hubbell's form factor (Hubbell, 1980), angular distribution is given by the product of the Klein Nishina formula and the scattering function given by Cullen (Cullen, 1995). Sampling of the final state is based on composition and rejection Monte Carlo methods Butcher and Messel (Butcher and Messel) and (R. Ford, W. Nelson SLAC-265, UC-32 (1985)). Updated to handle Doppler broadening via EGS database approach.
Pair production	Photon interaction with the field of a nucleus resulting in an electron –positron pair.	Standard: Cross-section determined by Hubbell and Gimm (Hubbell, 1980), also applies corrected Bethe-Heitler (Heitler, 1954) cross section along with Born Approximation. Triplet not modeled explicitly; however, it is taken into account in total cross-section. Low energy : N/A
Photonuclear effects	Direct interaction between an energetic photon and an absorbing nucleus. The nucleus absorbs the photon, generally resulting in the emission of a single neutron.	Giant Dipole Resonance region extending from 10 MeV to 30 MeV. The GEANT4 photonuclear database contains about 50 nuclei for which photonuclear cross-sections have been measured.

Table 2.7. Electron / positron interaction physics and the models governing the interactions.

Electron / Positron interaction	Description	GEANT4
Cross-section	data source	Evaluated Electron Data Library (EEDL) (Cullen, November 1991), Seltzer and Berger (Seltzer and Berger, 1985),
Bremsstrahlung	Electromagnetic radiation produced by the deceleration of charged particles.	Standard: Total cross-section obtained from EEDL database, In discrete Bremsstrahlung the final state is sampled according to the spectrum of Seltzer and Berger (Seltzer and Berger, 1985). Above 1 MeV Coulomb corrected screened Bethe-Heitler formula (Heitler, 1954) Low energy: Total cross section is obtained from low energy limit of EEDL database. Angular sampling handled by three distinct generators.
Scattering	electron-electron scattering (Møller) or electron-positron (Bhabha)	Møller scattering for e-, Bhabha scattering for e+.
Positron Annihilation	Positron (electron antiparticle) collides with electron resulting in annihilation with the total mass before annihilation transformed into one, two or three photons.	Cross-section and mean-free-path described by formula of Heitler (Heitler, 1954). It is assumed that annihilation processes one, or three or more photons are ignored.
Multiple scattering	Refers to the simulation of multiple scattering of charged particles in matter	Cross-sections from Goudsmit and Saunderson (1940) for energies < 1GeV. Default model (any energy) by Urban. EPSEPA code developed by Penelope group, implemented in its final state using EGSnrc method by Kawrakov et al. 1998 (Kawrakov and Bielajew, 1998) for precise electron transport. Multiple coulomb scattering is treated as a cumulative effect of small angle scatterings
Transport	Refers to algorithms which calculate whether a particle has crossed a geometric boundary.	Boundary crossing algorithm does not allow 'big' last steps at the boundary of a volume or 'big' first steps in the following volume.

2.10.3.1.1. The accuracy of Geant4

The accuracy of Geant4 has been verified previously by comparison to experimental data, as well as previously established Monte Carlo codes such as EGSnrc. Carrier *et al* (2004) evaluated Geant4 for medical physics applications. Their results were compared to published results using MCNP, EGS4 and EGSnrc and where possible, experimental data. Their study found differences of up to 5% for monoenergetic electrons in homogeneous mediums. Their study, however, found that the difference between Geant4 and experimental data for depth-dose curves yielded similar results to EGSnrc when EGSnrc was compared to the same data. Their study concluded that Geant4 was a promising toolkit for medical physics applications.

Faddegon *et al* (2008) benchmarked Geant4, EGSnrc and PENELOPE against published measurements of bremsstrahlung yield from thick targets for beams of energy 10 – 30 MeV. Their results showed that Geant4 produced results within three standard deviations of measured data for all non-zero angles. Furthermore, their study showed that Geant4 calculated spectra closely matched measurements at photon energies over 5 MeV. Photon spectra at and below 5 MeV were underestimated by as much as 5%. An important finding of this study was that the discrepancy was reduced with the use of the low-energy physics list. Poon *et al* (2005) validated the photon and electron transport of the Geant4 toolkit in the context of radiotherapy. Their study examined both cross-section and sampling algorithms of three electromagnetic physics models (standard, low energy and PENELOPE). Depth doses in water for monoenergetic beams were compared to EGSnrc. Their results showed Geant4 to be accurate to within 2% compared to EGSnrc in all regions except the build-up region. Larger differences were found with monoenergetic electron beams, however the accuracy could be improved by carefully imposing electron step limitations. Faddegon *et al* (2009) benchmarked EGSnrc, PENELOPE and Geant4 against published measurements of the angular distributions of 13 MeV and 20 MeV electrons scattered from foils of different atomic numbers and thicknesses. Initially, Geant4 was shown to overestimate the characteristic angle for the lower atomic number foils by as much as 10%.

By retuning the electron scatter distribution in Geant4, they were able to increase the agreement between the simulation and measured data. In doing so, Geant4 provided comparable accuracy to both EGSnrc and PENELOPE codes whose results were within one standard deviation with measured data. Lechner *et al* (2007) validated Geant4's low energy physics models against electron deposition and backscattering data. The low energy models are of particular relevance to radiotherapy, since low-energy in this case pertains to the MeV range and below. Lechner's study found that energy deposition by electrons modeled with Geant4 agreed well with no systematic deviation from measured and simulated data. For both beam energies (0.3 and 1.0 MeV), Geant4 reproduced the experimental values to within 2%. Backscattering measurements also agreed well with measured data over a large range of materials.

2.10.3.2 GATE

GATE is advanced open source software dedicated to numerical simulations in medical imaging. It has been in development since 2001 by a group of international institutions / laboratories. GATE was released publicly in 2004 under a Lesser General Public License (LGPL). Simulations with GATE are based on the Monte Carlo platform Geant4 (an all purpose Monte Carlo code: see 2.10.3.1) and its libraries (Agostinelli, Allison *et al.*, 2003, Allison, Amako *et al.*, 2006). Essentially, GATE provides a scripting interface between the C++ code-base of Geant4 and the end-user. It provides a way to model complex emission tomography systems such as SPECT and

PET systems by dealing with decay phenomena, moving detectors, time management and complex geometries (Jan, Santin *et al.*, 2004, Jan, Benoit *et al.*, 2011).

GATE allows the user to build up a description of the different components that make up a PET scanner. This process starts with the definition of the scanner geometry (detectors and geometrical arrangement), physics processes and phantom geometries and ends with the detailed description of a processing chain for the detected events. The software also lets the user activate various physics processes which are based on Geant4 and have therefore been benchmarked thoroughly (Parach and Rajabi, 2011, Maigne, Perrot *et al.*, 2011, Chauvie, Guatelli *et al.*, 2004). The physics employed by Geant4 allows modeling of radioactive sources as well as particle interactions for standard and low-energy cases. The user can also determine which gamma-ray interactions should be considered i.e. photoelectric, Compton and Rayleigh scattering and gamma-ray conversion. For these processes, energy-cuts in particular regions of the detection architecture are applied that dictate the production of secondary gamma-rays and electrons.

A particularly important feature of the GATE simulation framework is the handling of time. Time dependence is taken into account at all steps of the simulation. The time-dependence of PET simulations in GATE means that realistic simulations of count-rates and source-decay as well as dynamic geometry such as a rotating scanner or moving phantoms can be achieved. The GATE simulation package is the basis for the PET portion of this thesis and therefore a detailed introduction and outline of the software's functionality is necessary. The following sections are dedicated to this.

2.10.3.2.1. Software architecture.

GATE is written in C++ and follows a modular structure with three layers:

1. Core layer
2. Application layer
3. End user layer

The core layer defines all the basic functionality available in GATE relating to geometry definition, source definition, time management, digitisation and output. The application layer is a set of classes based on the core classes which model specific objects and processes. The end user or scripting layer enables the user to define a simulation through the use of an input file. This layer acts as a translator and converts simple user commands for use by the application and core layers. A complete nuclear medicine simulation can be defined via this interface (Jan, Benoit *et al.*, 2011, Jan, Santin *et al.*, 2004). The structure of GATE is outlined in Figure 2.11.

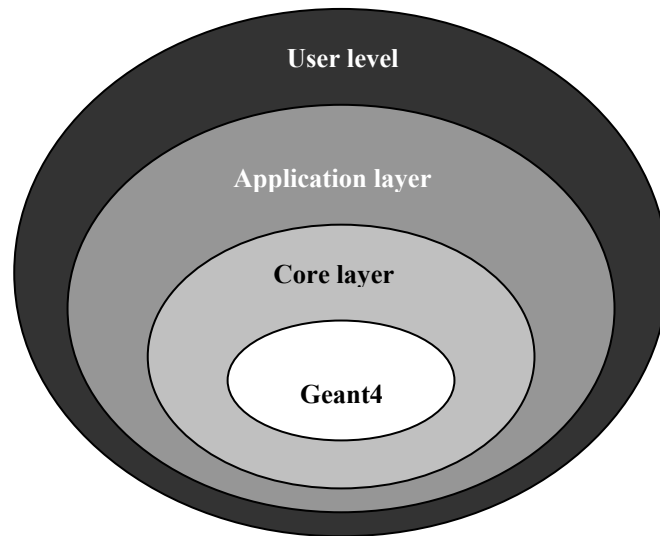


Figure 2.11. The structure of GATE, adapted from (Jan, Santin *et al.*, 2004)

2.10.3.2.2. Systems available for simulation

There are a number of predefined geometries in GATE that enable the user to simulate a scanner. Each group of templates forms a system. Each system can be described by a specific tree-level structure with each component playing a certain role. If the user wanted to create a *cylindricalPET* scanner, the geometrical volumes are arranged into matrices containing the crystal detectors. These sub modules are then grouped into larger modules to form a group of detector clusters. The top level of the detection system is then grouped into a whole and repeated around the cylindrical geometry. Table 2.8 shows the various systems that can be modeled using the GATE platform.

Table 2.8. Systems available for simulation via the GATE platform. The first column shows the type of system. The second column describes the keywords used to define the system, the third column outlines the shape of the entire ‘mother’ volume and the fourth column shows the available outputs. This table was adapted from (Jan, Santin *et al.*, 2004).

System	Components	Shape	Output
Scanner	• <i>Level 1</i>	No fixed geometry	Ascii, ROOT
	• <i>Level2</i>	-	-
	• <i>Level3</i>	-	-
	• <i>Level4</i>	-	-
	• <i>Level5</i>	-	-
CTScanner	• <i>Block</i>	Box	Binary CT image, Ascii or ROOT
	• <i>Pixel</i>	Box	
cylindricalPET	• <i>Rsector</i>	Box	Ascii, ROOT, Raw, specific List Mode Format (LMF)
	• <i>Module</i>	Box	
	• <i>Submodule</i>	Box	-
	• <i>Crystal</i>	Box	-
	• <i>Layer</i>	Box	-
CPET	• <i>Crystal</i>	Cylinder	Ascii, ROOT and Raw
SPECTHead	• <i>Crystal</i>	No fixed geometry	Ascii, ROOT, Raw, PROJECTIONSET or INTERFILE
	• <i>Pixel</i>	-	
Ecat	• <i>Block</i>	Box	Ascii, ROOT, Raw, SINOGRAM or ECAT7
	• <i>Crystal</i>	Box	
ecatAccel	• <i>Block</i>	Box	Ascii, ROOT, Raw, SINOGRAM or ECAT7
	• <i>Crystal</i>	Box	
OPET	• <i>Rsector</i>	Box	Ascii, ROOT, Raw and specific LMF.
	• <i>Module</i>	Box	
	• <i>Submodule</i>	Box	-
	• <i>Crystal</i>	Box	-
	• <i>layer</i>	wedge	-

2.10.3.2.3. Geometry

Geometry is defined in a unique module based manner in GATE. All volumes used in simulation must be defined as either daughters or grand daughters of the world volume. The world volume constitutes the boundary of the simulation universe. In the case of a PET system, the world volume would be a box centered at the origin within which all components making up the system must reside. For this reason, the user must ensure that the world volume is made large enough to house all the components. The world volume is also important with regards to the tracking of particles. For any particle that is generated within the world volume, tracking stops upon the particle breaching the boundary of the world. Following the construction of the world volumes, logical volumes (daughters and grand daughters) must also be defined. A logical volume is defined by all its properties except its position within the world volume. One would define a logical volume by assigning it a particular shape, size and composite material. Upon the placement of a logical volume, that volume is termed a physical volume in that it now has a place within the world

universe. The user can then use repeater volumes which are multiples of the physical volumes with some geometrical transformation / rotation / translation applied in succession.

Using these methods, complex structures can be constructed by combining ring, linear and quadrant designations for particular physical volumes. All logical volumes must be assigned a material from a material database so that Geant4 can calculate the interaction cross-sections. Movement of objects *during* simulation is forbidden by the GEANT geometry architecture, however, between each event generation, the geometry can be updated. Since the duration of a single event typically takes place in a much shorter time frame (ms for particle transport) compared to say, the motion of a phantom, the elements are considered to be at rest during each event.

2.10.3.2.4. Physics

All the physics in GATE are handled by Geant4 (See Section 2.10.3.1). Two packages are available to handle the electromagnetic processes which are the most relevant to PET. The two packages are: The Standard Energy Electromagnetic Processes (SEP) and the Low Energy Electromagnetic Processes (LEP). Low energy in the context of Geant4 generally refers to the regime below 100 GeV. Both packages can generate and transport positrons, electrons, γ -rays, X-rays, optical photons, hadrons, muons and ions. The physics processes are outlined in detail in the physics reference manual provided with the Geant4 (Manual, 2010). Detailed validations of the models are provided in several references (Carrier, Archambault *et al.*, 2004, Lazaro, Buvat *et al.*, 2004, Paganetti and Gottschalk, 2003, Poon and Verhaegen, 2005, Schmittlein, Kirov *et al.*, 2006). A brief overview of the physics specific to GATE is provided here since the core physics is handled by Geant4 and described in Table 2.6 and Table 2.7.

The SEP package of Geant4 covers the energy range from 10 keV to several PeV and is generally used in high-energy nuclear physics applications. For photons, Compton Scattering, photon conversion, pair production and the Photoelectric Effect are simulated. For electrons / positrons, ionisation, bremsstrahlung and positron-electron annihilation can all be simulated with this model. The ionisation class calculates the continuous energy loss due to ionisation and simulates the discrete processes of the ionisation. The discrete interactions simulated are: Møller scattering (e^-e^-), Bhabha scattering (e^+e^-) and delta-ray production. Multiple scattering in the SEP is based on Lewis theory (Lewis, 1950).

The LEP package is an extension to the standard physics. The LEP package has been validated down to 250 eV and covers the interaction of photons and electrons in materials with atomic numbers between 1 and 100. Classes within this package relate to the following interactions:

Compton Scattering, Rayleigh Scattering, Photoelectric Effect, Ionisation and Bremsstrahlung. The user can also implement atomic relaxation. Processes induced by positrons are treated the same as in the SEP package. Models and cross-sections are based on theoretical calculations and the exploitation of previously evaluated data. The data used for the determination of cross-sections and for sampling of the final state are evaluated from the following data libraries (Manual, 2010):

- EPDL97 (Evaluated Photons Data Library)
- EEDL (Evaluated Electrons Data Library)
- EADL (Evaluated Atomic Data Library)
- Stopping power data
- Binding energy values based on the data of Scofield.

From these data libraries, the energy dependence of the total cross-section is derived for each process. With each of the libraries providing cross sections for a set of discrete incident energies, the total cross section for a given energy E needs to be interpolated according to the formula:

$$\log(\sigma(E)) = \frac{\log(\sigma_1)\log(E_2/E) + \log(\sigma_2)\log(E/E_1)}{\log(E_2/E_1)} \quad (2.5)$$

Here, E_1 and E_2 are the closest lower and higher energies respectively for which data (σ_1 and σ_2) is available (Manual, 2010). The final state is then defined by the four-momenta of the final state products which are determined according to distributions derived from the evaluated data. Detailed descriptions of the models for: Compton Scattering, Rayleigh Scattering, Photoelectric Effect, Bremsstrahlung and Ionisation in Geant4 are provided in Table 2.6 and Table 2.7.

2.10.3.2.5. Production cuts

Geant4, and therefore GATE does not use tracking cuts. Instead, all particles are tracked down to zero kinetic energy unless they pass the boundary of the world volume. A ‘production cut’ refers to the fact that photons and secondary electrons are generated only above a given kinetic energy threshold. This method is done to ensure the simulation remains accurate whilst limiting the large number of secondary particles which would hinder the performance of the simulation (Agostinelli, Allison *et al.*, 2003). GATE allows users to either define the cut in range or energy as well as define specific cuts that are applied to electrons, X-rays and delta-rays.

2.10.3.2.6. Positron emission

Positron emission in GATE is handled differently than in Geant4. Two specific modules dedicated to PET were developed. The first uses the von Neumann algorithm to generate the positron energy (randomly) according to the β^+ spectra. This method bypasses the decay of radionuclide processes

in Geant4 and hence greatly increases the speed of the simulation. The second method deals with the acollinearity of the generated annihilation quanta by using a 0.58° FWHM Gaussian blur over the emission angles.

2.10.3.2.7. Radioactive sources

Radioactive sources are modeled via the General Particle Source (GPS) classes provided in Geant4. The GPS is used to generate particles of a given type in a given direction with a given kinetic energy. A source in Geant4 is defined by the type of emission (radionuclide, gamma, electron, etc.), position, energy (spectrum), direction and activity. The lifetime of a radioactive source can either be provided by the Geant4 database or set by the user. The decay rate is determined by the activity of the source during the simulation time. Sources in GATE can also be defined from voxelised phantoms or patient data. These types of sources allow for realistic simulation of emission data as well as anatomically accurate voxelised attenuation maps that convert the gray scale values into material definitions using a translator table. This methodology is described in Section 5.4.

2.10.3.3 The NURBS based *C*ardiac and *T*orso (NCAT) and *e*xtended *C*ardiac and *T*orso (XCAT) phantoms

The NCAT phantom is part of a family of computerised phantoms for medical imaging research developed by Paul Segars (Segars, Mahesh *et al.*, 2008, Segars, Sturgeon *et al.*, 2010, Segars, Tsui *et al.*, 2004). The phantom is obtained through a yearly license agreement with the author and the maintaining facility (Duke University). The software is based on the UNIX platform, though windows versions have recently become available. The NCAT/XCAT software is essentially used to generate CT data-sets based on input parameters that dictate the specifications of the virtual human. The male and female anatomies can then serve as standard templates upon which anatomical variations may be modeled through user-defined parameters. Anatomical motion is achieved through parameterised models for the cardiac and respiratory motions. The motion models are based on high-resolution cardiac and respiratory gated multislice CT data.

The NCAT phantom is an extension of the 4-D MCAT phantom and allows for realistic modeling of the human anatomy. The phantom's organs are constructed from nonuniform rational B-splines (Piegl and Tiller, 1997) (NURBS) rather than voxelised patient data based models previously used in computerised phantoms. NURBS are widely used in computer graphics and animation and the design of three-dimensional surfaces. A natural extension of these surfaces is the modeling of complex anatomical shapes. The organ shapes within the NCAT phantom are based on the 3D Visible Human CT dataset (Ackerman, 1998). NURBS also offer flexibility with regards to transformation as their shape is defined by a set of control points which form a convex hull around the surface itself.

With the use of NURBS, the NCAT phantom is able to simulate cardiac and respiratory motion and also the resultant organ motion induced by these physiological cycles. The cardiac motion is based on 4D tagged MRI data obtained from Johns Hopkins University and the National Institute of Health. The respiratory motion is based on a set of respiratory gated CT (Section 2.6.1.2) data from the University of Iowa. The motion of organs within the respiratory structures was based on tracking landmark points on these organs and formulating a general motion model for each organ.

The XCAT phantom (Segars, Mahesh *et al.*, 2008) is an extension of the NCAT phantom beyond nuclear medicine. The XCAT phantom includes highly detailed anatomy and is constructed entirely of NURBS surfaces. The XCAT phantom includes the whole body and has a greater level of detail than that of its basis model, the NCAT phantom. The XCAT phantom allows higher resolution imaging applications such as CT or MRI. 3D renderings of the XCAT are shown in Figure 2.12 and Figure 2.13. The modeling of respiratory motion is shown in Figure 2.14. Figure 2.15 shows an example of the image data generated with the XCAT phantom showing respiratory induced tumour motion.

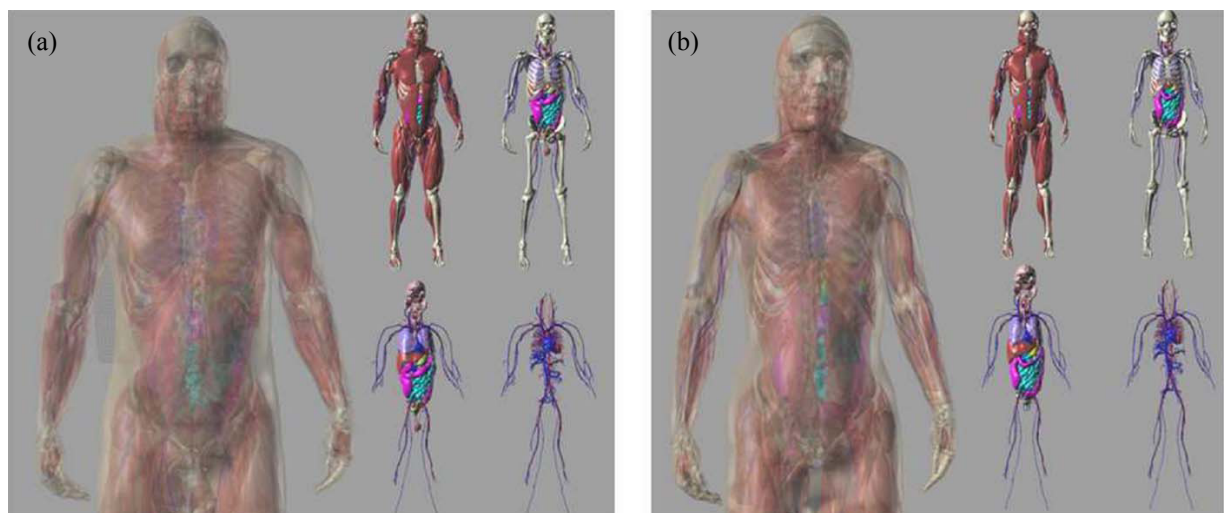


Figure 2.12. (a) Male and (b) female renderings of the XCAT phantom with different levels of detail shown building up to the complete model. The skeletal muscles, circulatory system, organs and glands are shown. Adapted from (Segars, Sturgeon *et al.*, 2010).

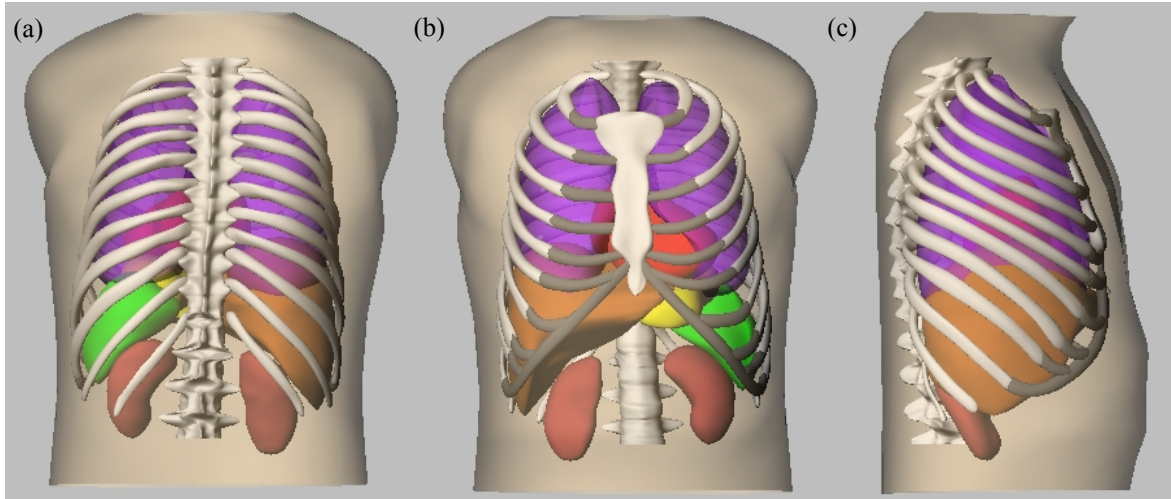


Figure 2.13. (a) Posterior, (b) anterior and (c) saggittal renderings of the XCAT phantom showing the anatomical realism of the organs and their placements. Adapted from (Segars, Mahesh *et al.*, 2008).

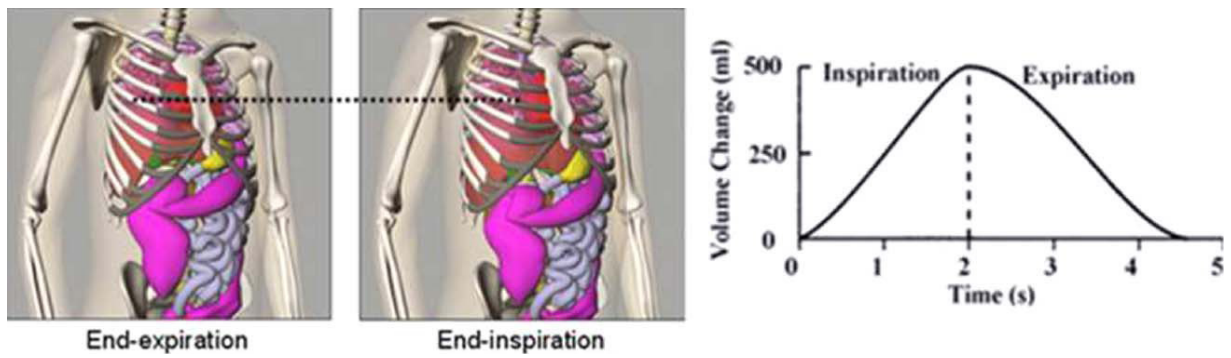


Figure 2.14. Modeling of respiratory motion in the XCAT phantom. Adapted from (Segars, Sturgeon *et al.*, 2010).



Figure 2.15. Series of XCAT CT images showing a tumour in the left lung. Five different phases of respiratory motion are shown. The red dashed lines indicate the deviation of the position of the tumour from the 0% phase of the respiratory cycle.

2.10.3.4 Using the NCAT or XCAT phantom in conjunction with GATE

Descourt *et al* (2006) developed a new C++ class to incorporate the NCAT / XCAT phantom into the GATE framework. GATE already allowed for voxelised activity distributions, however, prior to the work by Descourt it did not enable the incorporation of physiological motion effects on these distributions. The ‘GateRTPhantom’ class developed by Descourt *et al* was introduced to simulate physiological motion in real time with voxelised phantoms such as the NCAT / XCAT phantom described above in Section 2.10.3.3. Using this class, computational phantom data output from the NCAT / XCAT platform as a series of 32-bit binary images can be used as a voxelised phantom source within the GATE platform. The NCAT / XCAT phantom can be used to create a series of ‘frames’, which are complete 3D datasets for a particular period of time. For example, if the NCAT / XCAT phantom’s respiratory motion period was set to 4 s and the number of frames was set to 40, 40 complete datasets each showing the phantom at 0.1 s intervals are created. These 40 datasets, or frames can then be incorporated into GATE, and using a range translator table, the activities and attenuation properties of organs, lesions and structures can be assigned by converting pixel values to activity in Bq and using the raw attenuation data from the simulated XCAT CT data-set respectively.

During the Monte Carlo simulation, annihilation photons are recorded during each time frame. Once 0.1 s has passed, the simulation is paused and the phantom geometry is updated to the next frame and the simulation recommenced. If a PET acquisition lasts for 600 seconds and the 40 frames only cover 4 s of respiratory motion, the whole process is repeated so that 150 full respiratory cycles are simulated during the Monte Carlo simulation. Using this method, realistic activity distributions, incorporating physiological motion, can be simulated.

2.10.3.5 EGSnrc

The Electron Gamma Shower (EGS) Monte Carlo code is a general purpose radiation transport modeling package for simulating the transport of electrons and photons through user-defined geometries. EGSnrc has been validated with energies ranging from the keV range up to hundreds of GeV. Although EGSnrc was used in this work, other versions exist. A detailed description of the code is given by (Kawrakow, 2000b) and in the EGSnrc user manual.

2.10.3.5.1. Radiation interactions in EGSnrc.

The radiation transport of photons and electrons can be simulated in any element, mixture or compound. The dynamic range of charged particle kinetic energies ranges from tens of keV to hundreds of GeV. Table 2.9 shows the physics processes that are taken into account by EGSnrc for photons Table 2.10 describes the electron interactions.

Table 2.9. Photon interactions and their modeling in EGSnrc (descriptions of the interactions are provided in Table 2.6).

Photon Interaction	Description
Photoelectric effect	Dominant process in the keV energy range. Relaxation of excited atoms after vacancies are created create fluorescent photons (K, L, M shells) and Auger and Coster-Kronig electrons may be produced and tracked if requested.
Coherent scatter	Rayleigh scattering: EGSnrc uses total coherent scattering cross-sections from (Storm and Israel, 1970). negligible for megavoltage beams, a relatively small contribution for kV energies
Incoherent scatter	A.k.a Compton scattering: The Klein-Nishina or bound Compton models can be used.
Pair production	Pair production: total cross sections are based on partial-wave analysis calculations which are known to be accurate to much better than 1%.
Photonuclear effects	Not simulated.

Table 2.10. Electron interactions and their modeling with EGSnrc (descriptions of the interactions are provided in Table 2.7).

Electron / Positron interaction	EGSnrc modeling
Bremsstrahlung	Bremsstrahlung production using either Bethe-Heitler cross sections or NIST cross sections.
Scattering (inelastic)	Møller scattering for e-, Bhabha scattering for e+. Interactions with energy transfer large compared to the binding energies: Bethe-Bloch stopping power theory
Positron Annihilation	Positron annihilation in flight and at rest (the annihilation quanta are followed to completion).
Multiple scattering	Handled using a new multiple scattering theory which overcomes the shortcomings of Molière multiple scattering theory. It allows for steps of any size and moves seamlessly from a single scattering model for short steps to an accurate multiple scattering model at large steps. Rutherford scattering or scattering accounting for relativistic and spin effects can be simulated by the user.
Transport	Condensed History (CH) simulation (Kawrakow, 2000b) and Presta II – Electron Transport Algorithm
Boundary crossing algorithm	and Exact (Kawrakow, 2000a)

2.10.3.5.2. The accuracy of EGSnrc

Monte Carlo simulations currently provide the most accurate means to model dose distributions. In medical physics in particular, EGSnrc has been used extensively for a number of years and been benchmarked extensively. As such, EGSnrc is often cited as the “gold standard” Monte Carlo code, and indeed newer codes are often benchmarked by comparing results of simulations to identical simulations performed with EGSnrc. EGSnrc has been shown to produce sub percentage agreement with experimental data for both electrons and photons (Chibani and Li, 2002, Doucet, Olivares *et al.*, 2003).

2.10.4. Monte Carlo simulation and tumour motion

Most currently available Monte Carlo simulation packages do not explicitly allow temporal variation of geometries during simulation. As a result of this, not much has been published regarding the explicit incorporation of moving geometries and dose calculation. Geant4 allows for semi-temporal variation in that the simulation can be paused and the geometry updated. Using this method, Paganetti *et al* (Paganetti, Jiang *et al.*, 2004) implemented object-oriented programming to study the irradiation of tumours undergoing induced respiratory motion. Keall *et al* (Keall, Siebers *et al.*, 2004) simulated 4D Monte Carlo by performing separate dose calculations on phase-bin data-sets from 4D-CT. By using deformable image registration the group mapped each phase-bin dose matrix back to the deep-exhale dose matrix effectively yielding a 4D Monte Carlo calculation

of dose.

2.10.5. Stereotactic radiotherapy and tumour motion

The bulk of research into motion management in radiotherapy has been directed towards conventional radiotherapy. With regards to treatment delivery, stereotactic radiotherapy provides a unique challenge when considering motion management. The reason for this is that the margin for error is reduced based on the decreased number of treatment fractions and increased dose per fraction. The relationship between tumour motion and this fact has yet to be thoroughly investigated. Small mobile tumours also present challenges for modern imaging methodologies. For example, the current resolution of modern PET machines is approximately 4 mm. The small tumours commonly treated with SBRT may not be visible on a PET scan since their uptake may be lost against the background. This fact, coupled with target motion, may decrease the chances of effective treatment with SBRT, unless 4D imaging can be employed.

As there is a smaller margin for error in SBRT, accurate imaging and planning are essential. As the use of SBRT becomes accepted clinically, understanding the effects motion has on dose distributions and imaging of small lesions is of increasing importance. Throughout this work the goal has been to evaluate the impact of lesion motion on images acquired with CT and PET as well as to perform Monte Carlo studies to investigate the complexities of delivering radiation to moving targets.

2.10.6. Key points

- Motion in SBRT presents a unique challenge.
- Phantoms are useful tools in credentialing and providing quality assurance of new motion management strategies in SBRT. Two improvements are needed: (1) Programmable patient-like motion and (2) Simple QA phantoms that can be used to investigate the impact of lesion size on images acquired with CT and 4D-CT.
- The impact of motion on images acquired with CT is well known for larger size lesions typical for conventional radiotherapy. The effect of smaller, more mobile lesions typically seen in SBRT on images acquired with CT and 4D-CT, is not well known.
- The use of PET and PET/CT in SBRT is hindered by the resolving power of PET when imaging small lesions. The reduction in SUV and overestimation of volume may hinder diagnoses and treatment efficacy evaluation. Computational studies with both Monte Carlo and noise-free XCAT images presented in this thesis provide insight into the impact of motion on images acquired with PET.
- The impact of motion on dose distributions in SBRT is not well known. Specifically, treatment

planning is either done on an average intensity projection from 4D-CT, or, a pseudo-4D treatment plan is pursued performing dose calculation on each phase-bin data-set from 4D-CT. The equivalence of these approaches has not been rigorously demonstrated.

Chapter 3. The development of motion phantoms

“When you aim for perfection, you discover it’s a moving target.”

- George Fisher

3.1. INTRODUCTION

The previous chapter described the problems that can arise throughout the radiotherapy process due to the respiratory induced motion of lung tumours. The latter half of Chapter 2 dealt with reported motion management methodologies / technologies and the introduction of Monte Carlo radiation transport modeling and the Monte Carlo packages used in this thesis.

In this chapter, the development of two motion phantoms is presented. Firstly, a see saw motion phantom for 4D-CT QA is presented. The development of this phantom and the verification of a mathematical motion model are presented. The see-saw motion phantom can be used to provide quality assurance of 4D-CT in the context of small lesions typically seen in SBRT of lung cancer. Aspects of work presented in this chapter have appeared in a publication in Medical Physics, see (Dunn, Kron *et al.*, 2012)).

Secondly, an upgrade to a commercially available motion phantom is presented. This phantom provides a complete QA package for motion management in SBRT. Custom made software detailed in Section 3.3.2.1 allows for the importation of patient motion data recorded with the Varian RPM system, as well as several ‘test’ patterns. The upgraded QUASAR phantom presented in this chapter (Section 3.3) allows for patient specific QA of SBRT treatment plans. The upgrade of this phantom has been outlined in Australasian Physical & Engineering Science in Medicine (Dunn, Kron *et al.*, 2011a), the use of this phantom to provide patient specific quality assurance is presented in Radiation Measurements (Kron, Clements *et al.*, 2011). The use of this phantom to evaluate the motion effects on SUV and lesion volume in 3D and 4D PET scanning is presented in Australasian Physical & Engineering Science in Medicine (Callahan, Binns *et al.*, 2011).

3.1.1. *Surrogate markers*

Surrogate markers have previously been defined in Section 2.5.1. Two surrogate marker systems used in this work are the Varian Real-time Position Management system and the Phillips ‘Bellows’ system. Both of these systems are used to record the AP chest-wall motion of a patient during imaging and / or treatment.

3.1.1.1 *The Varian RPM system*

The Varian Real-time Position Management (RPM) system (Varian Medical Systems, Palo Alto, CA, USA) is a video-based infra-red tracking system. This system, shown in Figure 3.1, uses an infra-red camera to track a reflective marker on the patient’s chest. A live-feed of the position of

the marker allows clinicians to determine the correlation between the respiratory cycle and the tumour motion in 4D imaging. The RPM system allows gating, as well as breath-hold and free breathing protocols to be established in both imaging and during treatment. Figure 3.2 shows patient respiratory motion data output from the RPM system. The Varian RPM system has been described and used in a number of publications, including, a paper by the author (Dunn, Kron *et al.*, 2011b, Steve B, 2006, Ramsey, Cordrey *et al.*, 1999, Ramsey, Scaperoth *et al.*, 1999, Vedam, Keall *et al.*, 2001, Vedam, Kini *et al.*, 2003).

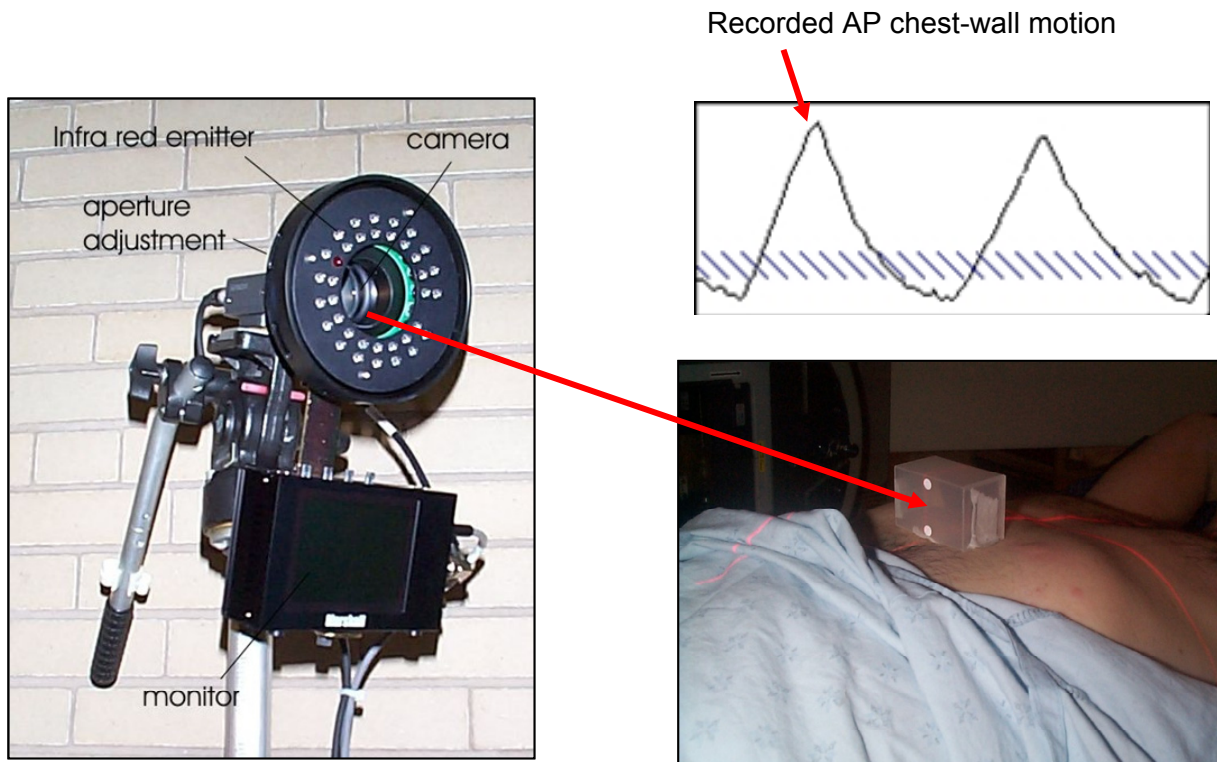


Figure 3.1. The Varian RPM's infrared camera system capturing the motion of a reflective marker placed on the patient's abdomen and the resulting waveform showing the position of the marker as a function of time.

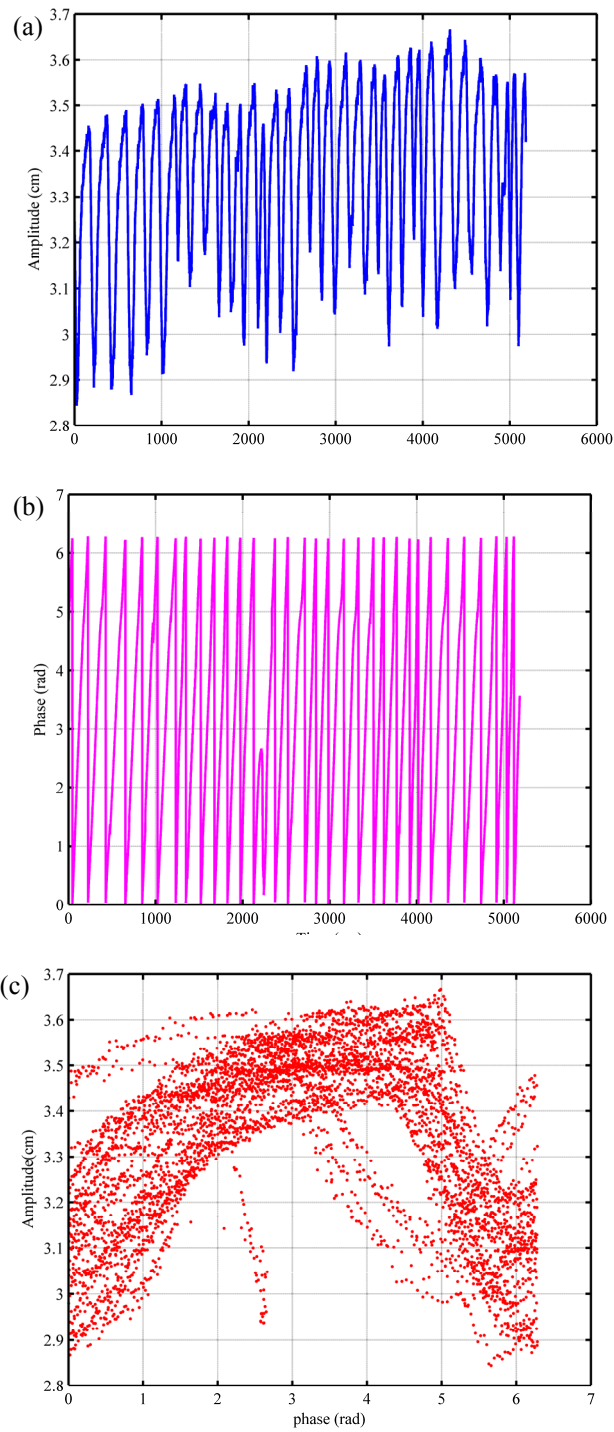


Figure 3.2. Respiratory motion data output from the RPM system. (a) The amplitude of the reflective marker as a function of time (arbitrary units). (b) The phase of the patient's respiratory cycle as a function of time (arbitrary units) and (c) the amplitude as a function of phase.

3.1.1.2 Phillips Bellows system

The Phillips Bellows system (Phillips Medical Systems, Cleveland, Ohio, USA) is an elastic belt which wraps around the patient's abdomen. The belt contains a pressure transducer which converts the pressure waveform to a respiratory cycle. The output signal from the Bellows system is interfaced with the CT scanner and used to provide the respiratory signal in 4D-CT. Figure 3.3 shows the Bellows system setup with the Quasar respiratory motion phantom (Modus Medical Devices, London, Ontario, CA). The Phillips Bellows system has been described and used in a number of publications (Huang, Park *et al.*, 2010b, Heinzerling, Bland *et al.*, 2011, Heinzerling, Anderson *et al.*, 2008)

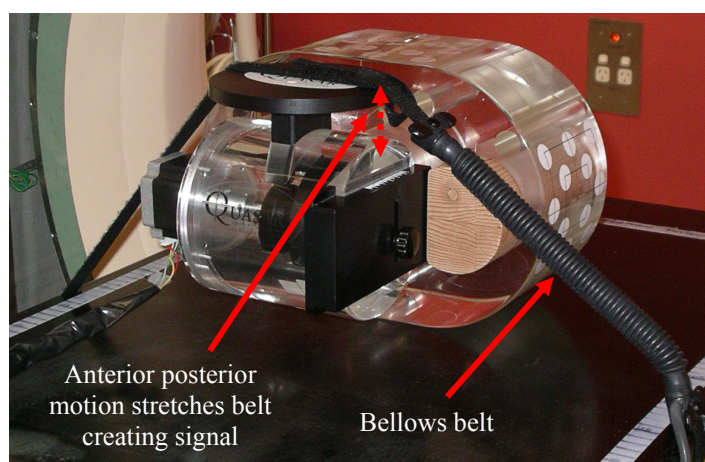


Figure 3.3. An illustration of the Phillips Bellows system. The expansion and contraction of the chest-wall cause the pressure inside the belt to change, which, in turn is converted to a respiratory signal.

3.1.2. MATLAB

MATLAB® Version R2010a (The MathWorks, Natick, Massachusetts, U.S.A.) is a numerical computing environment which can be used to analyse data and interface with other languages such as C, C++, Java and FORTRAN. MATLAB can also be used to create executable software outside of the MATLAB environment. In this thesis, MATLAB was used extensively for both software development and analysis of results.

3.2. DEVELOPMENT OF MOTION PHANTOMS - THE SEE-SAW MOTION PHANTOM

Localisation of the target is of the utmost importance in SBRT where the dose per fraction is large. (D'Souza, Nazareth *et al.*, 2007). As a consequence, 4D-CT is now becoming the standard of care for planning of SBRT. The technological advancement of CT scanner technology now allows for

the millimeter / sub millimeter degree of accuracy (Kalender, 2006) required by SBRT and with the use of 4D-CT becoming more prevalent for planning of SBRT, phantoms are also needed that facilitate quality assurance (QA) of such technologies. Quality assurance phantoms assess system performance and allow for a routine QA programs to be established. QA phantoms should be designed so that the maximum performance information can be gathered with minimal additional time at the scanner.

This section focuses on the development of a phantom to provide quality assurance of CT and 4D-CT. Material in this section has been published by the author in Medical Physics in 2012 see (Dunn, Kron *et al.*, 2012)

The objective of this work was to design and test a simple moving phantom for 4D-CT QA protocols and investigate binning artifacts and motion effects, with particular emphasis on small lesions typical in stereotactic body radiotherapy. The design of the phantom gives particular consideration to:

- Large peak-to-peak amplitudes (> 20 mm in both SI and AP directions) enabling fast problem identification with minimal additional time required at the CT scanner.
- Variable-amplitude, variable-frequency motions.
- Multiple adjustable motions; coupled SI and AP motions, or, only one-dimensional motion in either direction.
- Compatibility with most commercial signal acquisition technologies (e.g. Varian RPM, Philips Bellows, Siemens Anzai).
- Consistency between moving and static CT numbers and geometry.
- Inclusion of both moving and stationary objects of the same size and composition within the field-of-view.

A low cost ‘see-saw’ (cantilever) design was selected to meet the above criteria. Important features of the see-saw phantom’s design include the compatibility for use with commercial surrogate signal acquisition hardware from multiple vendors, and the ability to simulate motion both axially and inter-slice.

3.2.1. Materials

A phantom was designed to enable quality assurance and testing of 4D-CT, as well as investigate the impact of lesion size and motion on images obtained using 4D-CT. The phantom was designed from the ground-up to enable multiple motion profiles, respiratory motion signal acquisition

hardware universality, a range of amplitudes and the ability to compare stationary and moving targets within the field-of-view. A see-saw design was chosen since it allows for variable amplitudes by adjusting the motor's drive point from the central fulcrum, as well as providing a means to mount a platform orthogonally to the main cantilever for an additional SI (inter-slice) motion. The phantom was constructed from Perspex and is shown in Figure 3.4 and Figure 3.5. Its dimensions are 30 x 15 x 15 cm (l x w x h). The motion platform has a width of 5 cm and a length of 30 cm. The SI (inter-slice) platform is adjustable and its height can be set anywhere between 11.0 cm and 15.5 cm from the cantilever platform. The AP motion profile of the phantom is controlled via a rotating disc with offset axis of rotation mounted behind a central pivot. Its distance from the central pivot is variable, resulting in a range of peak-to-peak AP amplitudes between 0.2 – 7.4 cm. Six discrete AP amplitudes can be chosen via changes in the drive-wheel contact point. Further continuous variation can be achieved by placing objects at different positions along the cantilever platform. AP motion amplitudes of 7.4 cm represent extreme cases. However, small lesions with excursions of up to 6.0 cm have been seen by colleagues of the author². Furthermore, large amplitudes exceeding 3.0 cm are useful in ensuring all likely cases are covered and problems arising from such motions can be identified easily. The equations defining the motion are similar to those describing rotating cams in internal combustion engines (Heywood, 1988). Equation 3.1 describes the AP motion. Attached orthogonally to the main platform is the SI platform. The SI motion amplitude is controlled via the platform's height and the drive-wheel to pivot distance. Its motion is described by Equation 3.2. The variables which control the SI and AP amplitudes (d , d_o , h) are indicated in Figure 3.5. r and l in Equations 3.1 and 3.2 are the radius of the drive wheel (3.0 cm) and the centre-to-offset distance (fixed at 1.0 cm) respectively. θ is the angle between r and l as the wheel rotates.

$$X_{AP}(\theta, d, d_o) = \frac{d_o}{d} \left[l \cdot \cos \theta + \sqrt{r^2 - l^2 \sin^2 \theta} \right] \quad (3.1)$$

$$Y_{SI}(\theta, h, d) = \frac{h}{d} \left[l \cdot \cos \theta + \sqrt{r^2 - l^2 \sin^2 \theta} \right] \quad (3.2)$$

A KTA-195 high current DC motor (rated up to 55V (20A)) speed controller (Ocean Controls, Seaford, Victoria, Australia) controls the sinusoidal motion period and enables frequencies of up to 40 revolutions per minute (rpm). This control is operated in either analogue (via potentiometer) or digital mode for high precision. The see-saw phantom has a support system which can also accommodate the Varian Real-time Position Management (RPM) (Varian Medical Systems, Palo

² J. Callahan, Peter MacCallum Cancer Centre, private communication.

Alto, CA, USA) system's infra-red reflective marker, the 'Anzai' belt (AZ-733V, Anzai Medical, Tokyo, Japan), as used in Siemens 4D-CTs and the Phillips 'Bellows' (Philips Medical Systems, Cleveland, OH) air-pressure transducer system.

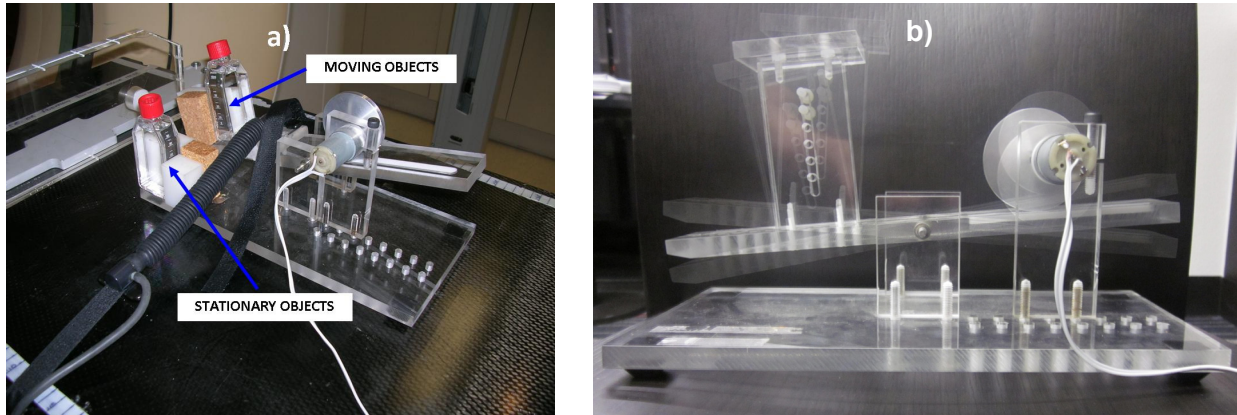


Figure 3.4. (a) An experimental QA setup designed to compare moving and static HUs within the FOV. (b) An overlay of the see-saw phantom's motion profile. In this image, the AP motion platform can be seen. This adjustable platform, along with the adjustable anterior-posterior platform, provides coupled motions in two dimensions.

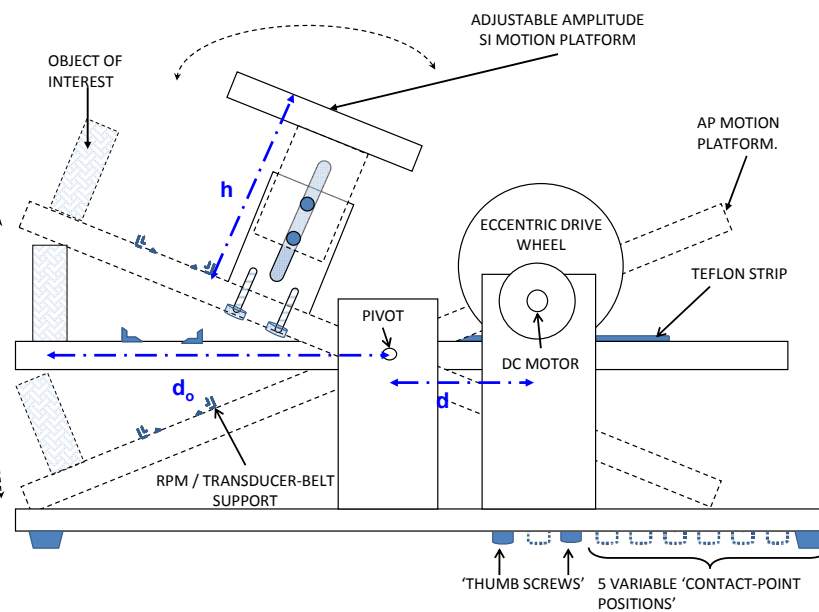


Figure 3.5. Schematics of the see-saw motion phantom (dimensions $l \times w \times h$): $30 \times 15 \times 15$ cm). Variables which determine the motion of the phantom are shown in blue with dash-dot lines representing adjustments that can be made to change the amplitude of motion in both AP and SI directions.

3.2.2. Methods

3.2.2.1 Validation of a mathematical model defining the AP and SI motion profiles

The Varian RPM system was used to record both SI and AP motion profiles. Motion profiles for all six drive-wheel positions were recorded for the AP direction. For the SI case, only the motion profile with the SI platform at maximum extension was recorded. A mathematical model describing the motion was derived and the model was then compared to the physical motion recorded with the RPM system.

3.2.2.2 Inter-vendor compatibility tests: GE Discovery STE PET/CT acquisition methodology

The see-saw phantom was tested for inter-vendor compatibility, by using scanners with different respiratory signal acquisition systems, as well as different acquisition protocols (Helical vs. Cine). A study was performed on the GE Discovery STE PET/CT (General Electric Medical Systems, Milwaukee, WI, USA). The GE Discovery acquires a respiratory signal with an optical based system (Varian RPM) in contrast to the Phillips system, which uses the Bellows system discussed previously. Imaging data presented in Chapter 4 was all acquired using the Philips Brilliance Big Bore CT scanner.

Three imaging studies were carried out on the GE system. The first was a standard CT acquisition of the see-saw phantom with no motion. In the second study, the amplitude was set to 2 cm in the AP direction with a period of 4 s (15 rpm). No 4D capability was initiated during the second study, and as a result, this data represented a ‘free-breathing’ 3D-CT. In the third study, the phantom’s AP motion signal was recorded optically using the Varian RPM system during acquisition for 4D reconstruction. The amplitude in the AP direction for the 4D study was again set to 2 cm, with the correlated SI amplitude being 2.5 cm (peak-to-peak) and the motion period was again set to 4 s.

In the 4D study, data was acquired in ‘cine’ mode with cine duration 5.0 s, a slice thickness of 2.5 mm, 1.024 pixels per mm resolution, FOV of 500 x 500 x 360 mm³ (512 x 512 x 144 pixels), X-ray tube current of 30 mA, 140 kVp and rotation time of 0.5 s. For the 3D acquisitions (stationary and free-breathing), data was acquired in helical mode with a slice thickness of 2.5 mm, pitch factor of 1.35, 0.975 pixels per mm resolution, FOV 525 x 525 x 362.5 mm³ (512 x 512 x 145 pixels) and rotation time of 0.5 s.

3.2.3. Results – The see-saw motion phantom

The specifications of the see-saw phantom are provided in Table 3.1. The see-saw phantom is compact (overall dimensions: 30 x 15 x 15 cm), light-weight (total weight 2.6 kg) and is capable of

producing large amplitude motions up to 7.4 cm, with variable periods from 1.5 s – 10 s (6 - 40 rpm). Table 3.2 shows the motion capabilities of the see-saw phantom. The full range of possible AP amplitudes is determined by both the drive-cam location relative to the pivot point and the location of the sample placed on the AP platform. These options allow a range of amplitudes between 0.2 cm ($d_0 = 1.0$ cm, $d = 10.35$ in Equation 3.1) to 7.4 cm ($d_0 = 15.0$ cm, $d = 4.05$ cm in Equation 3.1). The SI amplitudes are also variable and depend on the distance from the SI platform mount to the central pivot, the height of the SI platform with respect to the AP platform and the drive-cam to pivot distance. Multiple motion amplitudes are available, ranging from a minimum of 1.5 cm to a maximum of 6.5 cm in the SI (inter-slice) direction. The motor control system was found to be accurate and its frequency setting matched the frequencies reported by the Bellows system and the RPM system. Since the phantom is mechanically driven by a rotary cam, its motion profile and amplitude is consistent and reproducible within the resolution of the RPM system, 0.6 mm (Mostafavi, H. (2001). *U.S. Patent No. 6,937,696*. Washington, DC: U.S.).

Due to its cantilever design, the see-saw platform is able to support the Bellows system or RPM infrared reflective marker, as well as a number of objects of varying masses and densities. The coupled two dimensional motion means that both axial and inter-slice motion can be used for quality assurance tests in a highly portable (12 V battery operated), cheap and easy to implement system. Furthermore, the adjustable coupling of SI and AP motion makes numerous amplitude combinations possible.

Table 3.1. Specifications of the see-saw motion phantom.

Dimensions	30 x 15 x 15 cm (l x w x h)
Weight:	
Phantom:	1.4 kg
Battery:	0.6 kg
Controller:	0.6 kg
Power	12V Battery
Battery life	20+ hrs (full charge)

Table 3.2. Motion capabilities of the see-saw phantom. Both the AP amplitudes and SI amplitudes are continuously variable between these minimum and maximum amplitudes.

	Min	Max	Description
Period	1.5 s	10.0 s	The period is varied via a potentiometer or by digitally setting the motor frequency.
SI Amplitude	1.5 cm	6.5 cm	The SI amplitude is variable and depends on the height of the platform, the distance from the SI platform to the central pivot and the drive-wheel cam to pivot distance.
AP Amplitude	0.2 cm	7.4 cm	The AP amplitude is variable and depends on the object's distance from the central pivot and the drive-wheel cam to pivot distance.

3.2.3.1 Accuracy of the motion model

To assess the accuracy of the motion model (Equations 3.1 and 3.2), AP and SI motion profiles were recorded with the Varian RPM. The motion model predictions were then compared with the Varian RPM recorded data. These results are shown in Figure 3.6 and Figure 3.7.

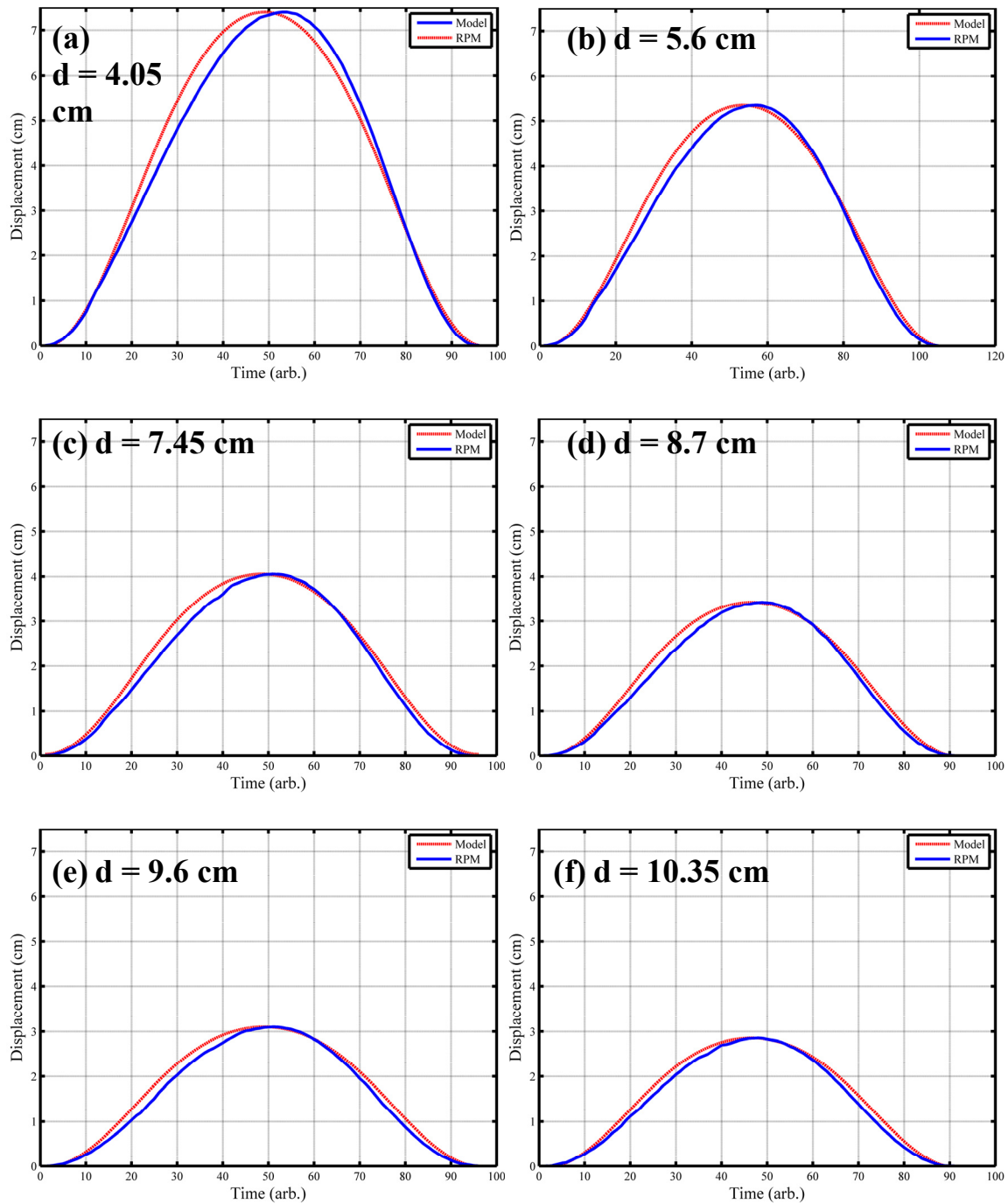


Figure 3.6. The phantom's AP motion profile. The solid blue line indicates the profile as recorded by the Varian RPM system and the red line indicates the motion described by Equation 3.1. (a) Large amplitude motion with the drive wheel close to the central pivot point, (b-f) the five other drive wheel locations in order of increasing distance from the central pivot (decreasing amplitude).

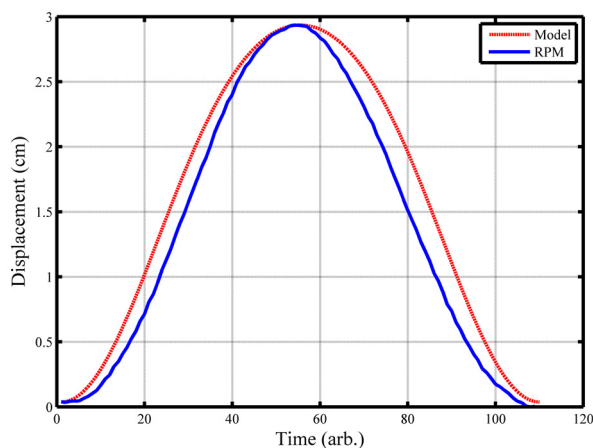


Figure 3.7. A phantom SI platform motion profile. The blue line shows the motion profile as measured with the RPM and the red line shows the profile as modelled by Equation 3.2.

3.2.3.2 Compatibility of the see-saw phantom with different acquisition protocols

Stationary, ‘free-breathing’ 3D-CT and 4D sagittal images are shown in Figure 3.8. The images clearly show both the inter-slice and axial motion directions. The purpose of this investigation was to determine if the see-saw phantom can be used with different hardware and an optical based respiratory signal acquisition system and demonstrate the two motions (axial and inter-slice). The phantom was found to be compatible with other 4D acquisition hardware and acquisition protocols and therefore inter-vendor comparisons can be made, making the see-saw phantom a useful tool for large clinics with multiple CT scanners from different vendors.

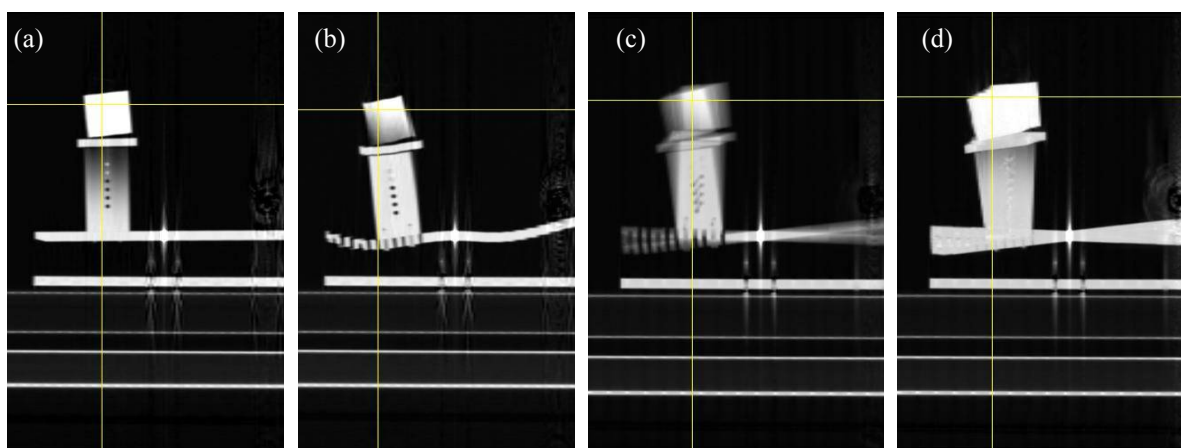


Figure 3.8. Sagittal reconstructions of (a) stationary see-saw phantom. (b) 3D Helical acquisition with moving phantom, amplitude 2.0 cm period 4 s, (c) AIP from a 4D-CT (cine mode) reconstructed into ten distinct phase-bins and (d) MIP from a 4D-CT (cine mode) acquisition. In the AIP and the MIP, the motion amplitude was 2 cm in the AP direction with a period of 4 s. The amplitude of the platform in the SI direction was 2.5 cm.

3.2.4. Discussion – *The see-saw motion phantom*

The see-saw motion phantom was envisaged to fulfill the role of a QA phantom for 4D-CT. The phantom was specifically designed to be highly portable and used to directly compare both moving and stationary objects within the same field-of-view. The see-saw phantom can be used to test 4D-CT acquisition protocols by comparing moving and stationary objects, both in terms of HU and geometric properties. The see-saw motion phantom is presented in Section 3.2, where the design and construction is outlined, and Section 3.2.3, where the accuracy of a motion model (Equations 3.1 and 3.2) characterising the phantom's motion is assessed.

Figure 3.6 shows a comparison between the AP motion recorded with the RPM system and the mathematical model describing the AP motion (Equation 3.1). Discrepancies between the model and the recorded RPM data arise from the fact that the drive-wheel contact does not contact at a single point, but sweeps a small area due to the cam motion and the changing angle of the cantilever. Equations 3.1 and 3.2 do not take this into account and use a single value d as the drive-wheel to pivot distance. As such, Equations 3.1 and 3.2 represent a (good) approximation to the true motion profile. It can be seen in Figure 3.6 that as the area swept by the drive-wheel contact with the platform becomes smaller (decreasing amplitude), so too does the discrepancy between the model and the measured RPM data. The amplitudes match to within the resolution of the system.

Figure 3.7 shows a comparison between the SI profile of the see-saw phantom and the motion as described by Equation 3.2. The SI profile was recorded by holding the phantom on its side. Although this is not ideal, the equation governing the SI motion was able to tested Again, discrepancies can be seen between the mathematical model and the recorded phantom profile. These discrepancies are due to the way the SI profile was recorded as well as approximations made in the mathematical equation governing the motion. Figure 3.8 (a) demonstrates that the phantom is compatible with X-ray CT. A saggittal view of a stationary phantom can be seen in this figure. A small metal artifact associated with the metal fulcrum pin can be seen. All relevant objects however appear artifact free. Figure 3.8 (b) shows the phantom moving during a conventional CT scan. The interplay between the motion and imaging period can clearly be seen This figure provides an excellent example of the effect motion can have on conventional CT. Figure 3.8 (c) and (d) demonstrate average and maximum intensity projections and highlight the motion profile of the phantom.

The phantom design, battery operation and small size facilitate inter-centre portability with one phantom able to be used to perform QA in multiple facilities. The DC motor speed controller is easy to use, whilst the thumb screw and variable amplitude settings means there is no need for additional tools. Of particular interest is the ability to achieve large motion amplitudes in both SI and AP directions. This allows the user to identify problems easily with minimal time added at the scanner. Multiple objects could also be placed at different positions on the platform so that different motion amplitudes can be captured in the same scan.

The see-saw phantom presented in this work provides a valuable tool to effectively assess the accuracy and limitations of 4D technology. Although a number of commercial motion phantoms exist, ease of use and numerous coupled inter-slice / axial motion profiles make the see-saw phantom a useful and easy-to-use tool for commissioning and quality assurance of 4D-CT. The phantom as a package can be built for under \$250 (USD), making it an affordable option that can be shared between centers (or fit in the traveling kit of a physicist servicing several diagnostic facilities) for routine quality assurance and commissioning of new hardware. The see-saw motion phantom can also be used with different motion signal acquisition systems making it inter-vendor friendly.

3.3. DEVELOPMENT OF MOTION PHANTOMS: THE QUASAR RESPIRATORY MOTION PHANTOM UPGRADE

3.3.1. Materials

3.3.1.1 The QUASAR Respiratory motion phantom from Modus Medical

The standard QUASAR respiratory motion phantom is a thoracic phantom featuring an (SI) oscillating insert and an AP reciprocating platform for driving surrogate monitoring systems such as the RPM. It is capable of coupled target and surrogate motion and is shown in Figure 3.9. The motion of the insert is controlled by a rotating cam and variable frequency DC motor. The insert motion is sinusoidal in nature and coupled to the surrogate motion so that the two motions are in phase. Although this platform is suitable for routine QA of motion management, in order to be able to perform patient-specific quality assurance, the phantom needed to be upgraded to produce irregular motion, as well as replicate realistic, decoupled, patient respiratory / chest-wall motion. Decoupling of the surrogate and insert motions was achieved by designing and constructing a separate lift platform controlled by a separate stepper motor. In order to achieve irregular and patient-specific motion, the standard DC motor was replaced with a computer controlled stepper

motor for finite position control. Unlike regular DC or AC motors which have commutator brushes to switch the coils in the motor on and off automatically, stepper motors require individual activation of coils by the use of a stepper motor driver circuit, and have no brushes. The major advantage of stepper motors over regular motors is their finite position control, which is virtually impossible with a regular motor. The use of stepper motors and control software allows patient respiratory motion data recorded via a respiratory monitoring system to be downloaded to the phantom controller. Detailed below are the hardware upgrades added to the QUASAR motion phantom to allow irregular motion to be achieved.

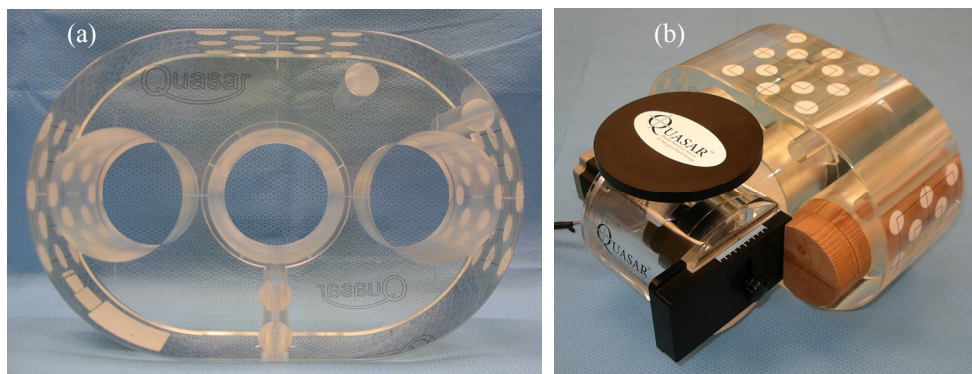


Figure 3.9. (a) The standard QUASAR respiratory motion phantom shell without any inserts or motion control systems (b) The QUASAR™ respiratory motion phantom from Modus Medical shown with moving insert and standard motion control system.

3.3.1.2 Upgrade components: Mot-102 stepper motor

There are two main types of stepper motor, unipolar and bipolar. The Mot – 102 bipolar stepper motor from Ocean Controls (Ocean Controls, Seaford, Vic, Australia) runs on a current of 0.71 A and has a microstep capability of 1600 steps / rev. Speed tests conducted show that the motor has a top speed of 6000 Hz (steps / sec) as per the manufacturer’s specifications, reducing to 5000 Hz when a tight grip is applied to the motor shaft. The motor’s capabilities are summarised in Table 3.3.

Table 3.3. The physical specifications of the Mot-102 stepper motor

Physical Specification	Value
Steps / Rev	1600
Step angle	0.45°
Resolution (variable)	0.001 – 0.1 mm/step
Maximum Speed (ms / Step)	0.159
Maximum Frequency (Hz)	6300

3.3.1.3 Upgrade components: M325 micro-stepping driver

The M325 (Leadshire Technology Co. Ltd., Nanshan Dist. Shenzhen, China) is a high-performance micro stepping driver used to send pulses to the stepper motors for movement. The M325 uses a constant current chopping technique that allows greater speed and power to be extracted from the stepper motor. The M325 also allows precise current control, which is important since it determines the accuracy of the stepper motor being driven. The M325 runs off the 24 V power supply as the motor controller (see Section. 3.3.1.4) and has an output current up to 2.5 A with a pulse frequency of up to 100 kHz. The M325 has a variable stepping resolution that can be activated by selecting the number of steps per revolution of the stepper motor. The three main hardware components of the upgrade are shown below in Figure 3.11 and are wired according to Figure 3.12.

3.3.1.4 Upgrade components: Stepper Motor Controller Model kta-190

To control the stepper motor and provide an interface to the computer software a stepper motor controller was purchased. The Ocean Controls (Ocean Controls, Seaford, Vic, Australia) kta-190 Serial Stepper Motor Controller is controlled via the serial port of a personal computer. It has a baud rate of 9600, 8 data bits, 1 start bit, 1 stop bit and no parity (9600,8,N,1). The kta-190 allows control of up to four stepper motors simultaneously and is powered by either a 12 or 24 V power supply. The commands for the controller are in the form:

@AA CMND XXXXCR

Where AA is the two digit number of the motor being addressed, between 01 and 16, CMND is a four letter command (Table 3.4), XXXX is a numeric value associated with the command, and CR is the carriage return byte (0x0D).

Table 3.4. kta-190 motor commands to be sent from the PC to the kta-190 controller. Taken from the manufacturer's operators manual.

Command	Description
POSN	Set the position that motor AA is currently at to be XXXX where XXXX is between -99,999,999 and 99,999,999
PSTT	Returns the position of motor AA
AMOV	Move motor AA to the absolute position XXXX where XXXX is between -99,999,999 and 99,999,999
RMOV	Move motor AA relatively from the current position by XXXX where XXXX is between -99,999,999 and 99,999,999
STOP	Stop motor AA immediately
STAT	Get the status of the motors
ACCN	Set the maximum stepping rate of motor AA to XXXX where XXXX is between 0 and 9999
ACCI	Set the Acceleration interval of motor AA to XXXX where XXXX is between 1 and 9999
RATE	Set the minimum stepping rate of motor AA to XXXX where XXXX is between 1 and 9999

3.3.1.5 Upgrade components: Separate chest-wall motion platform

To simulate different levels of correlation between the patient's chest-wall and their internal anatomy (Gierga, Brewer *et al.*, 2005, Hoisak, Sixel *et al.*, 2004, Hunjan, Starkschall *et al.*, 2010, Ionascu, Jiang *et al.*, 2007), a separate lift platform was designed to allow decoupling of the standard QUASAR insert and chest-wall platform. The platform, shown in Figure 3.10, consists of two identical pieces of steel joined by two brass guide rails that house Teflon bushes to decrease friction. As the stepper motor rotates clockwise or anti-clockwise, the platform is raised or lowered via a screw. The thread of the screw was custom made so that a larger than normal pitch of 3 mm could be obtained for faster translation. The platform has a maximum translation of 60 mm and a maximum speed of 11.25 mm.s⁻¹. Using the kta-190 controller, two commands can be sent simultaneously to two M325 drivers. Software was developed that can initiate phase-shifts between the chest-wall platform and the insert motion. This feature is particularly useful for investigating dosimetric consequences of gating radiation delivery based on an assumed 1:1 correlation between the external surrogate and internal anatomy, where, in reality, the correlation may be dynamically changing.

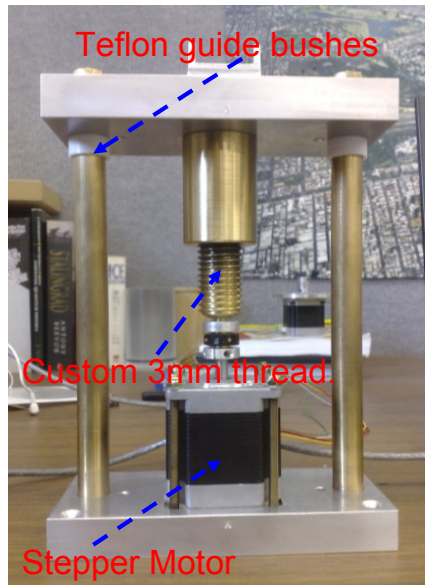


Figure 3.10. Custom built separate chest-wall motion platform. Showing the stepper motor, Teflon guide bushes and custom made 3 mm pitch raising / lowering screw.

3.3.2. Methods

3.3.2.1 Control system and hardware upgrade.

Figure 3.11 shows the control architecture upgrade to achieve arbitrary programmable motion. Figure 3.12 shows a wiring diagram for a two motor system using these components. Irregular motion is achieved with the use of custom software and serial communication protocols.

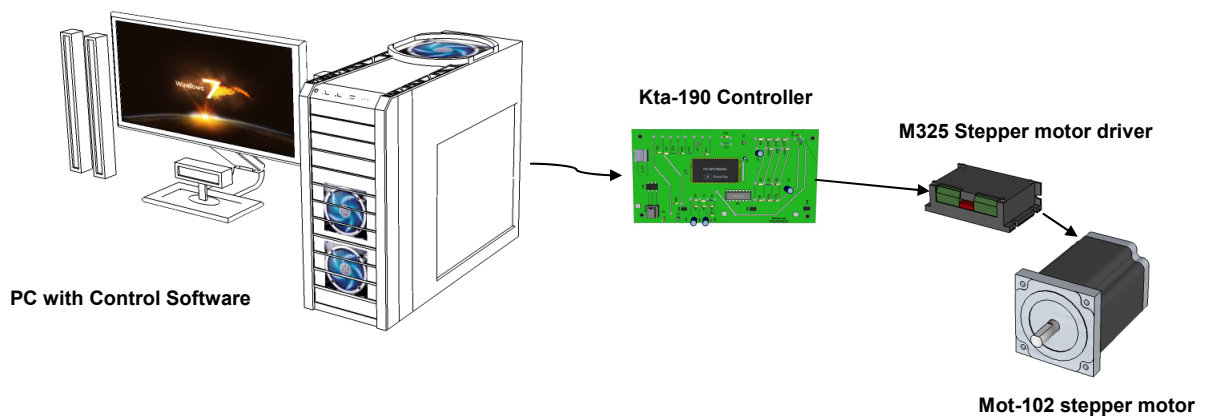


Figure 3.11. The control architecture for the upgraded QUASAR phantom. A PC with custom software is used to communicate with a serial stepper motor controller. The serial stepper motor controller then sends pulse signals to the M325 stepper motor driver which in turn sends step signals to the motor.

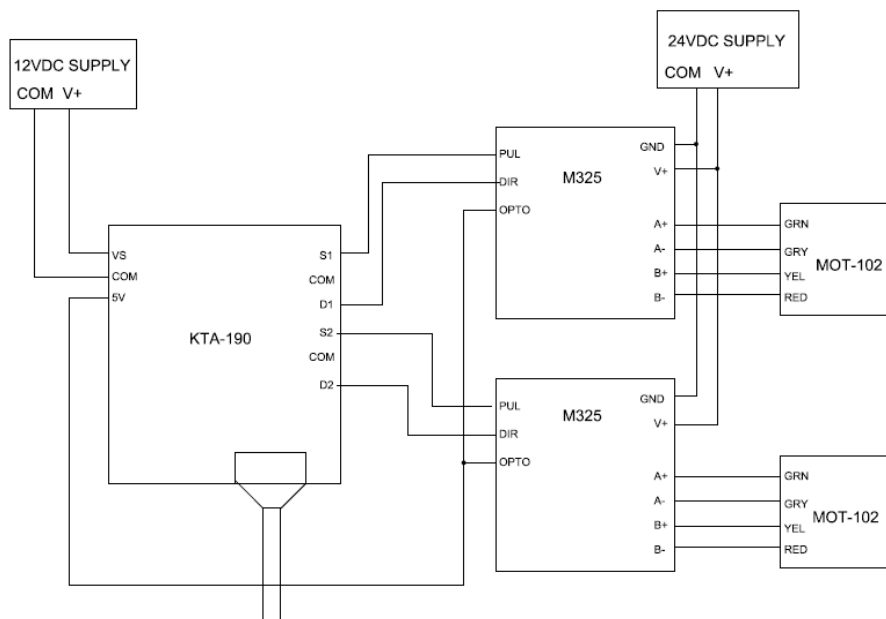


Figure 3.12. Wiring diagram for the components that make up the control system.

3.3.2.2 Software development for motion control

A complete graphical user interface (GUI) written in MATLAB (3.1.2) was developed to control the upgraded QUASAR phantom. Each command consisting of the number of steps to be moved and the rate at which to move is sent to the kta-190 via the serial port. Following each command, the system needs to wait for the motion to be completed before sending the next command. Determining the time to wait for the motion to be completed is a simple calculation. In addition to this; another factor must be subtracted to ensure that the time for replication is accurate. This factor accounts for signal transmission time between the PC and the control system, drivers, and ultimately, the motor. It can be calculated by noting that the speed of serial transmission is 9800 baud, or, 9800 symbols per second, therefore, to determine the time it takes to send a signal across serial transmission, one needs only the length of the communication.

The GUI for control software version 1.1 is shown in Figure 3.13. The upgrade allows for not only patient specific replication of motion patterns, but also a number of test and sinusoid patterns. The GUI also provides a link to the user defined profiles, as well as the ability to simulate breath-holds (see Section 2.5.3), “Lujan” patterns (Lujan, Balter *et al.*, 2003, Lujan, Larsen *et al.*, 1999) and simple sinusoidal patterns with a range of amplitudes and frequencies.

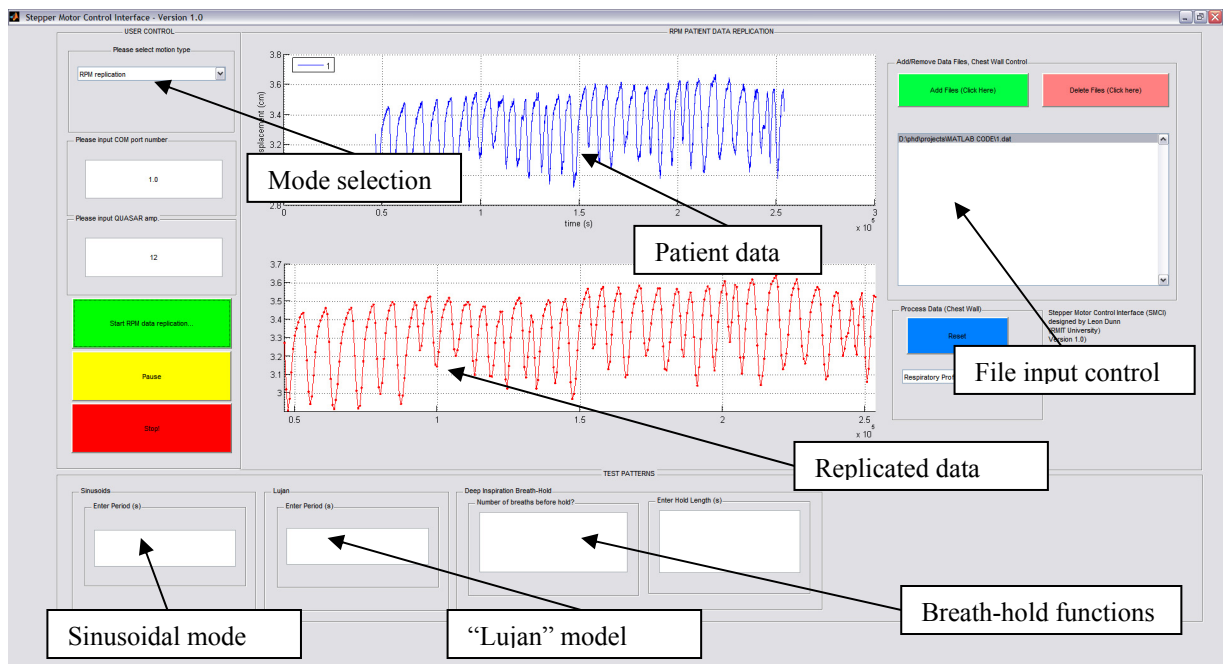


Figure 3.13. Version 1.1 of the Graphical User Interface of the motor control software. Key features are highlighted with details of the various functions outlined in Section 3.3.2.2.

To replicate realistic patient-like motion, an algorithm was developed which imports patient data-sets exported from the Varian RPM system. High-frequency noise exists in the RPM recorded data (see Figure 3.14). Therefore, before the algorithm can work, the data from the RPM needs to be smoothed using a moving average filter. Following this the maxima and minima in the trace must be found. A peak detection algorithm takes respiratory motion data recorded with the RPM system and determines the locations of all the peaks and troughs in the data (Figure 3.15). Following the application of the moving average filter, for each minimum to minimum (complete breath cycle), the length of the data is divided into a user specified number of blocks. This procedure is shown in Figure 3.16. Finally, the distance in time and space between these points is then calculated and converted into a number of stepper motor steps at a specific rate.

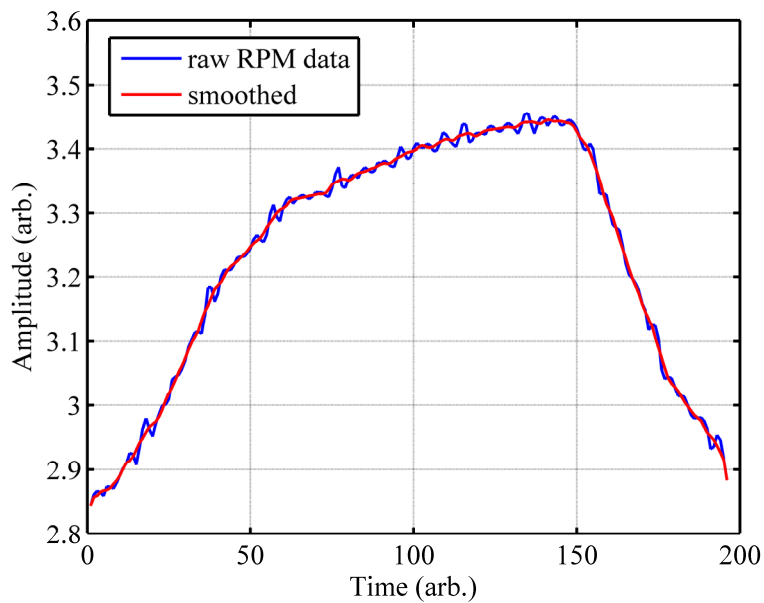


Figure 3.14. Demonstration of the need for a moving average filter to smooth RPM prior to peak detection for respiratory cycle analysis to be effective.

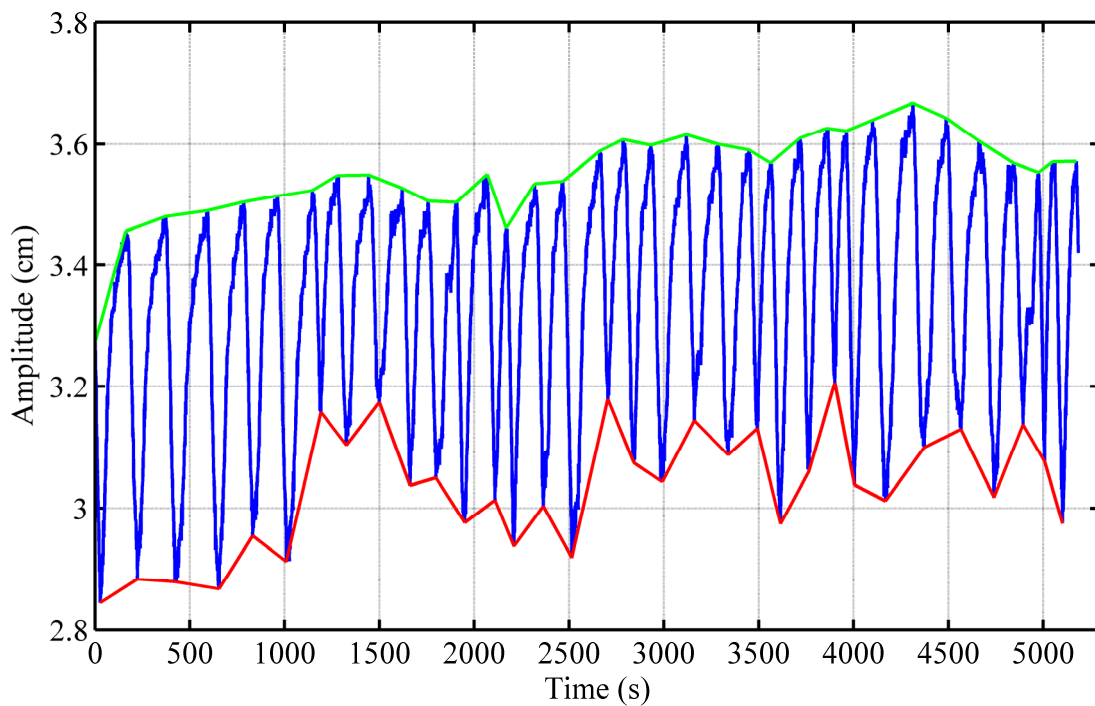


Figure 3.15. Peak detection: The location of the maxima and minima detected by the code is shown overlaid on a patient's respiratory trace. The green line shows a line connecting all locations of the maxima and the red line shows a line connecting all locations of the minima.

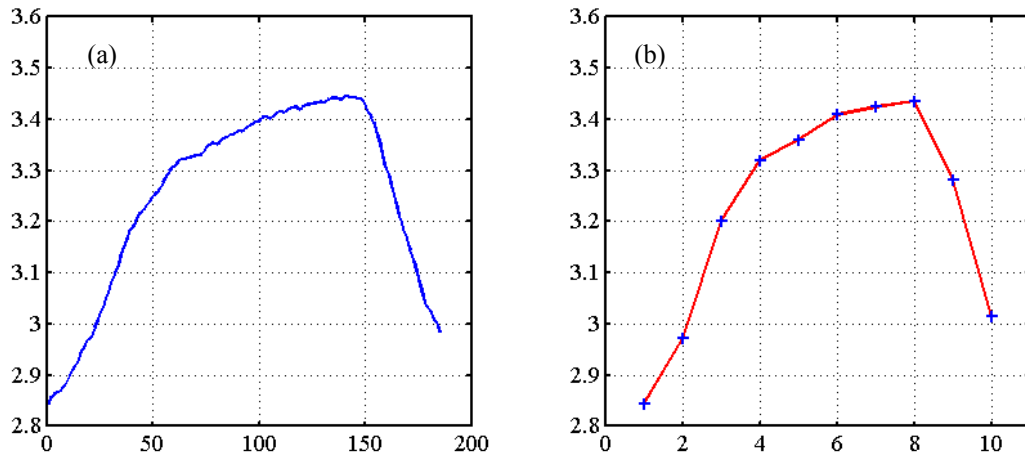


Figure 3.16. (a) A single breath recorded with the RPM system. (b) The trace in (a) broken down into 10 points (blue crosses) between successive minima. The x-axes show the arbitrary time base and the y-axis shows arbitrary amplitude.

An idealised sinusoidal motion profile is an unrealistic representation of actual tumour motion (Chen, Weinhaus *et al.*, 2001, Fitzpatrick, Starkschall *et al.*, 2005, Kissick, Flynn *et al.*, 2008, Sato and Robbins, 2001, Thorndyke, Xing *et al.*, 2005). Lung tumours often experience irregular trajectories which are difficult to model explicitly with periodic functions. To replicate this irregular behavior, a software GUI was also developed to allow the user to draw any desired trajectory they wish.

The GUI shown in Figure 3.17 is a simple graph in which the user defines a profile to be replicated with the mouse. The user can select the number of points by which they want to define their profile as well as the time base. The maximum amplitude of the motion is limited to 4 cm, which is the mechanical limit of the QUASAR phantom's insert motion. The user can then set the number of times they want this particular profile to be cycled. Software that can analyse patient's respiratory motion profile and provide useful statistics was also developed.

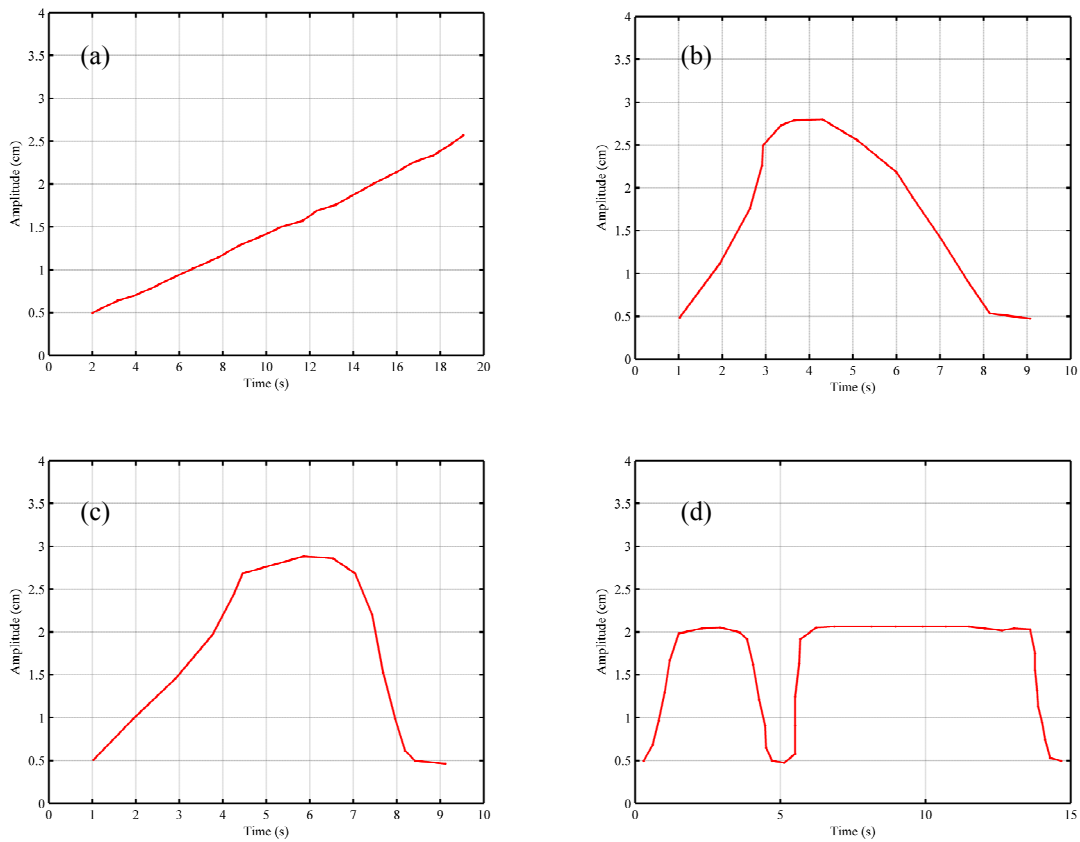


Figure 3.17. Examples of motion patterns that can be designed by the user. (a) A continuous prostate target drift as described by (Kupelian, Willoughby *et al.*, 2007). (b) A commonly seen respiratory pattern where the duration of inhale is less than the duration of exhale. (c) The inverse of (b), where the inhale period is longer than the exhale period. (d) A breath-hold scenario where a single breath is replicated before a 10-second breath-hold.

3.3.2.3 Respiratory pattern analysis software

A software GUI (shown in Figure 3.18 - Figure 3.20) that can import and analyse patient respiratory motion data from the RPM was developed in MATLAB as part of the upgrade. This software was designed to enable clinicians to interpret a patient's respiratory characteristics and provide valuable information about the patient's respiratory characteristics. The following parameters are reported by the GUI:

- Total No. of data points
- Total length of recorded trace in seconds
- No. Of maxima
- No. Of minima
- No. of complete respiratory cycles
- Maximum base-line drift
- Maximum variation in peak inhale position
- Maximum variation in peak exhale position
- Average peak inhale chest position
- Average peak exhale chest position
- Average respiratory cycle length
- Maximum respiratory cycle length
- Minimum respiratory cycle length
- Maximum displacement of the chest-wall
- Average time spent in inhale phases for all cycles
- Average time spent in exhale phases for all cycles
- Maximum time spent in inhale phase over all cycles
- Minimum time spent in inhale phase over all cycles
- Maximum time spent in exhale phase over all cycles
- Minimum time spent in exhale phase over all cycles

The respiratory analysis software provides a valuable tool for assessing the benefits of biofeedback. A patient's respiratory regularity can be assessed following biofeedback training. Furthermore, the statistics provided by the software can be used to determine the best gating parameters on a patient by patient basis.

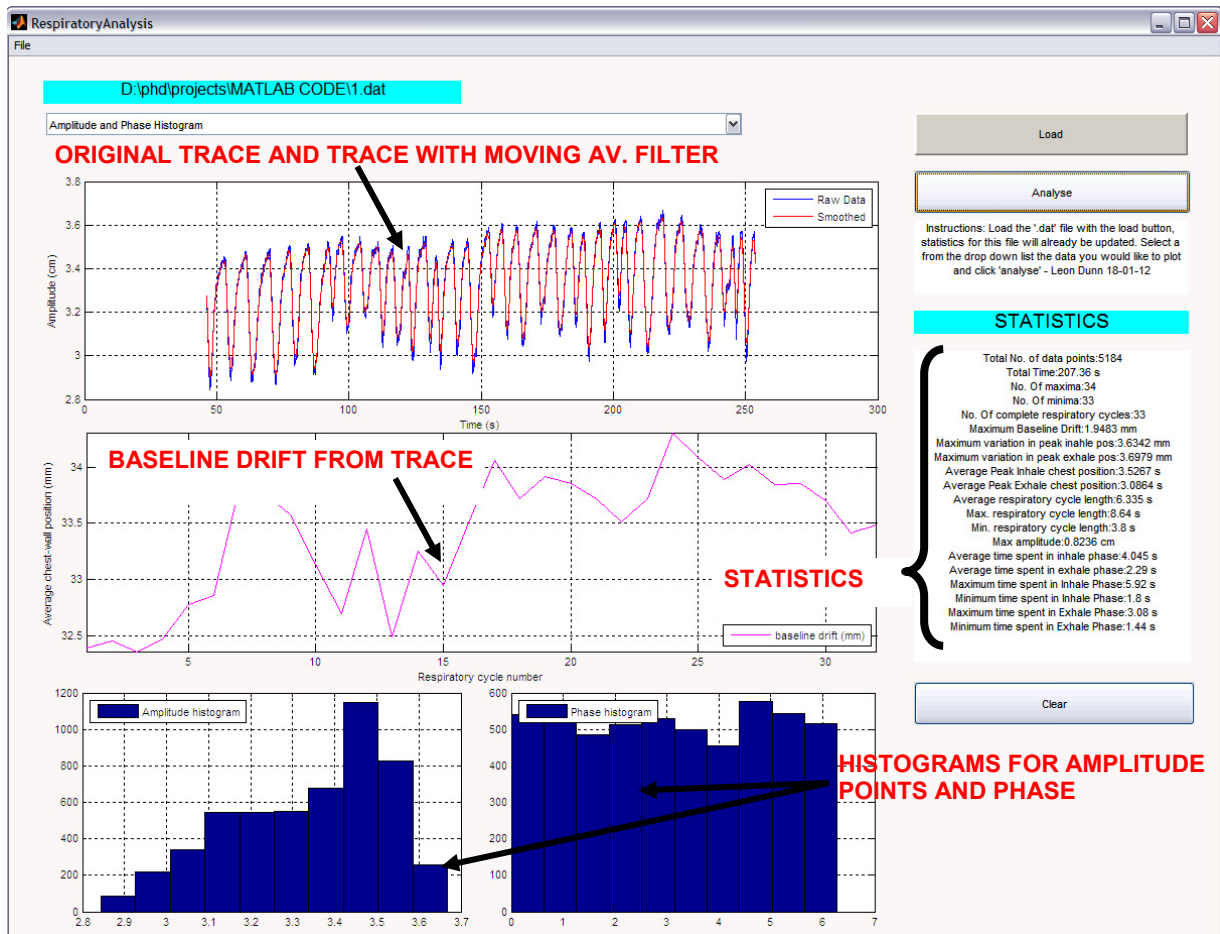


Figure 3.18. GUI of respiratory analysis software, showing the imported trace from the Varian RPM system, the baseline drift of the trace, as selected by the drop-down menu, amplitude and phase histograms showing the distribution of chest-wall positions and phase distributions. Statistics for the trace are shown on the right hand panel.

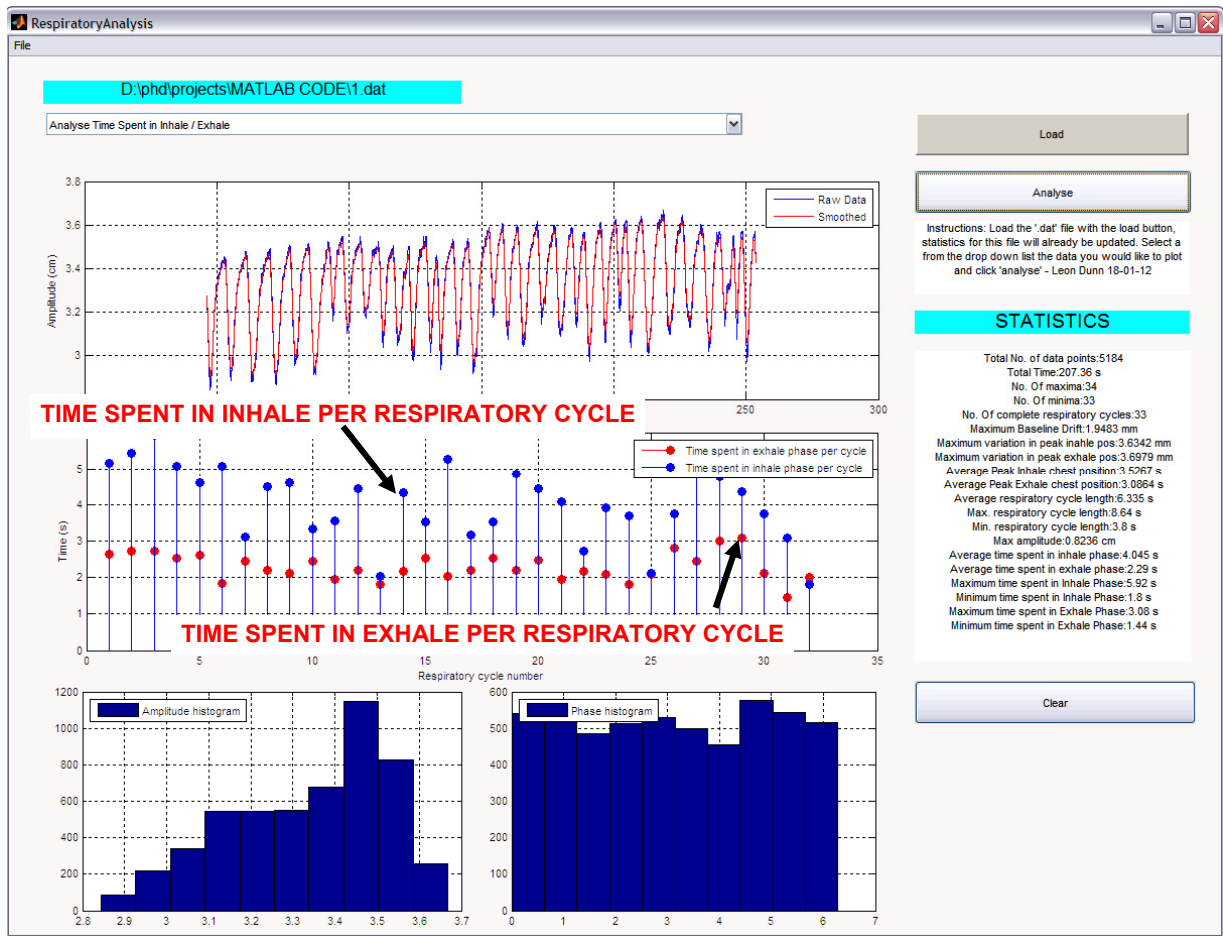


Figure 3.19. GUI of respiratory analysis software, showing the imported trace from the Varian RPM system, a stem plot of the time spent in exhale and the time spent in inhale phases per full respiratory cycle and phase and amplitude distributions. Statistics for the trace are shown on the right hand panel.

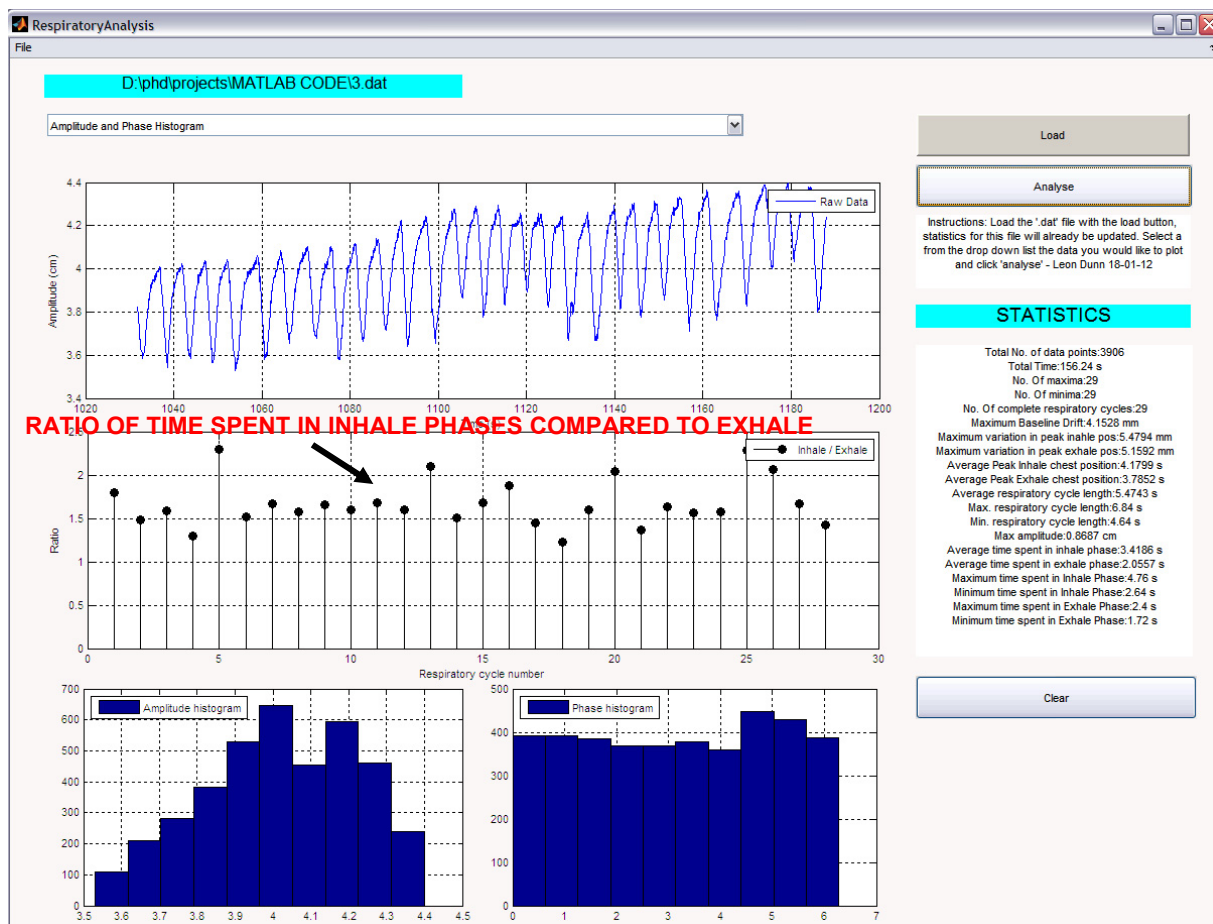


Figure 3.20. GUI of respiratory analysis software, showing the imported trace from the Varian RPM system and a stem plot of the ratio of time spent in inhale per cycle compared to time spent in exhale along with the usual statistics and amplitude and phase distributions.

The complete hardware upgraded QUASAR system is shown in Figure 3.21. The upgraded phantom provides a complete motion management QA system due to the interchangeable inserts. The upgraded QUASAR phantom and software presented in this chapter provide the means to investigate and optimise motion management protocols. This feature, along with the ability to generate a large number of motion patterns, makes the upgraded phantom described in this chapter an invaluable tool for routine QA and research into motion management. Imaging quality assurance, prostate motion studies, the development of 4D Cone Beam CT (Clements, Kron *et al.*, 2013) algorithms and credentialing of clinical trials have all used the upgraded QUASAR motion phantom presented in this work. Furthermore, patient specific QA for stereotactic lung patients at Peter MacCallum Cancer Centre (PMCC) is now carried out using the upgraded phantom (Kron, Clements *et al.*, 2011).

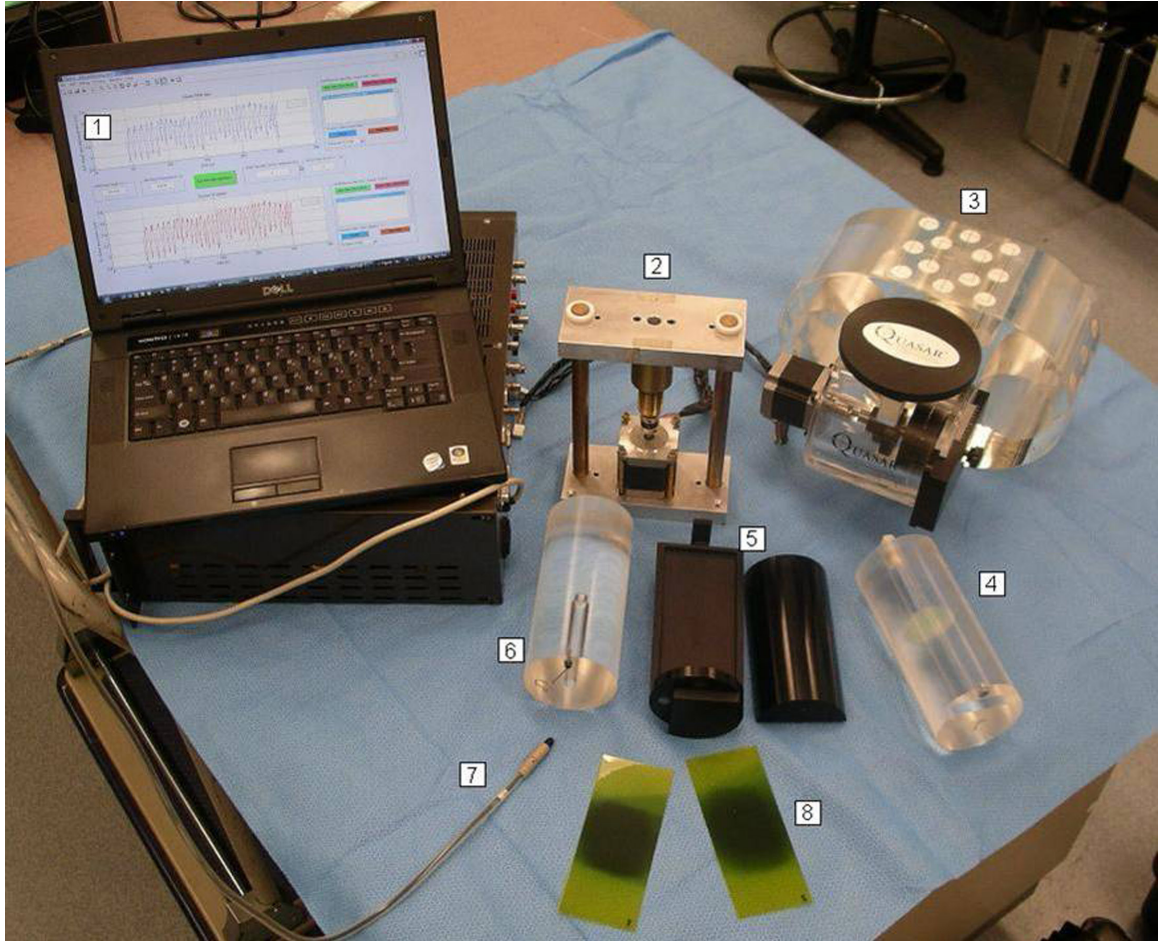


Figure 3.21. The complete QUASAR motion phantom with additional accessories. (1) Laptop showing control software. (2) Custom built lift platform on separate stepper motor. (3) Upgraded QUASAR motion phantom with upgraded motor attached. (4) Bladder insert. (5) Film insert. (6) Ion chamber insert. (7) Ion Chamber. (8) Exposed film showing moving insert dose distributions.

3.3.3. Results – The QUASAR respiratory motion phantom upgrade

An existing QUASAR respiratory motion phantom (3.3.1.1) was upgraded to allow for patient respiratory motion replication. In this section, the phantom’s accuracy in patient motion replication, as well as a number of test patterns for quality assurance are evaluated. The upgrade procedure and software development is outlined in Section 3.3.2.

3.3.3.1 Patient replication

Patient AP respiratory motion data recorded with the Varian RPM system (3.1.1.1) was replicated through the upgraded phantom. Replicated motion was also recorded with the RPM system and compared to the original data. Results for two patient data-set replications are shown in Figure 3.22 and Figure 3.23. Replication of six data-sets showed a maximum p-value of 0.014, indicating a statistically significant degree of correlation with the original patient data. The p-value was obtained by comparing all data spatial data-points in the patient data-set (RPM recorded) and replicated data-set (RPM recorded). Differences between maxima and minima locations in space were found to have mean differences of 0.034 cm for maxima and 0.0102 cm for minima.

Table 3.5 shows the correlation p-value for six patient traces. All replicated data showed good correlation to the actual patient data.

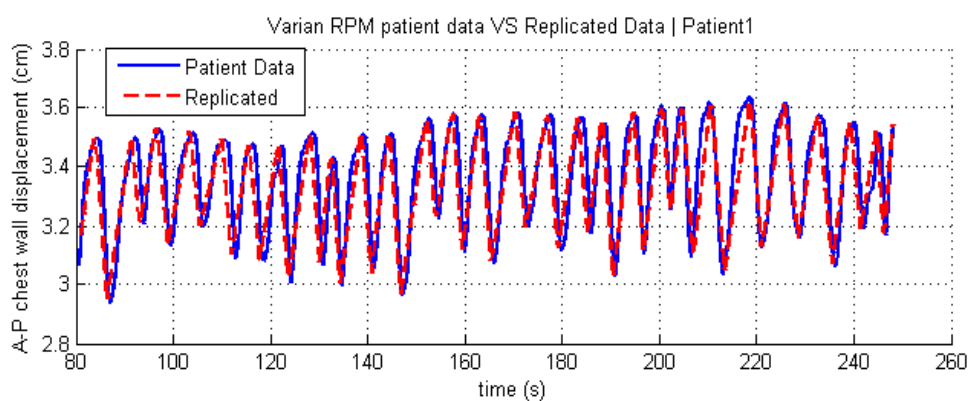


Figure 3.22. Patient AP motion recorded with the RPM system (solid blue line) compared to AP motion replicated with the upgraded phantom system (dashed red line).

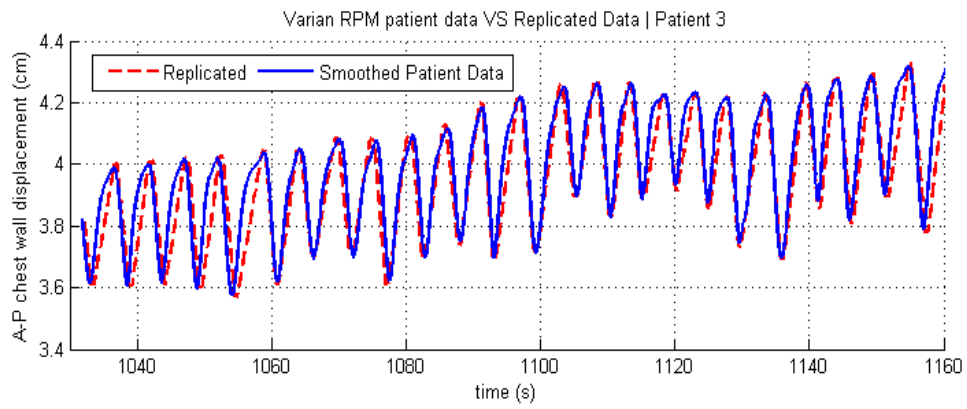
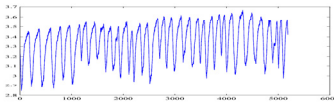
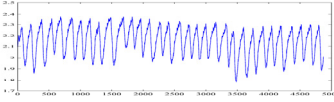
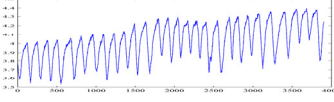
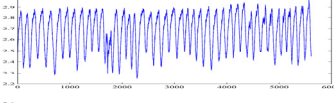
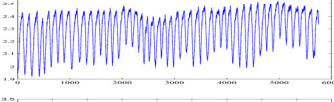
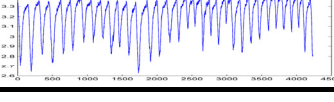


Figure 3.23. Replication of an irregular patient trace with base-line drift and irregularities in amplitude.

Table 3.5. Six patient respiratory traces recorded with the RPM system and their correlation to data replicated with the upgraded QUASAR phantom.

Patient No.	Respiratory Profile	Correlation p
1		0.0045
2		<< 0.05
3		<< 0.05
4		0.0136
5		<< 0.05
6		<< 0.05

3.3.3.2 Test patterns

Test patterns and breath-hold scenarios are shown in Figure 3.24. The sudden change in motion shown in Figure 3.24 (a) tests that the RPM system's predictive filter correctly initiates a beam-off signal instantly when the motion deviates significantly from the prediction. The motion platform allowed large, extreme breath-hold scenarios to be tested, allowing the RPM's predictive and gating limitations to be ascertained. The RPM's predictive system was found to be able to handle large 20 s breath-holds as long as there is at least five full respiratory cycles before the initiation of a hold so that the predictive filter can learn the cycle.

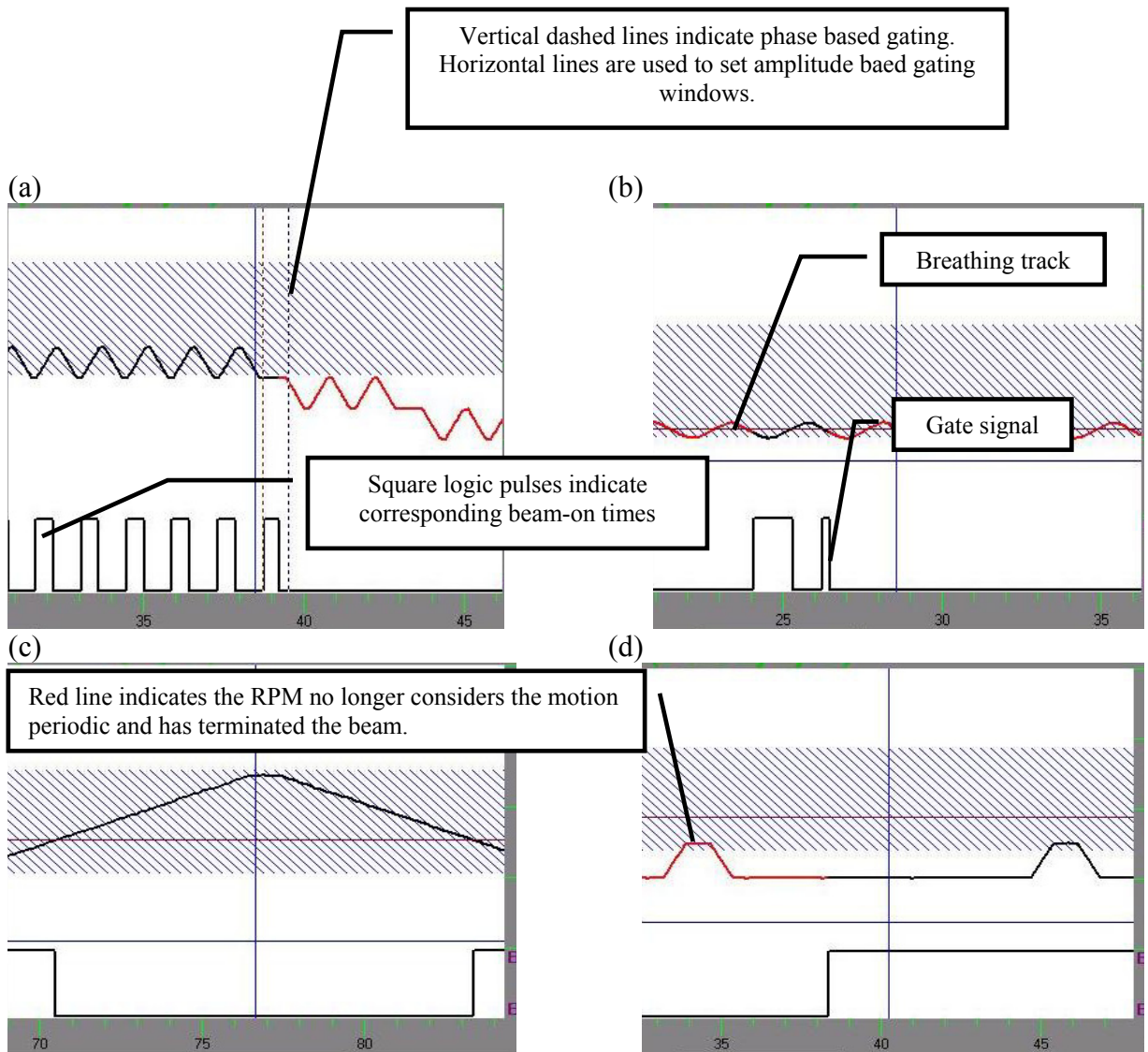


Figure 3.24. Test patterns designed to commission and test the RPM system. In these diagrams, the red line indicates that the RPM considers the motion unpredictable. The figures also indicate where the RPM has initiated a 'beam OFF' signal, this can be seen where the square wave gate signal pulse representing the 'beam ON' time drops to zero. (a) Respiratory pattern that tests the termination of gating where patient respiratory motion differs from prediction. This can be seen by the red line in (a). (b) Sinusoidal trace with small amplitude to test predictability / gateability and resolution of the RPM system in dealing with small amplitude motions. (c) Example of a large amplitude / period (~15s) to test the RPM's ability to accurately predict large motions. (d) Example of a ten second breath-hold simulation.

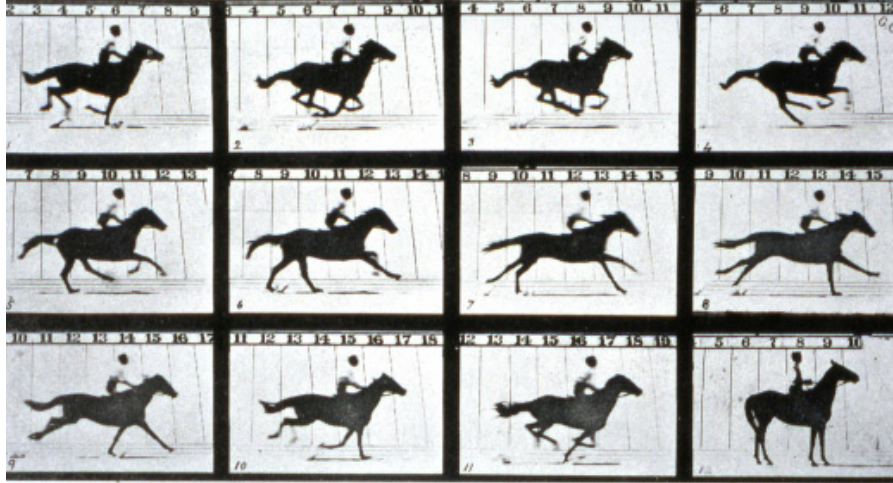
3.3.4. Discussion – The QUASAR respiratory motion phantom

The QUASAR respiratory motion phantom is presented in Section 3.3. The aim of this work was to upgrade the system to allow for the replication of actual patient respiratory motion. Patient respiratory motion is often treated as a sinusoidal motion, and though this is a reasonable first order approximation, it is simply not realistic and sometimes insufficient for QA purposes. Numerous authors have noted the variability in respiratory motion (Nehmeh, Erdi *et al.*, 2004b, Ren, Nishioka *et al.*, 2007, Sato and Robbins, 2001, Thorndyke, Xing *et al.*, 2005, Chen, Weinhous *et al.*, 2001, Kissick, Flynn *et al.*, 2008, Verschakelen and Demedts, 1995). This can also be seen in Figure 2.3 where six patients' respiratory profiles were recorded with the Varian RPM system (Figure 3.1). The data shows that not only does a patient's breathing pattern change from cycle to cycle, but hysteresis, and baseline drift can all result in a deviation from a regular periodic function.

Test patterns were also programmed to test the limitations of respiratory motion management systems like the Varian RPM system. These patterns, some of which are shown in Figure 3.24, include breath-hold patterns, simulated sudden deviation motions, for example, a simulated cough as well large and small magnitude movements which test the resolution of the system.

A commercially available phantom was upgraded to allow for irregular motion typically seen in patients. By upgrading the standard QUASAR respiratory motion phantom, accessories in the form of inserts can also be constructed. Aside from the commercially available inserts from Modus Medical, custom made inserts have been constructed to house film, ion chambers, radio-sensitive gels, Thermoluminescence dosimeters, optically stimulated luminescence dosimeters and implanted seeds for analysis of prostate motion using CBCT. Clinically, the upgraded QUASAR phantom presented in this work is currently used in the QA of radiotherapy treatment plans for patients undergoing stereotactic radiotherapy (Kron, Clements *et al.*, 2011).

Chapter 4. The impact of motion: CT imaging



- Eadward Muybridge: 'The Horse in Motion'

4.1. INTRODUCTION

During conventional three-dimensional Computed Tomography (3D-CT) imaging procedures of the thorax and abdomen regions, anatomical motion can lead to considerable artifacts in the acquired data set due to respiratory, cardiac and gastro-intestinal (GI) movements (Balter, Ten Haken *et al.*, 1996a, Allen, Siracuse *et al.*, 2004, Vedam, Keall *et al.*, 2003b). Such artifacts can manifest themselves as inconsistent boundaries of anatomical structures (Keall, Kini *et al.*, 2002) and in some cases, even mimic disease (Tarver, Conces *et al.*, 1988). Errors at the CT simulation stage can lead to the implementation of inappropriate margins during radiotherapy planning, which could result in unnecessary irradiation of healthy tissue (ICRU, 1993, ICRU, 1999).

Four-dimensional Computed Tomography (4D-CT) (Low, Nystrom *et al.*, 2003, Vedam, Keall *et al.*, 2003b, Keall, Starkschall *et al.*, 2004, Pan, Lee *et al.*, 2004) provides means of reducing the breathing related artifacts associated with free-breathing 3D-CT via correlation of the data-acquisition to a respiratory signal. By binning the data as a function of the breathing-phase acquired from an external respiratory monitor, the target (tumor) can be imaged over a complete respiratory cycle, thus effectively providing the extent of the tumor motion trajectory over a single breath-period. Data from 4D-CT can be used to create an internal target volume (ITV), a ‘snapshot’ of the tumor at each designated respiratory phase and a mean tumor position (Mageras, Pevsner *et al.*, 2004b, Ford, Mageras *et al.*, 2003a, Rietzel, Liu *et al.*, 2006a, Underberg, Lagerwaard *et al.*, 2005, Underberg, Lagerwaard *et al.*, 2004, Keall, 2004a).

In many radiotherapy departments, 4D-CT has become standard for the treatment planning of lung cancer lesions. Since 4D-CT data can be used as the basis for dose calculation, spatial and temporal accuracy is important. To ensure such accuracy and quantify the potential errors of such technologies, it is important that phantoms are available that enable quality assurance (QA) to be performed on the motion management protocol being implemented (Keall, Mageras *et al.*, 2006b, Jiang, Wolfgang *et al.*, 2008, Mutic, Palta *et al.*, 2003). Motion phantoms have previously been used in conjunction with 4D and 3D-CT to assess the impact of motion velocity that may cause motion artifacts within the target volume (Nakamura, Narita *et al.*, 2009b), evaluate the interplay between parameters affecting temporal resolution and the accuracy of the resulting images (Mutaf and Brinkmann, 2008), as well as aid in determining the optimal respiration phase assignment (Mutaf, Antolak *et al.*, 2007).

The objective of the 4D-CT component of this work was to use the see-saw phantom (see Section 3.2) to determine the effect of motion on binning and motion artifacts in data sets acquired with 4D-CT. Since these projections are commonly used for planning purposes, particular interest was given to MIP and AIP artifacts (Objective 2). Objective 2: *“Quantify the influence of lesion size and motion amplitude on data acquired from 4D-CT”* The methods and materials of this investigation are outlined in Section 4.2 and 4.3. This chapter’s results are in part taken from a paper published in Medical Physics in 2012 entitled “A Phantom for Testing of 4D-CT for radiotherapy of small lesions” (Dunn, Kron *et al.*, 2012).

4.2. MATERIALS

Two CT scanners (Phillips Big Bore Brilliance CT scanner and the GE Discovery STE PET/CT) were chosen to demonstrate the utility of the see-saw phantom using both helical and axial 4D-CT acquisition protocols, as well as transducer belt and infrared optical respiratory signal acquisition systems. Five materials (Table 4.1) (Cork, Water, Teflon, Perspex and Nylon) were chosen to cover the relevant spectrum of HUs though other materials could easily be used due to the design of the phantom. The phantom was oriented so that the motor and drive wheel were inferior to the field-of-view (FOV), with the object and phantom movement occurring in the AP direction (axial motion). The motion signal was acquired using the Phillips Bellows belt system, as well as the Varian RPM system for the GE Discovery STE scans.

Table 4.1. Overview of relevant materials and their approximate tissue equivalence. The static HU were measured with a consistent region of interest for all materials from scans using the Phillips Big Bore Brilliance CT.

Material	Dimensions (l x w x h) [mm]	Density (g/cm ³)	Approximate Equivalence	Measured Static HU		
				Min	Max	Mean ± SD
Cork	30 x 20 x 50	~ 0.25	Lung	-838	-703	-784 ± 20.9
Water	38 x 52 x 100	1.0	Tissue	-14	14	-1.09 ± 4.8
Polytetrafluoroethylene 'PTFE'(e.g.Teflon)	50 x 20 x 50	~ 2.2	Bone	314	359	340 ± 7.5
Polymethylmethacrylate 'PMMA' (e.g. Perspex)	70 x 50 x 10	~ 1.18	N/A	63	99	84.8 ± 5.8
Polyamide 'PA' (e.g. Nylon)	50 x 20 x 50	~ 1.15	Cartilage	-91	-62	-74.5 ± 5.0

4.3. METHODS

4.3.1. *Phillips Big Bore Brilliance CT setup*

4D-CT scans were carried on the Philips Big Bore Brilliance CT scanner (Philips Medical Systems, Cleveland, OH, USA). The 4D-CT data was acquired helically with a pitch factor of 0.059, gantry rotation period of 0.44 s, 3 mm slice thickness, 0.931 pixels per mm resolution, FOV 550 x 550 x 153 mm³ (512 x 512 x 51 pixels), 30 mA X-ray tube current, exposure of 233 mAs and 140 kVp. The Philips Bellows system (Philips Medical Systems, Cleveland, OH) was used to acquire the external respiratory signal needed for 4D-CT. This system is described in Section 3.1.1.2.

Tumor Localisation On Console (L.O.C.) software version 2.3.0 was used to retrospectively create Maximum Intensity Projections (MIP), as well as Average Intensity Projection (AIP) 3D data sets. MIP 3D data sets contain voxels whose values are derived from the maximum voxel intensity throughout the 4D-CT data set. A MIP image thus provides a ‘highlighted’ tumor volume over all phases of the respiratory cycle and can be used for ITV construction. Correspondingly, an AIP 3D dataset contains voxels whose values are derived from the arithmetic mean of the corresponding voxels of the 4D CT dataset. AIP data provides a ‘blurred’ image of the moving tumor trajectory over all phases and is used for dose calculation. Figure 3.4 shows the experimental setup using the see-saw phantom and the materials described in Table 4.1. Figure 4.1 shows the method for measuring CT numbers and amplitudes on MIP images. The following investigations were undertaken with the Phillips Big Bore Brilliance CT scanner:

- HU consistency between moving and stationary objects.
- Inter-phase variability of HUs (2.5 cm amplitude, period of 4 s).
- MIP and AIP artifacts as a function of the number of phase-bins (5, 10, and 20 phase-bins) for an amplitude of 6.0 cm and a period of 4 s.
- Verification of motion amplitude using MIP (amplitudes of 6.0, 3.0, 2.5, 2.0 and 1.5 cm, period = 4s).

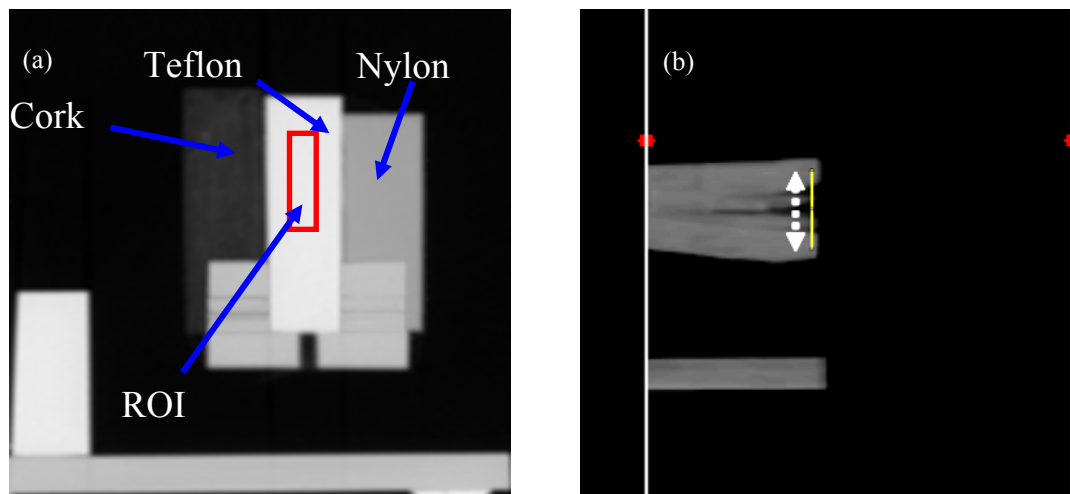


Figure 4.1. MIP images (Cropped to 365 x 365 mm): Amplitude analysis, (a) axial and (b) sagittal mid plane, upper-surface to upper-surface point at minimum and maximum arm elevation used to measure amplitude. (Note: sagittal image has had window and leveling modified for better visualisation.) The red rectangle in (a) shows an example of the ROI used for HU determination. The dashed white line in (b) shows the extent of motion excursion from a sagittal perspective.

4.3.2. HU consistency of moving and stationary objects

Dose calculation in radiotherapy is fundamentally reliant upon HU data from CT. 4D-CT allows the incorporation of motion specific phase-bin data into the treatment plan. The see-saw motion phantom allows comparison between phase-bin HU to a single HU measurement in the AIP, as used in the single plan approach. To assess the effect of motion velocity on HU consistency, the period was fixed at 4 s (15 rpm) and 4D-CTs of amplitudes 6.0, 3.0, 2.5, 2.0, and 1.5 cm were acquired using the Phillips Big Bore Brilliance CT scanner. Data was then retrospectively binned into ten phases, with each phase-bin corresponding to a particular subset of the complete motion cycle. HUs of static and moving objects within the same FOV were then compared for each phase-bin as well as the AIP projection. The region of interest (ROI) was selected to be consistent in size and position within each phase-bin as well as ensuring that it is never overlapping the boundary of the object. To establish the effect of motion frequency on HU variability between moving and static objects, the amplitude was fixed at 6.0 cm and the period of oscillation was varied from two to eight seconds (2 second intervals). 4D CT scans were acquired for each of the four periods and HUs for static and moving objects compared in the 50% phase-bin of each data set.

4.3.3. MIP and AIP artifacts as a function of the number of phase-bins

The minimum number of phase-bins required to ensure a complete MIP data set was evaluated by visual investigation of MIP data for two motion amplitudes (6.0 and 2.5 cm, period = 4 s). The amplitude was set to 6.0 cm and five (0, 20, 40, ..., 80%), and ten (0, 10, 20, ..., 90%) phase-bins were used. MIP images were analysed visually to ascertain completeness of the data set. The Philips Brilliance scanner allows a maximum of ten phase-bins to be used. However, since the motion of the phantom is symmetrical, ten phase-bins over the half the motion is equivalent to 20 over the whole range of motion. As such, ten bins over half the motion cycle were investigated (0, 5, 10, 15, ..., 45%) and images were assessed for artifacts.

4.3.4. Geometric consistency between MIP images and reality

The geometric consistency tests were performed retrospectively using ImageJ image analysis software (National Institute of Health, USA). Apparent motion amplitudes were measured using MIP projection data (Figure 3). This was done for amplitudes 1.5, 2.0, 2.5, 3.0 and 6.0 cm. The MIP derived amplitudes were then compared to calculated amplitudes (Equations 3.1 and 3.2).

4.4. RESULTS

The results presented in this section pertain to a number of studies as listed below. All investigations used the see-saw motion phantom in conjunction with a number of objects of varying densities to cover the relevant spectrum of CT numbers (see Table 4.1).

1. Evaluate the HU consistency, and possible inter-phase variability, between moving and stationary objects within the same field of view in 4D-CT data-sets.
2. Determine the quality of projections (MIP and AIP) with respect to the number of phase-bins.
3. Verify the geometrical consistency of MIP images (i.e. do the amplitudes measured on an MIP represent the calculated amplitudes?)

4.4.1. HU consistency between moving and stationary objects

Figure 4.2 shows the inter-phase variability in HU for water. In this figure, the displacement of maximum corresponds to the 30 and 70 % phase-bins and the minimum displacement corresponds to the 0 and 50% phase-bins. These data, plotted as a function of phase percentage, initially appear to show a phase dependent effect on the measurement of HU. Close scrutiny of individual data

sets, together with that of stationary objects, reveals that the variation is not systematic. It appears that the spread of measurements is greater in the inter maxima / minima phases, where the residual motion within the phase window is greatest, however it is not inconsistent with the usual expected HU uncertainty (shown in Table 4.1). No systematic phase dependent variation was evident for Nylon, Water, Cork and Teflon.

To determine the effect of motion frequency on HU evaluation, the period was varied from two to eight seconds at a constant large amplitude of 6.0 cm. Figure 4.2 (b) shows the effect of motion period on HU determination. Again, the data appears to exhibit a period-dependent variation, but the relationship is not systematic. The largest discrepancy for a moving object occurs for the slower motion (8 s period) and is no worse than the HU for the stationary sample in the shorter (2 s) period case indicating that there is no period dependence in this case.

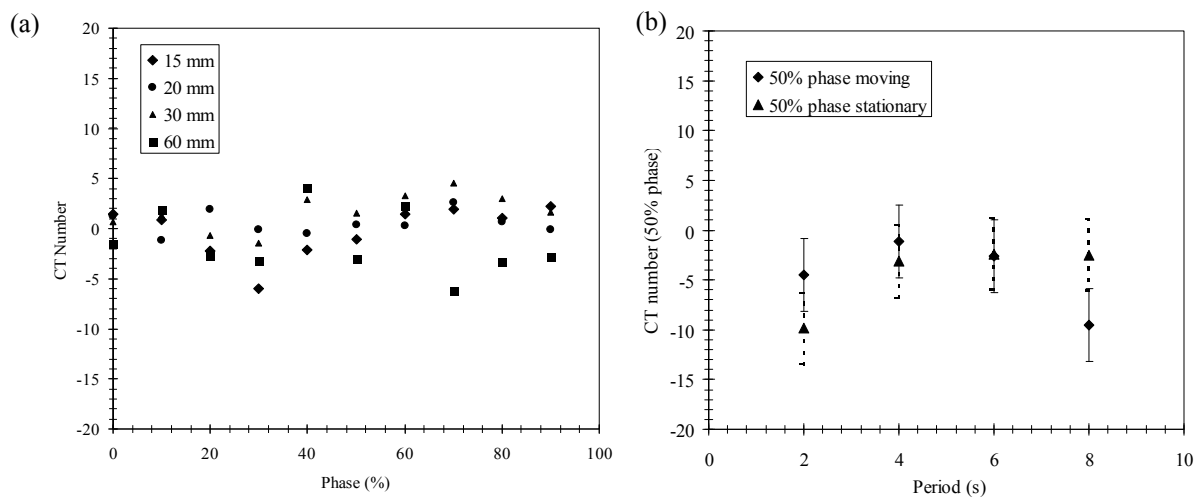


Figure 4.2. (a) Inter-phase variation in the HU of water. Random variations about the ‘true’ HU for water show no systematic dependence on phase-bin over all amplitudes of motion. A standard ROI shown in Figure 3.4 (area = 377 pixels) was used for all measurements. (b) The effect of motion frequency on HU variation. For a large motion amplitude of 6.0 cm a comparison was made between the HU of water for a moving and stationary object in the 50% phase-bin. Error bars represent the standard uncertainty in the measured HU values.

Table 4.2 shows a comparison between the mean HU for water evaluated on each individual phase-bin and averaged, compared to the HU for water from a single measurement on an AIP from the ten phases. For the largest amplitude (6.0 cm), if the ROI is retained in the same position for all phases, then errors will be seen associated with partial volume effects. This is because the edge of the objects will move into even a small ROI. Thus, the ROI must be moved for large amplitude phase images to ensure it lies completely within the object of interest. An example of the failure to do this is shown in the bottom row of Table 4.2 where the HU for water is erroneously measured to be -184 HU when averaged from the ten phases. A motion related artifact can also be seen in the AIP value for the 6.0 cm amplitude. The HU for water is underestimated as -18 HU primarily due to streaking and undersampling artifacts, as can be seen in Figure 4.3 (b). This discrepancy is not mirrored by the average HU from the ten phases due to the cancelling of contributions from the two phases that yielded the maximum and minimum HU which are of similar magnitude (see Moving range Table 4.2). For a large amplitude (6.0 cm), the individual phase images themselves feature artifacts which can contribute to this average.

Table 4.2. Comparison of the mean HU for water measured on all ten phase-bins to the HU of water as measured on the AIP. Comparisons were performed for both the stationary and moving objects within the same FOV. The global mean and standard deviation for all stationary measurements is 0.07 ± 1.5 (-31 – 34).

Amplitude [cm]	Mean CT# (H ₂ O) 10 Phases ± SD (range)		Mean CT# (H ₂ O) AIP ± SD (range)	
	Stationary	Moving	Stationary	Moving
1.5	-0.93 ± 0.86 (-17 – 16)	-1.45 ± 0.99 (-13 – 17)	- 1.16 ± 1.63 (-6 – 5)	-1.84 ± 2.14 (-2 – 6)
2.0	-2.90 ± 0.40 (-16 – 8)	-0.21 ± 0.53 (-10 – 11)	-2.71 ± 1.45 (-11 – 4)	0.24 ± 2.88 (-5 – 3)
2.5	-0.10 ± 0.73 (-14 – 14)	2.55 ± 0.75 (-12 – 15)	-0.01 ± 1.801 (-5– 6)	1.39 ± 2.41 (-2 – 8)
3.0	0.24 ± 1.20 (-19 – 20)	1.96 ± 0.91 (-15 – 21)	-0.20 ± 4.89 (-6 – 5)	3.22 ± 2.42 (-15 – 10)
6.0	2.42 ± 1.09 (-31 – 34)	0.36 ± 7.84 (-51 – 57)	-0.20 ± 4.37 (-12 – 6)	-18 ± 10.48 (-52 – 11)
6.0*	-	-183.9 ± 82.5 (-1024 – 160)	-	-

*erroneous value which occurs if ROI is not moved to coincide with phase position of object.

4.4.2. The quality of MIP and AIP with respect to the number of phase-bins

MIP and AIP data for 6.0 and 2.5 cm motion amplitudes are shown in Figure 4.3 (a-d). The MIP reconstruction over ten phase-bins for the 6.0 cm amplitude, Figure 4.3 (a), suffers from considerable artifacts for the moving objects when compared with static objects within the same FOV. Furthermore, missing reconstruction data due to the use of only ten phase-bins over a large excursion can also be seen. The AIP projection shown in Figure 4.3 (b) is similarly undersampled due to the extreme amplitude of motion.

For the 2.5 cm amplitude MIP and AIP images (Figure 4.3 (c) and (d) respectively), the artifacts associated with large amplitude motions are considerably reduced. In this scenario, a ten phase-bin reconstruction is adequate to provide a 'complete' data set. As can be seen, the MIP appears as a complete data set over the range of motion and could be used to delineate the ITV for the object's trajectory. The AIP image, Figure 4.3 (d), also shows better agreement with the 'expected' average density profile.

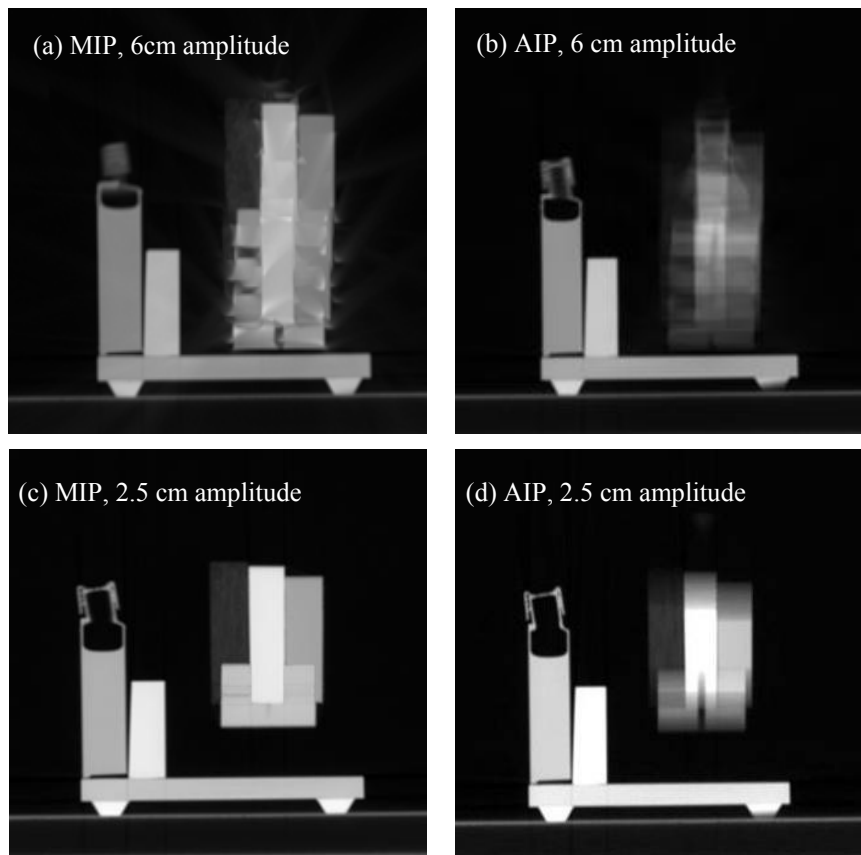


Figure 4.3. (a) MIP using ten phases 0 – 90% with an amplitude of 6.0 cm. (b) Average reconstruction for an amplitude of 6.0 cm. (c) MIP of 2.5 cm amplitude motion using ten phases. (d) Average reconstruction (2.5 cm amplitude).

The optimal number of phase-bins for accurate representation of the motion was found to depend on the amplitude of motion, object size, period and acquisition time per slice (typically 180 degree scanner rotation time). Figure 4.4 shows sagittal MIPs for the see-saw phantom undergoing a 6.0 cm amplitude motion with 4 s period. Five phase-bins (Figure 4.4 (a)) are insufficient to establish the true motion amplitude, as projection data is missing and thus sub-optimal trajectory information is obtained. Figure 4.4 (b) shows the same amplitude with ten phase-bins. A more complete data set is evident, resembling the true ITV motion envelope, although the data set is still incomplete. Lastly, Figure 4.4 (c) uses ten phase-bins over half the motion cycle (equivalent to 20 phase-bins over a complete cycle). It is important to note that the use of 20 phase-bins was only possible since the motion is symmetrical, where normal patient respiratory motion is of course variable and can be asymmetrical. Figure 4.5 shows a conceptual diagram of the interplay between an object's size and its amplitude of motion. This figure shows that using ten phase bins, the

unreconstructed data between phase-bins can result in gaps appearing in MIPs generated.

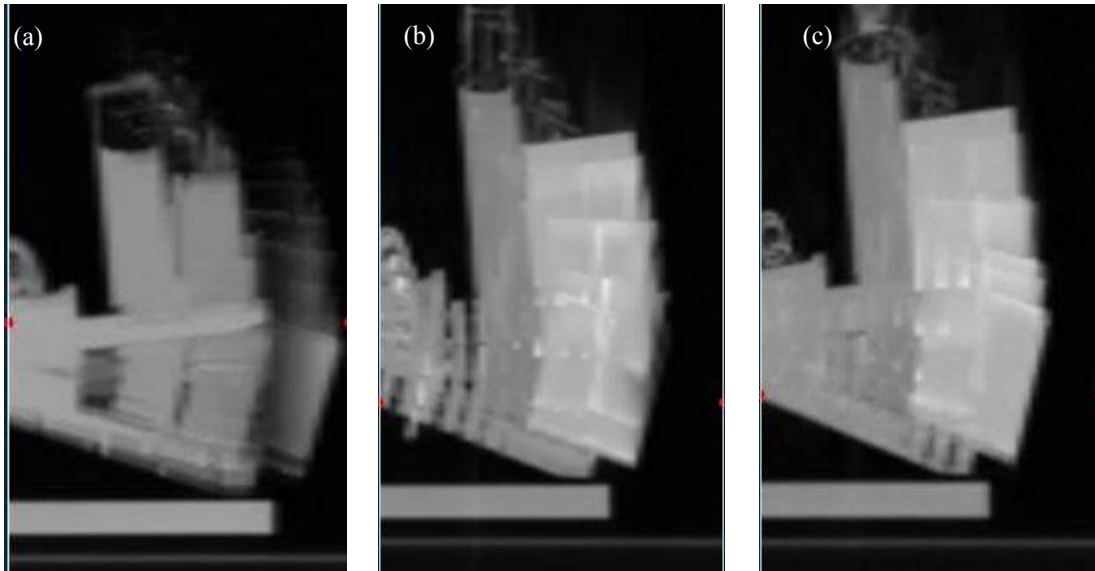


Figure 4.4. Sagittal MIPs for reconstructions based on (a) 5 (0,20,40,...,80%), (b) 10 (0,10,20,...,90%) and (c) 20 (0,5,10,...,45%) phase-bins. 20 phase-bins were constructed by exploiting the symmetrical nature of the motion and using ten phase-bins over half the motion cycle.

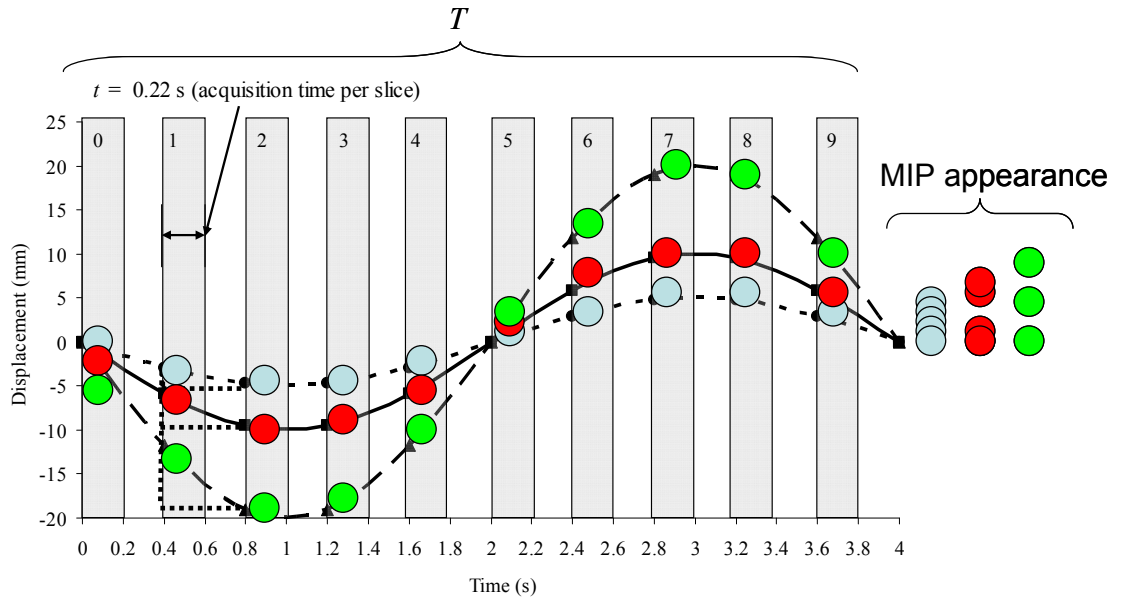


Figure 4.5. The interplay between motion amplitude and object size. Ten phase-bins used over three different amplitudes 4.0, 2.0 and 1.0 cm demonstrating the object amplitude / size interplay and the concept of a discontinuous data set for a MIP. The data-points represented by solid grey circles represent a small object moving with an amplitude of 1.0 cm, for this motion, the MIP constructed from the ten phase-bins would appear as a solid object. For the same size object with an amplitude of 2.0 (red circle) or 4.0 cm (green circle), gaps would appear in the MIP since only ten phase-bins are used.

The effect of undersampling of small objects undergoing large excursions can be summarised mathematically for a sinusoidal motion by noting that gaps in the MIP will appear when:

$$S < |x(t + \Delta t) - x(t)|_{\max} \quad (4.1)$$

Where:

$$x(t) = \frac{A}{2} \cos \frac{2\pi t}{T}$$

$$x(t + \Delta t) = \frac{A}{2} \cos \frac{2\pi(t + T/n)}{T}$$

Where, S is the diameter of the lesion, A is the peak-to-peak motion amplitude, T is the period of motion, n is the number of phase-bins and t is time. Equation 4.1, the ‘completeness criterion’ describes the undersampling effect, whereby an object of diameter S will appear undersampled in a

MIP if S is small compared to its bin-to-bin displacement. The risk of apparent gaps in the MIP depends on the object's speed and the number and temporal width of phase-bins. This effect is likely to be pronounced for small lesions typically seen in lung cancer patients receiving stereotactic treatment. Figure 4.6 demonstrates the interplay between the number of phase-bins, amplitude of motion and lesion size. For a small lesion with a diameter of 1.0 cm and amplitude of 2.0 cm, Figure 4.6 indicates that for five phase-bins, the maximum bin-to-bin displacement is approximately 1.1 cm. This is greater than the diameter of the lesion, therefore a MIP of the 4D-CT data set will be incomplete and gaps will be present. If missing data occurs at the extreme of motion, then an ITV delineated on this data set may be underestimated. Conversely, if ten phase-bins are used, we see that the bin-to-bin displacement is less than the lesion diameter and, as such, a MIP based on this 4D-CT data would be a 'complete' data set with no gaps. One may consider the possible clinical utility of this information. The phase binning required for a patient case is somewhat dependent upon the *a priori* knowledge of the lesion size. In some cases this might be known from earlier diagnostic imaging. In cases where it is not known until 4D-CT imaging is undertaken for planning purposes, Equation 4.1 can be used to inform the decision whether to proceed with planning or to make a clinical decision to compensate for information deficiencies that may be present, or to justify additional imaging. It is interesting to note that for tumour diameters equal to or above 2.0 cm, the most common phase-binning protocol, ten phase-bins, will result in a complete MIP data set for all amplitudes of motion.

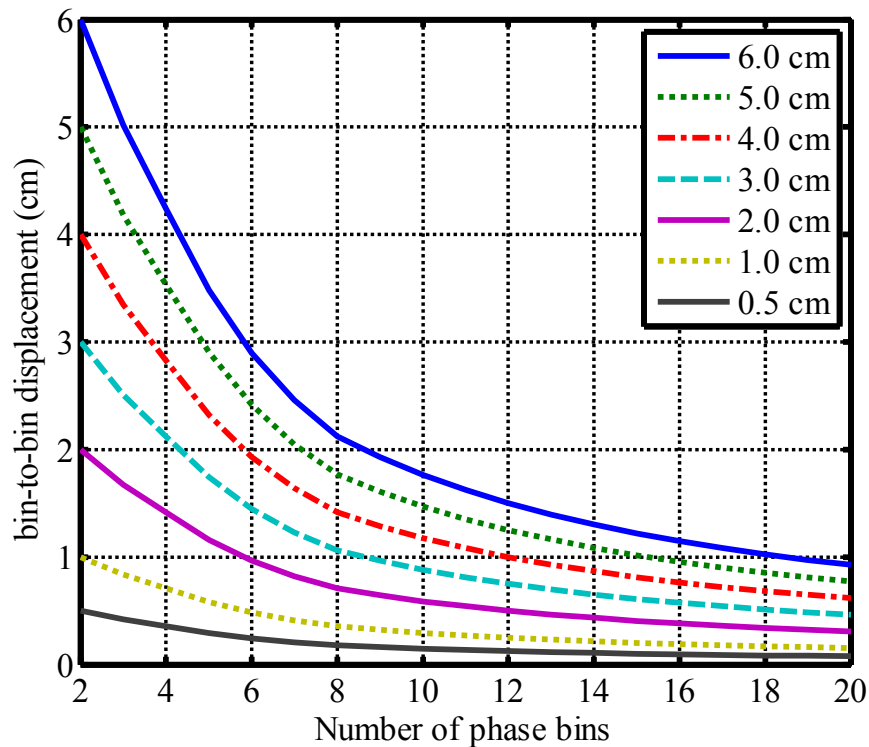


Figure 4.6. The maximum bin-to-bin displacement as a function of the number of phase-bins for a tumor moving with a sinusoidal profile. If the diameter of the tumor is smaller than its bin-to-bin displacement, an insufficient number of phase-bins will result in gaps appearing in the MIP. Data for sinusoidal peak-to-peak amplitudes of 0.5, 1.0, 2.0, 3.0, 4.0, 5.0 and 6.0 cm are shown.

4.4.3. XCAT simulations of the undersampling effect as a function of lesion size.

Figure 4.7 and Figure 4.8 illustrate a simulation of the undersampling effect outlined in 4.4.2. The interplay of lesion size, amplitude of motion and an insufficient number of phase-bins results in gaps appearing in projections obtained from an insufficient number of phase-bins. Simulations with a 10, 15 and 20 mm diameter tumour in the left lung, and five ten or 20 bins are shown. To generate these images, the XCAT's respiratory period was set to 4 s with 5, 10 or 20 time frames generated. The time frames in this case are representative of the phase-bin data obtained from 4D-CT. Figure 4.7 shows MIP data generated with the XCAT phantom. In this scenario, the XCAT's maximum diaphragm extension was set to 4.0 cm. The figure illustrates that a 10 mm diameter tumour moving with amplitude of 4.0 cm requires a larger number of phase-bins to provide a complete data-set on a MIP. Figure 4.8 represents the same data, however, the maximum

diaphragm amplitude has been reduced to 2.0 cm. With this reduced amplitude, the 10mm diameter lesion requires only five phase-bins to appear as a complete data-set. The simulation data presented in Figure 4.7 and Figure 4.8 further illustrate the experimental work with the see-saw motion phantom, particularly the results presented in Section 4.4.2.

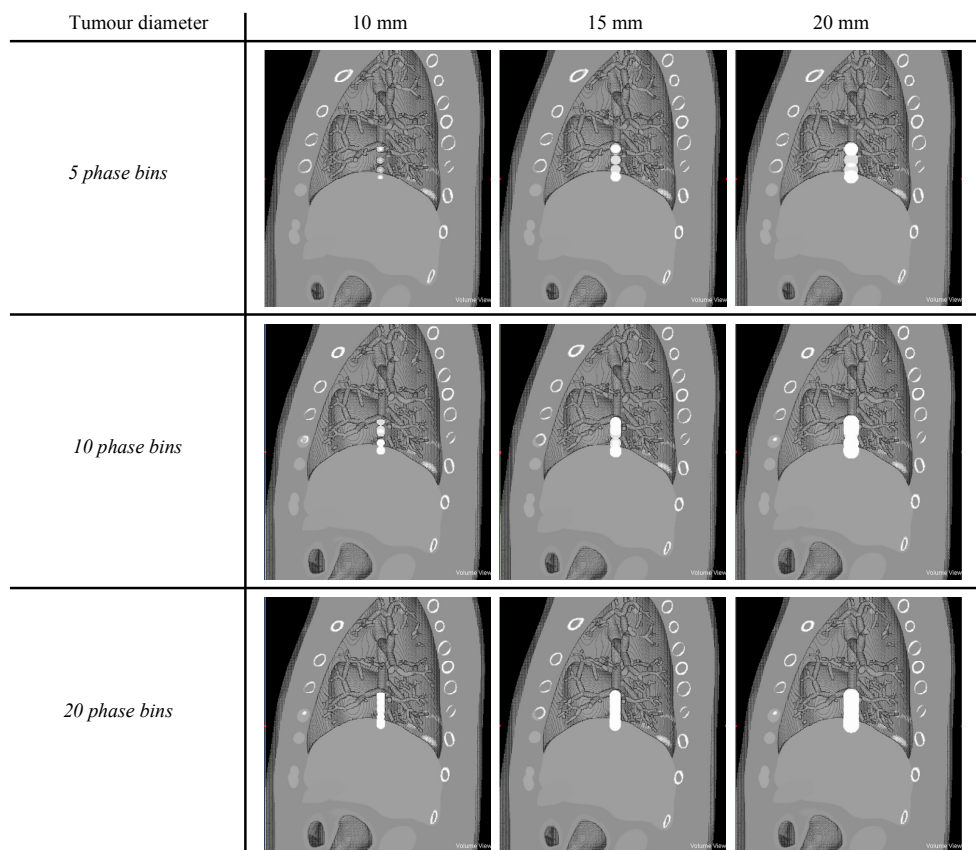


Figure 4.7. Simulations with the XCAT phantom and a maximum diaphragm extension of 4.0 cm. Gaps can be seen to appear in these MIP images for small lesions (10, 15 mm) if an insufficient number of phase-bins are implemented.

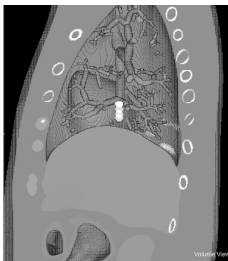
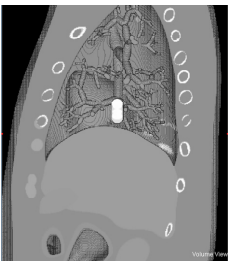
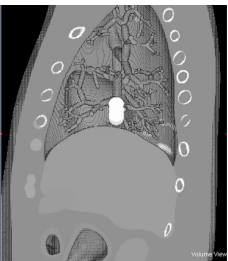
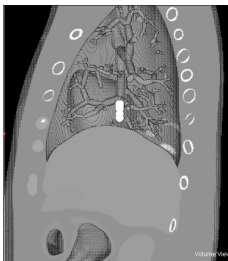
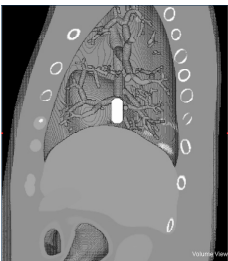
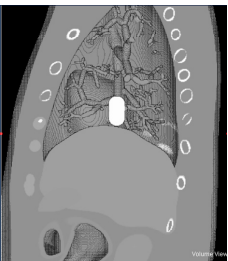
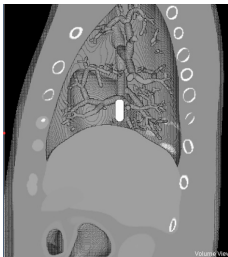
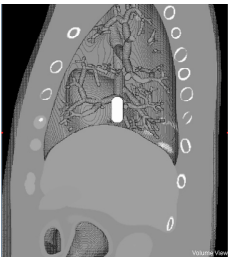
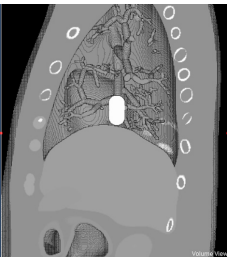
Tumour diameter	10 mm	15 mm	20 mm
5 phase bins			
10 phase bins			
20 phase bins			

Figure 4.8. Simulations with the XCAT phantom and a maximum diaphragm extension of 2.0 cm. The reduced diaphragmatic motion and therefore reduced lesion migration results in a reduction in the gaps appearing in MIP images as a result of insufficient phase-bin assignment.

4.4.4. The geometrical consistency of MIP images

Measurement of distance is important in the quality assurance of 4D-CT. Specifically, if an ITV is delineated from a MIP data set, the CT data shows a motion envelope. The size of the envelope should be measured against a known motion to assess the accuracy of the reconstruction. Ideally, this should be done for a wide range of motion amplitudes and frequencies. Figure 4.9 shows MIPs of five different motion amplitudes ranging from 1.5 – 6.0 cm. The amplitude of motion was derived from these images via the method shown in Figure 4.1. Calculated AP motion amplitudes (Equation 3.1) were compared to the MIP derived amplitude. Table 4.3 shows the results for the five tests. MIP derived amplitudes for 3.0, 2.5 and 1.5 cm showed sub-millimeter agreement with the true amplitude, whilst amplitudes of 6.0 and 2.0 cm demonstrated an underestimation of 2 mm and an overestimation of 1.5 mm respectively when comparing the calculated phantom motion to the motion as measured on a MIP.

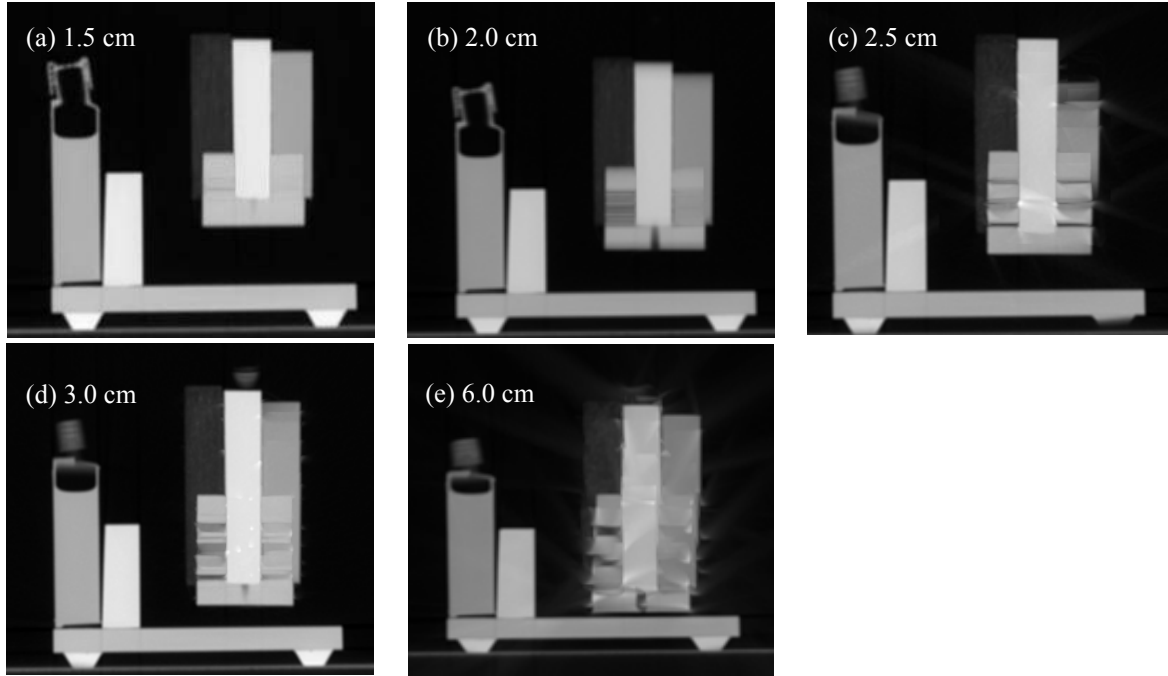


Figure 4.9. MIP's for five different amplitudes. (a) 1.5 cm, (b) 2.0 cm, (c) 2.5 cm, (d) 3.0 cm and (e) 6.0 cm. Each of these amplitudes was measured using the method shown in Figure 4.1 and data was binned using a ten phase-bin protocol. The MIP delineated amplitude was compared with the known amplitude.

Table 4.3. Comparison between MIP derived amplitudes and physical amplitudes. The amplitude of the objects was calculated for five AP amplitude settings using Equation 3.1. For the MIP derived amplitudes, the ruler function from ImageJ was used.

Calculated amplitude (mm)	MIP derived amplitude (mm)	Difference (mm)	Absolute difference (mm)
60	58.008	-1.992	1.992
30	29.650	-0.35	0.35
25	24.984	0.625	0.625
20	21.484	1.484	1.484
15	15.297	0.297	0.297
	Mean \pm SD	0.0128 \pm 1.30	0.95 \pm 0.75

4.5. DISCUSSION

The goal of imaging in SBRT is to provide a highly detailed visualisation of patient anatomy as it would appear during patient setup and throughout the treatment. The most appropriate imaging modality for SBRT depends on the tissue being imaged. Generally, CT makes up the primary imaging modality and forms the basis for SBRT treatment plans. This thesis explored how motion affects common practice methods like contouring on a maximum intensity projection and performing dose calculation on an average intensity projection.

4.5.1. *Inter-phase variation in HU*

This study evaluated the phase-variation of HU and compared each phase to the AIP. No systematic dependence was found in this study within the uncertainty of ± 10 HU. However, this was only evaluated for a sinusoidal motion. Irregular motion, as stated previously, can cause errors in phase-bin assignment. Furthermore, if the respiratory motion is fast compared to the acquisition time for all projections required for reconstruction of a phase then problems should arise. The see-saw phantom provides the means to evaluate the consistency as can be seen in Figure 4.2.

4.5.2. *The accuracy of projections from 4D-CT*

Implementing MIP and AIP information into treatment planning is only beneficial if the data provided by the MIP and AIP is accurate and complete. The accuracy of projections from 4D-CT has previously been investigated by Park *et al* (2009b). Park *et al* found that MIPs systematically underestimated the range of target motion and urged caution in using MIP when breathing is irregular. Zamora *et al* (2010a) identified cases in which a MIP generated from a 4D-CT under-represented the ITV by more than 10%. This error was largely due to auto-contouring of the data set. In this study, examples of incomplete data sets formed by objects undergoing large excursions during image acquisition have been presented. If auto-contouring was used as in the case put forward by Zamora *et al* (2010a), then underestimation or overestimation of the ITV could occur. In this work, MIP data based on 4D-CT accurately represented the true motion of the phantom to within 2 mm for amplitudes below 6.0 cm. These results are consistent with Ezhil *et al* (2009), who found that a MIP from 4D-CT represented the true ITV well when compared to other methods of ITV delineation (e.g. 2-phase addition, ten phase addition etc.).

For a small object, this can result in gaps appearing in the MIP, since no data is reconstructed between phase-bins. The object would appear to be in a different position altogether. For the smaller amplitudes, although the objects have moved, their traversed bin-to-bin distance is smaller than the object's diameter and therefore an object of sufficient size would create a complete MIP data set with no apparent missing information.

The accuracy of the AIP is important for dose calculation purposes as will be discussed in Chapter 6. The consistency of HU in AIP is particularly important since it is generally used for dose calculation in a treatment plan based on 4D-CT (Guckenberger, Wilbert *et al.*, 2007, Rietzel, Chen *et al.*, 2005b, Rietzel, Liu *et al.*, 2004, Cai, Read *et al.*, 2008, Tian, Wang *et al.*, 2012). Inconsistencies in CT number to electron density calculations that are based on misrepresented CT data could contribute to dose calculation errors. In this work, the quality of AIPs for a sinusoidal motion was evaluated. Irregular motion could cause incorrect HU to electron density conversions due to the AIP formation being incomplete or containing artifacts from incorrect phase-bin assignment from 4D-CT. 4D-CT has been previously shown to produce errors if the patient's breathing is irregular, particularly for a helical acquisition (Pan, 2005, Park, Huang *et al.*, 2009a).

The present study has shown that ten phase-bins are adequate to provide a complete MIP dataset for amplitudes ≤ 3.0 cm and object sizes of > 1.0 cm. Amplitudes larger than this resulted in incomplete data sets when ten phase-bins or less were used. This effect has been quantified in what is termed "*the Completeness Criterion*" (Equation 4.1). Equation 4.1 demonstrates that if the 4D-CT scanner is capable of reconstruction into greater than ten phase-bins, then this should be pursued for small lesions undergoing large excursions, if only to compare to the ten phase-bin standard. The large amplitudes shown in our study (6.0 cm) represent extreme cases (Seppenwoolde, Shirato *et al.*, 2002b, Sixel, Ruschin *et al.*, 2003), though they have been observed clinically by the authors and lung tumour excursions up to 5.0 cm have been reported by Chen *et al.* (2001). It also appears appropriate that for commissioning and QA, extreme cases should be considered to highlight possible problems.

The clinical utility of such a criterion would be to establish the need for more phase-bins or the use of abdominal compression (Heinzerling, Anderson *et al.*, 2008, Han, Cheung *et al.*, 2010) based on a scout 4D scan. If the target was identified *a priori* as being highly mobile, the clinician could then use Equation 4.1 to determine if the criterion required more phase-bins than the default (10)

to ensure an artifact free MIP. A re-scan of the patient would then be completed with a higher number of phase-bins selected. The clinician could also implement a motion reduction strategy to minimise respiratory induced motion of the target.

The computational XCAT phantom was used to further explore the experimental results obtained with the see-saw phantom and the Completeness Criterion presented in Sections 3.2 and 4.4.2 respectively. The results are shown in Figure 4.7 for a 4.0 cm diaphragm extension and Figure 4.8 for a 2.0 cm diaphragm extension with multiple tumour diameters (10 mm, 15mm and 20mm) and phase-bin arrangements (5, 10, 20 bins). These simulations highlight the object size / amplitude relationship between the number of phases used for reconstruction, and the completeness of the MIP. The XCAT results show that a small lesion of the order of 1.0 to 2.0 cm undergoing a 2.5 – 4.0 cm excursion is incorrectly represented on a MIP with ‘missing’ data causing banding artifacts if less than 10 phase-bins are used.

4.6. CONCLUDING REMARKS ON THE EFFECT OF MOTION ON IMAGES OBTAINED FROM 4D-CT

Using a moving phantom it is possible to measure the HU consistency of moving and stationary objects of the same dimensions and material. The properties (HU values / dimensions) of moving objects can then be compared the stationary objects’ properties to determine the quality of images and projections from 4D-CT. In the present work, the effects of motion on images and projections obtained from 4D-CT using a custom built see-saw phantom have been presented. Further to this, a derivation of a mathematical quantification of the conditions needed for a ‘continuous’ MIP for sinusoidal motion (Equation 4.1) has also been presented. Sinusoidal profiles were used to quantify the object size / amplitude ratio that would lead to undersampling when using ten phase-bins. Figure 4.5 demonstrates that for a moving object with a period of 4 s and acquisition time per slice (temporal phase-bin width) of 0.22 s, an object smaller than 0.5 cm with an amplitude of 4.0 cm will appear discontinuous on the MIP if ten phase-bins are used. For amplitudes below 3.0 cm (object size > 1.0 cm), ten phase-bins are sufficient to delineate an ITV and obtain an AIP representative of the true motion and density profile, provided the breathing pattern is regular. Clinically, the amplitude and size of the object being imaged are of importance. Amplitudes of 6.0 cm are rare, but have been observed by the authors. A small lesion undergoing such a large amplitude excursion should be considered an extreme case. Regardless, small objects traversing large distances, along with the interplay of helical acquisition with object motion, can create

undersampling errors in the acquired MIP and AIP data sets. These errors manifest as artifacts or 'missing data'. Figure 4.5 demonstrates this effect for amplitudes of 1.0, 2.0 and 4.0 cm, whereby the magnitude of the object's displacement between successive phase-bins is greatest for larger amplitudes. 4D-CT has been shown to significantly reduce the artifacts associated with respiratory motion in conventional CT. By binning oversampled CT data into divisions of the respiratory cycle observed via an external surrogate, the tumour's excursion over a complete respiratory cycle can be evaluated. Projections from 4D-CT have been used for planning in SBRT with the MIP being used to delineate an ITV and the AIP used for dose calculation. This work has highlighted that the quality of these projections is based on a tumour size / amplitude relationship. The accuracy of these projections is critical in delivering an accurate dose to the treatment region in SBRT.

Chapter 5. The impact of motion: PET imaging

“Machines take me by surprise with great frequency.”

- Alan Turing

5.1. INTRODUCTION

PET is becoming increasingly used for treatment planning in SBRT in conjunction with 4D-CT. The impact of motion on PET imaging has been reported extensively in the literature and is outlined in this work in Section 2.3.3. However, less well documented is the impact the size of lesions will have on the known impact of motion in conventional PET. The objective of the PET component of this work was to assess the impact of lesion motion and size on images acquired with PET (Objective 3). Specifically:

1. With the limited resolution of modern PET systems, how does the lesion's size and amplitude of motion affect the system's ability to resolve the uptake hotspot?
2. What is the reduction in apparent activity that occurs as the motion amplitude increases and how does this depend on the lesion's size?
3. Can the volume overestimation and apparent activity reduction be recovered using 4D-PET?

An experimental investigation was conducted using the phantom described in Section 3.3 with a customised insert containing reservoirs of various sizes filled with ^{18}F -FDG. The objectives of this experimental study were:

1. Observe the effect that various magnitudes of lesion displacement have on 3D PET images on various size lesions.
2. Quantify the ability of the PET system to recover signal loss when using 4D PET scanning.

The above measurements have only been applied to the phantom study, observation of the analogous effects in an anthropomorphic geometry have been derived using Monte Carlo techniques. Monte Carlo allows a systematic study of these effects for lesions of different sizes undergoing different motion amplitudes that would otherwise be impossible on real patients.

The Monte Carlo portion of this study was conducted using the GATE platform (Section 2.10.3.2) in conjunction with the XCAT anthropomorphic phantom (Section 2.10.3.3). XCAT phantoms were generated with lesions in the mid to lower right lung. The lesion's size ranged from 10 – 30 mm with activity ratios of 10:1, 5:1 and 2:1 (lesion:background). These phantoms were then used as the geometry for Monte Carlo simulations. A complete Phillips allegro PET scanner was

modeled in GATE and used to detect annihilation quanta emanating from the XCAT phantom.

Experimental results, as well as results from Monte Carlo GATE and XCAT phantom simulations are presented. The experimental portion of this work was the subject of a paper published in the Australian Physical Scientists and Engineers in Medicine (APSEM) journal. The manuscript was entitled *Motion effects on SUV and lesion volume in 3D and 4D PET scanning* by Callahan, J., Binns, D., Dunn, L. and Kron, T. 2011. *Australas Phys Eng Sci Med*, 34, 489-95. The Monte Carlo and XCAT studies are in preparation for publication.

5.2. BACKGROUND

Over the past decade, PET and CT have become invaluable tools in the evaluation of oncologic processes. Both imaging modalities are affected by respiratory motion. The areas most affected by this are the lower lungs, liver and upper abdomen. Artifacts present in these images have the potential to affect the correct diagnosis of diseases, delineation of target volumes for radiotherapy, impair staging of disease before surgery and lead to incorrect quantitation in therapeutic monitoring.

The most common parameter used to characterise a lesion using PET is the Standardised Uptake Value SUV. The SUV is defined as the ratio of the tissue radioactivity concentration at time t and the injected activity at the time of injection ($t=0$) divided by the body weight. SUV indicates the degree of peripheral uptake by the tumour relative to the whole body background, and is therefore related to metabolism. Clinically, the SUV_{max} is an important factor (Larson, Nehmeh *et al.*, 2005). The SUV_{max} is defined as the maximum pixel SUV within a region of interest drawn around a lesion. Some studies have advocated the use of SUV_{max} as a threshold for differentiation of benign and malignant lung nodules (Hubner, Buonocore *et al.*, 1996, Garcia Vicente, Soriano Castrejon *et al.*, 2010). Thus the ability to measure voxel by voxel activity is important, and motion induced apparent changes need to be properly accounted for.

The use of PET in radiotherapy planning is a well established practice (MacManus, Nestle *et al.*, 2009). ^{18}F - fluorodeoxyglucose (^{18}F FDG) PET greatly enhances the sensitivity and specificity in staging and diagnosis compared to CT (Benedict, Yenice *et al.*, 2010, Lardinois, Weder *et al.*, 2003, Günther, Schenk *et al.*, 2004). In the context of radiotherapy treatment planning, dual imaging PET/CT using FDG is being increasingly used for delineation of target volumes (Mac

Manus and Hicks, 2012, Mac Manus, Hicks *et al.*, 2006, Zhang, Tachiya *et al.*, 2010). A limitation of PET scanning is the whole body scan time takes roughly 20 – 30 minutes (Callahan, Binns *et al.*, 2011, Callahan, Kron *et al.*, 2011), it is necessary therefore for the patient to breath freely during the acquisition. Free breathing acquisition can lead to blurring artifacts and mis-registration between the PET and CT scans makes accurate delineation difficult (Aristophanous, Berbeco *et al.*, 2012a).

It is well known that patient respiratory motion causes blurring of the activity distribution of a PET avid lesion (Xu, Yuan *et al.*, 2011, Xu, Xie *et al.*, 2012, Reyes, Malandain *et al.*, 2005, Park, Ionascu *et al.*, 2008, Osman, Cohade *et al.*, 2003, Nehmeh, Erdi *et al.*, 2003, Nehmeh, Erdi *et al.*, 2004b, Nehmeh, Erdi *et al.*, 2004a, Nehmeh, Erdi *et al.*, 2002b, Nehmeh, Erdi *et al.*, 2002a). The blurring of the activity distribution causes a *decrease* in the apparent activity of a lesion and an *increase* in the apparent volume. In the context of SBRT, accurate delineation of targets is essential. If respiratory motion is not managed in PET and PET/CT of the thorax, then the added functional information afforded by PET may actually be detrimental to treatment planning, diagnosis and assessment of tumour response following treatment. Recently, 4D PET/CT has been examined as a possible solution to the volume overestimation and intensity reduction associated with respiratory motion.

A number of phantom studies have been completed to determine the benefits and pitfalls of 4D PET/CT acquisition. Nehmeh *et al* (2002b) investigated the reduction in activity smearing with phantom studies and found that the reduction in activity smearing afforded by 4D-PET is dependent on lesion size, the number of bins used for data acquisition and the lesion amplitude. 4D-PET also improved the lesion / background ratio and consistency in the measurement of SUV. These studies however, evaluated these effects for target sizes larger than those typically seen in SBRT.

A more recent study published in Radiotherapy and Oncology (Mac Manus, Everitt *et al.*, 2013) demonstrated the benefits of PET/CT in planning for lung cancer radiotherapy. The study investigated the impact of radiotherapy planning FDG-PET/CT on management of non-small cell lung cancer and found that planning PET/CT frequently changed management and was associated with improved survival. PET/CT changed the way patients were selected for either curative or palliative treatments therefore allowing resources to be managed more effectively. Overall survival

for patients given chemotherapy in conjunction with radiation therapy (chemoRT) following PET/CT based planning was 77.5% and 35.6% at 1 and 4 years, respectively and was 32% for stage IIIA patients at 4 years compared to the 1-year and 4-year overall survival estimate of 56.8% and 24.9% respectively. Their study also showed that without PET, FDG-avid tumour would reside outside the planning target volume (PTV) in 36% of radical cases and in 25% of cases, less than 90% of the PTV would have received greater than 95% prescribed dose.

As the use of PET/CT becomes more prevalent, it is hoped that similar increases in overall survival such as those reported by Mac Manus *et al* can be achieved for patients undergoing SBRT. However, an understanding of the impact of motion on the use of PET and PET/CT for SBRT needs to be understood. This chapter aims to identify some of these issues and present tools to study these effects.

5.3. MATERIALS

5.3.1. *Experimental materials*

The upgraded QUASAR respiratory motion phantom outlined in Section 3.3 was used in conjunction with customised cylindrical inserts. The insert carriage contains four milled cylindrical reservoirs with varying diameters of 5, 10, 15 and 20 mm diameter reservoirs, each 15 mm in height. This phantom and custom made insert is shown in Figure 5.1.

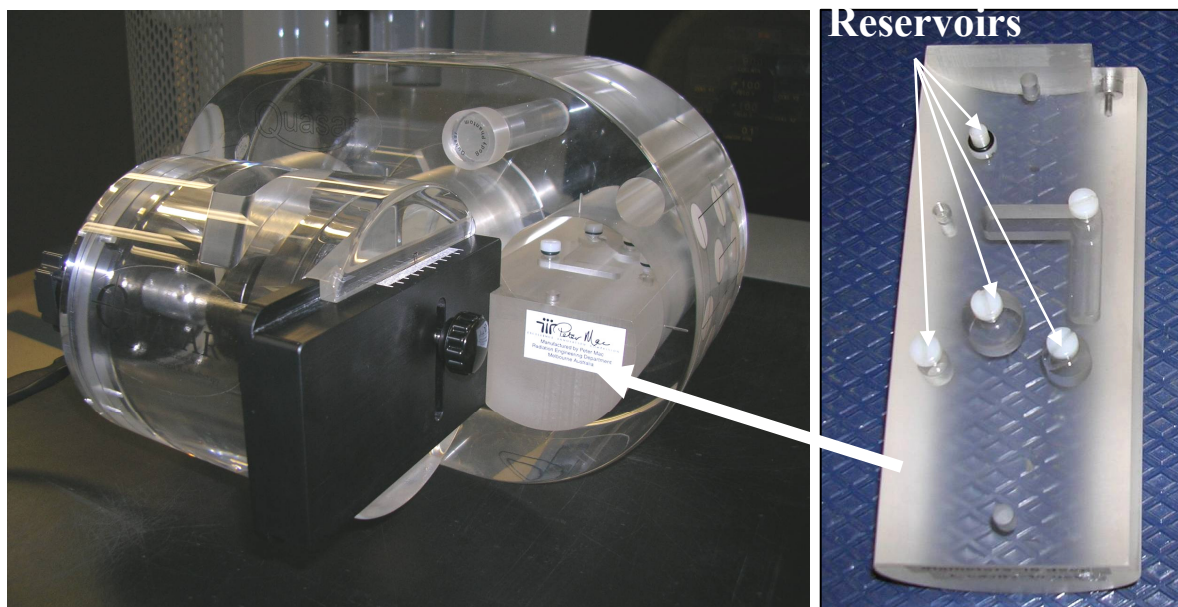


Figure 5.1. Upgraded QUASAR motion phantom left with moving insert right. The insert contains 5, 10, 15 and 20 mm diameter reservoirs each 15 mm in height. An ‘L’ shaped reservoir can also be seen.

5.3.2. Monte Carlo materials

A full Monte Carlo computational study was conducted using both the GATE platform (Section 2.10.3.2) and the XCAT phantom (Section 2.10.3.3). Simulations were run on the *tango* cluster at the Victorian Partnership for Advanced Computing (VPAC). The *tango* cluster is a large AMD Opteron system and consists of 111 compute nodes, each with two AMD Shanghai 2.5 GHz quad-core processors for a total of 888 CPUs. This permitted up to 20 simulations to be run simultaneously, each using one quad-core processor.

5.4. METHODS

5.4.1. Experimental methods

5.4.1.1 Phantom

Each of the four cylindrical reservoirs was filled with the same concentration of ^{18}F -FDG. No background activity can be used with the insert. Motion patterns of up to 4 cm peak-to-peak were generated with frequencies between 7.5 and 30 rpm. The full range of amplitudes and motions is listed below:

- 15 RPM / 1cm

- 15RPM / 2 cm
- 15 RPM / 4cm
- 30 RPM / 2cm
- 7.5 RPM / 2 cm

The range of 7.5 – 30 cycles per minute was chosen to represent the breathing rate most patients would fall into. The range of lesion displacements was also chosen to reflect a realistic range of tumour induced motion due to respiration. These ranges were selected based on literature (Seppenwoolde, Shirato *et al.*, 2002b) and clinical experience. Each scan was re-binned into ten phase-bins using the respiratory trigger and reconstructed using the same parameters with attenuation correction applied using the co-acquired CT.

5.4.1.2 Data acquisition

The phantom was scanned on the GE Discovery STE 8 PET/CT using the Varian RPM system for gating. Un-gated 3 minute 3D PET scans were acquired of the static phantom for baseline measurements. A stationary helical CT scan was also acquired for attenuation correction. A 10 minute 3D list mode PET scan with a respiratory trigger (Varian RPM) was then acquired of the phantom at five different sinusoidal respiratory motions (Frequency / Amplitude).

5.4.1.3 Data analysis

The Siemens TrueD image analysis software was used to analyse the maximum and mean activity A_{\max} , A_{mean} and volume of each lesion using a 40% A_{\max} threshold on the un-gated (3D) scan. The A_{\max} is defined as the maximum pixel activity within a region of interest drawn around a lesion. Correspondingly, the A_{mean} is the average pixel activity within a region of interest. To determine the activities the SUV_{\max} and SUV_{mean} functions of the software were used, however, in the phantom studies, the body-mass and activity concentration normalisations are arbitrary, so the relative activities are the quantities of interest. In this work, the volume of interest was selected using a semi-automated threshold method to outline the lesion. The 40% threshold method was chosen to reduce operator bias and has previously been shown as a reproducible method of contouring tumour volumes (Bradley, Thorstad *et al.*, 2004). The same parameters were measured in all ten bins of the 4D-PET scan. The average A_{\max} , A_{mean} and lesion volume were compared to the values obtained from the 3D-PET scan. All values were then compared to the baseline data

corresponding to the maximum and mean activity recorded for a static phantom.

5.4.2. Monte Carlo simulations

As no patients are experimentally possible for a systematic investigation to assess the impact of lesion size and motion on images acquired with PET, Monte Carlo methodologies using the GATE platform were pursued.

5.4.2.1 XCAT phantoms

Firstly, XCAT anthropomorphic male torso phantom datasets were created with simulated respiratory and cardiac motion. Each phantom was created with a pixel size of $5 \times 5 \text{ mm}^2$ with a slice thickness of 5 mm resulting in a phantom with dimensions of $200 \times 128 \times 128$ pixels. The respiratory period was kept constant at 4 s with a total of 40 output frames (0.1 s in length each). Both CT attenuation and activity phantoms were generated. The CT attenuation phantoms were used to define the material properties for the geometry in a GATE simulation. The activity phantoms were used to translate the voxel values for specific organs / lesions into activities in the GATE simulations.

Five diaphragm displacements that control the deformation and translation of the organs / lesions affected by respiratory motion were simulated. Phantoms with diaphragm displacements of 0 (no motion activated), 0.5, 1.0, 2.0 and 3.0 cm were then created. Amplitudes of greater than 3 cm were not simulated as the XCAT phantom has a maximum diaphragm extension of 3.0 cm. For each of these amplitudes, spherical lesions of 0.5, 1.0, 2.0 and 3.0 cm diameters were added to the mid-to-lower right lung close to the diaphragm so that the associated lesion amplitude matched closely to the diaphragm's extension (see Figure 5.2). This resulted in four phantoms (with different lesion sizes) per diaphragm extension.

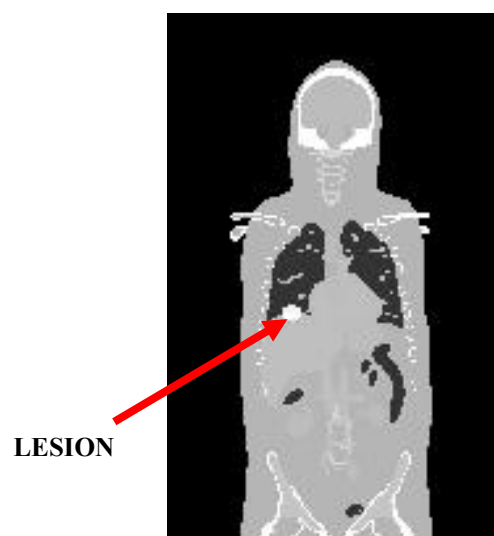


Figure 5.2. Location of the lesion within the right lung for GATE simulations.

5.4.2.2 Construction of the Phillips Allegro PET scanner

A Phillips Allegro scanner was modelled with GATE. The parameters for the input file are based on manufacturer's specifications and reported values from (Lamare, Turzo *et al.*, 2006). This scanner model was chosen as Lamare *et al* have previously extensively benchmarked this scanner in GATE against measured data. The Phillips Allegro scanner's technical features and physical performance are outlined in Table 5.1 and Table 5.2 respectively. The scanner consists of 28 flat blocks arranged in a ring, with each block made of 22 x 29 Gadolinium orthosilicate (GSO) crystals. Each crystal element has a surface area of 4 x 6 mm² and is 20 mm thick. A schematic of this scanner, created in GATE is shown in Figure 5.3. To create the scanner in GATE, an input file was generated outlining the scanner's geometrical properties, detection systems and signal processing specifications. These values were taken from Table 5.1 with the signal processing variables defined by (Lamare, Turzo *et al.*, 2006). The Phillips Allegro / GEMINI PET scanner was simulated in GATE and used in conjunction with the XCAT phantom. Lamare *et al* have previously evaluated the accuracy of the detection system through a comparison of simulated and measured results obtained with the Allegro / GEMINI systems for a number of NEMA NU2-2001 performance protocols. These included, spatial resolution tests, sensitivity and scatter fraction comparisons. In addition, an approximate model of the system's dead time at the level of detected single events and coincidences was developed in an attempt to simulate the count rate related

performance characteristics of the scanner. The group also developed a reconstructed image quality protocol which was used to assess the overall performance. Their results indicated an agreement of less than 3 % in scatter fraction, with a difference between 4 % and 10 % in the true and random coincidence count rates respectively, over a range of activity concentrations and under various imaging conditions. Simulated and measured count rates demonstrated less than 8% difference (noise equivalent count rates). The image quality validation study revealed a good agreement in signal-to-noise ratio and contrast recovery coefficients for a number of different volume spheres and two different (clinical level based) tumour-to-background ratios.

Table 5.1. Technical features of the Phillips Allegro PET scanner (Tarantola, Zito *et al.*, 2003).

Feature	Allegro Factory Specifications
Number of rings	28
Ring diameter (mm)	860
Patient port (mm)	565
Crystals number	17,864
Crystals material	Gadolinium orthosilicate (GSO)
Crystal size (mm)	4 x 6 x 20
PMT number	420
Crystals/block	No blocks
Energy window width (keV)	435-590
Coincidence window (ns)	8
Acquisition mode	Full 3D
Transaxial FOV (mm)	576
Axial FOX (mm)	180
Number of image planes	90
Slice Thickness (mm)	2
Septa material	N/A
Septa dimensions	N/A

Table 5.2. Physical performance and other features of the Philips Allegro PET scanner (adapted from (Tarantola, Zito *et al.*, 2003).

Performance	Allegro Factory Specifications
Transaxial resolution	
FWHM (mm) at 1 cm	4.8
FWHM (mm) at 10 cm	5.9
Axial resolution	
FWHM (mm) at 0 cm	5.4
FWHM (mm) at 10 cm	6.5
Scatter fraction (%)	25
System sensitivity (net trues) (cps/Bq/mL)	19.0
Energy resolution (FWHM)	15%
Filtered	
Backprojection	YES (3D)
Iterative algorithms	FORE / OESM, 3D-RAMLA
Transmission source	¹³⁷ Cs
Source activity (MBq)	740
Source geometry	Point
Transmissive energy window (keV)	600 -720
Whole body scan length (cm)	198

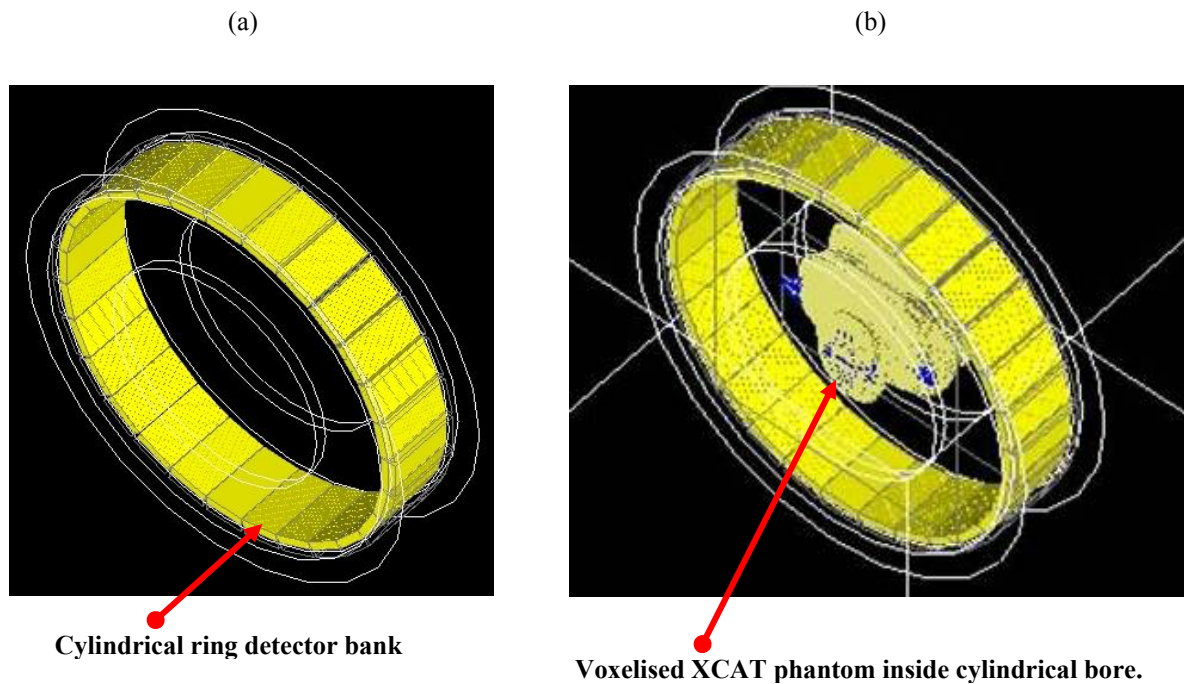


Figure 5.3. (a) Schematic of the Phillips Allegro scanner detection geometry in GATE. (b) The same scanner with the voxelised XCAT phantom shown.

5.4.2.3 Incorporating the XCAT phantom into GATE

Incorporating the XCAT as the phantom geometry in GATE involved converting all XCAT datasets to 16-bit integers and using a range translator to convert pixel values to materials used by gate (i.e. organ compositions). Following this, activity distributions were assigned to the tumour and lungs for each phantom dataset. The phantom was then imported using an ‘InterFile’ format where the number of frames, dimensions of the phantom, attenuation and activity translators are defined. The centre of the XCAT phantom was placed at the origin (0,0,0) of the ‘world’ volume. The C++ class described by Descourt *et al* (2006) was then implemented to read successive XCAT datasets during the Monte Carlo simulation. This process is shown in Figure 5.4. This process was then repeated for each phantom set, consisting of a particular amplitude and lesion size depending on the simulation. The activity of the tumour was set to 10 kBq with the lung background activity

set to 1, 2 or 5 kBq to define different activity ratios. The rest of the voxel activities were set to zero, equivalent to no background outside the lung to decrease the simulation times which take approximately 2-3 days using 20 processors per simulation. Figure 5.5 and Figure 5.6 show a selection of XCAT phantoms that were generated and used as the phantom geometry in the Monte Carlo GATE simulations.

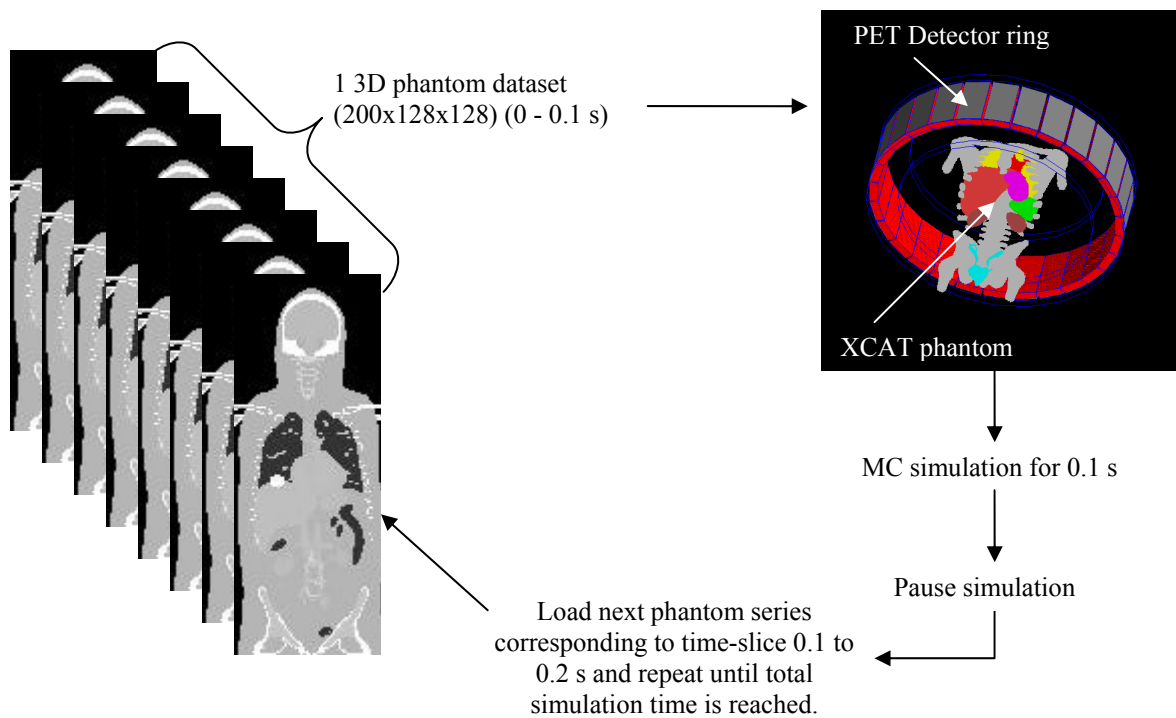


Figure 5.4. A diagram illustrating the way XCAT phantoms are incorporated into the GATE Monte Carlo framework.

5.4.2.4 PET Acquisition settings

For every diaphragm amplitude and tumour size (Table 5.3) PET data was acquired for 600 seconds with the phantom's geometry being updated every 0.1 s. This resulted in 150 (600/4) full 4 s respiratory cycles being simulated during the course of a simulation.

5.4.2.5 4D- PET simulations

4D-PET simulations are presently unavailable with the GATE software. To simulate a 4D

acquisition, a novel methodology was developed. To begin, each simulation was made to run for no longer than the XCAT's respiratory period (4 s) so that the inbuilt job splitter could be used to split the single respiratory period into distinct phases. To achieve an equivalent level of counts as the previous 3D studies, which are acquired over 600 s, the activity of the target and background was increased by the ratio of scan lengths i.e. a factor of 150 (600/4). Using the GATE job splitter, a single simulation covering 4 s of acquisition was split into separate simulations of 5, 10 or 20 individual files. Each macro file then corresponds to the total scan time, divided by the number of splits. Therefore, each data set produced corresponds to the data akin to that found in a particular phase of the respiratory cycle of a 4D-PET acquisition.

Table 5.3. Complete list of simulations with the XCAT phantom and GATE Monte Carlo platform.

Phantom No.	Max. Diaphragm Amplitude (cm)	Lesion diameter (mm)	Activity Ratios (lesion / background)	Simulation type
0	0	10, 20, 30	10:1, 5:1, 2:1	3D and 4D (5, 10 and 20 bins)
1	0.5	10, 20, 30	10:1, 5:1, 2:1	3D and 4D (5, 10 and 20 bins)
2	1.0	10, 20, 30	10:1, 5:1, 2:1	3D and 4D (5, 10 and 20 bins)
3	2.0	10, 20, 30	10:1, 5:1, 2:1	3D and 4D (5, 10 and 20 bins)
4	3.0	10, 20, 30	10:1, 5:1, 2:1	3D and 4D (5, 10 and 20 bins)

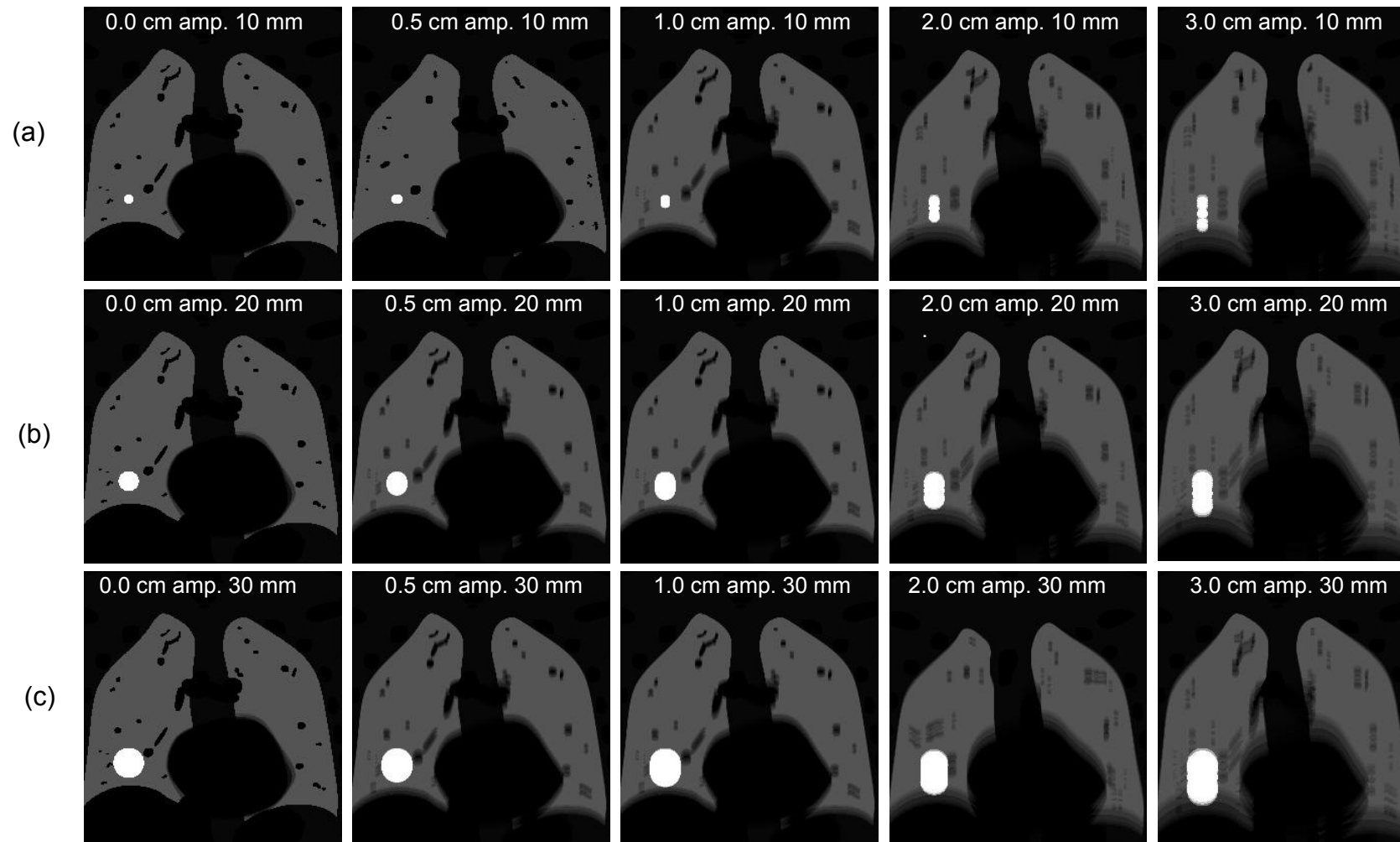


Figure 5.5. XCAT phantoms generated for use in the GATE Monte Carlo simulations, showing a (a) **10 mm**, (b) **20 mm** and (c) **30 mm** diameter lesion residing in the lower right lung with a **10:1 activity ratio**. The phantom's diaphragmatic amplitude was varied from 0 to 3.0 cm. Note: the motion in GATE occurs in real-time, and depictions of the motion shown in these images are used to indicate the magnitudes of lesion motion that were set using the XCAT phantom and therefore, the motion that occurred during the Monte Carlo PET simulations.

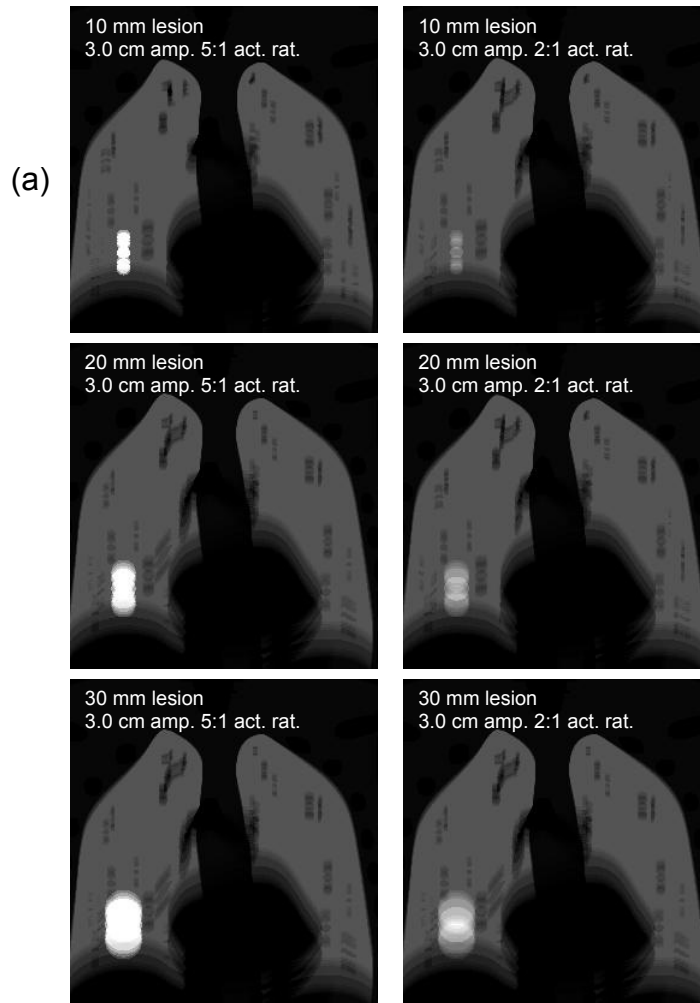


Figure 5.6. XCAT generated phantoms used in Monte Carlo GATE simulations. Activity ratios of 5:1 and 2:1 (lesion:background) respectively are shown. Here phantoms with the diaphragm amplitude set to 3.0 cm are shown, as stated previously, the motion is in real-time during the Monte Carlo simulation and these average intensity phantoms are shown for display purposes only to highlight the degree of motion that was assigned to the phantoms. The complete list of XCAT phantoms created for use with GATE is shown in Table 5.3.

5.4.2.6 Data output

Each PET simulation in GATE results in a ‘.root’ file. ROOT is an object oriented framework written in C++ which provides all the functionality needed to handle and analyse large amounts of data in an efficient manner. ROOT allows histogramming, curve fitting, graphics and visualisation classes and function evaluation to be performed in batch mode or parallel processing environments. The ROOT files output from GATE contain the complete history of every particle (primary and secondary) generated during the course of a simulation. The GATE system creates the complete list of singles (annihilation photon hits), false positive coincidences and true coincidences.

5.5. RESULTS

5.5.1. Experimental results

Figure 5.7 shows the apparent activity for the reservoirs displayed in Figure 5.1 scanned in both 3D (top row) and 4D modes. In 3D mode, the blurring of the apparent activity of each reservoir is evident as the amplitude of motion increases. For the largest amplitude, Figure 5.7 (c), the impact of the motion profile can also be seen, with the ‘dumbbell’ shape occurring as the phantom spends more time at peak exhale and inhale (sinusoidal motion).

Figure 5.7 (bottom row) demonstrates the reduction in motion blurring that can be achieved using 4D scanning techniques. A single phase-bin of data allows a closer approximation of the true lesion size to be ascertained even for large amplitude motions and smaller lesions. Figure 5.8 shows a 4 cm displacement split into ten phases. At the inter-maxima / minima phases, the blurring of the 5 and 10 mm diameter lesions can be seen to increase due to residual motion associated with an increased target velocity coupled with partial volume effects.

Figure 5.9 (a) shows the effect of lesion motion and size on the reduction in A_{\max} recorded. The apparent A_{\max} can be seen to decrease with increasing amplitude irrespective of the lesion size. The differences in A_{\max} for different lesion sizes with no motion is attributed to the partial volume effect, which is known to be more severe for smaller lesions (Soret, Bacharach *et al.*, 2007). Figure 5.9 (b) shows the A_{\max} recorded using 4D-PET. Figure 5.9 (c) shows the increase in the apparent volume of a lesion if 3D scanning is used. Figure 5.9 (d) shows the degree of true lesion volume recovered when 4D scanning is used. Figure 5.10 shows the impact of various respiration rates on the A_{\max} reported. Changing the respiration rate can be seen to have little effect with the determination of the A_{\max} for each respiration rate showing little variation.

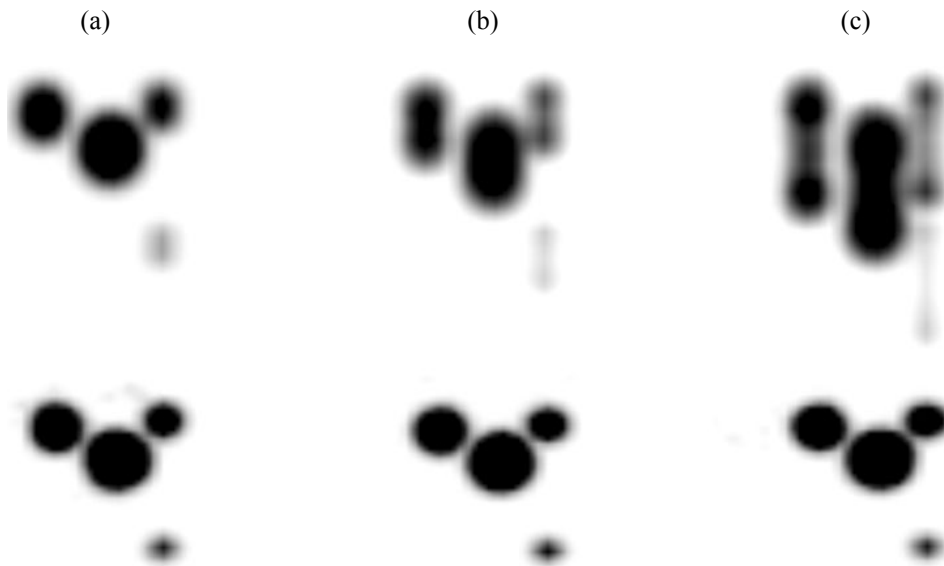


Figure 5.7. 3D (top row) and 4D (bottom row) PET images of (a) a 15 RPM 1cm motion, (b) a 15 RPM 2 cm motion and (c) a 15 RPM 4.0 cm motion. Data from the 1st phase bin was taken for the 4D data.



Figure 5.8. 4 cm of displacement split into ten phase-bins.

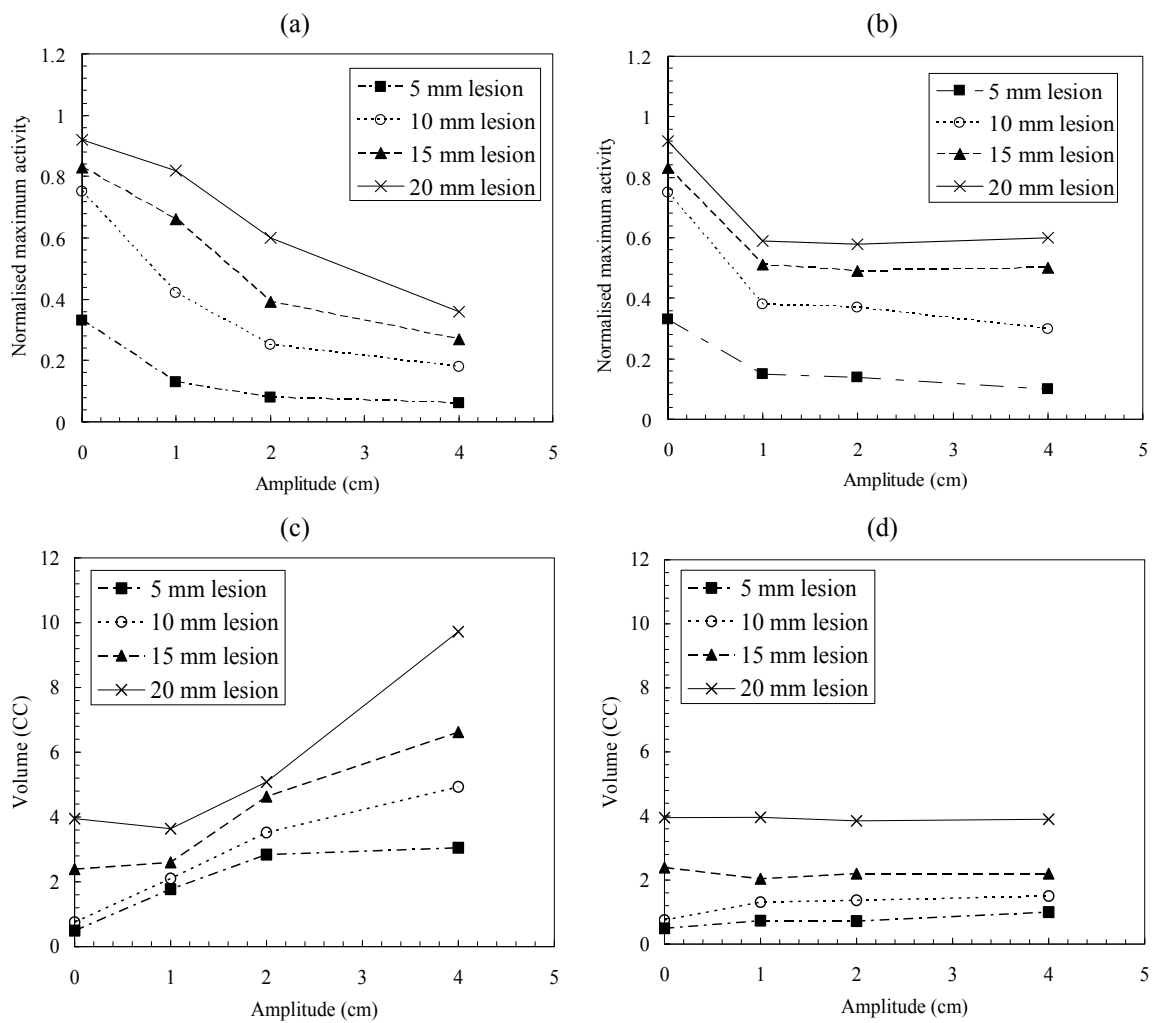


Figure 5.9. (a) Apparent lesion maximum activity normalised to the injected activity concentration as a function of motion displacement and lesion size for a 3D scan. (b) The activity recorded through a 4D acquisition. (c) Volume overestimation as a function of lesion size and amplitude for a 3D scan. (d) Volume recovery with a 4D scan.

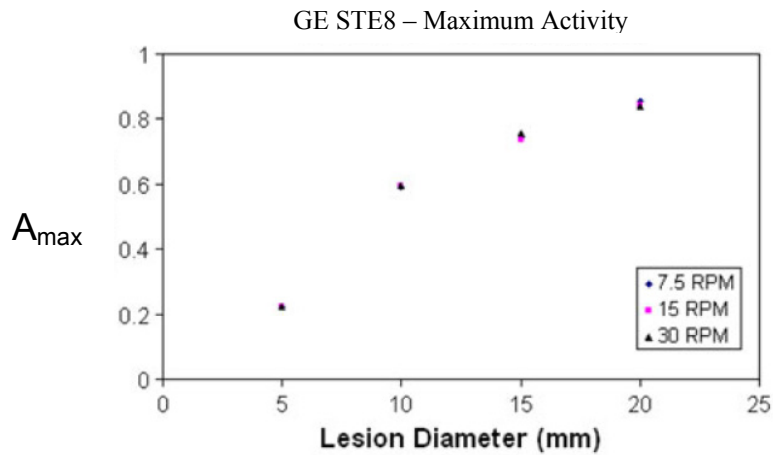


Figure 5.10. The impact of the motion frequency rate on activity, A_{max} , normalised to the injected activity concentration, for three motion frequencies (2 cm motion amplitude).

5.5.2. Monte Carlo and XCAT simulations

The impact of motion in PET images incorporating anthropomorphic geometry, and the inclusion of lung background activity, was systematically investigated using both the XCAT phantom and the GATE Monte Carlo package for Geant4. The method of this investigation is outlined in Section 5.4.2. Table 5.3 outlines the complete list of simulations that were carried out. Data presented in this section is in the form of activity distribution images and line profiles through the centre of the lesion in the direction of motion (SI). Figure 5.11 shows activity distribution images for a 30 mm tumour located in the lower right lung influenced by respiratory motion. The first image in this series, Figure 5.11 (a) shows the activity distribution of a static 30 mm diameter tumour. The tumour's activity was set to 10 kBq with the lung background activity set to 1 kBq. Figure 5.11 (f) indicates the reduction in maximum activity over a line profile through the centre of the lesion along the dashed line shown in the panels (a) – (e). The width of these profiles indicates the increase in apparent lesion size. Figure 5.11 (g) shows 3D isosurface representations with isosurfaces at 0.1 %, 20% and 60 % of the maximum activity. Figure 5.13 shows similar data for a 10 mm diameter lesion. Here, a static lesion and a lesion undergoing a 3.0 cm motion amplitude are shown. The differences between the experimental and Monte Carlo aspects of this work can be attributed to the anthropomorphic geometry, used in the Monte Carlo study as opposed to the phantom based experimental work.

5.5.2.1 3D-PET GATE activity distributions for a 10:1 (tumour:background) activity ratio

Figure 5.11 shows a typical set of data output from a GATE simulation using the XCAT phantom. In this sagittal slice taken through the centre of the lesion, the uptake hotspot of the 30 mm diameter lesion can be seen against the background of the lung. As the amplitude of motion increases, the reduction in the apparent activity can be seen in the line profiles (Figure 5.11 (f)). Each of these images has its colour scale maximum set to the maximum activity recorded in the stationary case. The colour bar for each image demonstrates the maximum reduction in apparent activity normalised to the stationary case for the 3.0 cm motion. This can also be seen in the line profiles, Figure 5.11 (f). Figure 5.12 shows 3D isosurface representations of a static 30 mm diameter lesion and a lesion moving with 3.0 cm motion amplitude.

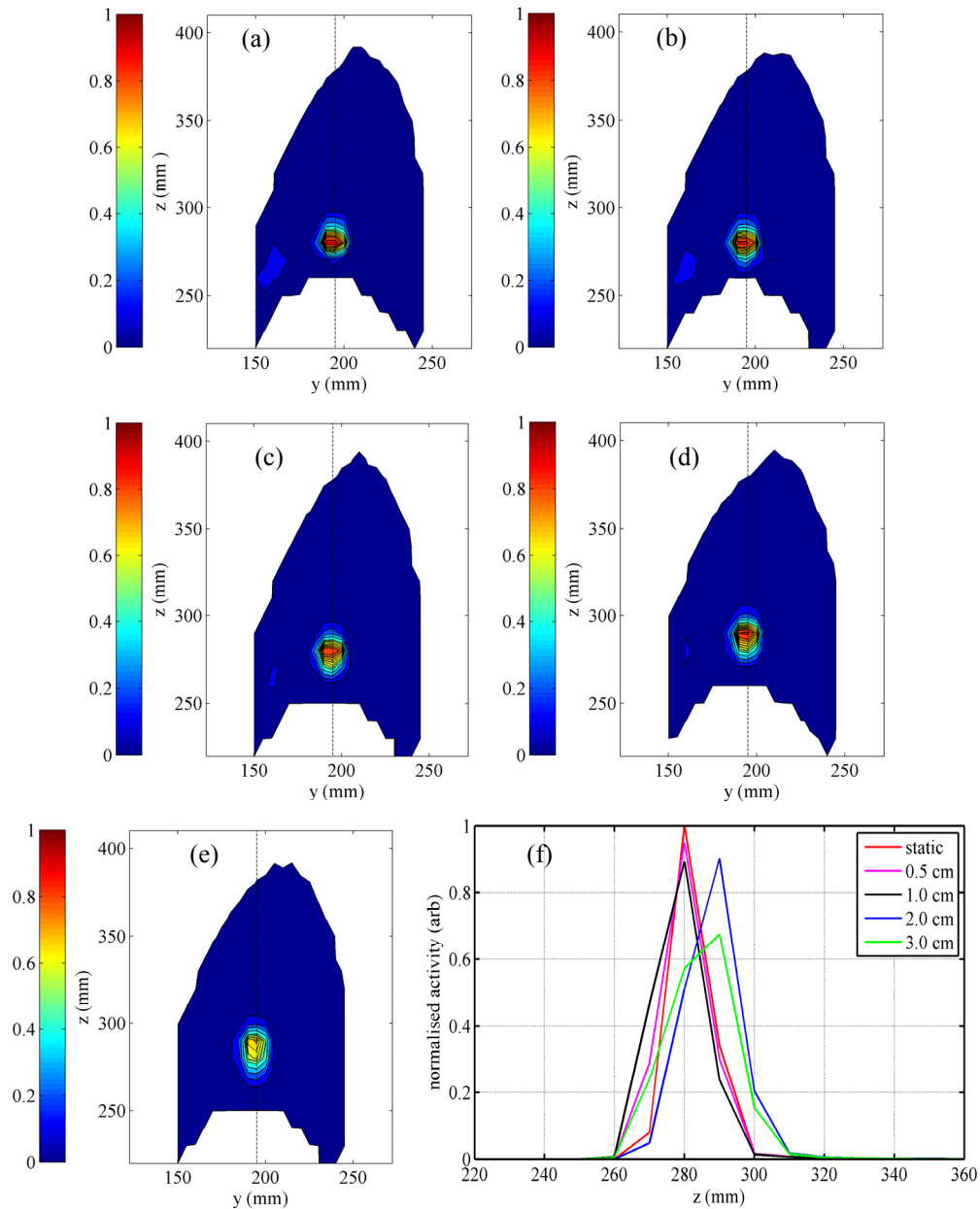


Figure 5.11. Sagittal activity distributions for a 30 mm diameter tumour moving in the SI direction with a sinusoidal motion profile. The tumour's activity was set to 10 kBq, with the background of the lungs set to 1 kBq. (a) Static 30 mm diameter tumour, (b) 0.5 cm amplitude, (c) 1.0 cm amplitude, (d) 2.0 cm amplitude and (e) a 3.0 cm amplitude. (f) Line profiles through the centre of the lesion as indicated by the vertical dashed line in (a) – (e). The colourbars show the normalised activity with respect to the stationary case. The coarseness of the resolution in these images arises from the 5 mm³ voxel size of the XCAT phantom.

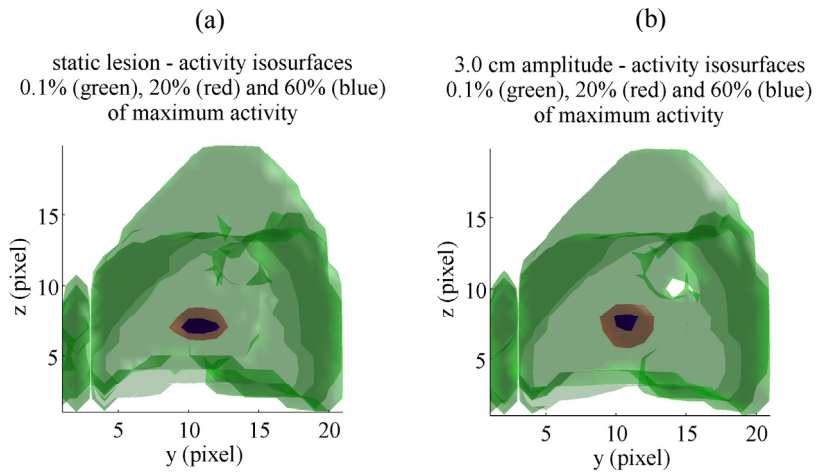


Figure 5.12. 3D isosurfaces of constant activity levels of 0.1 (green), 20 (red) and 60 % (blue) of the maximum activity demonstrating the increase in apparent lesion size. (a) Static 30 mm lesion and (b) the same lesion with a 3.0 cm amplitude.

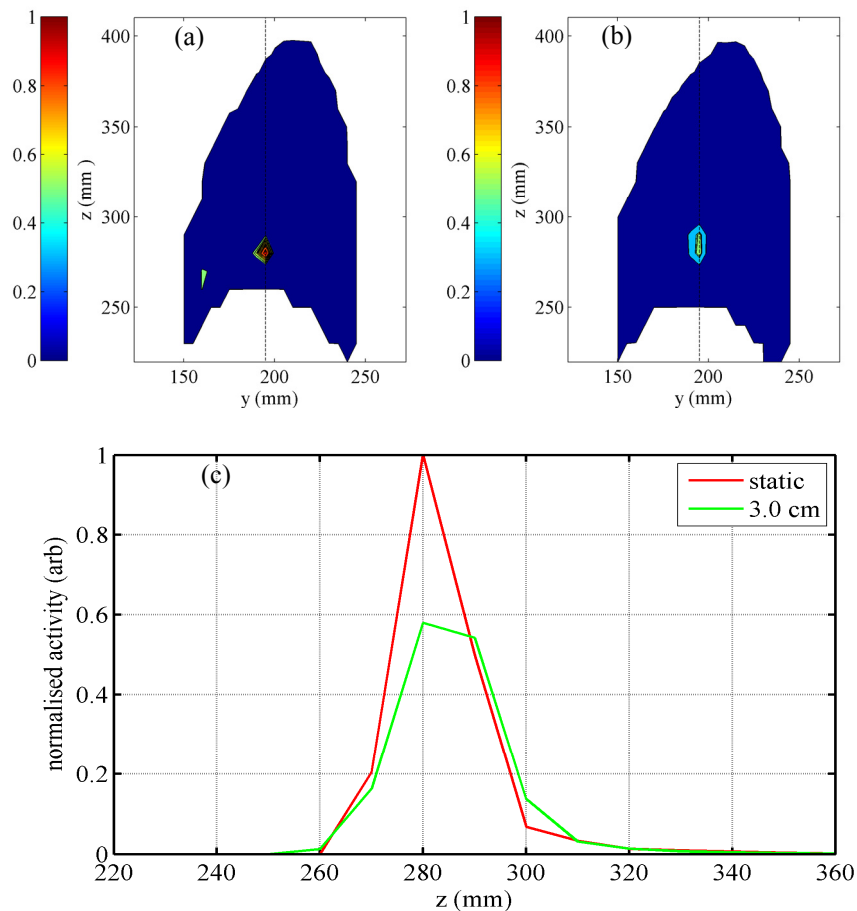


Figure 5.13. Sagittal activity distributions for a slice through the centre of a **10 mm** diameter tumour moving in the SI direction with a sinusoidal motion profile. The tumour's activity was set to 10 kBq, with the background of the lungs set to 1 kBq. (a) Static 10 mm diameter tumour, (b) 3.0 cm amplitude, (c) line profiles showing overestimation of lesion size and reduction in apparent activity. Note the colour bar scale in image (b) is normalised to the maximum activity found in the static case. The background activity of the lung can also be seen. Compared to the 30 mm lesion, the reduction in apparent activity is greater for a moving lesion of smaller dimensions.

Figure 5.14 shows line profiles for the Monte Carlo simulations. All cases with the lesion in motion show a reduction in activity for all lesion sizes and activity ratios simulated. The largest recorded reduction in apparent activity was found to be 42 % for a 10 mm lesion moving with an amplitude of 3.0 cm. In comparison to the experimental results presented in Figure 5.9 (a), the degree of apparent activity reduction is, on average, lower. However, both methods showed a strongly correlated reduction in activity associated with increasing lesion motion. For activity ratios of 10:1 and 5:1, the 10 mm lesion suffered a greater reduction in activity compared to the 20 and 30 mm lesion, respectively.

Interestingly, for a 2:1 activity ratio, the increased lung activity results in increased activity ‘spill-over’ into the tumour from partial volume effects which negates some of the reduction in apparent activity as a result of motion. This is evident in the fact that for a 2:1 activity ratio, the 10 mm lesion is affected the least, compared to the 20 and 30 mm lesions respectively. The ‘spilling-in’ of activity from lung regions surrounding the lesion makes the smaller lesions appear more aggressive than they are (Soret, Bacharach *et al.*, 2007) which in turn will cause one to think that there may be more viable tumor tissue within the tumor center than there really is and appears to offset the reduction in apparent activity due to motion. This effect is illustrated below in Figure 5.15 taken from (Soret, Bacharach *et al.*, 2007).

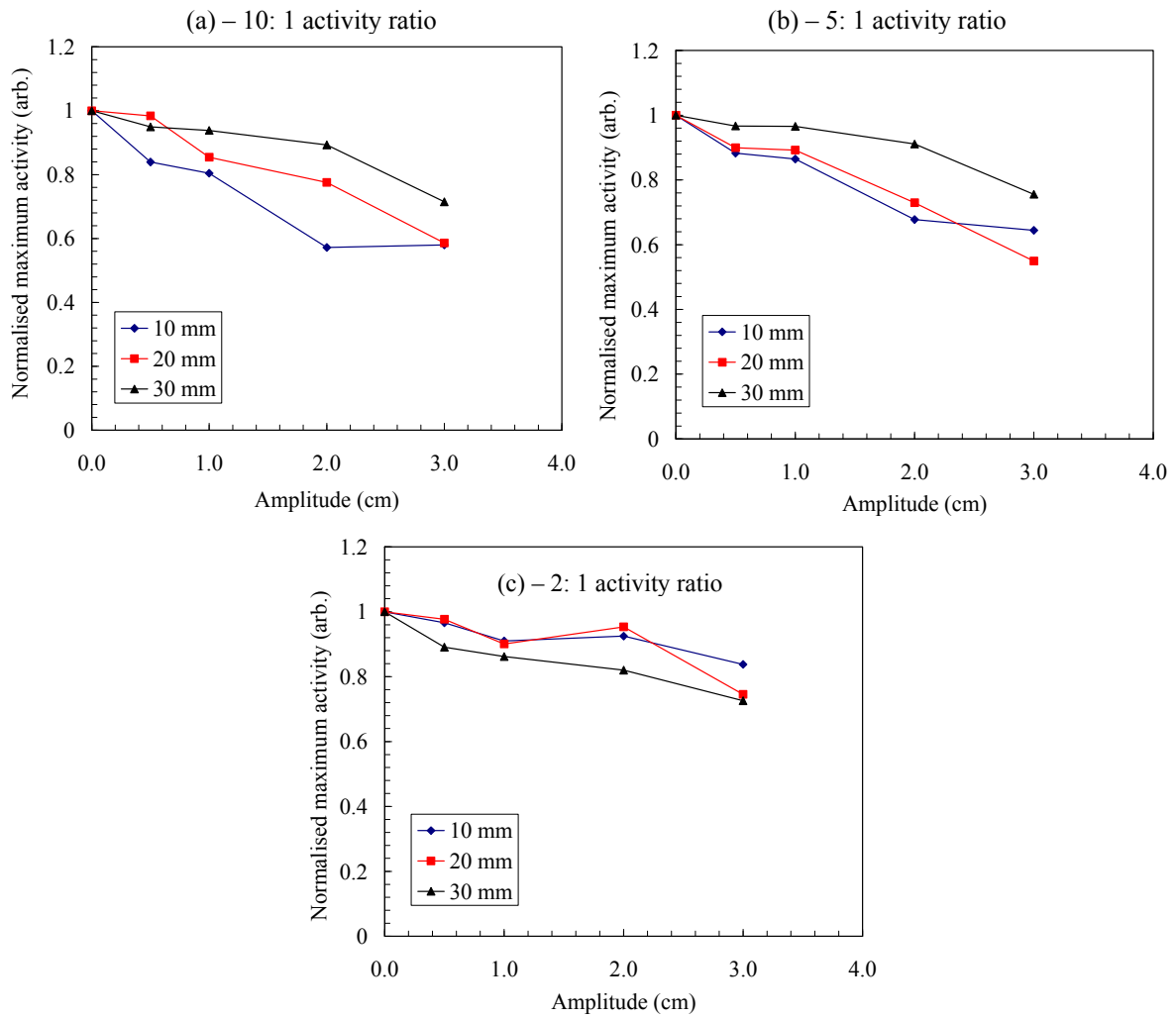


Figure 5.14. PET scans simulated with the GATE system using the XCAT phantom as the source. A consistent reduction in the apparent activity can be seen for all activity ratios as the amplitude increased beyond 1 cm. (a) Reduction in maximum activity across a line-profile through the centre of the lesion for a 10:1 activity ratio, (b) 5:1 activity ratio and (c) 2:1 activity ratio.

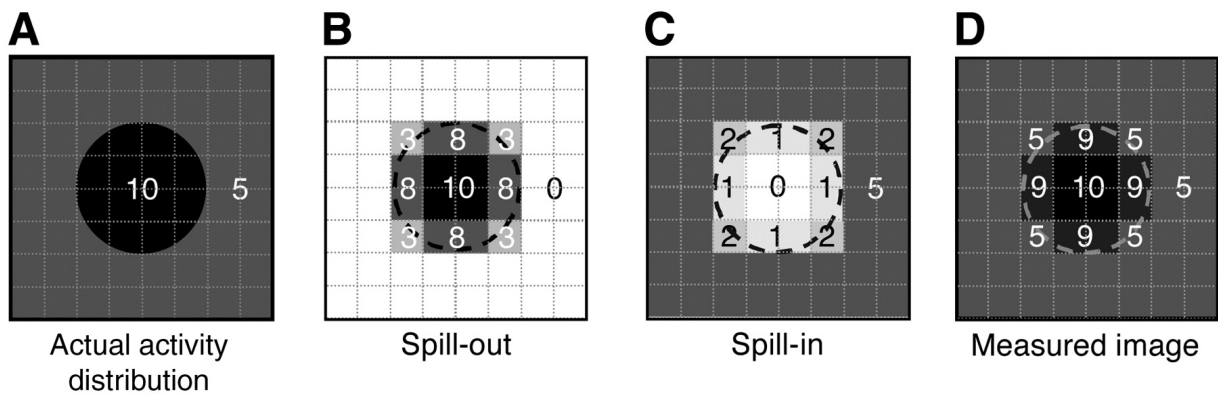


Figure 5.15. Illustration of 'spill-in', 'spill-out' effects taken from (Soret, Bacharach *et al.*, 2007). The measured image (D) of the true activity distribution (A) is the result of the sum of the spill-out (B) and spill-in (C).

5.5.2.2 4D simulations for a 10:1 activity ratio and 10 mm lesion size.

Phase-bin line-profiles through the centre of lesion for 4D simulations are shown in Figure 5.16 - Figure 5.18. The reduction in counts increases the noise of a real 4D simulation, and as such the 4D data is often acquired over an extended period of time. Figure 5.16 shows five phase-bin data sets of a 10 mm diameter lesion with an activity 10 kBq (10:1, lesion:background). The diaphragm extension in the XCAT phantom input data was set to 3.0 cm with a 4 s respiratory period. With five phase-bins a representation of the tumour's excursion over a complete respiratory cycle can be acquired. Figure 5.17 shows the same data using ten phase-bins. With ten phase-bins, there is increased information about the position of the lesion over a respiratory cycle with some residual blurring occurring at phases where the velocity of the lesion is at a maximum. The residual blurring results in a 7 % (approximate) reduction in apparent activity compared to the maximum inhale / exhale phases. Figure 5.18 shows the same data with 20 phase-bins. Using greater than ten phase-bins is not recommended as there is an increase in noise in the phase-bin data due to the reduction in counts per phase-bin. This is illustrated in Figure 5.18. If the volume of the lesion was to be delineated on the 0% phase-bin, the lesion would appear larger than in the 3D case.

It must be noted that the partial volume effect associated with the small lesion size (10 mm) causes the lesion to appear larger than in reality due to increased activity spill-over into the surrounding. These effects have previously been characterised by (Soret, Bacharach *et al.*, 2007).

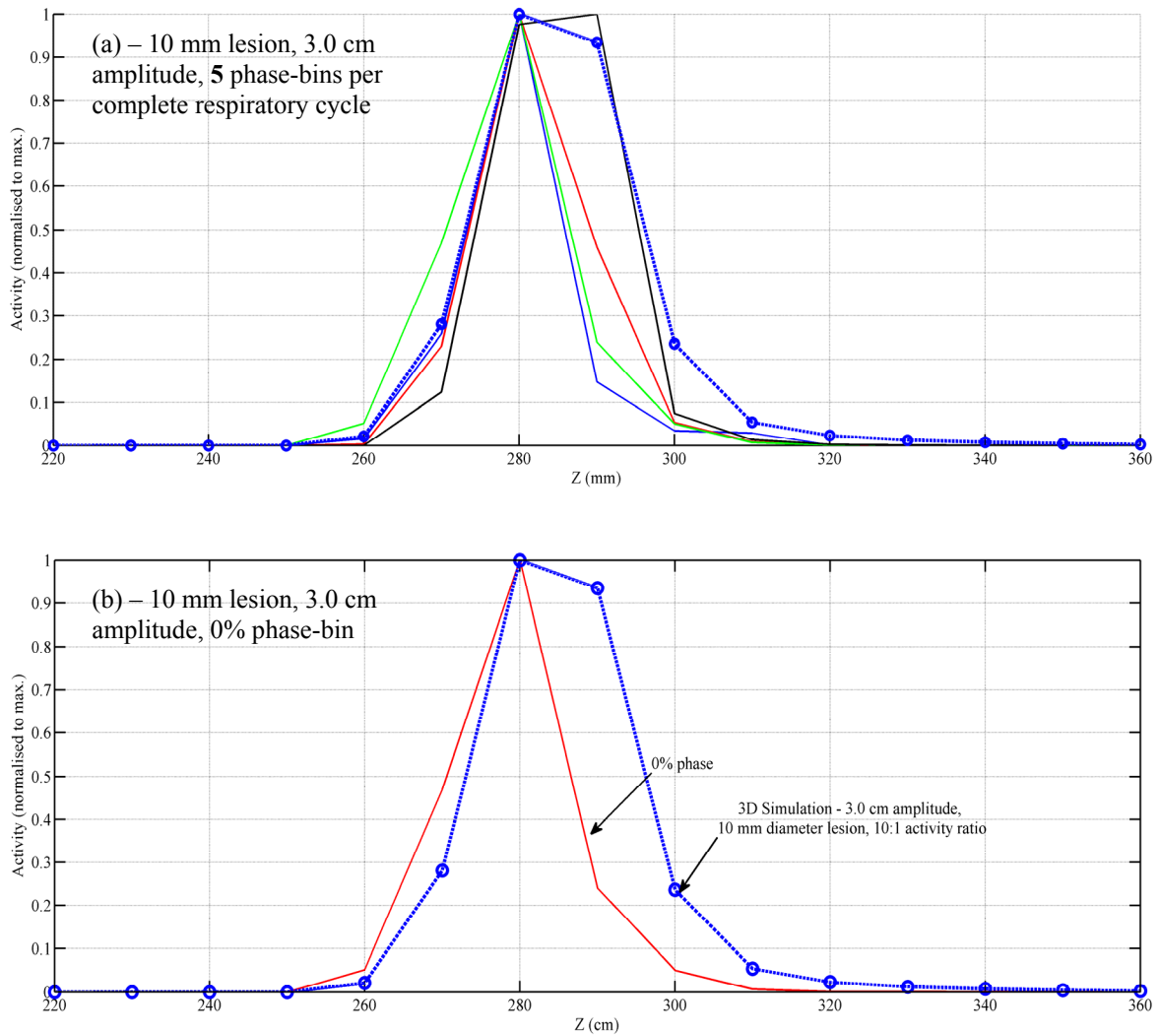


Figure 5.16. Line profiles through the centre of a 10 mm diameter lesion over 5 phase-bins from a 4D PET simulation. The 3D line profile is shown with a blue dashed line and circle markers. The displacement of the diaphragm was set to 3.0 cm with a 4 s respiratory period and the lesion's activity set to 10 kBq with the lung background at 1 kBq. (a) All phase-bin and 3D simulation line profiles superimposed, (b) the 0% phase-bin from 4D-PET compared with the 3D simulation.

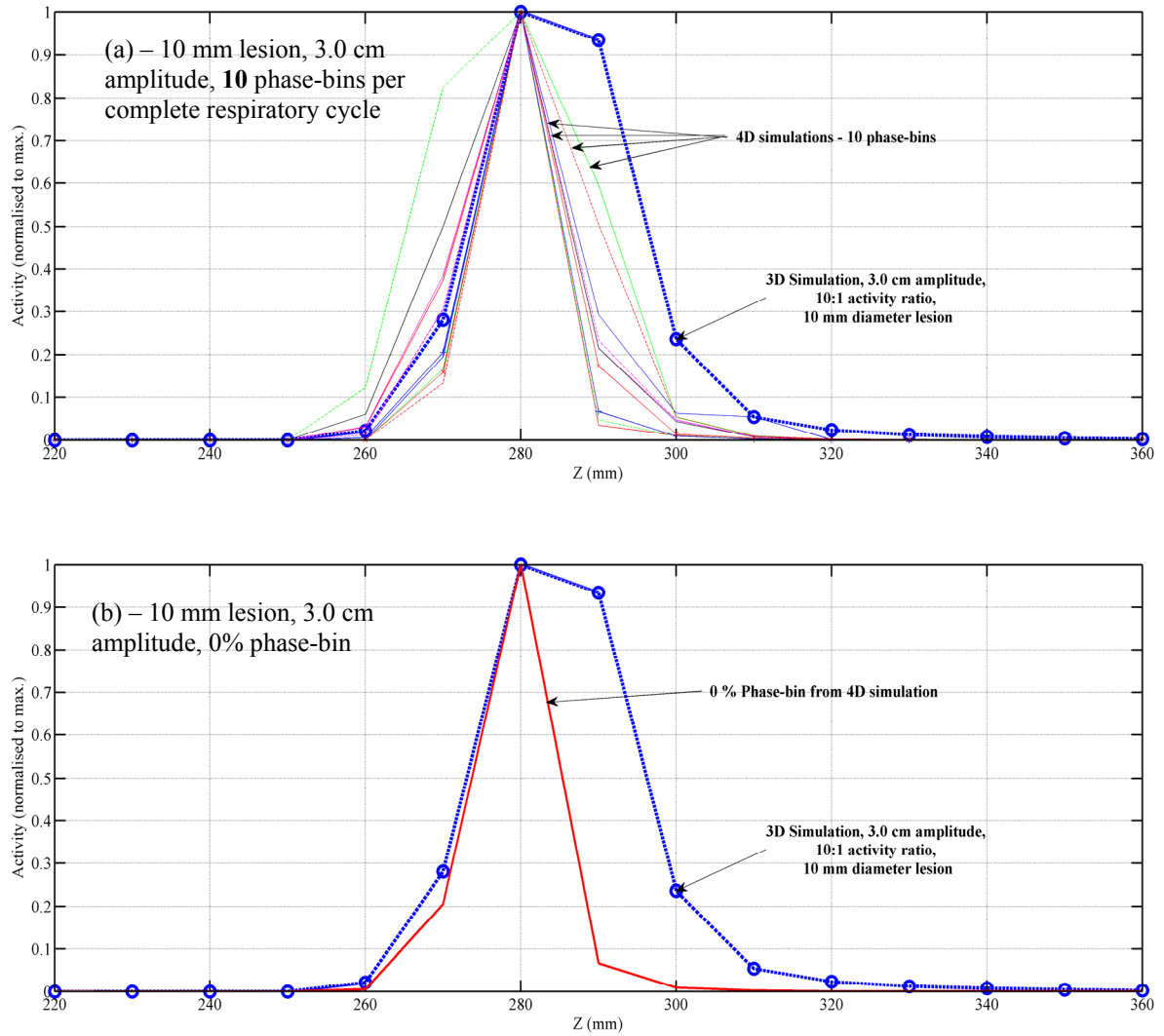


Figure 5.17. Line profiles through the centre of a 10 mm diameter lesion over 10 phase-bins from a 4D PET simulation. The 3D line profile is shown with a blue dashed line and circle markers. The displacement of the diaphragm was set to 3.0 cm with a 4 s respiratory period and 10:1 activity ratio. (a) All phase-bin line profiles superimposed, (b) the 0% phase-bin from 4D-PET compared with the 3D simulation.

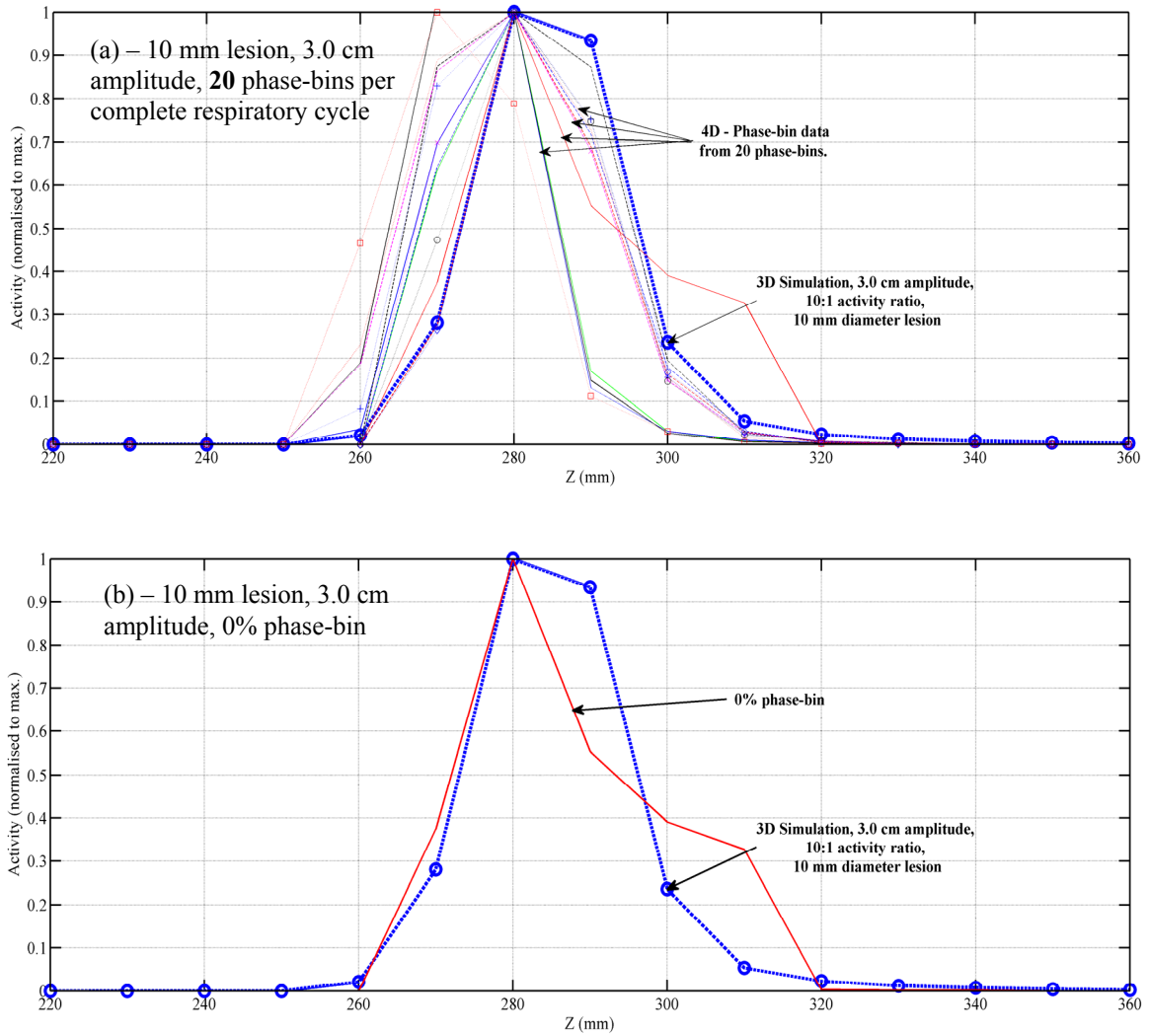


Figure 5.18. Line profiles through the centre of a 10 mm diameter lesion over **20** phase-bins from a 4D PET simulation. The 3D line profile is shown with a blue dashed line and circle markers. The displacement of the diaphragm was set to 3.0 cm with a 4 s respiratory period and 10:1 activity ratio. (a) All phase-bin line profiles superimposed, (b) the 0% phase-bin from 4D-PET compared with the 3D simulation. With 20 phase bins, there is a considerable increase in noise due to the reduction in counts per phase-bin.

5.6. DISCUSSION

5.6.1. *Experimental phantom study*

In the experimental work presented in this chapter, the upgraded QUASAR phantom (Section 3.3) was utilised to observe a relationship between the degree of lesion displacement and Standardised Uptake Value (SUV). 4D PET was then implemented to determine the degree of SUV restoration and true lesion volume recovery. The results, shown in Figure 5.9 demonstrated that with increasing lesion excursion the SUV_{max} and SUV_{mean} decreased and the volume increased. Using un-gated 3D scanning there was a clear correlation between a lesion's apparent size and the magnitude of motion. For a 4 cm amplitude motion there was up to a seven-fold increase in the measured volumes of lesions compared to the baseline. Across all lesion sizes and displacements, gated scans completely restored the volume overestimation as compared to the static case.

There was also a clear correlation between increased lesion motion and a loss of SUV on the un-gated scans when compared to the baseline static case. The smaller lesions (5 and 10 mm) showed a greater drop in SUV_{max} at the highest displacement when compared to larger lesions, 15 and 20 mm diameters, respectively.

The study showed that by using 4D imaging, the SUV_{max} , SUV_{mean} and volume were mostly recovered regardless of the amount of lesion displacement. In the experimental portion of this work, it has been shown that given the significant loss in SUV signal observed in moving lesions it will be difficult to use absolute SUV as a determinant of malignancy in lung cancer. This would be seen to complicate attempts to auto contour lesions based on a percentage of SUV_{max} or a fixed SUV threshold. Respiratory Gated PET scanning was shown to improve the recovery of the SUV_{max} and reduce the distortion in lesion volume associated with motion. Furthermore, changes in SUV between two scans are used to indicate changes in tumour metabolism. A difference in motion amplitude due to a change in breathing pattern / depth could mimic changes in metabolism. 4D-PET is therefore recommended where lesion motion is in excess of 1 cm.

5.6.2. *Computational simulations to determine the effect of motion on images acquired with PET*

In this work, Monte Carlo simulations were utilised to systematically evaluate the effect of motion on images acquired with PET. The results are shown in Section 5.5.2.

5.6.3. Simulation results: GATE 3D PET Simulations

Over all amplitudes and tumour sizes simulated, there was a decrease in the maximum activity found over a line profile of the tumour that increased with amplitude. Examples of saggittal activity distribution images for a 30 mm diameter lesion undergoing respiration induced motion are shown in Figure 5.11. The activity distribution correspond to a 600 s PET acquisition of moving XCAT 3D phantoms with lesions of varying diameter in the lower right lung. In this scenario the tumour's activity was set to 10 kBq with the background lung activity set to 1 kBq. The lesion is visible over all amplitudes with distinct blurring for diaphragm displacements greater than 2.0 cm. Figure 5.14 shows a measurable motion related reduction in apparent activity can be seen for diaphragm amplitudes greater than 1.0 cm. A summary of the results obtained is presented in Table 5.4. From Table 5.4 it can be seen that there is a consistent reduction in activity as the lesion's motion amplitude is increased. The largest reduction of which occurred of this reduction was on, average largest for the 10 mm lesion 16.6 % over all amplitudes and activities (lesion and background) simulated. On average, the 20 and 30 mm lesions suffered a 14.4 % and 10.7 % reduction respectively, over all amplitudes and activity ratios simulated.

Table 5.4. Summary of the 3D PET MC results as a function of lesion size, amplitude, and activity ratio with respect to the background.

Lesion Diameter (cm)	Amplitude (cm)	Reduction in activity relative to static case (%) 10:1, 5:1, 2:1		
		10:1	5:1	2:1
1.0	0.5	16	12	3
-	1.0	20	14	9
-	2.0	43	32	8
-	3.0	42	36	16
-2.0	0.5	2	10	2
-	1.0	15	11	10
-	2.0	23	27	5
-	3.0	41	45	25
3.0	0.5	5	3	11
-	1.0	6	4	14
-	2.0	11	9	18
-	3.0	29	24	27

For smaller lesions, the partial volume effect is exacerbated where even for a static case, the lesion will appear larger and of lower activity than it really is. The partial volume effect strongly depends on the size of the tumor. The smaller the lesion, the greater the underestimation of the uptake. As a result of this, different size tumors with the same uptake value yield tumor images with different degrees of brightness and hence different estimated uptake values. This effect is compounded even further when a small lesion is undergoing a large displacement and suffers motion related activity smearing along with increased partial volume effects.

‘Spill-out’ effects, where activity spills out from the lesion to the surrounding tissue and ‘spill-in’ effects, where activity spills in from surrounding tissues could be seen as both the size of the lesion and activity of the lung were varied. Spilling in of the activity increased as the background activity of the lung increased falsely negating some of the activity lost through motion related smearing.

5.6.4. Simulation Results: GATE 4D-PET simulations

At present, the GATE platform does not allow for 4D simulations to be performed. However, one can simulate a 4D acquisition in the following manner. If the respiratory period of the XCAT phantom is 4 s then one can simply set the total simulation time to 4 s. The *jobsplitter* in GATE can then be used to set the number of phase-bins, each corresponding to a particular portion of the phantom’s anatomical state over a complete respiratory cycle. This obviously requires the lesion and background activities to be increased. The factor to be applied is dependent on the total time difference between a full and ‘gated’ simulation (T_f and T_G respectively). For example, the original simulations here had a total scan time of 600 s with the lesion’s activity set to 10 kBq and the background activity set to 1 kBq. To ensure the same number of counts in the gated simulation, the lesion and background activities must be increased by a factor of $T_f / T_G = 600/4 = 150$. The *jobsplitter* can then for example set 5 jobs to be assigned, this means that the first job covers the respiratory cycle time 0 – 0.8 s, the second job 0.8 – 1.6 and so forth. This is the method by which gating was simulated in these experiments and to the author’s knowledge has not been described before.

4D simulations for a 20 mm lesion (3.0 cm diaphragm displacement), with an activity ratio of 10:1 (lesion:background) are shown in Figure 5.16 - Figure 5.18. With a high activity ratio between the lesion and the background it is possible to increase the number of phase-bins, however, lower activity ratios require an increased scan time or smaller number of bins. For 5, 10 and 20 phase-bins, this work demonstrates that motion related artifacts can be mitigated with the use of gating. For most clinical applications, 5 – 10 phase bins are sufficient to capture the spatio-temporal data needed to inform decisions without overly increasing the scan time.

5.6.5. Limitations and future direction for the use of Monte Carlo and computational phantoms

A limitation of the work pertaining to the use of the XCAT phantom in conjunction with the GATE platform is the large computational resources required. A voxel size of 5 mm³ for the XCAT phantoms was chosen to provide a balance between computational resources and the current capabilities of the GATE platform. Further work would make use of the data already obtained here and repeat the simulations with reduced voxel dimensions. This work would determine what effect, if any, this has on the impact of motion on images acquired with PET.

5.6.6. Comparisons between results obtained via experimental and Monte Carlo methodologies

In the two methodologies (phantom study, Monte Carlo) used to assess the impact of motion on images obtained with PET there was a decrease of apparent activity associated with lesion motion and the smearing of the apparent activity distribution. An overall increase in apparent lesion size was also found that was strongly correlated to the lesion's amplitude of motion when using 3D scanning. Figure 5.19 shows a comparison in the reduction in activity as a function of lesion motion amplitude for the two methodologies with a 10 and 20 mm diameter lesion used for comparison. Differences between the data arise due to the varying investigation methodologies. The phantom experiment was conducted with no background activity and in a phantom geometry and the Monte Carlo simulation provided an accurate anatomical geometry with a lung background activity present. Overall, both methods show an associated decrease in apparent activity that is strongly correlated with increasing lesion motion amplitude though the magnitude is varied.

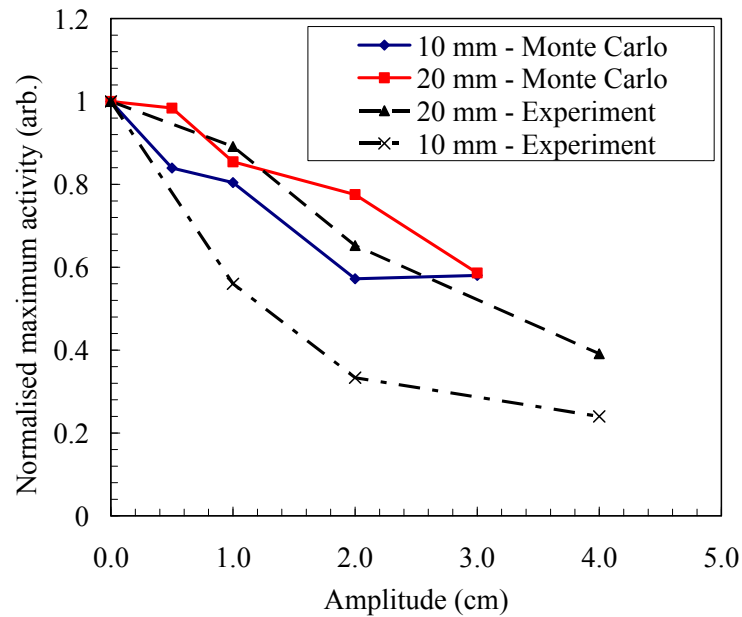


Figure 5.19. Comparison of the reduction in maximum activity measured as a function of lesion amplitude for the two methods. Lesions with diameters of 10 and 20 mm are shown with the lesion activity set to 10 kBq in the Monte Carlo simulations. Experimental, in phantom results showed the highest decrease in activity compared to Monte Carlo. Note that a 4 cm motion amplitude was not possible in the Monte Carlo simulation due to limitations in the XCAT phantom's motion simulation.

5.6.7. Comparisons to published data

It is understood that the apparent SUV of PET avid lesions residing in the lungs is reduced due to respiratory induced motion in a conventional PET scan (Nehmeh, Erdi *et al.*, 2002a, Nehmeh, Erdi *et al.*, 2004a, Nehmeh, Erdi *et al.*, 2003). In this study it has been shown via Monte Carlo methods, in conjunction with computational phantoms that the effect of motion on images acquired with both conventional and 4D PET is significant for small lesions typical of SBRT. Furthermore, the ability to accurately measure a small lesion's SUV is hampered by partial volume effects, which serve to make even a static lesion appear larger and cooler than it is in reality.

PET/CT is now emerging as a way to provide functional, as well as anatomical, localisation of lung lesions. In a large patient study ($n = 26$), Lupi *et al* (2009) investigated gated PET/CT and found that regardless of the gating method chosen, SUV showed a marked increase from a mean of 9.2 ± 6.9 in conventional PET to an average of 13.4 ± 11.7 over the gated studies. Their study concluded that in lung cancer, triggering procedures increase the signal to noise ratio, and that the increase in SUV determined by 4D-PET is very variable.

5.6.8. *Clinical consequences*

In this work it has been demonstrated that the effect of motion on PET images is to make a PET-avid lesion appear fainter and larger against the background. Respiratory motion tends to reduce the SUV and therefore has the potential to cause radiotherapy planning errors, affect the correct diagnoses of disease and impair staging of disease. Incorrect clinical analysis of malignancies and false lesion sizes also has an impact on therapeutic monitoring.

A number of studies have advocated SUV_{max} thresholds as a differentiator for benign and malignant lesions. Examples of this method have been reported in the literature where an SUV_{max} of less than 2.5 is used to differentiate between benign and malignant lesions in the lung (Garcia Vicente, Soriano Castrejon *et al.*, 2010, Hubner, Buonocore *et al.*, 1996). This work has shown that the SUV metric can break down due to motion related effects for small lesions undergoing large displacements. Therefore, an accurate measurement of SUV_{max} is often not possible. With 4D-PET and PET/CT however, consistently higher SUVs have been found upon the use of motion correction (Lupi, Zaroccolo *et al.*, 2009).

The results presented in this work demonstrate that when the effect of motion is combined with a small-sized lesion, which is also subject to a partial volume effect, then a lesion with uptake of a metabolic tracer can become falsely negative or falsely positive if the lesion includes a necrotic region, and activity ‘spill-in’ is prevalent. As PET is often used to assess tumour response to radiation therapy, SUVs based on pre and post treatment may be unreliable as a result of motion blurring. In the case of radiation therapy treatment planning, the contours of a lesion as seen on a PET image may encompass more than the real metabolically active part of the tumor due to the limited spatial resolution in PET images (~5 mm). In PET/CT, the fusion of the PET and CT images usually clearly shows this discrepancy between the tumor contours as displayed on the CT image and those on the PET image. However, the contours seen on the CT image may not delineate the metabolically active part of the lesion as CT does not show metabolically active tissue. Only high-resolution PET imaging provides an accurate delineation of the metabolically active part of the tumor. The results presented here also establish that the GATE platform can be used to simulate a 4D PET acquisition using the XCAT phantom and the *jobsplitter*. To the author’s knowledge, this has not been achieved prior to this work.

Chapter 6. The impact of motion:
Treatment planning and dose calculation

*“The first principle is that you must not fool yourself
and you are the easiest person to fool.”*

— Richard Phillips Feynman

6.1. INTRODUCTION

SBRT of the lung is not only complicated by motion, but also a direct calculation of dose is difficult due to the lack of electronic equilibrium (Section 2.9.1). In the context of radiotherapy of lung tumors, this may affect the minimum dose received by lesions and is particularly important when prescribing to covering isodoses. Furthermore, dose calculation in areas of heterogeneous density is a complicated process. In the context of lung cancer, the lack of electronic equilibrium at interfaces between the low density lung and tumour is known to cause an underdosage at the periphery of the lesion (Metcalf, Kron *et al.*, 2007).

Part 1 of this work evaluated the extent of underdosage to lung lesions using Monte Carlo radiation transport methods for a range of tumour sizes, field sizes and positions relative to the chest-wall. The degree of peripheral underdosage is shown to vary with positional parameters such as depth behind the chest-wall (due to secondary build-up effects). Therefore, the 2nd part of this study explicitly models the cumulative effect where motion changes this parameter. This method is akin to incorporating data from 4D-CT into dose calculation.

Poor image quality and mismanagement of motion can have detrimental consequences for treatment planning and delivery. At present, the incorporation of 4D information from 4D-CT into dose calculation is not facilitated in most treatment planning systems. As such, alternate methods such as a single dose calculation on an average intensity projection from 4D-CT (3D) are often pursued for dose calculation.

It is for this reason that the hypothesis of Part 2 of this work, was that performing dose calculation on an average intensity projection in multi-field SBRT does not result in clinically significant differences in dose, compared to accumulating dose on each individual phase data-set from 4D-CT.

Part 1 of this work is published in the manuscript entitled “*Determination of peripheral underdosage at the lung-tumor interface using Monte Carlo radiation transport calculations.*” in Medical Dosimetry (Taylor, Dunn *et al.*, 2011). The study was carried out using two Monte Carlo codes (EGSnrc & Geant4) to facilitate a more rigorous approach while at the same time comparing the two codes. The second part of this study addresses Objective 5: “*To evaluate dose calculation on lung tumours, in particular quantifying the differences between 4D calculations, which explicitly account for dynamic geometry, and conventional 3D calculation, based on AIP.*” This work is in preparation to be submitted for publication in Physics in Medicine and Biology.

6.2. BACKGROUND: INCORPORATION OF 4D INFORMATION INTO DOSE CALCULATION

This explicit incorporation of temporal information into treatment planning is termed 4D treatment planning (Keall, Siebers *et al.*, 2004, Keall, Joshi *et al.*, 2005, Keall, Joshi *et al.*, 2003, Keall, 2004b). The traditional method of dose calculation relies on the AIP from 4D-CT to determine the dose distribution to the ITV. This method is much less laborious planning wise as it involves a single dose calculation, whereas the 4D method involves contouring the lesion (GTV) and organs-at-risk in all phases from 4D-CT, performing dose calculation on each GTV, then registering and summing the respective dose distributions. Section 6.5.2 is dedicated to determining the equivalency of these two methods since they are both used in clinics today in multi-field SBRT treatments. In this Monte Carlo study, only dose calculation on the treatment volumes is performed. The influence of target motion direction, amplitude and motion profile (breathing pattern) on the equivalency between the two methods are each investigated as well as a confirmation of the expected breakdown in equivalency when contributions from a single beam only are examined.

Temporal variation in anatomy and tumour motion can introduce significant errors in imaging (Shepp, Hilal *et al.*, 1979, Tarver, Conces *et al.*, 1988, Shimizu, Shirato *et al.*, 2000), treatment planning (ICRU, 1999) and radiation delivery (Jiang, Pope *et al.*, 2003, Bortfeld, Jiang *et al.*, 2004). Carcinomas residing in the lung are particularly subject to movement due to respiration (Shirato, Seppenwoolde *et al.*, 2004, Keall, Mageras *et al.*, 2006b). Generally, without the use of motion management, uncertainties in target location and temporal motion can necessitate larger field margins and may result in target under-dosage or greater irradiation of healthy tissue.

Recent developments in imaging technology, such as Four-Dimensional Computed Tomography, (4D-CT) (Ford, Mageras *et al.*, 2003a, Vedam, Keall *et al.*, 2003b, Keall, Starkschall *et al.*, 2004) are becoming widely used in the treatment planning of radiotherapy for lung carcinoma. 4D-CT provides the means to reduce the breathing related artifacts associated with 3D-CT via correlation of the data-acquisition to a respiratory signal, as well as allowing the clinician to explicitly incorporate patient-specific respiratory motion into the treatment plan (Rietzel, Liu *et al.*, 2008b).

A particularly useful feature of 4D-CT is that it can be used to improve upon 3D images of tumour excursion used to delineate an ITV, by using projection data such as MIPs. By using the MIP from a 4D-CT data-set, a more accurate representation of the complete motion trajectory over a respiratory cycle can be achieved. The AIP is however still used for dose calculation since it more

accurately represents the probability density function of the tissue densities within the ITV.

With the advent of 4D-CT, the clinician now has the ability to create a ‘four-dimensional’ treatment plan (Antony, Carlson *et al.*, 2007, Esthappan, Santanam *et al.*, 2008, Guckenberger, Wilbert *et al.*, 2007, Rietzel, Chen *et al.*, 2005a). An example of a ‘four dimensional’ treatment plan would be to perform separate dose calculations on each individual phase data set obtained from a 4D-CT. In this work, combining the doses from individual phase data-sets is termed ‘U10V’ or Union of 10 Volumes. The U10V is formed by registering and adding the dose distributions on each respiratory phase data-set obtained by 4D-CT to form a composite, or ‘union’ of ten dose distributions but has the complication that the same tissue occupies different spatial voxels in different phases. The common less laborious *approximation* to the aforementioned method is a single dose calculation on an AIP, with the contouring derived from a MIP. In this work, this is termed ‘AVG’ and is equivalent to a 3D dose calculation.

Since 4D-CT is now the standard of care in treatment planning for SBRT of lung cancer (Benedict, Yenice *et al.*, 2010) and conventional radiotherapy (Senan, De Ruyscher *et al.*, 2004), clinicians can now explicitly incorporate 4D-CT data into the treatment plan by performing dose calculation on multiple breathing phase data sets, or calculating on a single data set, representing the average density, the AIP. The question naturally arises as to the equivalency of these approaches and the benefits of incorporating the additional information afforded by 4D-CT into the treatment plan, which is generally more time consuming. In this work, the aim was to determine whether dose calculation on an AIP is equivalent to accumulating and registering dose calculations on each individual phase of the breathing cycle when considering dose to the treatment volume. Monte Carlo simulation is used to systematically determine the degree of equivalency of these two methods with respect to motion amplitude, motion profile, single field versus multiple fields and the direction of tumour motion relative to the beam direction.

6.3. MATERIALS

Both Geant4 (Section 2.10.3.1) and EGSnrc (Section 2.10.3.5) were used to perform Monte Carlo simulation. Simulations were performed on the Victorian Partnership for Advanced Computing (VPAC) *tango* server with each simulation typically using four to ten processors (AMD, Barcelona 2.3 GHz quad core).

6.4. METHODS

6.4.1. METHOD I: Determination of peripheral underdosage at the lung-tumour interface using Monte Carlo radiation transport calculations.

In this work, Monte Carlo calculations using Geant4 (Section 2.10.3.1) are used to develop a set of data which could be routinely used by clinicians as a reference to determine errors in dose prediction that could occur due to limitations of treatment planning systems. Monte Carlo simulation facilitates greater accuracy in areas of heterogeneous density typically seen in lung cancer SBRT treatment planning. The aim of this work was to determine the extent of underdosage that exists at the periphery of a tumour relative to the centre, and to evaluate the dependence on a number of parameters. These parameters are outlined in Table 6.1.

Table 6.1. Systematic simulation parameters.

Variable	
Photon beam energy, E (MVp)	6 and 15
Field size, FS (mm ²)	30 x 30, 35 x 35, 40 x 40, 50 x 50 and 70 x 70
Tumour diameter, \varnothing (mm)	10, 16, 20, 30 and 50
Distance from chest-wall to tumour boundary d (mm)	5, 10, 20 and 40

The lung is lower in density than both the chest-wall and the tumour itself. To model this geometry in Geant4, a three-stage geometry was developed. This geometry is shown in Figure 6.1. The geometry consists of a polyenergetic photon beam incident on a region with the density of soft tissue ($\rho = 1.06 \text{ g/cm}^3$) representative of the chest-wall. A spherical tumour ($\rho = 1.00 \text{ g/cm}^3$) is located within a region of lung equivalent density ($\rho = 0.26 \text{ g/cm}^3$) directly adjacent to the preceding chest-wall region. The composition of these tissues is outlined in Table 6.2

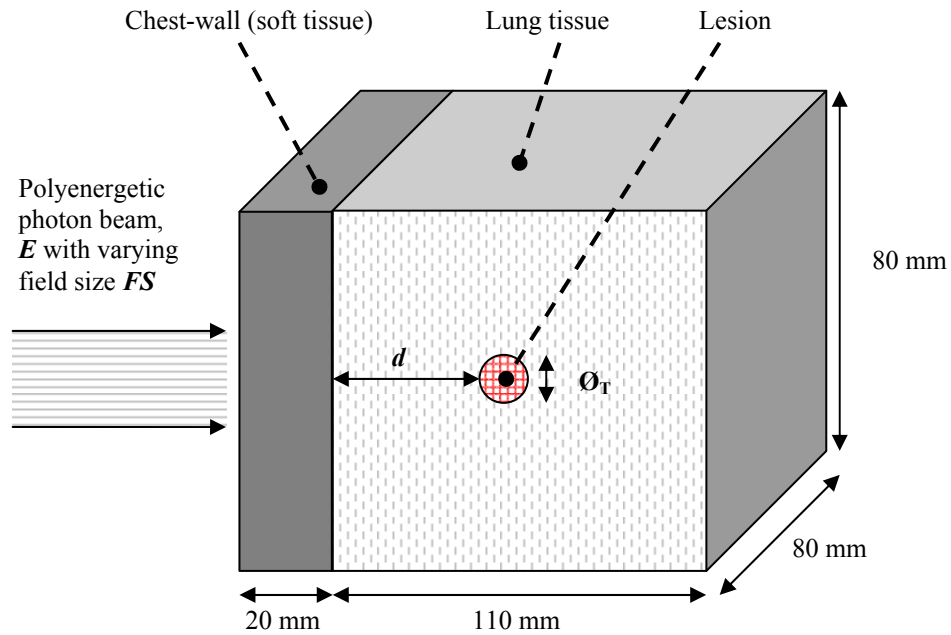


Figure 6.1. Monte Carlo geometry. A photon beam of energy E and field size FS is incident upon a region of tissue equivalent density representative of the chest-wall ($20 \times 80 \times 80 \text{ mm}^3$). The chest-wall is then followed by a region of lung equivalent density with dimensions ($110 \times 80 \times 80 \text{ mm}^3$). Inside the lung tissue region, a spherical lesion of diameter \varnothing is placed at a distance d from the chest-wall. The distances (d) and tumour size (\varnothing) are variable. The tumour's size determines the field size.

The scoring region of interest was the tumour itself. To facilitate the determination of the degree of underdosage of the shell relative to the centre, key spherical scoring voxels were implemented within the spherical tumour. A schematic of the key dose points is shown in Figure 6.2. The entrance, exit and lateral dose points were chosen as they experience different effects with respect to forward, backward and lateral scattering and electronic disequilibrium. The central dose was chosen as the underdosage of the periphery must be described relative to the centre. Although the central dose will also be affected by these effects to a lesser extent. 'Entrance' and 'exit' refer to the closest and furthest points on the tumour with respect to the source of the beam. 'Lateral' refers to the four lateral sides of the lesion, i.e. top, bottom, left and right of centre.

A parallel beam was chosen to remove inverse square effects related to isocentric configurations. Field sizes were chosen based on the tumour diameter and extend to 10 mm beyond the tumour boundary. Photon spectra for both 6 and 15 MV were simulated with data obtained from (Mohan, Chui *et al.*, 1985). These spectra are shown in Figure 6.3.

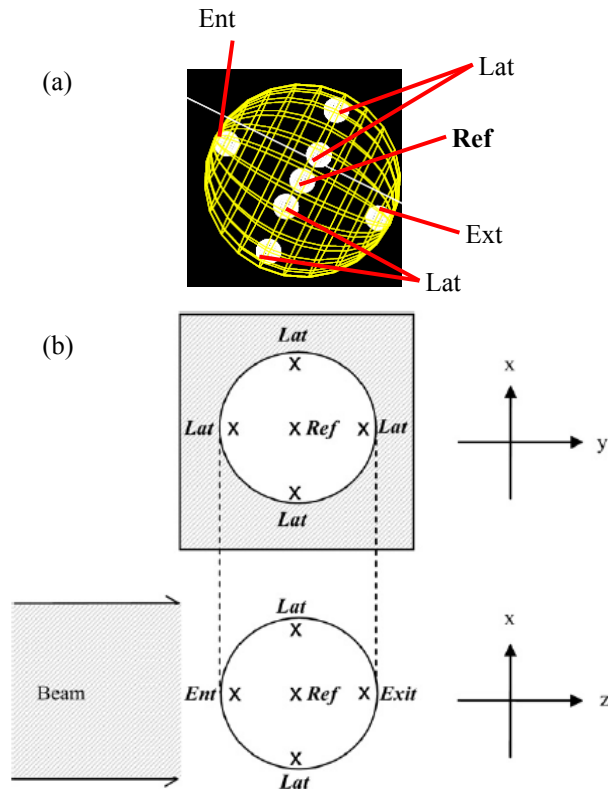


Figure 6.2. (a) The scoring geometry simulated with Geant4. The 1 mm diameter voxels; entrance (Ent), exit (Ext), Reference (Ref) and lateral dose points both vertical and horizontal (Lat) are shown. (b) A schematic of the key dose points indicating the regions of interest for scoring dose. The points are marked with a black X and the field in both views is indicated by a shaded region.

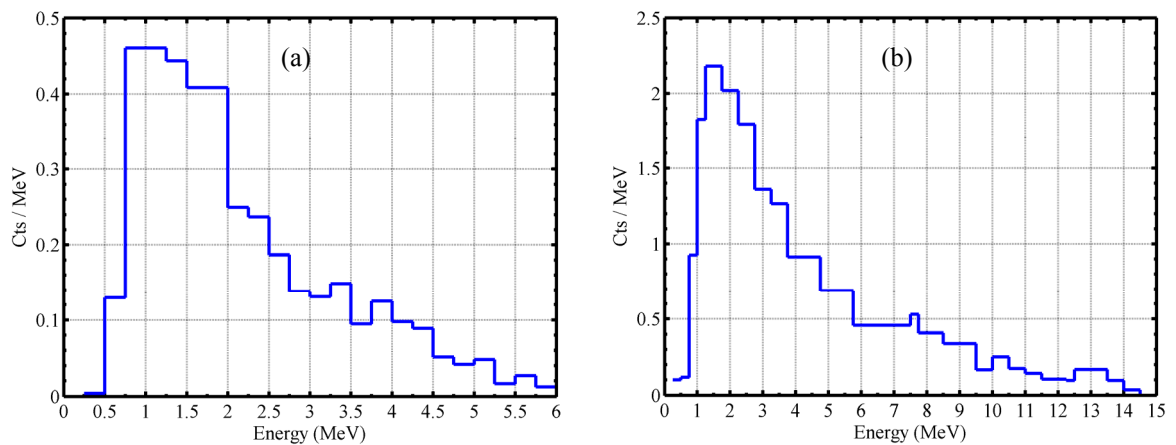


Figure 6.3. (a) 6 MV and (b) 15 MV photon spectrum from (Mohan, Chui *et al.*, 1985). This data was used as the photon spectra incident on the chest-wall as seen in Figure 6.1.

The tissue compositions and fractional elemental compositions used in the geometry are shown in Table 6.2. These tissue compositions, with the exception of the lung carcinoma, were obtained from ICRU Report 44 (Units, Measurements *et al.*, 1989). The density of lung carcinoma was set to that of water (1.00 g.cm⁻³) with its elemental composition obtained from combustion studies of excised squamous cell carcinoma reported by (Maughan, Chuba *et al.*, 1997).

Table 6.2. The density and elemental composition of the relevant tissues modeled in the study. Values are presented as percentage by weight. Lung carcinoma data was determined by combustion studies of excised squamous cell lung carcinoma reported by (Maughan, Chuba *et al.*, 1997). Soft tissue and lung tissue definitions were taken from ICRU Report 44 (Units, Measurements *et al.*, 1989).

Density / Elemental Comp.	Soft Tissue	Lung Tissue	Lung Carcinoma
ρ (g.cm ⁻³)	1.06	0.26	1.00
H	10.2	10.3	9.9
C	14.3	10.5	19
N	3.4	3.1	4.5
O	70.8	74.9	65.45
Na	0.2	0.2	0.1265
P	0.3	0.2	0.253
S	0.3	0.3	0.322
Cl	0.2	0.3	0.1955
K	0.3	0.2	0.253

The physics processes activated in Geant4 (version 4.9.4 *beta*) include Bremsstrahlung production, positron annihilation (both in flight and at rest), pair and triplet production, multiple scattering, Compton scattering, Rayleigh scattering, the photoelectric effect, Møller scattering, Bhabha scattering, continuous energy loss through discrete events, atomic relaxation and electron impact ionisation. The relevant physics models assigned above are described in Table 2.6 and Table 2.7. Production cut offs were set to 990 eV and 40 keV respectively for photons and electrons. These energy cut offs correspond to range cuts of 0.1 mm.

6.4.2. METHOD II: The incorporation of 4D information into dose calculation.

MATLAB (The Mathworks Inc., Natick, Massachusetts) was used to create 3D voxelised virtual phantoms as shown in Figure 6.4. The phantoms contain a chest-wall region (160 x 160 x 20 mm) of density 1.00 g/cm³ and a region of lung tissue (160 x 160 x 120 mm) with density equal to 0.25 g/cm³. A voxelised spherical ‘tumour’ (diameter = 40 mm) was also created and added to the primary matrix. The density of lung is known to change from 0.25 – 0.4 g/cm³ depending on both the respiratory state and the health of the patient’s lungs (Keall, Mageras *et al.*, 2006a). Normal

tumour density is around 1.00 g/cm^3 and with a lung density in the lower range, the maximum effect relating to the difference in density can be examined.

The entire composite geometry (lung + chest-wall + tumour) is divided into 1 mm^3 voxels. The location of the tumour with respect to the chest-wall was determined by a motion profile vector containing ten locations within the lung. These ten data-sets represent the phase-bin data sets obtained in a 4D-CT scan. An AIP was then created using the same method as 4D-CT by taking the voxel-by-voxel mean across all ten phase data-sets. The AIP therefore contains a mixture of densities between a minimum of lung and a maximum of the tumour density. The density profiles throughout the virtual phantom are therefore motion profile dependent and therefore are naturally weighted by the time the tumour spends at particular phases.

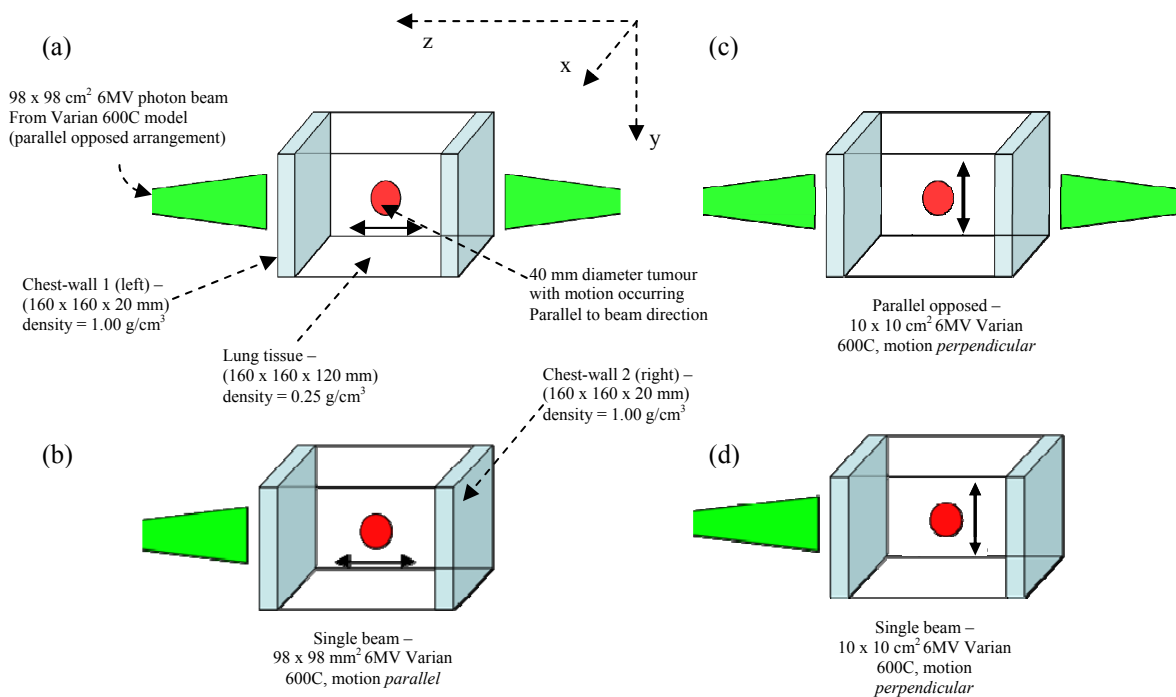


Figure 6.4. Beam, geometry and motion direction arrangements for the present study. (a) Geometry and beam arrangements showing a 40 mm diameter tumour in a region of lung equivalent density ($160 \times 160 \times 120 \text{ mm}^3$), a $10 \times 10 \text{ cm}^2$ field of 6MV photons is incident on a tissue equivalent region ($160 \times 160 \times 20 \text{ mm}^3$) with a parallel opposed beam arrangement, in this scenario, the tumour's motion is parallel to the beam direction. (b) A single field scenario with the tumour's motion again occurring parallel to the beam direction. (c) A parallel opposed arrangement with the tumour's motion occurring perpendicular to the beam direction and (d) a single field arrangement with the tumour motion occurring perpendicular to the beam direction.

The positions of the tumour at each phase within the virtual phantoms are assigned based on a position array. The position array's elements have a specific pattern based on breathing patterns commonly seen in patients. The breathing profiles are described below and examples are shown in

Figure 6.5. The time axes is shown, however, it is arbitrary as only one full respiratory cycle is used to assign the tumour's location within the lung.

1. Motion 1 (sinusoidal): Inspiration period = expiration period.
2. Motion 2 (Asymmetric): Inspiration period < expiration period.
3. Motion 3 (Asymmetric): Inspiration period > expiration period.
4. Motion 4 (Asymmetric): Inspiration period = expiration period followed by a pause.

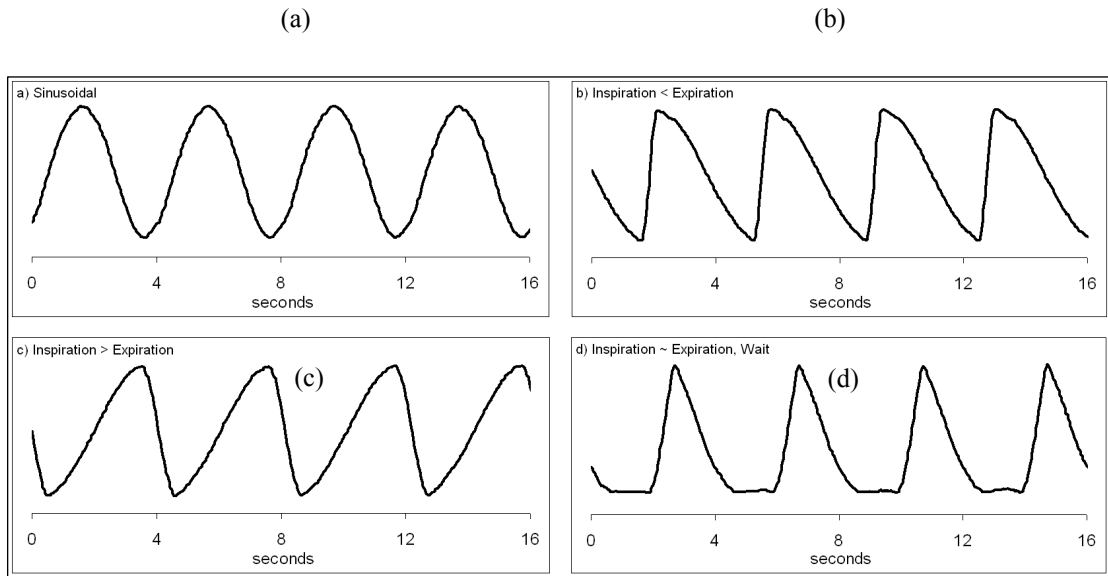


Figure 6.5. The motion profiles that were chosen as the basis for determining the location of the tumour within each of the ten phase-bins. (a) Motion 1 - symmetrical (b) Motion 2 - asymmetrical: Inspiration < expiration, (c) Motion 3 - asymmetrical: inspiration > expiration and (d) Motion 4 - Asymmetrical with a pause in-between breaths.

As is done in a 4D acquisition, one respiratory cycle from these patterns is divided into ten phase bins (commonly) corresponding to a particular phase percentage of the breathing cycle. Motion amplitudes of; 5.0, 3.5, 2.0 and 0.5 cm were assigned to each of the four motion profiles with the following beam arrangements:

1. Two beams (*parallel opposed*) with target motion occurring *parallel* to the beam.
2. A single beam incident on the chest-wall with the motion of the target *parallel* to the beam direction.
3. Two beams (*parallel opposed*) with target motion occurring *perpendicular* to the beam.
4. A single beam incident on the chest-wall with target motion occurring *perpendicular* to the beam motion.

The beam arrangements are shown in Figure 6.4 and were chosen to represent worst case scenarios (single beams) and investigate the discrepancies for multi-beam scenarios with different lesion motion directions relative to the beams.

The Monte Carlo package EGSnrc (Kawrakow, 2000b) was used along with BEAMnrc (Rogers, Faddegon *et al.*, 1995) and the user-code DOSXYZnrc for dose-calculation. For each of the four motion profiles and amplitudes, 11 full Monte Carlo simulations were performed corresponding to the ten individual phases (U10V) plus a single calculation on the AIP (AVG). With two beam arrangements and two tumour motion directions resulting in 352 separate Monte Carlo simulations. For each motion profile both *in beam* or parallel (anterior-posterior), motion was simulated as well as target motion *perpendicular* (superior-inferior) to the beam direction. In all simulations, a 6 MV, 98 x 98 mm² field was incident upon the *z-face* of the phantom. The ‘phase-space’ file used to generate the primary photons was previously generated by a BEAMnrc model of a Varian 600C Clinac with a mounted BrainLAB m3 mini-multileaf collimator (MMLC).

The model was developed based on schematics provided by Varian Medical Systems and BrainLAB under non-disclosure agreements (Kairn, Aland *et al.*, 2010, Kairn, Kenny *et al.*, 2010). The model of the Varian 600C with MMLC was dosimetrically-matched to measured data using percent depth-dose curves, beam profiles and scatter factors. For each simulation, 4x10⁹ photon histories were simulated per-phase and AIP simulation. EGSnrc parameters for electron and photon transport cut-offs were 0.561 MeV and 0.001 MeV respectively. The PRESTA-II electron-step, along with the EXACT boundary crossing algorithms were used with a step size of 0.25 (maximum fractional energy loss, ESTEPE). EGSnrc has been shown to produce step-size independent results at a sub 0.1 % level even at interfaces of high Z media in fine geometries (Kawrakow, 2000b, Verhaegen, 2002).

To compare key points on both U10V and AVG, doses to the entrance (A), central (B) and exit (C) voxels of the tumour in each of the ten phase bins were compared to the entrance (A(AIP)), central (B(AIP)) and exit (C(AIP)) voxels on the AIP. The accumulated dose of these voxels over the ten phases was compared to the AIP voxels as a ratio. This comparison highlights the potential differences that may arise due to the density difference at the borders of lung tissue and the tumour in both methods as well as being highly motion path (respiratory profile) dependent. A schematic of this method is shown in Figure 6.6.

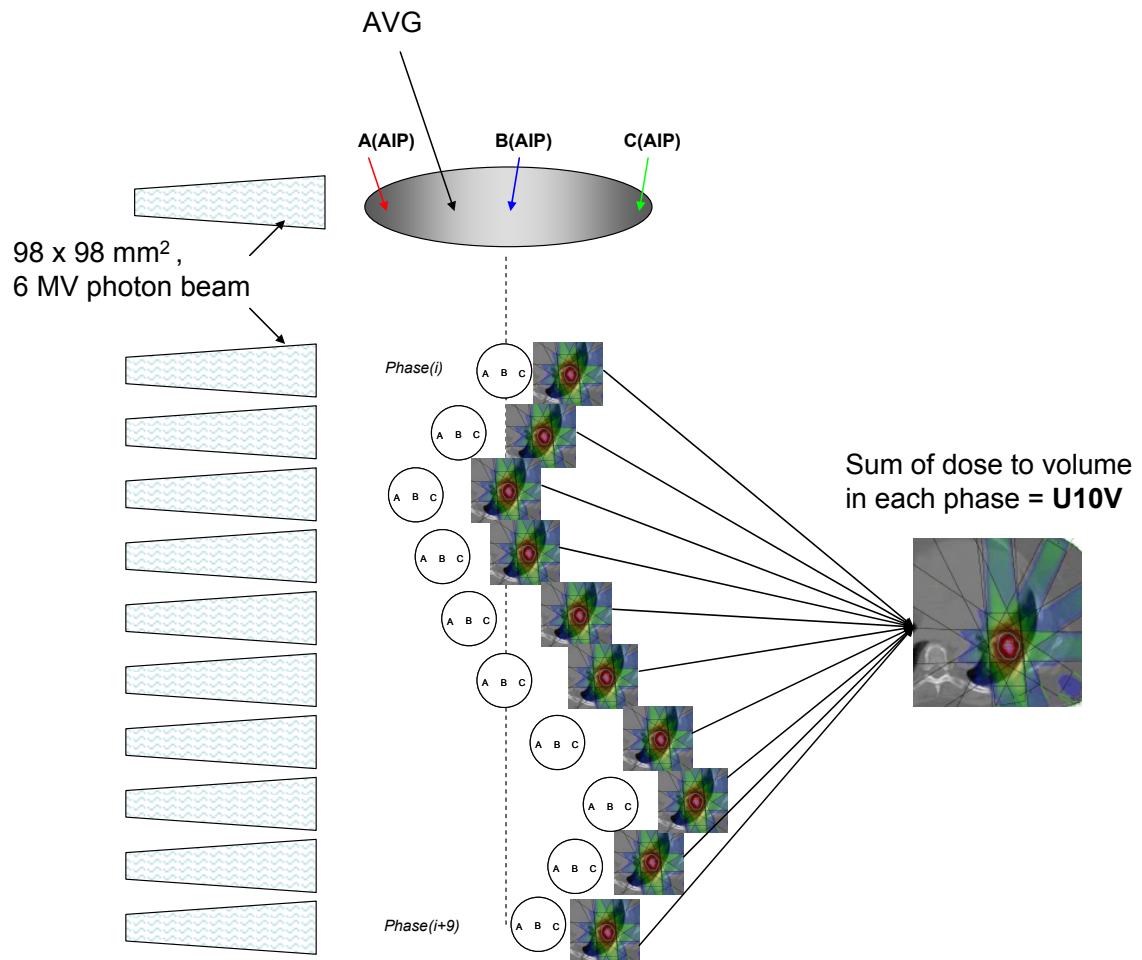


Figure 6.6. A schematic of the comparison between the two dose calculation methodologies. At each of the ten phases the entrance (A), central (B) and exit (C) doses are recorded as well as the dose to GTV. The entrance, central and exit doses, as well as the dose to the ITV (AVG) volume are also recorded for comparison. The dose to the lesion volume in each phase-bin is added to form the U10V. Note the assignment of phases in this scenario is arbitrary. The AVG is derived from the 10 phases from 4D-CT. Its boundary is defined by the MIP and the distribution of densities within the ITV derived directly from the AIP. In this work, simulations are conducted with the lesion moving in both the SI and AP directions relative to the beam. The parallel opposed fields are in the AP direction.

Cumulative DVHs were calculated using a MATLAB script which read in three-dimensional dose files ('3ddose') from the Monte Carlo simulations. An algorithm then extracted the target volume (spherical tumour) within each phase-bin and the AIP volume (defined by the ITV) for DVH analysis. The dose distributions from each of the ten phase-bins were then added to form the composite target volume dose and the DVH (U10V) calculated. The boundary of the AIP volume for DVH (AVG) analysis was defined from the ITV as would be delineated from a Maximum Intensity Projection (MIP) showing the extrema of target motion. The U10V dose bins are 1% of the maximum dose found within the target volume within a particular phase-bin. For AVG, the dose bins are 1% of the maximum dose found within the ITV. The Gross Tumour Volume (GTV)

in each individual phase data-set is delineated mathematically and there is no additional margin. It is important to note that registering the GTVs in each individual phase-bin data set was accomplished via translation only. This methodology for the construction of the U10V is only possible since the tumour is uniform in shape (spherical) and is always within the boundary of the beam. A more clinically relevant case requires deformable registration to track delivered dose across varying anatomical states (Rietzel and Chen, 2006b).

6.4.3. Computing hardware

All simulations were run on the ‘Tango’ cluster at the Victorian Partnership for Advanced Computing (VPAC). The Tango cluster is a large AMD Opteron system and consists of 111 compute nodes, each with two AMD Shanghai 2.5 GHz quad-core processors for a total of 888 CPUs. This permitted up to 20 simulations to be run simultaneously, each using one quad-core processor.

6.5. RESULTS

6.5.1. RESULTS I: Determination of peripheral underdosage at the lung-tumor interface using Monte Carlo radiation transport calculations.

Because of the complicated build-up then build-down and then build-up convolution arising from chest-wall, lung, tumour interfaces respectively, even the dose to the centre of each tumour is a complex function of tumour size and location within the lung. As a result of this, results presented below are given as the ratio of points on the boundary of the lesion to that of the central dose voxel for each lesion. The specific points are outlined in Figure 6.1 and Figure 6.2 respectively. The points represent the boundary point on the lesion facing the beam, the boundary point where the beam exits the lesion and the four lateral sides of the tumour intersected by Cartesian axes, with the origin being the centre of the lesion. This ratio can be summarised for beam and geometry parameters outlined in Table 6.1 as:

$$R(d, FS, \varnothing_t, E) = \frac{D_{boundary}}{D_{ref}} \quad (6.1)$$

Where R is the ratio of the dose at the point on the boundary ($D_{boundary}$) to the reference dose point (D_{ref}). Here, the reference point refers to the dose calculated at the centre of the lesion. R is a function of the distance from the chest-wall to the tumour boundary, d , the field size, FS , and the tumour diameter \varnothing_t on which the field size is based. The results presented in Table 6.3 and Table 6.4, are values of R calculated with Geant4 and refer to the entrance, exit and lateral ratios for a 6

and 15 MV photon beam respectively. The ratios are presented for various tumour distances d , field sizes FS and tumour diameters \varnothing_τ and energy E .

Table 6.3. Dose ratios (Equation 6.1) for a 6MV photon spectrum from Figure 6.3 (a). The entrance-to-central dose, exit-to-central dose and average of the lateral-to-central dose is shown. The standard uncertainty is shown in brackets.

\varnothing_τ (mm) / FS (mm ²)					
ENTRANCE DOSE					
d (mm)	10 / 30 x 30	16 / 35 x 35	20 / 40 x 40	30 / 50 x 50	50 / 70 x 70
5	1.02(±0.03)	1.04(±0.04)	1.03(±0.05)	0.99(±0.06)	1.02(±0.08)
10	1.01(±0.03)	1.02(±0.04)	1.00(±0.05)	1.05(±0.06)	0.99(±0.08)
20	1.01(±0.04)	1.01(±0.04)	0.99(±0.05)	0.99(±0.06)	0.98(±0.08)
40	1.00(±0.04)	0.98(±0.04)	1.00(±0.05)	0.99(±0.06)	0.97(±0.08)
EXIT DOSE					
d (mm)	10 / 30 x 30	16 / 35 x 35	20 / 40 x 40	30 / 50 x 50	50 / 70 x 70
5	0.98(±0.03)	0.99(±0.04)	0.94(±0.05)	0.94(±0.06)	0.94(±0.08)
10	0.97(±0.04)	0.98(±0.04)	0.95(±0.05)	0.96(±0.06)	0.93(±0.08)
20	0.99(±0.04)	0.99(±0.04)	0.95(±0.05)	0.94(±0.06)	0.87(±0.08)
40	0.99(±0.03)	0.97(±0.04)	0.95(±0.05)	0.93(±0.06)	0.91(±0.09)
LATERAL DOSE					
d (mm)	10 / 30 x 30	16 / 35 x 35	20 / 40 x 40	30 / 50 x 50	50 / 70 x 70
5	0.99(±0.05)	0.98(±0.06)	0.97(±0.07)	0.97=8(±0.09)	0.98(±0.11)
10	0.98(±0.05)	0.96(±0.07)	0.95(±0.07)	1.00(±0.09)	0.96(±0.12)
20	0.97(±0.06)	0.96(±0.07)	0.97(±0.07)	0.95(±0.09)	0.94(±0.12)
40	0.97(±0.05)	0.95(±0.07)	0.96(±0.07)	0.97(±0.09)	0.96(±0.12)

Table 6.4 Dose ratios (Equation 4.2) for a 15MV photon spectrum from Figure 6.3 (b). The entrance-to-central dose, exit-to-central dose and average of the lateral-to-central dose is shown. The standard uncertainty is shown in brackets. The standard uncertainty is shown in brackets.

	$\text{Ø}\tau$ (mm) / FS (mm ²)				
ENTRANCE DOSE					
<i>d</i> (mm)	10 / 30 x 30	16 / 35 x 35	20 / 40 x 40	30 / 50 x 50	50 / 70 x 70
5	1.01(±0.03)	0.98(±0.03)	0.95(±0.04)	0.89(±0.04)	0.86(±0.06)
10	1.01(±0.03)	0.95(±0.03)	0.95(±0.04)	0.93(±0.05)	0.86(±0.06)
20	0.99(±0.03)	0.96(±0.03)	0.96(±0.04)	0.93(±0.05)	0.86(±0.06)
40	0.97(±0.03)	0.94(±0.03)	0.92(±0.04)	0.93(±0.05)	0.93(±0.06)
EXIT DOSE					
<i>d</i> (mm)	10 / 30 x 30	16 / 35 x 35	20 / 40 x 40	30 / 50 x 50	50 / 70 x 70
5	1.01(±0.03)	1.01(±0.03)	0.99(±0.04)	0.95(±0.05)	0.92(±0.06)
10	1.02(±0.03)	0.99(±0.03)	0.97(±0.04)	0.98(±0.05)	0.90(±0.06)
20	1.04(±0.03)	1.01(±0.03)	1.01(±0.04)	0.96(±0.04)	0.92(±0.06)
40	1.02(±0.03)	1.01(±0.03)	0.98(±0.04)	0.97(±0.05)	0.97(±0.06)
LATERAL DOSE					
<i>d</i> (mm)	10 / 30 x 30	16 / 35 x 35	20 / 40 x 40	30 / 50 x 50	50 / 70 x 70
5	0.97(±0.05)	0.92(±0.05)	0.91(±0.06)	0.88(±0.07)	0.86(±0.07)
10	0.97(±0.05)	0.91(±0.05)	0.89(±0.06)	0.91(±0.07)	0.85(±0.07)
20	0.96(±0.05)	0.92(±0.05)	0.92(±0.06)	0.89(±0.07)	0.84(±0.07)
40	0.95(±0.05)	0.90(±0.05)	0.89(±0.06)	0.89(±0.08)	0.89(±0.08)

6.5.1.1 The dose reduction factor (DRF)

A dose reduction factor was developed as a means to express the underdosage of the ‘shell’ of the lesion with respect to the central (reference) dose. The dose reduction factor is outlined in Equation 4.3 and is intended for clinical purposes where multiple conformal beams are incident upon the tumour from multiple directions. The net effect will be approximated by the average of each of the contributing terms.

$$DRF = \frac{1}{6D_{ref}} \left(D_{entrance} + D_{exit} + \sum_{i=1}^4 D_{lateral,i} \right) \quad (6.2)$$

Using this metric, the degree of shell underdosage can be calculated. The results of these calculations are shown in Table 6.5 and Table 6.6.

Table 6.5. DRFs calculated using Equation 6.2 for a 6MV photon spectrum as a function of the tumour's size ($\varnothing r$) and distance from the chest-wall (d). Standard uncertainty is 0.5%.

6 MV d (mm)	$\varnothing r$ (mm)				
	10	16	20	30	50
5	1.00	1.00	0.97	0.98	0.98
10	0.98	0.97	0.96	1.00	0.96
20	0.98	0.97	0.97	0.95	0.94
40	0.98	0.96	0.96	0.97	0.96

Table 6.6. DRFs calculated using Equation 6.2 for a 15MV photon spectrum as a function of the tumour's size ($\varnothing r$) and distance from the chest-wall (d). Standard uncertainty is 0.5%.

15 MV d (mm)	$\varnothing r$ (mm)				
	10	16	20	30	50
5	0.98	0.95	0.93	0.89	0.87
10	0.98	0.93	0.91	0.92	0.86
20	0.98	0.94	0.93	0.91	0.86
40	0.97	0.93	0.91	0.91	0.91

6.5.2. RESULTS II: The incorporation of 4D information into dose calculation

The previous section quantified the underdosage that occurs in key regions of lung tumours. The development of a metric to estimate such underdosage was also presented. In this section, we look at how 4D-CT based dose calculation can take this into consideration. The methodology of this investigation is outlined in 6.4.2.

6.5.2.1 Comparisons between U10V and AVG: Characteristic points

The results for the comparison between the points A, B and C for both AVG and U10V dose calculation methods are shown in Figure 6.7 and Figure 6.8. The characteristic point locations and method for comparison are shown in Figure 6.6. The value R in Figure 6.7 and Figure 6.8 corresponds to the ratio of the accumulated entrance (A), central (B) and exit (C) doses over the ten separate phase based dose calculations (U10V) to the single calculation on an average intensity projection (AVG). Negative values in Figure 6.7 and Figure 6.8 indicate that, on average, the specific point received a lower dose over the ten phases when compared to the dose prediction based on the AIP. The uncertainty in all Monte Carlo simulations within the region of interest was 0.5-1.0% with 4×10^9 primary photons.

For a static scenario, the lesion is centered between the walls. For the moving case, inspiration corresponds to the tumour moving away from the left side chest wall, chest wall (1) in Figure 6.4 and expiration has the tumour moving towards the left side chest wall if the lesions motion is parallel to the beam direction. ‘Entrance’, point A, refers to the dose to the entrance of the lesion if only a single beam were incident upon the target from the outside the left-hand chest wall, chest wall (1) in Figure 6.4.

The entrance and exit points on the ITV were chosen since they lie in a heterogeneous region of high density gradient and therefore should receive a lower dose than points in homogenous regions in the inner areas of the lesion due to the lack of electronic equilibrium (Taylor, Dunn *et al.*, 2011). Central dose voxels were chosen for comparison since clinically, they are often chosen as a reference dose point. The largest discrepancy for a single field was found to be 16.73% (at the exit side of the tumour. This discrepancy occurred for a tumour moving with an amplitude of 5.0 cm and motion Type 3 (Figure 6.4 (c)). With a parallel opposed field (Figure 6.7) however, the largest discrepancy was reduced to 2.86 % and was found for a 5.0 cm amplitude with the target moving with motion Type 2 (Figure 6.4 (b)). For a parallel opposed field, all motion profiles and

amplitudes simulated result in differences between the two methodologies of less than 5% with no significant trends for the entrance, exit and central dose points. A single field on the other hand produces larger variation between the two methods with up to 16% variation in entrance doses for a 5.0 cm motion amplitude.

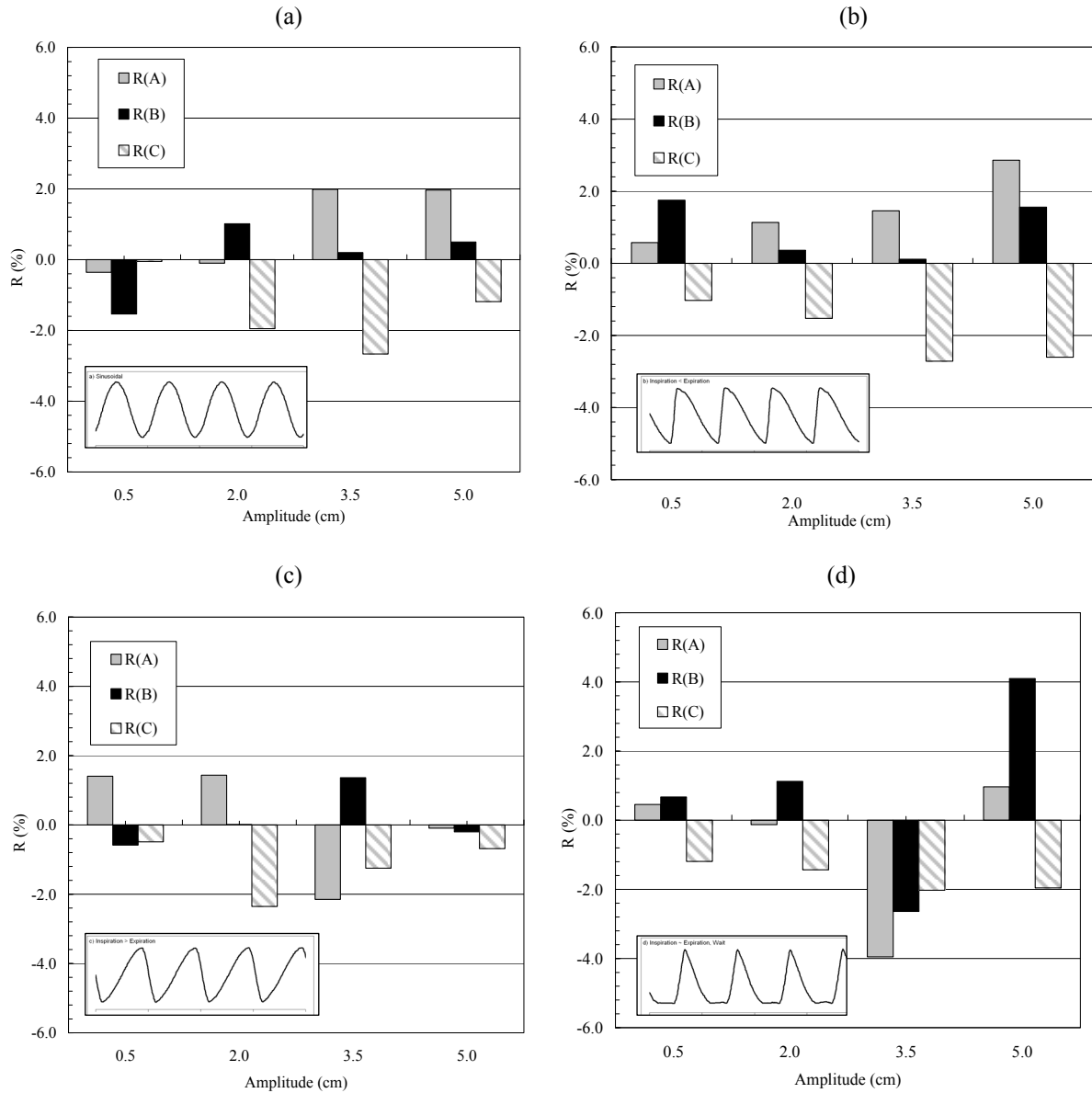


Figure 6.7. Analysis of characteristic points over all motion profiles and amplitudes simulated for a parallel opposed beam arrangement. Data presented here is the ratio of the accumulation of the point over the ten phases, to the single point on the AIP. Here, $R(A)$ represents the ratio of the entrance voxels, $R(B)$ the ratio of central dose voxels and $R(C)$, the ratio of exit dose voxels. The method of comparison is outlined in Figure 6.6. The four motion types outlined in Figure 6.5 are shown. (a) Sinusoidal motion (motion Type 1) (b) inspiration period less than expiration (motion Type 2) (c) inspiration period greater than expiration (motion Type 3) and (d) inspiration and expiration period followed by a pause (motion Type 4).

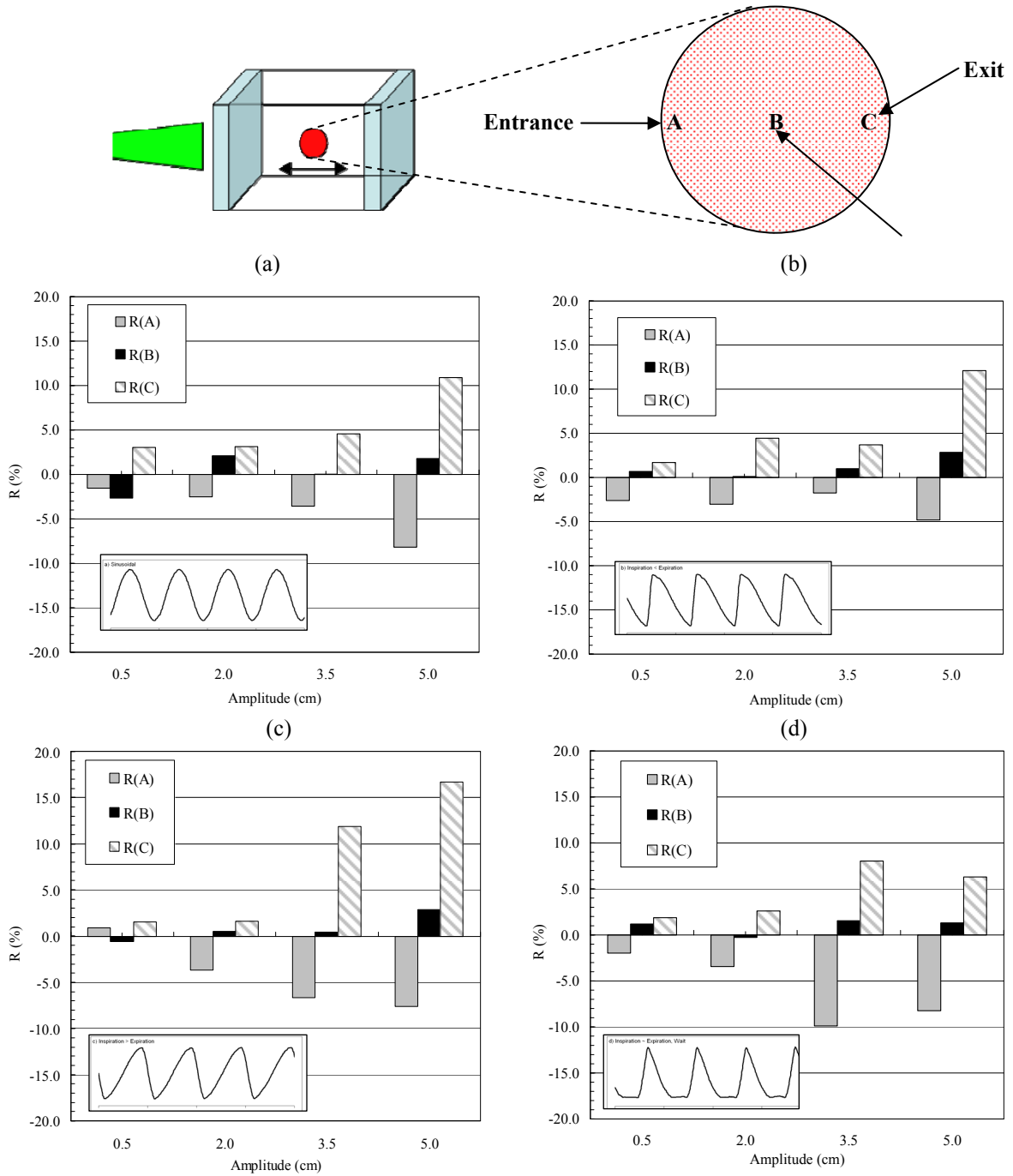
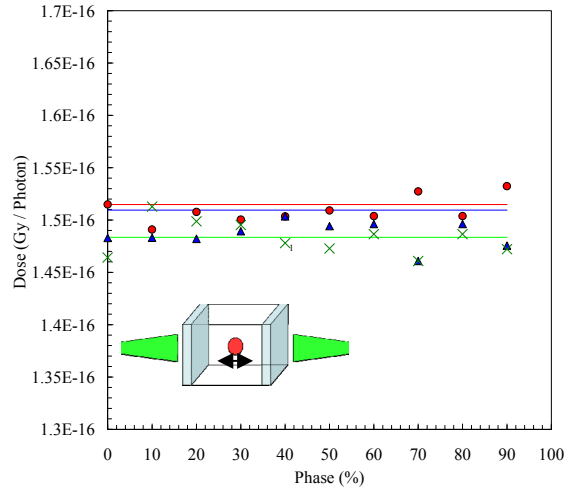
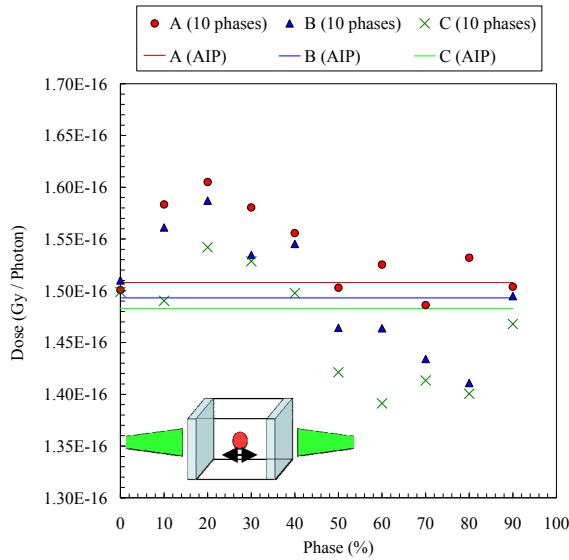


Figure 6.8. Analysis of characteristic points over all motion profiles and amplitudes simulated for a single field. Data presented here is the ratio of the accumulation of the point over the ten phases, to the single point on the AIP. Here, $R(A)$ represents the ratio of the entrance voxels, $R(B)$ the ratio of central dose voxels and $R(C)$, the ratio of exit dose voxels. The method of comparison is outlined in Figure 6.6. The four motion types outlined in Figure 6.5 are shown. (a) Sinusoidal motion (motion Type 1) (b) inspiration period less than expiration (motion Type 2) (c) inspiration period greater than expiration (motion Type 3) and (d) inspiration and expiration period followed by a pause (motion Type 4). The schematic above illustrates the points of interest.

The net results for each point over the motion cycle as shown in Figure 6.7 and Figure 6.8 arises due to the different contributions from the time spent at different depths. Figure 6.9 shows the per-phase variation in dose over ten phases compared to a single calculation on the AIP. A 5.0 and 0.5 cm amplitude motion for both parallel opposed and single fields are shown. This figure highlights the dependence on field arrangements and amplitudes on the agreement between the two methodologies when considering characteristic points. The figure demonstrates the magnitude of differences that can occur between the two methodologies if single fields are used and large amplitudes are present. For smaller amplitudes, the discrepancy between the two methods reduces. This can be seen in Figure 6.9 (b) and (d).

(a) – Parallel opposed field, 5.0 cm amp

(b) – parallel opposed field 0.5 cm amp.



(c) – Single field, sinusoidal, 5.0 cm amp.

(d) Single field, sinusoidal, 0.5 cm amp.

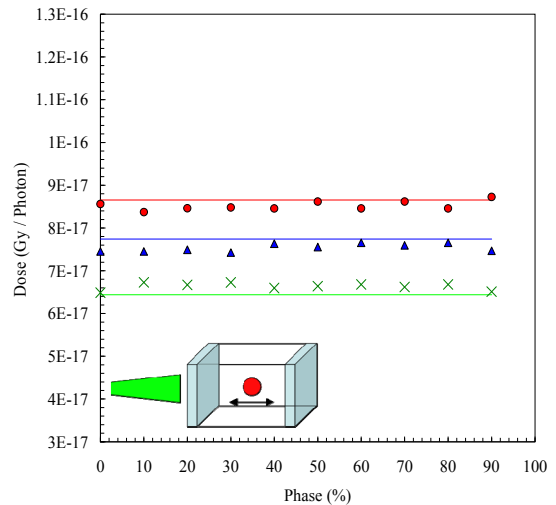
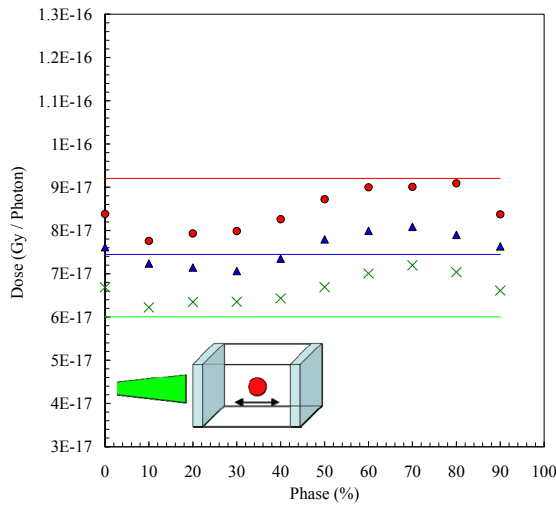


Figure 6.9. (a) Dose differences between the two methodologies per phase. Here, the points represent the dose to the entrance, central and exit voxels on the tumour in each of the ten phases. The straight lines represent the dose measured on the average intensity projection dataset formed by the ten phases for the same points (A, B, C). This method is outlined Figure 6.6. (a) 5.0 cm amplitude with motion of Type 1 (sinusoidal), in a parallel opposed field arrangement. (b) 0.5 cm amplitude motion for a parallel opposed field and motion of Type 1. (c) A 5.0 cm amplitude motion of Type 1 in a single field arrangement and (d) 0.5 cm motion of Type 1 in a single field arrangement. Note the y-axes scale differences between multiple and single field scenarios, respectively.

6.5.2.2 Comparisons between U10V and AVG: DVH analysis

Dose volume histograms were used to analyse the entire dose distribution for both methods (U10V and AVG). Results presented here are for target motion both parallel and perpendicular to the beam direction. The focus, however, is on target motion parallel to the beam direction as the contributions from attenuation and inverse-square effects within the dose distributions can contribute and therefore the largest possible discrepancies should become evident.

Figure 6.10 demonstrates the differences between the two methodologies presented in this work, U10V and AVG. The single dose calculation (AVG) volumes increase in size as the amplitude of motion increases since the ITV motion envelope increases. Whereas, in the case of the U10V method, the individual GTVs are delineated and registered and so the volume in this case is simply the original volume of the GTV. Provided of course that the GTV is delineated exactly the same in each phase-bin data-set.

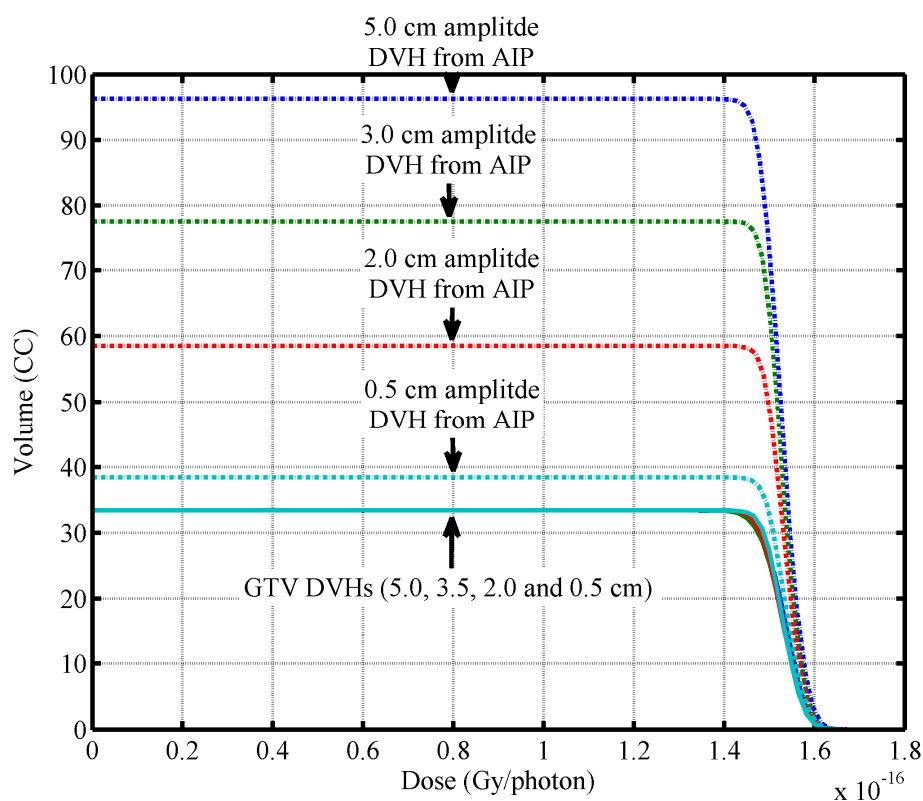


Figure 6.10. The two methods (U10V and AVG) produce different volumes for treatment. The U10V method involves contouring the target volume in each of the respiratory phases and then registering and summing the individual dose distributions. The AVG method, on the other hand performs a single dose calculation on the ITV (if the PTV is set to ITV). Data presented here is for a parallel opposed arrangement and sinusoidal motion profile.

6.5.2.2.1. DVH analysis: Parallel opposed arrangement

Figure 6.11 shows DVHs for a tumour moving with a sinusoidal motion profile (Figure 6.5(a)) and amplitudes of 5.0, 3.5, 2.0 and 0.5 cm. A parallel opposed field is incident on the tumour. The figures indicate that the agreement between the U10V and AVG dose distributions is only significantly different for amplitudes above 2.0 cm.

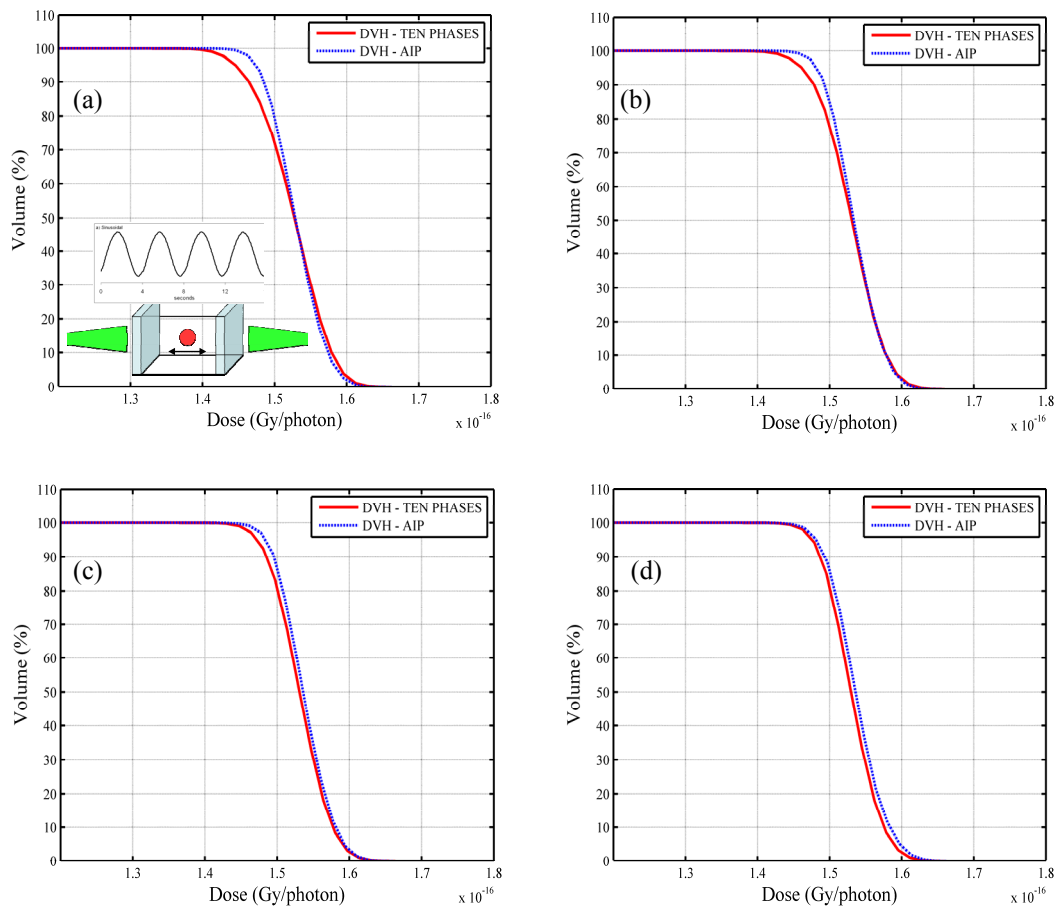


Figure 6.11. (a) DVHs for a 5.0 cm amplitude sinusoidal motion with **parallel opposed** fields, showing U10V (red line) and AVG (blue line). (b) 3.5 cm amplitude (c) 2.0 cm amplitude and (d) 0.5 cm amplitude.

6.5.2.2.2. DVH analysis: Single field arrangement

Figure 6.12 shows DVHs for a tumour moving with a sinusoidal motion profile (Figure 6.5 (a)) and amplitudes of 5.0, 3.5, 2.0 and 0.5 cm. In this simulation, a single field is incident on the tumour. The figures indicate that the discrepancy between the U10V and AVG dose distributions is significant for amplitudes above 0.5 cm.

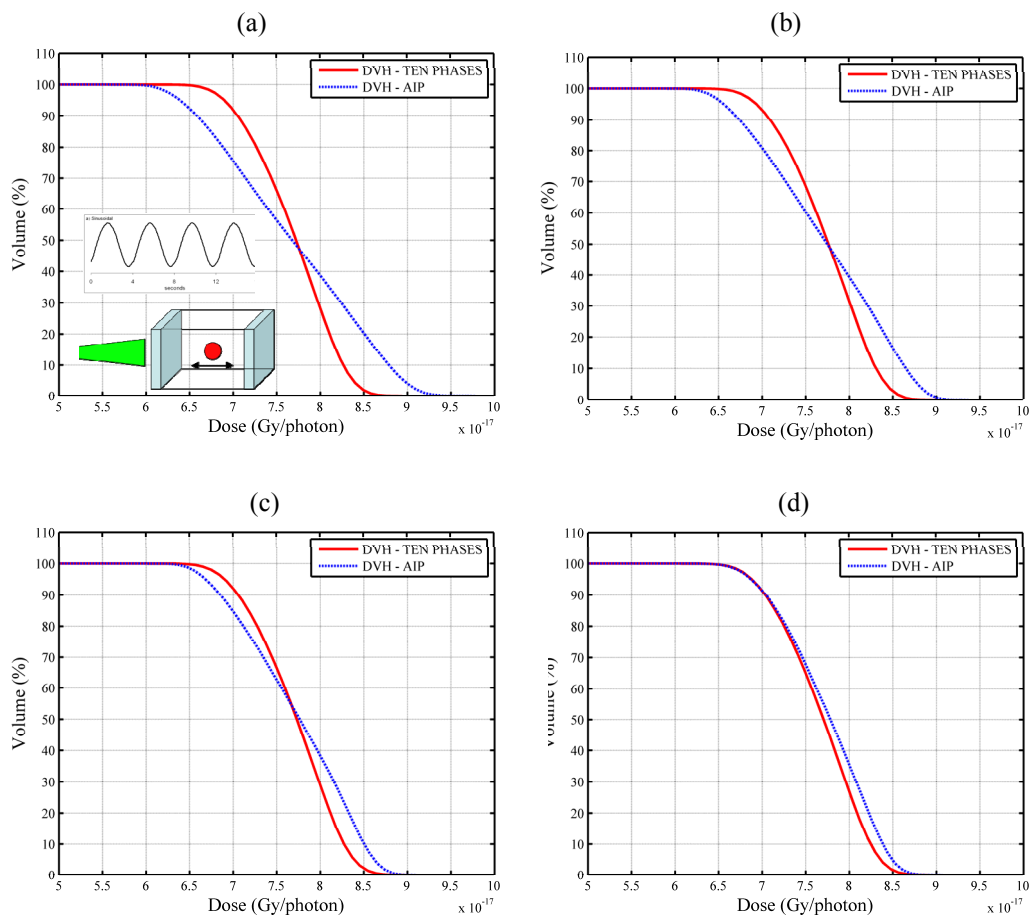


Figure 6.12. (a) DVHs for a 5.0 cm amplitude sinusoidal motion with a **single field**, showing U10V (red line) and AVG (blue line). (b) 3.5 cm amplitude (c) 2.0 cm amplitude and (d) 0.5 cm amplitude.

6.5.2.2.3. DVH analysis: Target motion perpendicular to the beam

DVH analyses for tumour motion perpendicular to the beam are shown in Figure 6.13. In comparison to the data presented in Figure 6.12 (single field, motion parallel), the discrepancy between the DVH for U10V and AVG for motion perpendicular to the beam direction is reduced. This scenario, where tumour motion occurs perpendicular to the beam direction is more likely to reflect the clinical scenario, where tumour motion would be occurring predominately in the SI direction (Seppenwoolde, Shirato *et al.*, 2002b). The data presented in Figure 6.13 indicates that even for a single field, the discrepancy between the two methods is minimal below amplitudes of 3.5 cm. This is predominately due to the removal of contributions from the inverse square law and attenuation within the ITV. Since the tumour's in-beam motion is zero and for a sufficiently large

field size the tumour is always in a region of consistent dose gradient. Irrespective of the beam arrangement, the differences in density between AVG and U10V have little effect.

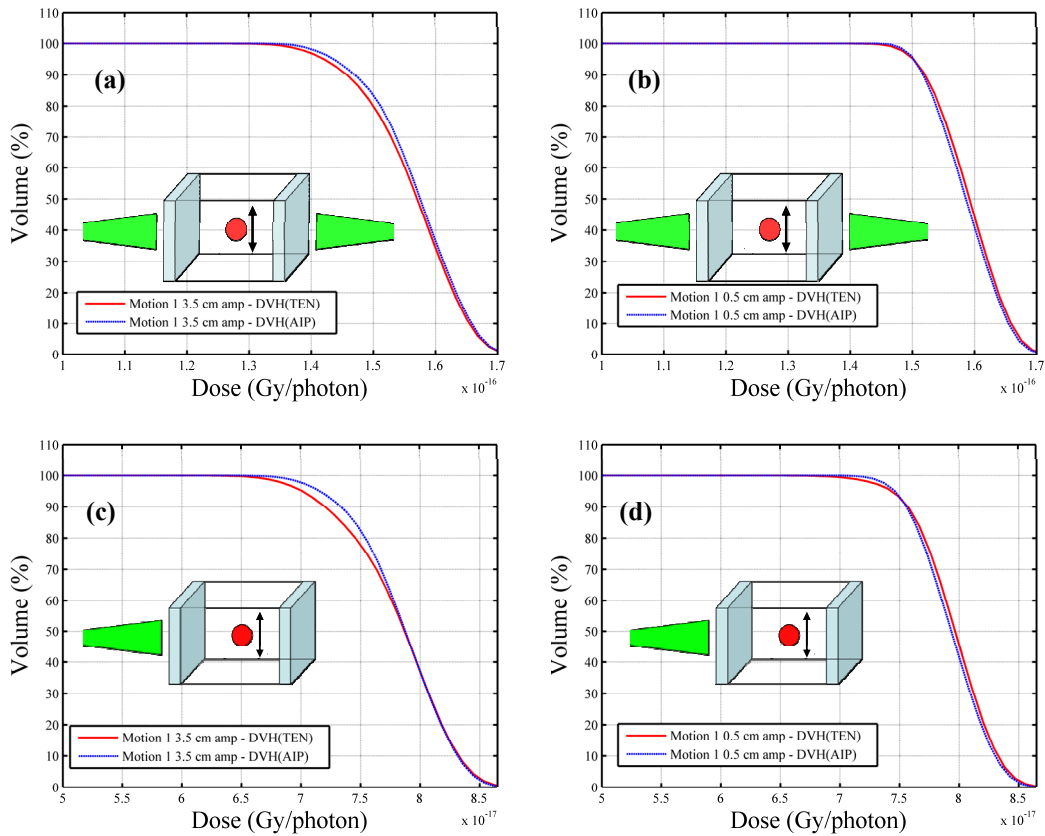


Figure 6.13. Motion of the lesion perpendicular to the beam. Comparison of the two methods for a 3.5 and 0.5 cm amplitude of motion respectively. The target's motion relative to the beam results in greater agreement in single fields for motion perpendicular to the beam direction compared to the parallel motion scenario.

6.5.2.2.4. DVH analysis: Dependence on motion profile

The dose distributions within the U10V and AVG volumes demonstrate a slight dependence on motion profile. This is demonstrated in Figure 6.14 where DVHs for a tumour moving parallel to the beam direction with motion amplitude of 5.0 cm are shown. Dose-volume histograms for each of the four motion profiles outlined in Figure 6.5 are shown. The large amplitude motion of 5.0 cm was chosen to highlight potential variation in the dose distribution as a consequence of different motion profiles.

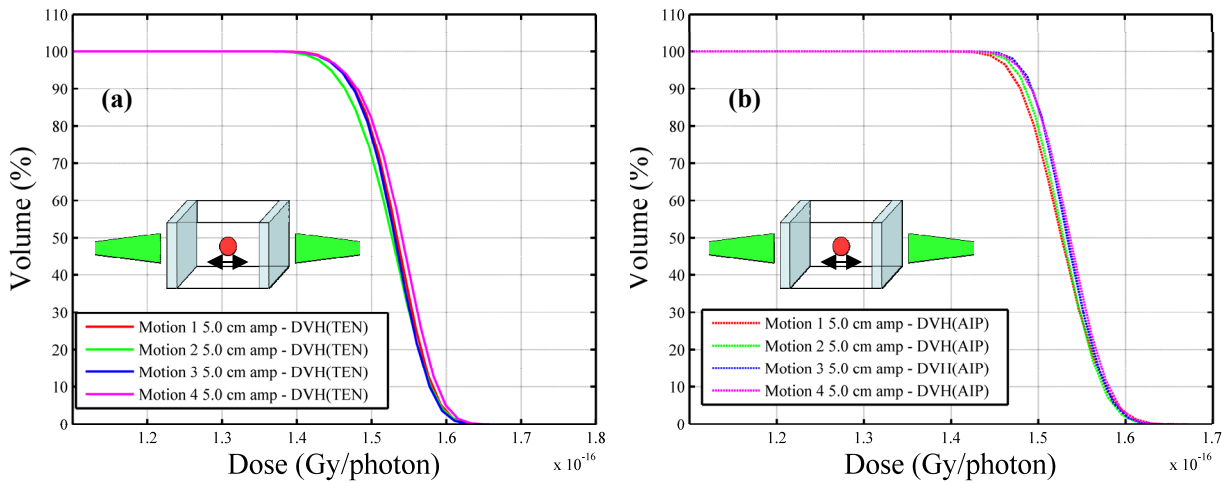


Figure 6.14. (a) The effect of motion profile on the cumulative dose-volume histograms (U10V) and (b) the effect of differing motion profiles on dose-volume histograms calculated from AVG.

6.6. DISCUSSION

The accurate calculation of dose distributions at interfaces of differing tissue densities is non trivial. In the context of radiotherapy of lung lesions, the differences in density between lung (0.25 – 0.4 g/cm³) and the lesion (~ 1.0 g/cm³) can result in underdosage of the periphery of the lesion due to electronic disequilibrium. With the advent of 4D-CT, new dose calculation options including dose calculation on individual phase data-sets is now possible. The objectives of this work were as follows:

- Quantify the extent of underdosage in key regions of the tumour boundary with respect to the central region and develop a factor for clinical estimation of this for a range of tumour sizes, field sizes and distances from buildup regions.
- Determine the equivalency of two methods of dose calculation based on data from 4D-CT. (1) Calculation on an average intensity projection and (2) cumulative dose calculation on individual phase-bin data-set from 4D-CT.

6.6.1. Determination of peripheral underdosage at the lung-tumor interface using Monte Carlo radiation transport calculations – Discussion of results

In this work, Monte Carlo simulations using Geant4 were used to determine a set of clinically relevant dose reduction factors that could be used to gauge the degree of peripheral underdosage of a lesion in the lung. Underdosage of the shell of a lesion residing in the lung derives from a number of processes. At the proximal region of the lesion, there is electronic disequilibrium due to the reduction of forward scattered electrons from the lung tissue. Lateral points on the periphery of the lesion are under-dosed due to a lack of lateral equilibrium. There is also reduced forward and backscatter that result in longitudinal disequilibrium. Doses to the distal regions of the lesion are consistently lower than central doses due to attenuation within the lesion itself and the loss of backscatter at the exit.

Considering the dose reduction of the shell is particularly important when considering dose prescription to covering isodoses. The dose to the centre of the tumour may also be affected by electronic disequilibrium. In the case of SBRT, the lesion is often less than 5 cm in diameter (Beitler, Badine *et al.*, 2006). A small lesion can provide insufficient build-up within the lesion itself, thereby resulting in disequilibrium.

Underdosage was found to be dependent on the tumour's size, position from the chest-wall and the beam energy used. On average, over all tumour diameters and distances from the chest-wall, a 6 MV beam results in an underdosage of 3% ($\pm 2\%$, 1σ) to the periphery of the lesion with respect to the centre. On the other hand a 15 MV beam results in an average of 8% ($\pm 4\%$, 1σ) reduction to periphery regions (Table 6.5 and Table 6.6). Underdosage was found to be more prevalent for the higher energy beam, larger tumour sizes and lesions situated at a larger distance from the chest-wall.

This data also provides validation for the choice of 6MV beams over higher energy beams (15 -18 MV) for treatment of lung lesions. This result is supported by Wang *et al* (2002), who showed that Monte Carlo dose calculation predicted increased penumbra width with increased photon energy resulting in decreased lateral dose homogeneity for 15 MV plans. Their study also showed that while the 15 MV dose distributions and DVHs generated by the clinical treatment planning calculations were as good as, or slightly better than, those generated for 6 MV, all target coverage indicators were significantly worse for 15 MV than for 6 MV. Particularly, the portion of the

planning target volume (PTV) receiving at least 95% of the prescription dose dropped dramatically for the 15 MV in comparison to the 6 MV. Their study concluded that lower energy photon beams (6 MV) are preferable over higher energies (15 - 18 MV) because of the significant loss of lateral dose equilibrium for high-energy beams in the low-density medium. Although their study was based on conformal plans and not SBRT plans, it is important to note, that although higher energy beams provide greater uniformity in radial dose across steep density gradients (which is preferable in SBRT) their use must be weighed carefully against the lateral beam degradation due to penumbra widening. Doses to the lateral regions in the Monte Carlo study here were, on average, over all conditions simulated, found to be underdosed by 11% and 8% for 15 MV and 6 MV respectively.

Conversely, in an IMRT planning study conducted by Weiss *et al* (Weiss, Siebers *et al.*, 2007) a study of 13 patients revealed, on average, no clinically or statistically significant differences between 6- and 18-MV plans. Their study concluded that high photon energies should therefore not be excluded *a priori* when a dose-calculation algorithm is utilised that accurately accounts for heterogeneities. Their study, however, was based on clinical treatment planning systems with superposition convolution dose calculation algorithms which have been shown to only approximate the penumbral broadening in low-density media when using high energy beams (Carrasco, Jornet *et al.*, 2004).

6.6.2. Determination of peripheral underdosage at the lung-tumor interface using Monte Carlo radiation transport calculations – Clinical relevance

Patients with early stage but medically inoperable lung cancer have a poor rate of primary tumor control (30% - 40%) and a high rate of mortality (3-year survival, 20% - 35%) with current management (Timmerman, Paulus *et al.*, 2010). Furthermore, lung cancers now account for 15% and 14% of all new cancer occurrences in men and women respectively. When treating with external beam radiotherapy, the photon beam is incident upon the chest-wall, of tissue equivalent density, then lung tissue of a lower density (roughly one third of normal tissue density), then into the lesion itself, which has a density roughly equivalent to that of tissue. Problems in dose calculation can arise due to the range of secondary electrons particularly if pencil-beam algorithms are used to calculate the dose to the lesion.

A typical SBRT treatment might involve the use of either an arc or multiple field arrangement with up to 9 fields (Hiraoka and Nagata, 2004, Hiraoka, Matsuo *et al.*, 2010, Hiraoka, Matsuo *et al.*, 2007, Hiraoka and Ishikura, 2007). For multiple fields, the contribution of the reduced entrance and exit doses over all beam angles incident on the lesion results in an underdosed periphery of the lesion with respect to the centre. Underdosage of the peripheral region may have significant consequences for the effectiveness of radiation therapy. The reduction of dose to this region can result in a reduction in the tumour control probability. Most clinically operational TPSs would not be able to predict the magnitude of dose reduction at the periphery of a lung lesion. This is mainly due to the calculation grid size, and the inability of the algorithms to calculate dose distributions in the presence of inhomogeneities on a millimeter scale. The DRF derived in this work presents a method to estimate the degree of underdosage compared to the centre of the lesion. This in turn could inform the prescription dose.

6.6.3. *The incorporation of 4D information into dose calculation*

In the era of 4D-CT, the clinician now has the ability to incorporate motion into the treatment plan and obtain useful information about tumour trajectories, as well as define treatment volumes with the use of MIPs. New dose calculation methodologies have also become available for SBRT based on data from 4D-CT. Namely, the treatment planner now has the ability to calculate dose on each individual phase data-set from 4D-CT and accumulate the individual distributions, or a planner can perform dose calculation on an average intensity projection (AIP) representative of the probability density function over the tumour's excursion of the densities that can be expected and is therefore equivalent to a 3D dose calculation.

This work aimed to determine the differences of two methods of dose calculation using a range of amplitudes, motion profiles, and beam arrangements in systematic full Monte Carlo simulations. The two generally accepted methods for dose calculation using 4D-CT data are as follows Figure 6.6.

- Performing dose calculation on each phase-bin dataset obtained from a 4D-CT and registering the cumulative distributions across the entire breathing cycle (U10V)

- Performing a single calculation on the ITV volume delineated from a MIP of all the tumour locations (phase bin information) whose voxel density values are derived from the AIP (AVG), equivalent to a 3D dose calculation.

In the present work, a comprehensive Monte Carlo study on the equivalency of two dose calculation methodologies based on data akin to that from 4D-CT was presented. Characteristic points in regions of high density gradient were analysed and compared for both the AVG (3D) method and the U10V method. The majority of points exhibited good agreement. When multiple fields (parallel opposed beams) were used, the two methods yielded equivalent results for lesion amplitudes below 3.5 cm (within the Monte Carlo uncertainty). Single fields however, produced large discrepancies (up to 16.73%). Dose-volume histogram analysis also confirmed these results. Overall parallel opposed fields, provided better homogeneity and agreement between the U10V and AVG methods, however, 5.0 cm motion amplitudes showed discrepancies in both single and parallel opposed beam arrangements. A 5.0 cm tumour motion amplitude would be considered an extreme case (Seppenwoolde, Shirato *et al.*, 2002a, Sixel, Ruschin *et al.*, 2003), with typical respiratory induced tumour motion being in the range 2 – 30 mm (Keall, Mageras *et al.*, 2006b). Nevertheless, it is pertinent to incorporate large amplitude motions to determine the limits of equivalency and to ensure the complete range of clinical amplitudes was covered.

Interestingly, the target's motion profile had little impact on the discrepancies between the two methodologies (U10V/AVG) for amplitudes less than 5.0 cm and multiple fields. Clinically, tumour motion is predominately in the superior-inferior direction (Seppenwoolde, Shirato *et al.*, 2002a), and as such, is generally perpendicular to the treatment beam. Simulations performed in this study, used a tumour motion parallel as well as perpendicular to the beam to highlight potential discrepancies between the two calculation methods. For a single field, simulations with the tumour motion perpendicular to the beam showed better agreement for the two dose calculation methods than the parallel case. This is due to the reduction in contributions from inverse square as well as attenuation effects. For a parallel opposed field, the dependency on tumour direction relative to the beam was also worse for target motion parallel to the beam direction (*'in-beam'*) though the discrepancy was reduced compared to a single beam scenario

Previous planning based studies have also concluded that performing dose calculation on an average intensity projection is equivalent to performing dose calculation on each individual phase from 4D-CT and combining the resulting distributions. However, these studies only assessed the equivalency for relatively small target motion excursions and were calculated with treatment planning systems and not full Monte Carlo simulation. Admiraal *et al* (2008a) concluded that when dose calculations were performed on the AIP, the dose distribution compared well to the cumulative dose-per-phase. The authors found that for nine out of ten patients undergoing stereotactic lung radiotherapy, the dose criterion (at least 54 Gy should be received by 99% of the PTV) was met when planning on the average intensity projection. The mean range of amplitudes for their study, however, was 0.2 – 0.3 cm and their work was based on treatment planning system (TPS) dose calculation algorithms. Ehler *et al* (2008) compared cumulative (ten phase) dose distributions for IMRT treatment planning in three data sets: a single 4D-CT phase, a 4D-CT phase with a density override to the tumour motion envelope and a plan on the average. The authors found that all three planning methods yielded acceptable treatment plans. However, planning on an average intensity projection qualitatively resulted in a more uniform dose to the tumour, especially for carcinomas residing in the periphery of the lung. Again, their study was based on TPS calculations. Starkschall *et al* (2009) retrospectively performed 4D dose calculations on CT data-sets for patients with stage II non-small-cell lung cancer. Target volume coverage and doses were compared to conventional 3D dose-calculation methodology. Their results showed that for 11 out of 15 patients, clinical target volume coverage was comparable in both 3D and 4D calculations and in 7 of the 15 patients, planning target volume coverage was comparable. For the other patients, the 4D calculation indicated a difference in target volume dose sufficiently large enough to warrant replanning. Vinogradskiy *et al* (2009a) quantified the increase in accuracy of using phase-bin data from 4D-CT for dose calculations versus 3D dose calculation. Their study employed motion phantoms along with deformable lung inserts. Their study also found no significant differences in the accuracy between the two dose calculation methods inside the GTV. Film measurements, on the other hand demonstrated that cumulative dose calculation (on each phase from 4D-CT) provided better accuracy than AIP dose calculations in heterogeneous dose regions. Wang *et al* (2009) investigated the dosimetric impact of using 4D-CT and multiphase (helical) CT images for treatment planning target definition in SBRT of lung cancer. Their study found that compared to the conventional approach using helical images for target definition, 4D CT and multiphase 3D CT treatment planning further reduces the amount of normal lung being irradiated while still providing good target coverage when image guidance was used.

6.6.4. Clinical application

There are several factors that need to be taken into account in a clinical situation. The results presented here are for idealised geometries. In reality, the lung represents a complex geometry whose density changes during delivery with the volume of air present and this may alter the density composition of the tissue surrounding the AVG. Furthermore, the GTV (U10V) and ITV (AVG) in this study are extracted perfectly, i.e. the target voxel dose values are mathematically extracted in the same way they were mathematically created. In a clinical situation, inter-observer variations in GTV delineation (Van de Steene, Linthout *et al.*, 2002, Giraud, Elles *et al.*, 2002) could contribute to the overall geometric error and also introduce differences in the DVHs. The study presented here seeks to quantify the discrepancy attributable to large amplitude motions and variable breathing patterns in a systematic fashion.

6.6.5. Chapter summary

6.6.5.1 The Dose Reduction Factor (DRF)

The aim of this work was to develop a dose-reduction metric, termed the Dose Reduction Factor (DRF) for use by clinicians and treatment planners to estimate the magnitude of underdosage of lung lesions due to electronic disequilibrium. The level of accuracy afforded by full Monte Carlo simulations performed here provides insights into underdosage at the periphery of lung lesions that may not be evident when using commercial treatment planning systems. Monte Carlo simulations performed with the Geant4 toolkit demonstrate that doses to the peripheral region of a lung lesion may be up to 14 % lower than the dose to the centre of the lesion. This work also demonstrated that the peripheral underdosage is generally more severe for higher energy beams compared to 6 MV. The underdosage was also shown to be partially mitigated by the cumulative effect of multiple beams from different directions.

6.6.5.2 Dose calculation on U10V versus AVG

Clinically, 4D dose calculation involves registering and combining separate dose calculations on phase-data from 4D-CT. The hypothesis of this work was that performing dose calculation on an average intensity projection in multi-field radiotherapy does not result in clinically significant differences in dose, compared to accumulating dose on each individual phase data-set from 4D-CT. Large amplitude motions (5.0 cm), were purposely simulated to exacerbate potential differences between the two dose calculation methodologies and therefore err on the side of

conservativeness.

With 4D-CT becoming the standard of care for treatment planning of lung cancer, the additional information obtained allows the clinician to evaluate the impact respiratory induced target motion may have on the treatment plan. Planning on an AIP was found to be sufficient for dose calculation purposes when compared to the more laborious method of contouring and calculating dose on each individual phase data-set, and registering / combining the resulting distributions in a union of GTVs.

Chapter 7. Conclusions & Outlook

“He knew that all the hazards and perils were now drawing together to a point: the next day would be a day of doom, the day of final effort or disaster, the last gasp.”

— J.R.R. Tolkien

“With all due respect, sir, I believe this is going to be our finest hour.”

— R. D. Franich, rejoinder (channeling Gene Kranz, Apollo 13 Mission Control)

7.1. INTRODUCTION

In this work the impact of motion on aspects of treatment planning for SBRT of lung cancer was assessed. SBRT differs from conventional radiotherapy lung treatments in that generally it is delivered to smaller lesions, with a reduced fractionation scheme characterised by higher doses per fraction. Of particular interest for the present work is also that margins around target volumes are typically substantially reduced with the need to account for any targeting uncertainties. The potential benefits of SBRT can only be fully realised if the inherent uncertainty in the target's position is minimised.

This work has presented a number of studies whereby some of the issues surrounding motion management in SBRT have been investigated by pursuing the following objectives:

Objective 1: Assess the effect of motion on the identification and delineation of small, moving tumours.

Objective 2: Quantify the influence of lesion size and motion amplitude on data acquired from 4D-CT

Objective 3: Determine the degree to which the same relationships affect PET data if and when this imaging modality is incorporated into the treatment planning process.

Objective 4: To assess the mitigation of motion effects in PET that can be achieved by implementing 4D phase-binned PET.

Objective 5: To evaluate dose calculation on lung tumours, in particular quantifying the differences between 4D calculations, which explicitly account for dynamic geometry and conventional 3D calculation, based on average intensity projection data from 4D-CT.

7.2. DEVELOPMENT OF MOTION PHANTOMS

To experimentally study the effects of motion on both imaging and delivery of radiation in SBRT, phantoms that are able to move with patient-like patterns are necessary. This work detailed the development of an upgrade to an existing commercially available respiratory motion phantom. Upon the creation of a new control system and software, the phantom can now import actual patient traces recorded with the Varian RPM system, as well as simulate custom profiles (see Figure 3.16 and Figure 3.17) accurately. The upgraded QUASAR phantom was found to be useful in testing the Varian RPM system as was published in the article (Dunn, Kron *et al.*, 2011a).

A second phantom, the see-saw motion phantom, was designed with quality assurance of 4D-CT in mind. The phantom's unique design enables motion in two directions (axial and inter-slice) with a large range of amplitudes and frequencies of motion. The see-saw phantom allowed for the investigation of the impact of motion on images and projections from 4D-CT. The see-saw phantom presents a unique 4D-CT QA phantom capable of a large range of coupled SI and AP motion profiles. The derivation of a motion model for the phantom matched the physical profiles well in both AP and SI direction and the motion model can be used to accurately calculate the amplitude of the phantom in any number of configurations which is useful for assessment of 4D measured data.

The two QA phantoms that have been presented in Chapter 3 can be used to assess the impact of motion on treatment planning for SBRT of lung cancer. These phantoms allow patient specific QA to be performed for SABR/SBRT patients and as SABR / SBRT techniques become more widespread, these phantoms provide an invaluable tool for QA. The AAPM Task Group Report 101 on "Stereotactic Body Radiation Therapy" recommends that treatment-specific and patient-specific QA protocols be established to govern both the treatment planning and delivery process (Benedict, Yenice *et al.*, 2010). The phantoms described in this work allow such protocols to be developed, and indeed, the modified QUASAR respiratory motion phantom presented here is currently used for patient-specific SBRT QA at the Peter MacCallum Cancer Centre. Furthermore, the TG-101 report recommended that for all SBRT patients with targets in the thorax or abdomen, a patient specific motion assessment be conducted.

The respiratory analysis software developed and presented as part of this thesis enables the statistics of respiratory traces recorded from a surrogate to be compared with lesion motion data collected with 4D-CT or fluoroscopy. This enables the correlation between the external and internal anatomy to be assessed and can inform the clinician whether a certain motion management technique is feasible. The software provides a number of metrics for analysing the patient's respiratory function and comparing respiratory traces recorded at different times throughout a treatment schedule or following bio-feedback respiratory coaching. The respiratory analysis software can also be used to determine if a patient's treatment would likely benefit from gating, another recommendation of the TG-101 report.

7.3. THE IMPACT OF MOTION ON IMAGES ACQUIRED WITH CT AND 4D-CT

The impact of motion on 4D-CT image quality for SBRT treatment planning was assessed in this thesis. Results obtained using the see-saw motion phantom indicate that if 4D-CT is to be used to assess the magnitude of motion and provide valuable spatio-temporal information to the treatment planning process, care needs to be taken to ensure that an adequate number of phase-bins is chosen to provide complete MIP and AIP data-sets. This is particularly relevant for patients with long breathing periods where consideration needs to be given to increasing the rotation period of the gantry.

A criterion which quantifies these effects has been presented, which indicates the number of phase-bins required to provide a complete data-set. This criterion was used to demonstrate that for lesions with diameters greater than 2.0 cm and displacements up to 4.0 cm, ten phase-bins are adequate to provide complete MIP and AIP data-sets. For smaller lesion sizes however, the interplay of large amplitude motions and small targets could have considerable consequences. Binning artifacts in 4D-CT and residual motion effects that have been described and evaluated as part of this thesis may result in an incorrect delineation of both the ITV and CTV if used for SBRT planning. This in turn can lead to dose delivery errors and a potential increase in normal-tissue dose or poor target coverage.

In SBRT, typical margins for defining the minimal distance separating the CTV and PTV surfaces are 0.5 cm in the axial planes and 1.0 cm in the superior/inferior directions (Timmerman, Papiez *et al.*, 2003, Benedict, Yenice *et al.*, 2010) indicating that the accuracy of data from CT and other sources is critical to the treatment efficacy. 4D-CT scanning parameters, such as scan time per revolution, slice thickness, inter-slice gap and the time-scale of any anatomical motion also directly affects the size and appearance of tumour volumes. In this work, it has been shown that 4D-CT imaging of small targets undergoing large motion excursions requires an understanding of the limitations of both the scanner and the 4D protocol being used to acquire the 4D data. By carefully selecting both the scanning parameters and 4D protocol parameters, one can potentially mitigate these effects. The see-saw motion phantom allows for investigation of these effects and can be used for QA and optimisation of 4D-CT acquisition protocols at a drastically reduced cost compared to commercially available phantoms.

The impact of motion on images acquired with 4D-CT described in this work in Chapter 4 may also have implications for image guided delivery techniques. 4D-Cone Beam CT (4D-CBCT) for example is an emerging imaging technique that can be used to resolve tumour motion, though a large number of projection angles are required for each respiratory phase and as such the scan length is longer than a conventional CBCT (~ 4 minutes) depending on the patient's breathing cycle. The projections from 4D-CBCT can be reconstructed into phase-bins and therefore a verification of the tumour position at each phase can be achieved. In addition, conventional CBCT provides an assessment of motion being a slow scanning modality, where image blurring is reflective of motion. As such it can be compared to the planning 4D-CT MIP and used as a verification of the patient setup just before treatment delivery though alignment issues have been reported (Clements, Kron *et al.*, 2013). The phantoms developed as part of the present work were used in these investigations.

7.4. THE IMPACT OF MOTION ON IMAGES ACQUIRED WITH PET

The impact of motion on PET images was evaluated in this work with a focus on the effects of lesion size and amplitude of motion on target delineation in 3D PET and the degree of mitigation afforded by the use of 4D-PET. At present, a PET/CT scan is considered the standard of care for lung cancer patients prior to commencement of radiation therapy (Mac Manus and Hicks, 2012, Mac Manus, Everitt *et al.*, 2013). In this thesis, experimental phantom studies were used to investigate a relationship between lesion size and amplitude and the measured activity and apparent lesion size. It was demonstrated that the reduction in activity associated with motion blurring is dependant on motion parameters, the size of the lesion and its apparent activity against the background. Monte Carlo GATE simulations using XCAT computational phantoms featuring lung lesions with diameters of 10 – 30 mm and activity ratios of 10:1, 5:1 and 2:1 were used to compare the anthropomorphic geometry case to the experimental phantom study results. Overall, Monte Carlo methods and experimental phantom studies predicted different magnitudes of activity underestimation, suggesting that predictions from either method may not be easily transferable between the two scenarios. These factors may have negative consequences on the benefits of PET for both target delineation and management. As a result of this, if motion of small lesions (≤ 2 cm) exceeds 1 cm then 4D-PET is recommended. 4D-PET was found to increase the recovery of apparent activity and decrease the blurring associated with motion over all amplitudes and lesion sizes measured and simulated.

There are a number of strategies currently available to compensate for lesion motion due to respiration in PET and PET/CT: non attenuation corrected PET, deep inspiration breath-hold PET, respiratory gated PET plus free breathing CT, respiratory gated PET plus breath-hold CT, respiratory gated PET plus respiratory gated CT (Callahan, Kron *et al.*, 2011). The gold standard protocol for obtaining the most information about target size and motion magnitude is to use 4D-PET and 4D-CT in a combined 4D-PET/CT where attenuation correction is performed for each phase of the PET scan using the corresponding 4DCT phase. The use of this hybrid imaging technology when available has recently been shown to have a beneficial impact on conventional NSCLC treatment planning to assist in the delineation of target volumes as it currently provides the most comprehensive planning data to assist in target delineation (Mac Manus, Everitt *et al.*, 2013) and it is likely to have an impact on treatment planning for SBRT.

7.5. THE IMPACT OF MOTION ON TREATMENT PLANNING AND DOSE CALCULATION

In SBRT of lung cancer, the primary concerns are the exposure of the target to a very high dose per fraction and minimisation of normal tissue receiving high doses outside of the target to limit treatment toxicity. As a result of this margins need to be tight and the gradient of the dose fall-off outside the target needs to be steep. Poor image quality and mismanagement of motion can have detrimental consequences for treatment planning and delivery. At present, the explicit incorporation of 4D information from 4D-CT into dose calculation algorithms is not facilitated in most treatment planning systems. As such, alternate methods such as a single dose calculation on an average intensity projection from 4D-CT, equivalent to a 3D calculation are often pursued for dose calculation.

A comparison between a single dose calculation using an average intensity projection and the ‘4D’ method of registering and accumulating the dose distributions on phase-bin data from 4D-CT using the EGSnrc Monte Carlo code has been presented. To facilitate a systematic approach with multiple motion profiles and lesion amplitudes, geometries for Monte Carlo calculations were created consisting of a lesion located within a lung equivalent box with slabs representing the chest-wall. To test the Monte Carlo methodology and ensure that differences between the average intensity projection and 4D methods could be discerned, Monte Carlo simulations of the static scenario were performed. These simulations quantified the underdosage of the periphery of the lesion consistent with what is expected due to the lack of electronic equilibrium. Monte Carlo dose calculation methodologies enable the full effect of this to be quantified more accurately than with

most currently available TPS dose calculation algorithms (Taylor, Dunn *et al.*, 2011). As a result of this work a Dose Reduction Factor (DRF) was developed which describes the underdosage ratio of the periphery with respect to the central region. The mean of this was found to be 0.97 and 0.92 for a 6 MV and 15 MV beam respectively. The DRF metric may assist clinicians in the estimation of the magnitude of potential discrepancies between prescribed and delivered dose distributions as a function of tumour size and location.

Monte Carlo simulations of the dynamic scenario revealed discrepancies between the two methods (AIP and 4D) for large amplitude motions (> 3.0 cm) of up to 4 % for parallel opposed fields which partially compensate for the 16 % discrepancy associated with each single field. As such, the use of the 4D method for dose calculation when considering small lesions with large motion is recommended. For amplitudes smaller than 3 cm however, the differences between the two calculation methodologies was found to be less than 2.5 %. This indicates that the use of average intensity projection CT image sets derived from 4D CT is adequate for dose calculation in most circumstances.

7.6. OUTLOOK

In assessing some of the effects and challenges of motion management in SBRT, tools have been developed and tested that can, and have been implemented clinically for patient specific QA of SABR / SBRT treatment plans, as well as QA devices for 4D imaging modalities used in SBRT planning for lung cancer. These phantoms have also proven to be useful for other studies including studying the effect of irregular breathing patterns on internal target volumes in four-dimensional CT and cone-beam CT images in the context of stereotactic lung radiotherapy (Clements, Kron *et al.*, 2013), exploring the use of radiochromic film for individual patient QA in extracranial stereotactic lung radiotherapy (Kron, Clements *et al.*, 2011) and validation of 4D-PET Maximum Intensity Projections for Delineation of Internal Target Volumes (Callahan, Kron *et al.*, 2013). The next step in the use of these phantoms is to develop other QA protocols based on them and extend their use to other fields. For example, as 4D-PET becomes more prevalent, the see-saw motion phantom can be adapted for 4D-PET QA and used to develop protocols for clinical use. In the future it is hoped, that the upgraded QUASAR phantom could also be used to develop and evaluate 4D-CBCT in preparation for routine clinical use.

In modern radiotherapy many dose measurements are accompanied by Monte Carlo calculations – either to characterise the detector, obtain information of a radiation field that cannot be measured (such as spectrum) or to calculate dose in circumstances where measurements are too difficult. Monte Carlo calculations have been used for the latter by determining dose at interfaces. Future work will determine if the DRF developed here proves to be of value for clinicians, in particular when solid targets move in a low density environment. It is also expected that Monte Carlo calculations will more widely used to assess dose distributions in moving targets. In principle the calculation times should not be significantly different from a static case as uncertainty only depends on the overall number of histories. This makes the Monte Carlo approaches used here well suited for more future studies.

Ultimately, the outcomes of this thesis should be used prospectively to inform substudies of clinical trials to assess 4D imaging for many real patients as a function of breathing pattern and tumour motion amplitude.

References

- Aarup, L. R., Nahum, A. E., *et al.* 2009. The effect of different lung densities on the accuracy of various radiotherapy dose calculation methods: implications for tumour coverage. *Radiother Oncol*, 91, 405-14.
- Abu Anas, E. M., Lee, S. Y., *et al.* 2010. Removal of ring artifacts in CT imaging through detection and correction of stripes in the sinogram. *Phys Med Biol*, 55, 6911-30.
- Ackerman, M. J. 1998. The Visible Human Project. *Proceedings of the IEEE*, 86, 504-511.
- Admiraal, M. A., Schuring, D., *et al.* 2008a. Dose calculations accounting for breathing motion in stereotactic lung radiotherapy based on 4D-CT and the internal target volume. *Radiotherapy and Oncology*, 86, 55-60.
- Admiraal, M. A., Schuring, D., *et al.* 2008b. Dose calculations accounting for breathing motion in stereotactic lung radiotherapy based on 4D-CT and the internal target volume. *Radiother Oncol*, 86, 55-60.
- Agostinelli, S., Allison, J., *et al.* 2003. Geant4 - a simulation toolkit. *Nuclear Instruments and Methods in Physics Research Section A: Accelerators, Spectrometers, Detectors and Associated Equipment*, 506, 250-303.
- Ahn, S., Yi, B., *et al.* 2004. A feasibility study on the prediction of tumour location in the lung from skin motion. *Br J Radiol*, 77, 588-96.
- Aihw 2008. Cancer in Australia: An overview. *2008 Cancer series*. Canberra.
- Allen-Auerbach, M., Yeom, K., *et al.* 2006. Standard PET/CT of the chest during shallow breathing is inadequate for comprehensive staging of lung cancer. *J Nucl Med*, 47, 298-301.
- Allen, A. M., Siracuse, K. M., *et al.* 2004. Evaluation of the influence of breathing on the movement and modeling of lung tumors. *Int. J. Radiat. Oncol. Biol. Phys.*, 58, 1251-7.
- Allison, J., Amako, K., *et al.* 2006. Geant4 developments and applications. *Nuclear Science, IEEE Transactions on*, 53, 270-278.
- Antony, J., Carlson, D. J., *et al.* 2007. Clinical Impact of 4D-CT Imaging on Lung Cancer Radiotherapy Treatment Planning and Biological Response. *International Journal of Radiation Oncology*Biological*Physics*, 69, S526-S526.
- Aristophanous, M., Berbeco, R. I., *et al.* 2012a. Clinical utility of 4D FDG-PET/CT scans in radiation treatment planning. *Int J Radiat Oncol Biol Phys*, 82, e99-105.
- Aristophanous, M., Berbeco, R. I., *et al.* 2012b. Clinical Utility of 4D FDG-PET/CT Scans in Radiation Treatment Planning. *International Journal of Radiation Oncology*Biological*Physics*, 82, e99-e105.
- Balter, J. M., Ten Haken, R. K., *et al.* 1996a. Uncertainties in CT-based radiation therapy treatment planning associated with patient breathing. *Int. J. Radiat. Oncol. Biol. Phys.*, 36, 167-74.
- Balter, J. M., Ten Haken, R. K., *et al.* 1996b. Uncertainties in CT-based radiation therapy treatment planning associated with patient breathing. *Int J Radiat Oncol Biol Phys*, 36, 167-74.
- Barnes, E. A., Murray, B. R., *et al.* 2001. Dosimetric evaluation of lung tumor immobilization using breath hold at deep inspiration. *Int J Radiat Oncol Biol Phys*, 50, 1091-8.
- Baró, J., Sempau, J., *et al.* 1995. PENELOPE: An algorithm for Monte Carlo simulation of the penetration and energy loss of electrons and positrons in matter. *Nuclear Instruments and Methods in Physics Research Section B: Beam Interactions with Materials and Atoms*, 100, 31-46.
- Barrett, J. F. & Keat, N. 2004. Artifacts in CT: Recognition and Avoidance 1. *Radiographics*, 24, 1679-1691.
- Battistoni, G., Muraro, S., *et al.* 2007. The FLUKA code: description and benchmarking. *Journal Name: AIP Conference Proceedings; Journal Volume: 896; Journal Issue: 1; Conference: Hadronic shower simulation workshop, Batavia, IL (United States), 6-8 Sep 2006; Other Information: DOI: 10.1063/1.2720455; (c) 2007 American Institute of Physics; Country of input: International Atomic Energy Agency (IAEA), Medium: X; Size: page(s) 31-49.*
- Beddar, A. S., Kainz, K., *et al.* 2007. Correlation between internal fiducial tumor motion and external marker motion for liver tumors imaged with 4D-CT. *International Journal of Radiation Oncology*Biological*Physics*, 67, 630-638.
- Beitler, J. J., Badine, E. A., *et al.* 2006. Stereotactic body radiation therapy for nonmetastatic lung cancer: an analysis of 75 patients treated over 5 years. *Int J Radiat Oncol Biol Phys*, 65, 100-6.
- Benedict, S. H., Yenice, K. M., *et al.* 2010. Stereotactic body radiation therapy: the report of AAPM Task Group 101. *Med Phys*, 37, 4078-101.
- Bielajew, A. F. 2001. *Fundamentals of the Monte Carlo method for neutral and charged particle transport*, University of Michigan, Michigan.
- Biggs, F., Lighthill, R 1990. Preprint Sandia Laboratory., *SAND*, 87-0070.
- Bjarngard, B. E., Tsai, J. S., *et al.* 1989. Attenuation in very narrow photon beams. *Radiat Res*, 118, 195-200.

- Bjarngard, B. E., Tsai, J. S., *et al.* 1990. Doses on the central axes of narrow 6-MV x-ray beams. *Med Phys*, 17, 794-9.
- Blomgren, H., Lax, I., *et al.* 1995. Stereotactic high dose fraction radiation therapy of extracranial tumors using an accelerator. Clinical experience of the first thirty-one patients. *Acta Oncol*, 34, 861-70.
- Bortfeld, T., Jiang, S. B., *et al.* 2004. Effects of motion on the total dose distribution. *Semin Radiat Oncol*, 14, 41-51.
- Bradley, J., Thorstad, W. L., *et al.* 2004. Impact of FDG-PET on radiation therapy volume delineation in non-small-cell lung cancer. *Int J Radiat Oncol Biol Phys*, 59, 78-86.
- Bradley, J. D., Nofal, A. N., *et al.* 2006. Comparison of helical, maximum intensity projection (MIP), and averaged intensity (AI) 4D CT imaging for stereotactic body radiation therapy (SBRT) planning in lung cancer. *Radiotherapy and Oncology*, 81, 264-268.
- Briesmeister, J. F. 1986. MCNP: a general Monte Carlo code for neutron and photon transport.
- Britton, K. R., Starkschall, G., *et al.* 2007. Assessment of Gross Tumor Volume Regression and Motion Changes During Radiotherapy for Non-Small-Cell Lung Cancer as Measured by Four-Dimensional Computed Tomography. *International Journal of Radiation Oncology*Biography*Physics*, 68, 1036-1046.
- Butcher, J. C. & Messel, H. Electron number distribution in electron-photon showers in air and aluminium absorbers. *Nuclear Physics*, 20, 15-128.
- Cai, J., Read, P. W., *et al.* 2008. The effect of respiratory motion variability and tumor size on the accuracy of average intensity projection from four-dimensional computed tomography: an investigation based on dynamic MRI. *Med Phys*, 35, 4974-81.
- Callahan, J., Binns, D., *et al.* 2011. Motion effects on SUV and lesion volume in 3D and 4D PET scanning. *Australas Phys Eng Sci Med*, 34, 489-95.
- Callahan, J., Kron, T., *et al.* 2013. Validation of a 4D-PET Maximum Intensity Projection for Delineation of an Internal Target Volume. *International Journal of Radiation Oncology* Biology* Physics*.
- Callahan, J., Kron, T., *et al.* 2011. The clinical significance and management of lesion motion due to respiration during PET/CT scanning. *Cancer Imaging*, 11, 224-36.
- Cardinale, R. M., Wu, Q., *et al.* 1999. Determining the optimal block margin on the planning target volume for extracranial stereotactic radiotherapy. *Int J Radiat Oncol Biol Phys*, 45, 515-20.
- Carrasco, P., Jorner, N., *et al.* 2004. Comparison of dose calculation algorithms in phantoms with lung equivalent heterogeneities under conditions of lateral electronic disequilibrium. *Med Phys*, 31, 2899-911.
- Carrier, J. F., Archambault, L., *et al.* 2004. Validation of GEANT4, an object-oriented Monte Carlo toolkit, for simulations in medical physics. *Med Phys*, 31, 484-92.
- Cervino, L. I., Chao, A. K., *et al.* 2009. The diaphragm as an anatomic surrogate for lung tumor motion. *Phys Med Biol*, 54, 3529-41.
- Chauvie, S., Guatelli, S., *et al.* Year. Geant4 low energy electromagnetic physics. In: Nuclear Science Symposium Conference Record, 2004 IEEE, 16-22 Oct. 2004 2004. 1881-1885 Vol. 3.
- Chen, G. T., Kung, J. H., *et al.* 2004. Artifacts in computed tomography scanning of moving objects. *Semin Radiat Oncol*, 14, 19-26.
- Chen, Q. S., Weinhaus, M. S., *et al.* 2001. Fluoroscopic study of tumor motion due to breathing: facilitating precise radiation therapy for lung cancer patients. *Med Phys*, 28, 1850-6.
- Chibani, O. & Li, X. A. 2002. Monte Carlo dose calculations in homogeneous media and at interfaces: a comparison between GEPTS, EGSnrc, MCNP, and measurements. *Med Phys*, 29, 835-47.
- Chinneck, C. D., Mcjury, M., *et al.* 2010. The potential for undertaking slow CT using a modern CT scanner. *Br J Radiol*, 83, 687-93.
- Chuang, K.-S., Chen, T.-J., *et al.* 2006. Reduction of motion artifacts for PET imaging by respiratory correlated dynamic scanning. *Nuclear Instruments and Methods in Physics Research Section A: Accelerators, Spectrometers, Detectors and Associated Equipment*, 569, 458-461.
- Clements, N., Kron, T., *et al.* 2013. The effect of irregular breathing patterns on internal target volumes in four-dimensional CT and cone-beam CT images in the context of stereotactic lung radiotherapy. *Medical Physics*, 40, 021904.
- Collaboration, G. 1999. Geant4 physics reference manual.
- Cossmann, P. H., Stuessi, A., *et al.* 2007. Video-Coaching as Biofeedback-tool to Improve Gated Treatments: 2 Years Clinical Experience. *International Journal of Radiation Oncology*Biography*Physics*, 69, S645-S645.
- Cui, G., Gopalan, S., *et al.* 2010. Commissioning and quality assurance for a respiratory training system based on audiovisual biofeedback. *J Appl Clin Med Phys*, 11, 3262.
- Cullen, D., Perkins, S., Seltzer, S.M. November 1991. Tables and Graphs of Electron Interaction Cross 10 eV to 100 GeV Derived from the LLNL Evaluated Electron Data Library (EEDL), Z = 1 - 100. *Lawrence Livermore National Laboratory*, 31.
- Cullen, D. E. 1995. A simple model of photon transport. *Nuclear Instruments and Methods in Physics Research Section B: Beam Interactions with Materials and Atoms*, 101, 499-510.

- Cullen, D. E., Et Al. October 1991. Tables and Graphs of Atomic Subshell and Relaxation Data Derived from the LLNL Evaluated Atomic Data Library (EADL), Z = 1 - 100. *Lawrence Livermore National Laboratory*, 30.
- D'souza, W. D., Nazareth, D. P., et al. 2007. The Use of Gated and 4D CT Imaging in Planning for Stereotactic Body Radiation Therapy. *Medical dosimetry : official journal of the American Association of Medical Dosimetrists*, 32, 92-101.
- De Koste, J. R., Lagerwaard, F. J., et al. 2003. Are multiple CT scans required for planning curative radiotherapy in lung tumors of the lower lobe? *Int J Radiat Oncol Biol Phys*, 55, 1394-9.
- Descourt, P., Segars, W. P., et al. Year. RTNCAT (Real Time NCAT): Implementing Real Time physiological movement of voxelized phantoms in GATE. In: Nuclear Science Symposium Conference Record, 2006. IEEE, Oct. 29 2006-Nov. 1 2006 2006. 3163-3165.
- Ding, G. X., Duggan, D. M., et al. 2007. Impact of inhomogeneity corrections on dose coverage in the treatment of lung cancer using stereotactic body radiation therapy. *Med Phys*, 34, 2985-94.
- Dinkel, J., Hintze, C., et al. 2009. [Computed tomography of the lungs. A step into the fourth dimension]. *Radiologe*, 49, 698-704.
- Disher, B., Hajdok, G., et al. 2012. An in-depth Monte Carlo study of lateral electron disequilibrium for small fields in ultra-low density lung: implications for modern radiation therapy. *Phys Med Biol*, 57, 1543-59.
- Doucet, R., Olivares, M., et al. 2003. Comparison of measured and Monte Carlo calculated dose distributions in inhomogeneous phantoms in clinical electron beams. *Phys Med Biol*, 48, 2339-54.
- Dunn, L., Kron, T., et al. 2011a. A programmable motion phantom for quality assurance of motion management in radiotherapy. *Australasian Physical & Engineering Science in Medicine*, 1-8.
- Dunn, L., Kron, T., et al. 2011b. A programmable motion phantom for quality assurance of motion management in radiotherapy. *Australas Phys Eng Sci Med*.
- Dunn, L., Kron, T., et al. 2012. A phantom for testing of 4D-CT for radiotherapy of small lesions. *Med Phys*, 39, 5372.
- Edet-Sanson, A., Dubray, B., et al. Serial assessment of FDG-PET FDG uptake and functional volume during radiotherapy (RT) in patients with non-small cell lung cancer (NSCLC). *Radiotherapy and Oncology*.
- Ehler, E. D. & Tomé, W. A. 2008. Lung 4D-IMRT treatment planning: An evaluation of three methods applied to four-dimensional data sets. *Radiotherapy and Oncology*, 88, 319-325.
- Ekberg, L., Holmberg, O., et al. 1998. What margins should be added to the clinical target volume in radiotherapy treatment planning for lung cancer? *Radiother Oncol*, 48, 71-7.
- Elwood, J., Cox, B., et al. 1992. *Effectiveness of Breast Cancer Screening by Mammography in Younger Women*, Department of Health.
- Engelsman, M., Damen, E. M., et al. 2001. Impact of simple tissue inhomogeneity correction algorithms on conformal radiotherapy of lung tumours. *Radiother Oncol*, 60, 299-309.
- Erridge, S. C., Seppenwoolde, Y., et al. 2003. Portal imaging to assess set-up errors, tumor motion and tumor shrinkage during conformal radiotherapy of non-small cell lung cancer. *Radiother Oncol*, 66, 75-85.
- Esthappan, J., Santanam, L., et al. 2008. Dosimetric Evaluation of 4D-CT-based Treatment Planning for SBRT of Mobile Lung Tumors. *International Journal of Radiation Oncology*Biological*Physics*, 72, S628-S629.
- Ezhil, M., Vedam, S., et al. 2009. Determination of patient-specific internal gross tumor volumes for lung cancer using four-dimensional computed tomography. *Radiat. Oncol.*, 4, 4.
- Faddegon, B. A., Asai, M., et al. 2008. Benchmarking of Monte Carlo simulation of bremsstrahlung from thick targets at radiotherapy energies. *Med Phys*, 35, 4308-17.
- Faddegon, B. A., Kawrakow, I., et al. 2009. The accuracy of EGSnrc, Geant4 and PENELOPE Monte Carlo systems for the simulation of electron scatter in external beam radiotherapy. *Phys Med Biol*, 54, 6151-63.
- Fitzpatrick, M. J., Starkschall, G., et al. 2005. A novel platform simulating irregular motion to enhance assessment of respiration-correlated radiation therapy procedures. *J Appl Clin Med Phys*, 6, 13-21.
- Fletcher, S. W., Black, W., et al. 1993. Report of the international workshop on screening for breast cancer. *J Natl Cancer Inst*, 85, 1644-1656.
- Ford, E. C., Mageras, G. S., et al. 2003a. Respiration-correlated spiral CT: a method of measuring respiratory-induced anatomic motion for radiation treatment planning. *Med. Phys.*, 30, 88-97.
- Ford, E. C., Mageras, G. S., et al. 2003b. Respiration-correlated spiral CT: a method of measuring respiratory-induced anatomic motion for radiation treatment planning. *Med Phys*, 30, 88-97.
- Fotina, I., Kragl, G., et al. 2011. Clinical comparison of dose calculation using the enhanced collapsed cone algorithm vs. a new Monte Carlo algorithm. *Strahlenther Onkol*, 187, 433-41.
- Fowler, J. F., Tome, W. A., et al. 2004. A challenge to traditional radiation oncology. *Int J Radiat Oncol Biol Phys*, 60, 1241-56.

- Fukumoto, S., Shirato, H., *et al.* 2002. Small-volume image-guided radiotherapy using hypofractionated, coplanar, and noncoplanar multiple fields for patients with inoperable Stage I nonsmall cell lung carcinomas. *Cancer*, 95, 1546-53.
- García Vicente, A. M., Soriano Castrejón, A., *et al.* 18F-FDG PET/CT and respiratory synchronization: effect in the detection and classification of pulmonary lesions. *Revista Española de Medicina Nuclear (English Edition)*, 28, 181-187.
- García Vicente, A. M., Soriano Castrejón, A., *et al.* 2009. 18F-FDG PET/CT and respiratory synchronization: effect in the detection and classification of pulmonary lesions. *Revista Española de Medicina Nuclear (English Edition)*, 28, 181-187.
- García Vicente, A. M., Soriano Castrejón, A. M., *et al.* 2010. (18)F-FDG PET-CT respiratory gating in characterization of pulmonary lesions: approximation towards clinical indications. *Ann Nucl Med*, 24, 207-14.
- Gavrila, M. 1959. Relativistic K-Shell Photoeffect. *Physical Review*, 113, 514.
- George, R., Chung, T. D., *et al.* 2006. Audio-visual biofeedback for respiratory-gated radiotherapy: Impact of audio instruction and audio-visual biofeedback on respiratory-gated radiotherapy. *Int J Radiat Oncol Biol Phys*, 65, 924-933.
- George, R., Vedam, S. S., *et al.* 2005. The application of the sinusoidal model to lung cancer patient respiratory motion. *Med Phys*, 32, 2850-61.
- Gierga, D. P., Brewer, J., *et al.* 2005. The correlation between internal and external markers for abdominal tumors: Implications for respiratory gating. *International Journal of Radiation Oncology*Biological*Physics*, 61, 1551-1558.
- Gierga, D. P., Chen, G. T. Y., *et al.* 2004. Quantification of respiration-induced abdominal tumor motion and its impact on IMRT dose distributions. *International Journal of Radiation Oncology*Biological*Physics*, 58, 1584-1595.
- Giraud, P., De Rycke, Y., *et al.* 2001. Conformal radiotherapy (CRT) planning for lung cancer: analysis of intrathoracic organ motion during extreme phases of breathing. *Int J Radiat Oncol Biol Phys*, 51, 1081-92.
- Giraud, P., Elles, S., *et al.* 2002. Conformal radiotherapy for lung cancer: different delineation of the gross tumor volume (GTV) by radiologists and radiation oncologists. *Radiotherapy and Oncology*, 62, 27-36.
- Glide-Hurst, C. K., Hugo, G. D., *et al.* 2008. A simplified method of four-dimensional dose accumulation using the mean patient density representation. *Med Phys*, 35, 5269-77.
- Goudsmit, S. & Saunderson, J. L. 1940. Multiple Scattering of Electrons. *Physical Review*, 57, 552.
- Guckenberger, M., Wilbert, J., *et al.* 2007. Four-Dimensional Treatment Planning for Stereotactic Body Radiotherapy. *International Journal of Radiation Oncology*Biological*Physics*, 69, 276-285.
- Günther, P., Schenk, J. P., *et al.* 2004. Abdominal Tumours in Children: 3-D Visualisation and Surgical Planning. *Eur J Pediatr Surg*, 14, 316-321.
- Han, K., Cheung, P., *et al.* 2010. A comparison of two immobilization systems for stereotactic body radiation therapy of lung tumors. *Radiother Oncol*, 95, 103-8.
- Hanley, J., Debois, M. M., *et al.* 1999. Deep inspiration breath-hold technique for lung tumors: the potential value of target immobilization and reduced lung density in dose escalation. *Int J Radiat Oncol Biol Phys*, 45, 603-11.
- Heinzerling, J., Bland, R., *et al.* 2011. Dosimetric and motion analysis of margin-intensive therapy by stereotactic ablative radiotherapy for resectable pancreatic cancer. *Radiation Oncology*, 6, 146.
- Heinzerling, J. H., Anderson, J. F., *et al.* 2008. Four-dimensional computed tomography scan analysis of tumor and organ motion at varying levels of abdominal compression during stereotactic treatment of lung and liver. *Int J Radiat Oncol Biol Phys*, 70, 1571-8.
- Heitler, W. 1954. *The Quantum Theory of Radiation*, Clarendon Press.
- Heywood, J. B. 1988. *Internal combustion engine fundamentals*, McGraw-Hill.
- Hiraoka, M. & Ishikura, S. 2007. A Japan clinical oncology group trial for stereotactic body radiation therapy of non-small cell lung cancer. *J Thorac Oncol*, 2, S115-7.
- Hiraoka, M., Matsuo, Y., *et al.* 2007. Stereotactic body radiation therapy (SBRT) for early-stage lung cancer. *Cancer Radiother*, 11, 32-5.
- Hiraoka, M., Matsuo, Y., *et al.* 2010. Stereotactic body radiation therapy for lung cancer: achievements and perspectives. *Jpn J Clin Oncol*, 40, 846-54.
- Hiraoka, M. & Nagata, Y. 2004. Stereotactic body radiation therapy for early-stage non-small-cell lung cancer: the Japanese experience. *Int J Clin Oncol*, 9, 352-5.
- Hof, H., Herfarth, K. K., *et al.* 2003. Stereotactic single-dose radiotherapy of stage I non-small-cell lung cancer (NSCLC). *Int J Radiat Oncol Biol Phys*, 56, 335-41.
- Hoisak, J. D., Sixel, K. E., *et al.* 2004. Correlation of lung tumor motion with external surrogate indicators of respiration. *Int J Radiat Oncol Biol Phys*, 60, 1298-306.
- Hounsfield, G. N. 1973. Computerized transverse axial scanning (tomography). 1. Description of system. *Br J Radiol*, 46, 1016-22.

- Huang, L., Park, K., *et al.* 2010a. A study on the dosimetric accuracy of treatment planning for stereotactic body radiation therapy of lung cancer using average and maximum intensity projection images. *Radiother Oncol*, 96, 48-54.
- Huang, L., Park, K., *et al.* 2010b. A study on the dosimetric accuracy of treatment planning for stereotactic body radiation therapy of lung cancer using average and maximum intensity projection images. *Radiotherapy and Oncology*, 96, 48-54.
- Hubbell, J. H., Gimm, H.A., Overbo I 1980. Pair, Triplet, and Total Atomic Cross Sections (and Mass Attenuation Coefficients) for 1 MeV-100 GeV Photons in Elements Z = 1 to 100. *J. Phys. Chem.*, 8, 1023.
- Hubbell, J. H., Overbo I. 1979. Relativistic Atomic Form Factors and Photon Coherent Scattering Cross Sections. *J. Phys. Chem.*, 8.
- Hubner, K. F., Buonocore, E., *et al.* 1996. Differentiating benign from malignant lung lesions using "quantitative" parameters of FDG PET images. *Clin Nucl Med*, 21, 941-9.
- Hugo, G., Vargas, C., *et al.* 2006. Changes in the respiratory pattern during radiotherapy for cancer in the lung. *Radiotherapy and Oncology*, 78, 326-331.
- Hunjan, S., Starkschall, G., *et al.* 2010. Lack of Correlation Between External Fiducial Positions and Internal Tumor Positions During Breath-Hold CT. *International Journal of Radiation Oncology*Biophysics*, 76, 1586-1591.
- Icru 1993. Prescribing, Recording and Reporting Photon Beam Therapy. *ICRU Report No 50*. Bethesda, MD: International Commission on Radiation Units and Measurement.
- Icru 1999. Prescribing, Recording and Reporting Photon Beam Therapy (Supplement to ICRU Report 50). *ICRU Report No 62*. Bethesda, MD: International Commission on Radiation Units and Measurements
- Ionascu, D., Jiang, S. B., *et al.* 2007. Internal-external correlation investigations of respiratory induced motion of lung tumors. *Med Phys*, 34, 3893-903.
- Jan, S., Benoit, D., *et al.* 2011. GATE V6: a major enhancement of the GATE simulation platform enabling modelling of CT and radiotherapy. *Phys Med Biol*, 56, 881-901.
- Jan, S., Santin, G., *et al.* 2004. GATE: a simulation toolkit for PET and SPECT. *Phys Med Biol*, 49, 4543-61.
- Jiang, H. & Paganetti, H. 2004. Adaptation of GEANT4 to Monte Carlo dose calculations based on CT data. *Med Phys*, 31, 2811-8.
- Jiang, S. B., Pope, C., *et al.* 2003. An experimental investigation on intra-fractional organ motion effects in lung IMRT treatments. *Phys Med Biol*, 48, 1773-84.
- Jiang, S. B., Wolfgang, J., *et al.* 2008. Quality assurance challenges for motion-adaptive radiation therapy: gating, breath holding, and four-dimensional computed tomography. *Int J Radiat Oncol Biol Phys*, 71, S103-7.
- Jiang, Y., Cerviño, L., *et al.* 2009. Spatial Variation of the Correlation between External Surface and Internal Tumor Motion. *International Journal of Radiation Oncology*Biophysics*, 75, S593-S593.
- Johns, H. E. & Cunningham, J. R. 1983. *The physics of radiology*, Charles C. Thomas.
- Kairn, T., Aland, T., *et al.* 2010. Adapting a generic BEAMnrc model of the BrainLAB m3 micro-multileaf collimator to simulate a local collimation device. *Phys Med Biol*, 55, N451-63.
- Kairn, T., Kenny, J., *et al.* 2010. Modeling a complex micro-multileaf collimator using the standard BEAMnrc distribution. *Med Phys*, 37, 1761-7.
- Kalender, W. A. 2006. X-ray computed tomography. *Phys Med Biol*, 51, R29-43.
- Kashani, R., Lam, K., *et al.* 2007. Technical note: a deformable phantom for dynamic modeling in radiation therapy. *Med Phys*, 34, 199-201.
- Kavanagh, B. D., Ding, M., *et al.* 2006. The dosimetric effect of inhomogeneity correction in dynamic conformal arc stereotactic body radiation therapy for lung tumors. *J Appl Clin Med Phys*, 7, 58-63.
- Kawrakow, I. 2000a. Accurate condensed history Monte Carlo simulation of electron transport. I. [small-caps EGS]nrc, the new [small-caps EGS4] version. *Med Phys*, 27, 485-498.
- Kawrakow, I. 2000b. Accurate condensed history Monte Carlo simulation of electron transport. I. EGSnrc, the new EGS4 version. *Med Phys*, 27, 485-98.
- Kawrakow, I. & Bielajew, A. F. 1998. On the condensed history technique for electron transport. *Nuclear Instruments and Methods in Physics Research Section B: Beam Interactions with Materials and Atoms*, 142, 253-280.
- Keall, P. 2004a. 4-dimensional computed tomography imaging and treatment planning. *Semin. Radiat. Oncol.*, 14, 81-90.
- Keall, P. 2004b. 4-dimensional computed tomography imaging and treatment planning. *Semin Radiat Oncol*, 14, 81-90.
- Keall, P. J., Joshi, S., *et al.* 2003. 4-Dimensional radiotherapy planning. *International Journal of Radiation Oncology*Biophysics*, 57, S233-S233.
- Keall, P. J., Joshi, S., *et al.* 2005. Four-dimensional radiotherapy planning for DMLC-based respiratory motion tracking. *Med Phys*, 32, 942-51.

- Keall, P. J., Kini, V. R., *et al.* 2002. Potential radiotherapy improvements with respiratory gating. *Australas. Phys. Eng. Sci. Med.*, 25, 1-6.
- Keall, P. J., Mageras, G. S., *et al.* 2006a. The management of respiratory motion in radiation oncology report of AAPM Task Group 76. *Med Phys*, 33, 3874-900.
- Keall, P. J., Mageras, G. S., *et al.* 2006b. The management of respiratory motion in radiation oncology report of AAPM Task Group 76. *Med. Phys.*, 33, 3874-900.
- Keall, P. J., Siebers, J. V., *et al.* 2004. Monte Carlo as a four-dimensional radiotherapy treatment-planning tool to account for respiratory motion. *Phys Med Biol*, 49, 3639-48.
- Keall, P. J., Starkschall, G., *et al.* 2004. Acquiring 4D thoracic CT scans using a multislice helical method. *Phys. Med. Biol.*, 49, 2053-67.
- Kimura, A., Aso, T., *et al.* Year. DICOM data handling for Geant4-based medical physics application. *In: Nuclear Science Symposium Conference Record, 2004 IEEE, 16-22 Oct. 2004 2004. 2124-2127 Vol. 4.*
- Kimura, A., Yamashita, T., *et al.* Year. DICOM-RT extension support of visualization tool for radiotherapy simulation. *In: Nuclear Science Symposium Conference Record (NSS/MIC), 2010 IEEE, Oct. 30 2010-Nov. 6 2010 2010. 1856-1859.*
- Kini, V. R., Vedam, S. S., *et al.* 2003. Patient training in respiratory-gated radiotherapy. *Med Dosim*, 28, 7-11.
- Kissick, M. W., Flynn, R. T., *et al.* 2008. On the impact of longitudinal breathing motion randomness for tomotherapy delivery. *Phys Med Biol*, 53, 4855-73.
- Krane, K. S. & Halliday, D. 1987. *Introductory nuclear physics*, Wiley.
- Kron, T., Clements, N., *et al.* 2011. Radiochromic film for individual patient QA in extracranial stereotactic lung radiotherapy. *Radiation Measurements*.
- Kubo, H. D. & Hill, B. C. 1996. Respiration gated radiotherapy treatment: a technical study. *Phys Med Biol*, 41, 83-91.
- Kubo, H. D., Len, P. M., *et al.* 2000. Breathing-synchronized radiotherapy program at the University of California Davis Cancer Center. *Med Phys*, 27, 346-53.
- Kuechler, S., Hoinkis, C., *et al.* 2004. Respiratory motion - first investigations on the optimization of gating parameters. *International Journal of Radiation Oncology*Biophysics*, 60, S579-S579.
- Kupelian, P., Willoughby, T., *et al.* 2007. Multi-institutional clinical experience with the Calypso System in localization and continuous, real-time monitoring of the prostate gland during external radiotherapy. *Int J Radiat Oncol Biol Phys*, 67, 1088-98.
- Kwa, S. L., Lebesque, J. V., *et al.* 1998. Radiation pneumonitis as a function of mean lung dose: an analysis of pooled data of 540 patients. *Int J Radiat Oncol Biol Phys*, 42, 1-9.
- Kwa, S. L., Theuvs, J. C., *et al.* 1998. Evaluation of two dose-volume histogram reduction models for the prediction of radiation pneumonitis. *Radiother Oncol*, 48, 61-9.
- Lamare, F., Turzo, A., *et al.* 2006. Validation of a Monte Carlo simulation of the Philips Allegro/GEMINI PET systems using GATE. *Phys Med Biol*, 51, 943-62.
- Lardinois, D., Weder, W., *et al.* 2003. Staging of non-small-cell lung cancer with integrated positron-emission tomography and computed tomography. *N Engl J Med*, 348, 2500-7.
- Larson, S. M., Nehmeh, S. A., *et al.* 2005. PET/CT in non-small-cell lung cancer: value of respiratory-gated PET. *Chang Gung Med J*, 28, 306-14.
- Lax, I., Blomgren, H., *et al.* 1994. Stereotactic radiotherapy of malignancies in the abdomen. Methodological aspects. *Acta Oncol*, 33, 677-83.
- Lazaro, D., Buvat, I., *et al.* 2004. Validation of the GATE Monte Carlo simulation platform for modelling a CsI(Tl) scintillation camera dedicated to small-animal imaging. *Phys Med Biol*, 49, 271-85.
- Lechner, A., Pia, M. G., *et al.* Year. Validation of Geant4 low energy physics models against electron energy deposition and backscattering data. *In: Nuclear Science Symposium Conference Record, 2007. NSS '07. IEEE, Oct. 26 2007-Nov. 3 2007 2007. 2001-2007.*
- Lee, E. K., Fox, T., *et al.* 2006. Simultaneous beam geometry and intensity map optimization in intensity-modulated radiation therapy. *Int J Radiat Oncol Biol Phys*, 64, 301-20.
- Lee, S. W., Choi, E. K., *et al.* 2003. Stereotactic body frame based fractionated radiosurgery on consecutive days for primary or metastatic tumors in the lung. *Lung Cancer*, 40, 309-15.
- Leksell, L. 1983. Stereotactic radiosurgery. *Journal of Neurology, Neurosurgery & Psychiatry*, 46, 797-803.
- Lewis, H. W. 1950. Multiple Scattering in an Infinite Medium. *Physical Review*, 78, 526-529.
- Liu, C., Pierce, L. A., 2nd, *et al.* 2009. The impact of respiratory motion on tumor quantification and delineation in static PET/CT imaging. *Phys Med Biol*, 54, 7345-62.

- Locklin, J. K., Yanof, J., *et al.* 2007. Respiratory Biofeedback during CT-guided Procedures. *Journal of Vascular and Interventional Radiology*, 18, 749-755.
- Low, D. A., Nystrom, M., *et al.* 2003. A method for the reconstruction of four-dimensional synchronized CT scans acquired during free breathing. *Med. Phys.*, 30, 1254-63.
- Lujan, A. E., Balter, J. M., *et al.* 2003. A method for incorporating organ motion due to breathing into 3D dose calculations in the liver: sensitivity to variations in motion. *Med Phys*, 30, 2643-9.
- Lujan, A. E., Larsen, E. W., *et al.* 1999. A method for incorporating organ motion due to breathing into 3D dose calculations. *Med Phys*, 26, 715-20.
- Lupi, A., Zarocolo, M., *et al.* 2009. The effect of 18F-FDG-PET/CT respiratory gating on detected metabolic activity in lung lesions. *Ann Nucl Med*, 23, 191-6.
- Mac Manus, M., Hicks, R. J., *et al.* 2006. Role of PET-CT in the optimization of thoracic radiotherapy. *J Thorac Oncol*, 1, 81-4.
- Mac Manus, M. P., Everitt, S., *et al.* 2013. The use of fused PET/CT images for patient selection and radical radiotherapy target volume definition in patients with non-small cell lung cancer: Results of a prospective study with mature survival data. *Radiotherapy and Oncology*.
- Mac Manus, M. P. & Hicks, R. J. 2012. The Role of Positron Emission Tomography/Computed Tomography in Radiation Therapy Planning for Patients with Lung Cancer. *Semin Nucl Med*, 42, 308-319.
- Machtay, M., Bae, K., *et al.* 2012. Higher biologically effective dose of radiotherapy is associated with improved outcomes for locally advanced non-small cell lung carcinoma treated with chemoradiation: an analysis of the Radiation Therapy Oncology Group. *Int J Radiat Oncol Biol Phys*, 82, 425-34.
- Macmanus, M., Nestle, U., *et al.* 2009. Use of PET and PET/CT for Radiation Therapy Planning: IAEA expert report 2006–2007. *Radiotherapy and oncology : journal of the European Society for Therapeutic Radiology and Oncology*, 91, 85-94.
- Mageras, G. S., Pevsner, A., *et al.* 2004a. Measurement of lung tumor motion using respiration-correlated CT. *International Journal of Radiation Oncology*Biophysics*, 60, 933-941.
- Mageras, G. S., Pevsner, A., *et al.* 2004b. Measurement of lung tumor motion using respiration-correlated CT. *Int J Radiat Oncol Biol Phys*, 60, 933-41.
- Mageras, G. S. & Yorke, E. 2004. Deep inspiration breath hold and respiratory gating strategies for reducing organ motion in radiation treatment. *Semin Radiat Oncol*, 14, 65-75.
- Maigne, L., Perrot, Y., *et al.* 2011. Comparison of GATE/GEANT4 with EGSnrc and MCNP for electron dose calculations at energies between 15 keV and 20 MeV. *Phys Med Biol*, 56, 811-27.
- Manual, G. P. R. 2010.
- Martens, C., Reynaert, N., *et al.* 2002. Underdosage of the upper-airway mucosa for small fields as used in intensity-modulated radiation therapy: a comparison between radiochromic film measurements, Monte Carlo simulations, and collapsed cone convolution calculations. *Med Phys*, 29, 1528-35.
- Maughan, R. L., Chuba, P. J., *et al.* 1997. The elemental composition of tumors: Kerma data for neutrons. *Med Phys*, 24, 1241-1244.
- McGarry, R. C., Papiez, L., *et al.* 2005. Stereotactic body radiation therapy of early-stage non-small-cell lung carcinoma: phase I study. *Int J Radiat Oncol Biol Phys*, 63, 1010-5.
- Metcalf, P., Kron, T., *et al.* 2007. *The Physics of Radiotherapy X-Rays and Electrons*, Medical Physics Publishing Corporation.
- Mohan, R., Chui, C., *et al.* 1985. Energy and angular distributions of photons from medical linear accelerators. *Med Phys*, 12, 592-597.
- Moore, G. E. 2006. Cramming more components onto integrated circuits, Reprinted from Electronics, volume 38, number 8, April 19, 1965, pp.114 ff. *Solid-State Circuits Newsletter, IEEE*, 11, 33-35.
- Muirhead, R., Mcnee, S. G., *et al.* 2008. Use of Maximum Intensity Projections (MIPs) for target outlining in 4DCT radiotherapy planning. *J Thorac Oncol*, 3, 1433-8.
- Murphy, M. J. 2004. Tracking moving organs in real time. *Semin Radiat Oncol*, 14, 91-100.
- Mutaf, Y. D., Antolak, J. A., *et al.* 2007. The impact of temporal inaccuracies on 4DCT image quality. *Med. Phys.*, 34, 1615-22.
- Mutaf, Y. D. & Brinkmann, D. H. 2008. An investigation of temporal resolution parameters in cine-mode four-dimensional computed tomography acquisition. *J. Appl. Clin. Med. Phys.*, 9, 2819.
- Mutic, S., Palta, J. R., *et al.* 2003. Quality assurance for computed-tomography simulators and the computed-tomography-simulation process: report of the AAPM Radiation Therapy Committee Task Group No. 66. *Med. Phys.*, 30, 2762-92.
- Nagata, Y., Matsuo, Y., *et al.* 2007. Current status of stereotactic body radiotherapy for lung cancer. *Int J Clin Oncol*, 12, 3-7.
- Nagata, Y., Takayama, K., *et al.* 2005. Clinical outcomes of a phase I/II study of 48 Gy of stereotactic body radiotherapy in 4 fractions for primary lung cancer using a stereotactic body frame. *Int J Radiat Oncol Biol Phys*, 63, 1427-31.

- Nagel, C. C., Bosmans, G., *et al.* 2006. Phased attenuation correction in respiration correlated computed tomography/positron emitted tomography. *Med Phys*, 33, 1840-7.
- Nakamura, M., Narita, Y., *et al.* 2009a. Effect of audio coaching on correlation of abdominal displacement with lung tumor motion. *Int J Radiat Oncol Biol Phys*, 75, 558-63.
- Nakamura, M., Narita, Y., *et al.* 2008. Geometrical differences in target volumes between slow CT and 4D CT imaging in stereotactic body radiotherapy for lung tumors in the upper and middle lobe. *Med Phys*, 35, 4142-8.
- Nakamura, M., Narita, Y., *et al.* 2009b. Impact of motion velocity on four-dimensional target volumes: a phantom study. *Med. Phys.*, 36, 1610-7.
- Nakayama, H., Mizowaki, T., *et al.* 2008. Development of a three-dimensionally movable phantom system for dosimetric verifications. *Med. Phys.*, 35.
- Negoro, Y., Nagata, Y., *et al.* 2001. The effectiveness of an immobilization device in conformal radiotherapy for lung tumor: reduction of respiratory tumor movement and evaluation of the daily setup accuracy. *Int J Radiat Oncol Biol Phys*, 50, 889-98.
- Nehmeh, S. A. & Erdi, Y. E. 2008. Respiratory motion in positron emission tomography/computed tomography: a review. *Semin Nucl Med*, 38, 167-76.
- Nehmeh, S. A., Erdi, Y. E., *et al.* 2002a. Effect of respiratory gating on quantifying PET images of lung cancer. *J Nucl Med*, 43, 876-81.
- Nehmeh, S. A., Erdi, Y. E., *et al.* 2002b. Effect of respiratory gating on reducing lung motion artifacts in PET imaging of lung cancer. *Med Phys*, 29, 366-71.
- Nehmeh, S. A., Erdi, Y. E., *et al.* 2007. Deep-inspiration breath-hold PET/CT of the thorax. *J Nucl Med*, 48, 22-6.
- Nehmeh, S. A., Erdi, Y. E., *et al.* 2004a. Four-dimensional (4D) PET/CT imaging of the thorax. *Med Phys*, 31, 3179-86.
- Nehmeh, S. A., Erdi, Y. E., *et al.* 2004b. Quantitation of respiratory motion during 4D-PET/CT acquisition. *Med Phys*, 31, 1333-8.
- Nehmeh, S. A., Erdi, Y. E., *et al.* 2003. Reduction of respiratory motion artifacts in PET imaging of lung cancer by respiratory correlated dynamic PET: methodology and comparison with respiratory gated PET. *J Nucl Med*, 44, 1644-8.
- Neicu, T., Shirato, H., *et al.* 2003. Synchronized moving aperture radiation therapy (SMART): average tumour trajectory for lung patients. *Phys Med Biol*, 48, 587-98.
- Nestle, U., Kremp, S., *et al.* 2006. Practical integration of [18F]-FDG-PET and PET-CT in the planning of radiotherapy for non-small cell lung cancer (NSCLC): The technical basis, ICRU-target volumes, problems, perspectives. *Radiotherapy and Oncology*, 81, 209-225.
- Neuner, G. A., Lu, W., *et al.* 2010. Biofeedback during 4D-CT Image Acquisition Does Not Enhance the Reliability of ITV-MIP for Radiation Treatment Planning of Thoracic and Abdominal Malignancies: A Prospective Trial. *International Journal of Radiation Oncology*Biophysics*, 78, S671-S671.
- Nioutsikou, E., Seppenwoolde, Y., *et al.* 2008. Dosimetric investigation of lung tumor motion compensation with a robotic respiratory tracking system: An experimental study. *Med. Phys.*, 35.
- Nishimaru, E., Utsunomiya, R., *et al.* 2005. [A new method of evaluating helical artifact by image subtraction technique]. *Nihon Hoshasen Gijutsu Gakkai Zasshi*, 61, 1021-6.
- Nyman, J., Johansson, K. A., *et al.* 2006. Stereotactic hypofractionated radiotherapy for stage I non-small cell lung cancer--mature results for medically inoperable patients. *Lung Cancer*, 51, 97-103.
- Ohuchi, N., Yoshida, K., *et al.* 1993. Improved Detection Rate of Early Breast Cancer in Mass Screening Combined with Mammography. *Cancer Science*, 84, 807-812.
- Onishi, H., Araki, T., *et al.* 2004. Stereotactic hypofractionated high-dose irradiation for stage I nonsmall cell lung carcinoma: clinical outcomes in 245 subjects in a Japanese multiinstitutional study. *Cancer*, 101, 1623-31.
- Onishi, H., Kuriyama, K., *et al.* 2004. Clinical outcomes of stereotactic radiotherapy for stage I non-small cell lung cancer using a novel irradiation technique: patient self-controlled breath-hold and beam switching using a combination of linear accelerator and CT scanner. *Lung Cancer*, 45, 45-55.
- Osman, M. M., Cohade, C., *et al.* 2003. Respiratory motion artifacts on PET emission images obtained using CT attenuation correction on PET-CT. *Eur J Nucl Med Mol Imaging*, 30, 603-6.
- Ozhasoglu, C. & Murphy, M. J. 2002. Issues in respiratory motion compensation during external-beam radiotherapy. *Int J Radiat Oncol Biol Phys*, 52, 1389-99.
- Paganetti, H. & Gottschalk, B. 2003. Test of GEANT3 and GEANT4 nuclear models for 160 MeV protons stopping in CH2. *Med Phys*, 30, 1926-31.
- Paganetti, H., Jiang, H., *et al.* 2004. Monte Carlo simulations with time-dependent geometries to investigate effects of organ motion with high temporal resolution. *Int J Radiat Oncol Biol Phys*, 60, 942-50.
- Pan, T. 2005. Comparison of helical and cine acquisitions for 4D-CT imaging with multislice CT. *Med Phys*, 32, 627-34.

- Pan, T., Lee, T. Y., *et al.* 2004. 4D-CT imaging of a volume influenced by respiratory motion on multi-slice CT. *Med. Phys.*, 31, 333-40.
- Pan, T., Sun, X., *et al.* 2008. A New Cost-effective and Workflow-efficient Amplitude-binning 4DCT. *International Journal of Radiation Oncology*Biophysics*, 72, S622-S622.
- Papanikolaou, N., Battista, J. J., *et al.* 2004. Tissue inhomogeneity corrections for megavoltage photon beams. In: COMMITTEE, R. T. (ed.) *AAPM Task Group No. 65*.
- Papiez, L. & Abolfath, R. M. 2008. Variable beam dose rate and DMLC IMRT to moving body anatomy. *Med Phys*, 35, 4837-48.
- Papiez, L., McMahon, R., *et al.* 2007. 4D DMLC leaf sequencing to minimize organ at risk dose in moving anatomy. *Med Phys*, 34, 4952-6.
- Papiez, L., Timmerman, R., *et al.* 2003. Extracranial stereotactic radioablation: physical principles. *Acta Oncol*, 42, 882-94.
- Parach, A. A. & Rajabi, H. 2011. A comparison between GATE4 results and MCNP4B published data for internal radiation dosimetry. *Nuklearmedizin*, 50, 122-33.
- Park, K., Huang, L., *et al.* 2009a. Do maximum intensity projection images truly capture tumor motion? *Int. J. Radiat. Oncol. Biol. Phys.*, 73, 618-25.
- Park, K., Huang, L., *et al.* 2009b. Do maximum intensity projection images truly capture tumor motion? *Int J Radiat Oncol Biol Phys*, 73, 618-25.
- Park, S. J., Ionascu, D., *et al.* 2008. Evaluation of the combined effects of target size, respiratory motion and background activity on 3D and 4D PET/CT images. *Phys Med Biol*, 53, 3661-79.
- Park, Y. K., Kim, S., *et al.* 2011. Quasi-breath-hold technique using personalized audio-visual biofeedback for respiratory motion management in radiotherapy. *Med Phys*, 38, 3114-24.
- Peng, Y., Vedam, S., *et al.* 2011. Implementation of feedback-guided voluntary breath-hold gating for cone beam CT-based stereotactic body radiotherapy. *Int J Radiat Oncol Biol Phys*, 80, 909-17.
- Pevsner, A., Nehmeh, S. A., *et al.* 2005. Effect of motion on tracer activity determination in CT attenuation corrected PET images: a lung phantom study. *Med Phys*, 32, 2358-62.
- Piegl, L. & Tiller, W. 1997. *The Nurbs Book*, New York, Springer - Verlag
- Plathow, C., Ley, S., *et al.* 2004. Analysis of intrathoracic tumor mobility during whole breathing cycle by dynamic MRI. *Int J Radiat Oncol Biol Phys*, 59, 952-9.
- Podgoršak, E. B. 2010. *Radiation Physics for Medical Physicists*, Springer.
- Podgoršak, E. B. & Agency, I. a. E. 2005. *Radiation oncology physics: a handbook for teachers and students*, International Atomic Energy Agency.
- Ponisich, F., Richter, C., *et al.* 2008. Attenuation correction of four dimensional (4D) PET using phase-correlated 4D-computed tomography. *Phys Med Biol*, 53, N259-68.
- Poon, E. & Verhaegen, F. 2005. Accuracy of the photon and electron physics in GEANT4 for radiotherapy applications. *Med Phys*, 32, 1696-711.
- Raghu, B. V., Amit, S., *et al.* 2008. Development and preliminary evaluation of a prototype audiovisual biofeedback device incorporating a patient-specific guiding waveform. *Phys Med Biol*, 53, N197.
- Rajagopalan, M. S. & Heron, D. E. 2010. Role of PET/CT imaging in stereotactic body radiotherapy. *Future Oncol*, 6, 305-17.
- Ramsey, C. R., Cordrey, I. L., *et al.* 1999. A comparison of beam characteristics for gated and nongated clinical x-ray beams. *Med Phys*, 26, 2086-91.
- Ramsey, C. R., Scaperth, D., *et al.* 1999. Clinical efficacy of respiratory gated conformal radiation therapy. *Med Dosim*, 24, 115-9.
- Remouchamps, V. M., Letts, N., *et al.* 2003a. Initial clinical experience with moderate deep-inspiration breath hold using an active breathing control device in the treatment of patients with left-sided breast cancer using external beam radiation therapy. *Int J Radiat Oncol Biol Phys*, 56, 704-15.
- Remouchamps, V. M., Letts, N., *et al.* 2003b. Three-dimensional evaluation of intra- and interfraction immobilization of lung and chest wall using active breathing control: a reproducibility study with breast cancer patients. *Int J Radiat Oncol Biol Phys*, 57, 968-78.
- Ren, Q., Nishioka, S., *et al.* 2007. Adaptive prediction of respiratory motion for motion compensation radiotherapy. *Phys Med Biol*, 52, 6651-61.
- Reyes, M., Malandain, G., *et al.* 2005. Respiratory motion correction in emission tomography image reconstruction. *Med Image Comput Assist Interv*, 8, 369-76.
- Riegel, A. C., Chang, J. Y., *et al.* 2009. Cine computed tomography without respiratory surrogate in planning stereotactic radiotherapy for non-small-cell lung cancer. *Int J Radiat Oncol Biol Phys*, 73, 433.

- Riegel, A. C., Sun, X., *et al.* 2008. Dose Calculation on Cine Respiration-averaged CT. *International Journal of Radiation Oncology*Biophysics*, 72, S636-S636.
- Rietzel, E. & Chen, G. T. 2006a. Improving retrospective sorting of 4D computed tomography data. *Med Phys*, 33, 377-9.
- Rietzel, E., Chen, G. T., *et al.* 2005a. Four-dimensional image-based treatment planning: Target volume segmentation and dose calculation in the presence of respiratory motion. *Int J Radiat Oncol Biol Phys*, 61, 1535-50.
- Rietzel, E., Chen, G. T., *et al.* 2003. 4D computed tomography for treatment planning. *International Journal of Radiation Oncology*Biophysics*, 57, S232-S233.
- Rietzel, E. & Chen, G. T. Y. 2006b. Deformable registration of 4D computed tomography data. *Med Phys*, 33, 4423-4430.
- Rietzel, E., Chen, G. T. Y., *et al.* 2005b. Four-dimensional image-based treatment planning: Target volume segmentation and dose calculation in the presence of respiratory motion. *International Journal of Radiation Oncology*Biophysics*, 61, 1535-1550.
- Rietzel, E., Liu, A. K., *et al.* 2008a. Maximum-intensity volumes for fast contouring of lung tumors including respiratory motion in 4DCT planning. *Int J Radiat Oncol Biol Phys*, 71, 1245-52.
- Rietzel, E., Liu, A. K., *et al.* 2004. Clinical implementation: 4D computed tomography for thoracic tumor treatment planning. *International Journal of Radiation Oncology*Biophysics*, 60, S609-S610.
- Rietzel, E., Liu, A. K., *et al.* 2008b. Maximum-Intensity Volumes for Fast Contouring of Lung Tumors Including Respiratory Motion in 4DCT Planning. *International Journal of Radiation Oncology*Biophysics*, 71, 1245-1252.
- Rietzel, E., Liu, A. K., *et al.* 2006a. Design of 4D treatment planning target volumes. *Int. J. Radiat. Oncol. Biol. Phys.*, 66, 287-95.
- Rietzel, E., Liu, A. K., *et al.* 2006b. Design of 4D treatment planning target volumes. *International Journal of Radiation Oncology*Biophysics*, 66, 287-295.
- Rietzel, E., Pan, T., *et al.* 2005. Four-dimensional computed tomography: image formation and clinical protocol. *Med Phys*, 32, 874-89.
- Rogers, D. W. 2006. Fifty years of Monte Carlo simulations for medical physics. *Phys Med Biol*, 51, R287-301.
- Rogers, D. W., Faddegon, B. A., *et al.* 1995. BEAM: a Monte Carlo code to simulate radiotherapy treatment units. *Med Phys*, 22, 503-24.
- Rosenzweig, K. E., Hanley, J., *et al.* 2000. The deep inspiration breath-hold technique in the treatment of inoperable non-small-cell lung cancer. *Int J Radiat Oncol Biol Phys*, 48, 81-7.
- Sadi, F., Lee, S. Y., *et al.* 2010. Removal of ring artifacts in computed tomographic imaging using iterative center weighted median filter. *Comput Biol Med*, 40, 109-18.
- Saito, T., Sakamoto, T., *et al.* 2009. Comparison of gating around end-expiration and end-inspiration in radiotherapy for lung cancer. *Radiotherapy and Oncology*, 93, 430-435.
- Saito, T., Sakamoto, T., *et al.* 2010. Predictive factors for lung dose reduction by respiratory gating at radiotherapy for lung cancer. *J Radiat Res (Tokyo)*, 51, 691-8.
- Saito, T., Sakamoto, T., *et al.* 2011. Effect of gating window width on lung dosimetric parameters and on treatment time at gated radiotherapy for lung cancer. *Acta Oncol.*
- Santanam, L., Malinowski, K., *et al.* 2008. Fiducial-Based Translational Localization Accuracy of Electromagnetic Tracking System and On-Board Kilovoltage Imaging System. *International Journal of Radiation Oncology*Biophysics*, 70, 892-899.
- Sato, J. & Robbins, P. A. 2001. Methods for averaging irregular respiratory flow profiles in awake humans. *J Appl Physiol*, 90, 705-12.
- Schmidtlein, C. R., Kirov, A. S., *et al.* 2006. Validation of GATE Monte Carlo simulations of the GE Advance/Discovery LS PET scanners. *Med Phys*, 33, 198-208.
- Schuring, D. & Hurkmans, C. W. 2008. Developing and evaluating stereotactic lung RT trials: what we should know about the influence of inhomogeneity corrections on dose. *Radiat Oncol*, 3, 21.
- Schweikard, A., Shiomi, H., *et al.* 2004. Respiration tracking in radiosurgery. *Med Phys*, 31, 2738-41.
- Seco, J., Sharp, G. C., *et al.* 2008. Dosimetric impact of motion in free-breathing and gated lung radiotherapy: a 4D Monte Carlo study of intrafraction and interfraction effects. *Med Phys*, 35, 356-66.
- Segars, W. P., Mahesh, M., *et al.* 2008. Realistic CT simulation using the 4D XCAT phantom. *Med Phys*, 35, 3800-8.
- Segars, W. P., Sturgeon, G., *et al.* 2010. 4D XCAT phantom for multimodality imaging research. *Med Phys*, 37, 4902-15.
- Segars, W. P., Tsui, B. M., *et al.* 2004. Development of a 4-D digital mouse phantom for molecular imaging research. *Mol Imaging Biol*, 6, 149-59.
- Seki, S., Kunieda, E., *et al.* 2007. Differences in the definition of internal target volumes using slow CT alone or in combination with thin-slice CT under breath-holding conditions during the planning of stereotactic radiotherapy for lung cancer. *Radiotherapy and Oncology*, 85, 443-449.

- Seltzer, S. M. & Berger, M. J. 1985. Bremsstrahlung spectra from electron interactions with screened atomic nuclei and orbital electrons. *Nuclear Instruments and Methods in Physics Research Section B: Beam Interactions with Materials and Atoms*, 12, 95-134.
- Senan, S. & De Ruysscher, D. 2005. Critical review of PET-CT for radiotherapy planning in lung cancer. *Critical Reviews in Oncology/Hematology*, 56, 345-351.
- Senan, S., De Ruysscher, D., *et al.* 2004. Literature-based recommendations for treatment planning and execution in high-dose radiotherapy for lung cancer. *Radiother Oncol*, 71, 139-46.
- Seppenwoolde, Y., Lebesque, J. V., *et al.* 2003. Comparing different NTCP models that predict the incidence of radiation pneumonitis. Normal tissue complication probability. *Int J Radiat Oncol Biol Phys*, 55, 724-35.
- Seppenwoolde, Y., Shirato, H., *et al.* 2002a. Precise and real-time measurement of 3D tumor motion in lung due to breathing and heartbeat, measured during radiotherapy. *Int J Radiat Oncol Biol Phys*, 53, 822-34.
- Seppenwoolde, Y., Shirato, H., *et al.* 2002b. Precise and real-time measurement of 3D tumor motion in lung due to breathing and heartbeat, measured during radiotherapy. *Int. J. Radiat. Oncol. Biol. Phys.*, 53, 822-34.
- Sharp, G. C., Jiang, S. B., *et al.* 2004. Prediction of respiratory tumour motion for real-time image-guided radiotherapy. *Phys Med Biol*, 49, 425-40.
- Shepp, L. A., Hilal, S. K., *et al.* 1979. The tuning fork artifact in computerized tomography. *Computer Graphics and Image Processing*, 10, 246-255.
- Sheridan, W. T., Keller, M. R., *et al.* 1980. Evaluation of edge-induced streaking artifacts in CT scanners. *Med Phys*, 7, 108-11.
- Shimizu, S., Shirato, H., *et al.* 2000. Impact of respiratory movement on the computed tomographic images of small lung tumors in three-dimensional (3D) radiotherapy. *Int J Radiat Oncol Biol Phys*, 46, 1127-33.
- Shirato, H., Seppenwoolde, Y., *et al.* 2004. Intrafractional tumor motion: lung and liver. *Semin Radiat Oncol*, 14, 10-8.
- Shirato, H., Shimizu, S., *et al.* 2000. Physical aspects of a real-time tumor-tracking system for gated radiotherapy. *Int J Radiat Oncol Biol Phys*, 48, 1187-95.
- Shirato, H., Suzuki, K., *et al.* 2006. Speed and amplitude of lung tumor motion precisely detected in four-dimensional setup and in real-time tumor-tracking radiotherapy. *Int J Radiat Oncol Biol Phys*, 64, 1229-36.
- Sixel, K. E., Ruschin, M., *et al.* 2003. Digital fluoroscopy to quantify lung tumor motion: potential for patient-specific planning target volumes. *Int. J. Radiat. Oncol. Biol. Phys.*, 57, 717-723.
- Smeenk, C., Gaede, S., *et al.* 2007. Delineation of moving targets with slow MVCT scans: implications for adaptive non-gated lung tomotherapy. *Phys Med Biol*, 52, 1119-34.
- Smith, R. L., Sawant, A., *et al.* 2009. Integration of real-time internal electromagnetic position monitoring coupled with dynamic multileaf collimator tracking: an intensity-modulated radiation therapy feasibility study. *Int J Radiat Oncol Biol Phys*, 74, 868-75.
- Smith, W. L. & Becker, N. 2009. Time delays in gated radiotherapy. *J Appl Clin Med Phys*, 10, 2896.
- Sonke, J. J., Zijp, L., *et al.* 2005. Respiratory correlated cone beam CT. *Med Phys*, 32, 1176-86.
- Soret, M., Bacharach, S. L., *et al.* 2007. Partial-volume effect in PET tumor imaging. *Journal of Nuclear Medicine*, 48, 932-945.
- Starkschall, G., Britton, K., *et al.* 2009. Potential dosimetric benefits of four-dimensional radiation treatment planning. *Int J Radiat Oncol Biol Phys*, 73, 1560-5.
- Starkschall, G., Forster, K. M., *et al.* 2004. Correlation of gross tumor volume excursion with potential benefits of respiratory gating. *Int J Radiat Oncol Biol Phys*, 60, 1291-7.
- Steve B, J. 2006. Technical aspects of image-guided respiration-gated radiation therapy. *Medical Dosimetry*, 31, 141-151.
- Stevens, C. W., Munden, R. F., *et al.* 2001. Respiratory-driven lung tumor motion is independent of tumor size, tumor location, and pulmonary function. *Int J Radiat Oncol Biol Phys*, 51, 62-8.
- Storm, E. & Israel, H. I. 1970. PHOTON CROSS SECTIONS FROM 1 keV TO 100 MeV FOR ELEMENTS Z = 1 TO Z = 100. *Journal Name: Nucl. Data, Sect. A 7: 565-81(Jun 1970).*; *Other Information: Orig. Receipt Date: 31-DEC-71*, Medium: X.
- Tarantola, G., Zito, F., *et al.* 2003. PET instrumentation and reconstruction algorithms in whole-body applications. *J Nucl Med*, 44, 756-69.
- Tarver, R. D., Conces, D. J., Jr., *et al.* 1988. Motion artifacts on CT simulate bronchiectasis. *AJR Am. J. Roentgenol.*, 151, 1117-9.
- Taylor, M., Dunn, L., *et al.* 2011. Determination of peripheral underdosage at the lung-tumor interface using Monte Carlo radiation transport calculations. *Medical Dosimetry*.
- Taylor, M. L., Kron, T., *et al.* 2011. A contemporary review of stereotactic radiotherapy: Inherent dosimetric complexities and the potential for detriment. *Acta Oncologica*, 50, 483-508.

- Thorndyke, B., Xing, L., *et al.* 2005. Effect of Respiratory Cycle Irregularities on Image Quality in Four-Dimensional Computed Tomography. *International Journal of Radiation Oncology*Biophysics*, 63, S506-S506.
- Tian, Y., Wang, Z., *et al.* 2012. Dosimetric comparison of treatment plans based on free breathing, maximum, and average intensity projection CTs for lung cancer SBRT. *Med Phys*, 39, 2754-60.
- Timmerman, R., Abdulrahman, R., *et al.* 2007. Lung cancer: a model for implementing stereotactic body radiation therapy into practice. *Front Radiat Ther Oncol*, 40, 368-85.
- Timmerman, R., Papiez, L., *et al.* 2003. Extracranial stereotactic radioablation: results of a phase I study in medically inoperable stage I non-small cell lung cancer. *Chest*, 124, 1946-55.
- Timmerman, R., Paulus, R., *et al.* 2010. Stereotactic body radiation therapy for inoperable early stage lung cancer. *JAMA*, 303, 1070-6.
- Timmerman, R. D. 2008. An overview of hypofractionation and introduction to this issue of seminars in radiation oncology. *Semin Radiat Oncol*, 18, 215-22.
- Timmerman, R. D., Park, C., *et al.* 2007. The North American experience with stereotactic body radiation therapy in non-small cell lung cancer. *J Thorac Oncol*, 2, S101-12.
- Tsai, H. Y., Chen, M. C., *et al.* 2011. Partial ring artifact on cardiac CT: image presentation and clinical implication. *Int J Cardiovasc Imaging*, 27, 689-93.
- Tsunashima, Y., Sakae, T., *et al.* 2004. Correlation between the respiratory waveform measured using a respiratory sensor and 3D tumor motion in gated radiotherapy. *Int J Radiat Oncol Biol Phys*, 60, 951-8.
- Tyldesley, S., Boyd, C., *et al.* 2001. Estimating the need for radiotherapy for lung cancer: an evidence-based, epidemiologic approach. *Int J Radiat Oncol Biol Phys*, 49, 973-85.
- Uematsu, M., Shioda, A., *et al.* 2001. Computed tomography-guided frameless stereotactic radiotherapy for stage I non-small cell lung cancer: a 5-year experience. *Int J Radiat Oncol Biol Phys*, 51, 666-70.
- Underberg, R. W., Lagerwaard, F. J., *et al.* 2004. Four-dimensional CT scans for treatment planning in stereotactic radiotherapy for stage I lung cancer. *Int. J. Radiat. Oncol. Biol. Phys.*, 60, 1283-90.
- Underberg, R. W., Lagerwaard, F. J., *et al.* 2005. Use of maximum intensity projections (MIP) for target volume generation in 4DCT scans for lung cancer. *Int. J. Radiat. Oncol. Biol. Phys.*, 63, 253-60.
- Units, I. C. O. R., Measurements, *et al.* 1989. *ICRU report*, International Commission on Radiation Units and Measurements.
- Van De Steene, J., Linthout, N., *et al.* 2002. Definition of gross tumor volume in lung cancer: inter-observer variability. *Radiotherapy and Oncology*, 62, 37-49.
- Van Houtte, P. 2003. New potentials of radiotherapy in non-small cell lung cancer: stereotactic therapy and IMRT. *Curr Probl Cancer*, 27, 60-3.
- Vedam, S. S., Keall, P. J., *et al.* 2004. Predicting respiratory motion for four-dimensional radiotherapy. *Med Phys*, 31, 2274-83.
- Vedam, S. S., Keall, P. J., *et al.* 2001. Determining parameters for respiration-gated radiotherapy. *Med Phys*, 28, 2139-46.
- Vedam, S. S., Keall, P. J., *et al.* 2003a. Acquiring a four-dimensional computed tomography dataset using an external respiratory signal. *Phys Med Biol*, 48, 45-62.
- Vedam, S. S., Keall, P. J., *et al.* 2003b. Acquiring a four-dimensional computed tomography dataset using an external respiratory signal. *Phys. Med. Biol.*, 48, 45-62.
- Vedam, S. S., Kini, V. R., *et al.* 2003. Quantifying the predictability of diaphragm motion during respiration with a noninvasive external marker. *Med Phys*, 30, 505-13.
- Verellen, D., Depuydt, T., *et al.* 2010. Gating and tracking, 4D in thoracic tumours. *Cancer/Radiothérapie*, 14, 446-454.
- Verhaegen, F. 2002. Evaluation of the EGSnrc Monte Carlo code for interface dosimetry near high-Z media exposed to kilovolt and 60Co photons. *Phys Med Biol*, 47, 1691-705.
- Verschakelen, J. A. & Demedts, M. G. 1995. Normal thoracoabdominal motions. Influence of sex, age, posture, and breath size. *Am J Respir Crit Care Med*, 151, 399-405.
- Vinogradskiy, Y. Y., Balter, P., *et al.* 2009a. Comparing the accuracy of four-dimensional photon dose calculations with three-dimensional calculations using moving and deforming phantoms. *Med Phys*, 36, 5000-6.
- Vinogradskiy, Y. Y., Balter, P., *et al.* 2009b. Verification of four-dimensional photon dose calculations. *Med Phys*, 36, 3438-47.
- Visvikis, D., Lamare, F., *et al.* 2006. Respiratory motion in positron emission tomography for oncology applications: Problems and solutions. *Nuclear Instruments and Methods in Physics Research Section A: Accelerators, Spectrometers, Detectors and Associated Equipment*, 569, 453-457.
- Wang, L., Hayes, S., *et al.* 2009. Dosimetric comparison of stereotactic body radiotherapy using 4D CT and multiphase CT images for treatment planning of lung cancer: Evaluation of the impact on daily dose coverage. *Radiotherapy and Oncology*, 91, 314-324.

- Wang, L., Yorke, E., *et al.* 2002. Dosimetric advantage of using 6 MV over 15 MV photons in conformal therapy of lung cancer: Monte Carlo studies in patient geometries. *J Appl Clin Med Phys*, 3, 51-9.
- Webb, S. 1988. *The Physics of Medical Imaging*, Hilger.
- Weckesser, M., Stegger, L., *et al.* 2006. Correlation between respiration-induced thoracic expansion and a shift of central structures. *Eur Radiol*, 16, 1614-20.
- Weiss, E., Siebers, J. V., *et al.* 2007. An analysis of 6-MV versus 18-MV photon energy plans for intensity-modulated radiation therapy (IMRT) of lung cancer. *Radiother Oncol*, 82, 55-62.
- Weiss, E., Wijesooriya, K., *et al.* 2007. Tumor and normal tissue motion in the thorax during respiration: Analysis of volumetric and positional variations using 4D CT. *International Journal of Radiation Oncology*Biophysics*, 67, 296-307.
- Wiersma, R. D., Mao, W., *et al.* 2008. Combined kV and MV imaging for real-time tracking of implanted fiducial markers. *Med Phys*, 35, 1191-8.
- Wink, N., Panknin, C., *et al.* 2006. Phase versus amplitude sorting of 4D-CT data. *J Appl Clin Med Phys*, 7, 77-85.
- Wolthaus, J. W. H. 2009. *Four-dimensional imaging in radiotherapy for lung cancer patients*, Nederlands Kanker Instituut-Antoni van Leeuwenhoek Ziekenhuis.
- Wong, J. W., Sharpe, M. B., *et al.* 1999. The use of active breathing control (ABC) to reduce margin for breathing motion. *Int J Radiat Oncol Biol Phys*, 44, 911-9.
- Wong, V. Y., Tung, S. Y., *et al.* 2010. Real-time monitoring and control on deep inspiration breath-hold for lung cancer radiotherapy--combination of ABC and external marker tracking. *Med Phys*, 37, 4673-83.
- Woo, M. K. & Cunningham, J. R. 1990. The validity of the density scaling method in primary electron transport for photon and electron beams. *Med Phys*, 17, 187-94.
- Wu, H., Zhao, Q., *et al.* 2008. Gating based on internal/external signals with dynamic correlation updates. *Phys Med Biol*, 53, 7137-7150.
- Wulf, J., Hadinger, U., *et al.* 2000. Stereotactic radiotherapy of extracranial targets: CT-simulation and accuracy of treatment in the stereotactic body frame. *Radiother Oncol*, 57, 225-36.
- Wulf, J., Hadinger, U., *et al.* 2004. Stereotactic boost irradiation for targets in the abdomen and pelvis. *Radiother Oncol*, 70, 31-6.
- Wulf, J., Haedinger, U., *et al.* 2004. Stereotactic radiotherapy for primary lung cancer and pulmonary metastases: a noninvasive treatment approach in medically inoperable patients. *Int J Radiat Oncol Biol Phys*, 60, 186-96.
- Wurm, R. E., Gum, F., *et al.* 2006. Image guided respiratory gated hypofractionated Stereotactic Body Radiation Therapy (H-SBRT) for liver and lung tumors: Initial experience. *Acta Oncol*, 45, 881-9.
- Xu, Q., Xie, K., *et al.* 2012. A statistical study of the factors influencing the extent of respiratory motion blur in PET imaging. *Comput Biol Med*, 42, 8-18.
- Xu, Q., Yuan, K., *et al.* 2011. Respiratory motion blur identification and reduction in ungated thoracic PET imaging. *Phys Med Biol*, 56, 4481-98.
- Yaremko, B., Riauka, T., *et al.* 2005. Thresholding in PET images of static and moving targets. *Phys Med Biol*, 50, 5969-82.
- Zamora, D. A., Riegel, A. C., *et al.* 2010a. Thoracic target volume delineation using various maximum-intensity projection computed tomography image sets for radiotherapy treatment planning. *Med. Phys.*, 37, 5811-20.
- Zamora, D. A., Riegel, A. C., *et al.* 2010b. Thoracic target volume delineation using various maximum-intensity projection computed tomography image sets for radiotherapy treatment planning. *Med Phys*, 37, 5811-20.
- Zhang, P., Hugo, G. D., *et al.* 2008. Planning study comparison of real-time target tracking and four-dimensional inverse planning for managing patient respiratory motion. *Int J Radiat Oncol Biol Phys*, 72, 1221-7.
- Zhang, T., Tachiya, Y., *et al.* 2010. Phantom study on three-dimensional target volume delineation by PET/CT-based auto-contouring. *Fukuoka Igaku Zasshi*, 101, 238-46.